The Role of Damage Rate on Cavity Nucleation with Co-Injected Helium in Dual Ion Irradiated T91 Steel

By

Stephen Taller

A dissertation submitted in partial fulfillment
of the requirements for the degree of
Doctor of Philosophy
(Nuclear Engineering and Radiological Sciences)
in The University of Michigan
2020

Doctoral Committee:

Professor Gary S. Was, Chair
Professor Fei Gao
Associate Research Scientist Zhijie Jiao
Professor Emmanuelle Marquis

Stephen Taller

Staller@umich.edu

ORCID iD: 0000-0002-7323-4786

Dedication

To those who came before, to those who endure the present,

and to those who will thrive in the future.

Acknowledgements

I begin these acknowledgements with a thankful bow to my advisor, Professor Gary S. Was, for providing the opportunity to dive deeper into the field of radiation effects in materials, and providing insight, advice, guidance, and sharing some wisdom of his experiences. I have grown as a scientist and as a person resultantly. I would also like to thank my committee members, Prof. Fei Gao, Prof. Emmanuelle Marquis, and Dr. Zhijie Jiao for their insight and input, which improved this thesis.

I am very grateful to the past and present members of the Was research group, Dr. Tyler Moss, Dr. Kale Stephenson, Dr. Anne Campbell, Dr. Stephen Raiman, Dr. Justin Hesterberg, Gerrit VanCoevering, Drew Johnson, Samara Levine, Katey Thomas, Dr. Peng Wang, Dr. Miao Song, Dr. Mi Wang, Dr. Calvin Lear, Dr. Wenjun Kuang, Dr. Donghai Du, Dr. Kai Chen, Valentin Pauly, and Logan Clowers. I am also thankful for the discussions with Dr. Michael Higgins, Prof. Kevin Field, Prof. Janelle Wharry, and T. M. Kelsy Green over the course of my time as a graduate student. I am especially thankful to those who worked heavily on ion irradiations, Dr. Shyam Dwaraknath, Dr. Elizabeth Getto, Dr. Anthony Monterrosa, and David Woodley, for their practical advice, scientific discussions, and time in the laboratory.

Thank you to the past and present staff members at the Michigan Ion Beam Laboratory, Dr. Ovidiu Toader, Dr. Fabian Naab, Dr. Ethan Uberseder, Thomas Kubley, Robert Hensley, and Dr. Prabir Roy, who helped transform the laboratory to a digitally remote controlled laboratory capable of ion irradiation with multiple ions beam simultaneously. Without their experience, and hard work, these experiments would not have been possible. I want to thank the administrative

staff in the Nuclear Engineering and Radiological Sciences department, Cherilyn Davis and Jennifer Melms, and the graduate coordinator Garnette Roberts. I also want to thank the staff at the Michigan Center for Materials Characterization for help with FIB liftouts, TEM, and STEM and care of the associated equipment. Thank you to the NEUP Graduate Fellowship Program for providing funding for some of this work along with the DOE NE IRP program DE-NE0000639.

To my family, my parents, Jessica and James Taller, my sister Mariah Taller, and my grandparents George and Ernestine Gardner who supported me throughout the years. Thank you for listening, for encouraging my inquisitive nature, and for the constant tethers to reality. You taught me the value of perseverance and provided the confidence to keep improving myself and overcome the obstacles in my path.

Lastly, I would like to thank Rigel Hanbury for the many, many insightful discussions and ability to raise my spirits throughout the days and nights. I could not have succeeded in this endeavor without your support and your ability to help me realize the importance of prioritization and delegation. When the weight is shared, the force on an individual is less burdensome. Thank you for being a wall to bounce ideas, a pillar of support, and a bright star that shines in the darkest of times.

TABLE OF CONTENTS

List of Tables

List of Figures

List of Appendices

Abstract

The desire for greener solutions to fossil fuels for baseload power generation drive an interest in new nuclear power designs. The development of radiation-tolerant materials for new nuclear power plants requires extensive research, development and deployment programs. Typically, radiation effects studies are conducted using materials test reactors followed by expensive and time-consuming post-irradiation examination because of the resulting neutron induced radioactivity. Additionally, the flux of neutrons and gamma rays in a reactor dictate the radiation damage rate, temperature, and helium generation rate interdependently making the analysis for the underlying mechanisms of cavity nucleation difficult. Ion irradiation experiments allow for the separation of single variable dependencies to uncover the processes and understand the mechanisms underlying cavity nucleation with orders of magnitude higher damage rates compared to reactor irradiations and no induced radioactivity.

The objective of this thesis is to understand the roles of temperature, co-injected helium, and high damage rates on the nucleation of cavities in T91 heat 30176 by comparing dual ion irradiation and reactor irradiation. A systematic study using dual ion irradiation was conducted at 17 dpa with variations in temperature from 406°C to 570°C, irradiation damage rates from 5×10^{-5} to 3×10^{-3} dpa/s and helium injection rates from 0 to 4 appm He/dpa to compare with reactor irradiations in the BOR-60 reactor from 376°C to 524°C at 15-19 dpa and 6-9 $\times 10^{-7}$ dpa/s. Transmission electron microscopy was used to characterize the dislocation loop population and cavity size distributions in each irradiation experiment.

Bimodal cavity size distributions were observed with helium co-injection rate. Dual ion irradiation exhibited the expected bell-shaped dependence on void density with temperature. With increasing helium co-injection rate, cavity densities increased. With increasing irradiation damage rate, cavity density decreased. The cavity size distributions and dislocation loop size distributions were identical between irradiation in the BOR-60 reactor and dual ion irradiation with a shift in the irradiation temperature and helium injection rate to compensate for the increased damage rate. The cavity growth rate equation with a helium trapping-release process was used to analyze the results.

With these results and model, several conclusions were drawn. The role of helium on bubble nucleation is determined by where helium is trapped in the microstructure. At low helium injection rates helium is in vacancy clusters that evolve into bubbles. At high helium injection rates, the implanted helium atoms became bound to dislocation loops in the microstructure as the nucleating bubbles saturated with helium. The dislocation loops arrive at a saturated trap behavior earlier in the damage process in reactor compared to dual ion irradiation. The mechanism of bubble to void transition shifts from being driven by helium accumulation to the critical bubble at low damage rates to being driven by spontaneous nucleation from stochastic vacancy fluctuation at high damage rates. At high temperatures, helium accumulation to a critical radius is the only void nucleation mechanism. An increase in the helium injection rate was needed to emulate reactor irradiation with ion irradiations to offset the decreases in the cavity nucleation rates imposed by the increased temperature and damage rate in ion irradiations.

This work provided substantial insight into the complex nucleation of bubbles and voids across a range of temperatures, helium injection rates, and orders of magnitude in damage rate.

Chapter 1: Introduction

The desire for greener solutions to fossil fuels for baseload power generation drive an interest in new nuclear power designs. The advanced reactor designs "Generation IV" nuclear power plants offer many advantages over the current nuclear reactor fleet with increased safety, reduced radioactive waste generation, an extremely low carbon footprint, and more efficient use of fuel through higher levels of burnup. However, the environments in these reactors will cause the structural materials of the reactors to experience more extreme radiation fields and temperature conditions.

The energetic neutrons in nuclear reactors cause atomic displacements when a neutron strikes an atom in the lattice of the material, transfers a portion of its kinetic energy to the atom, and displaces it from its lattice site. This atom in turn collides with nearby atoms, generating a cascade of damage until the energy of each particle is below the threshold energy for displacement. The atoms displaced out of lattice positions become interstitials and empty atomic sites become vacancies with the damage on the lattice being measured as displacements per atom (dpa). The accumulation of these defects into larger structures such as dislocations loops, dislocation lines, voids and bubbles depend on many factors including the energy distribution of the incoming particles, composition, temperature, and crystal structure. Radiation can also cause chemical changes within the material through transmutation reactions, or through the segregation of individual atomic specie, resulting in precipitation or grain boundary segregation. The accumulation of radiation induced defects can cause dramatic changes to the mechanical

performance and dimensional stability of the material which could eventually lead to mechanical failure through phenomena such as embrittlement, hardening, reduction in fracture toughness, and swelling. Understanding how the processes of radiation damage work in each material is critical to enable the design of components around the detrimental effects on the properties of materials or to developing new alloys that are more tolerant to the harsh environments inside a nuclear reactor.

Historically, austenitic stainless steels were used for structural materials in light-water reactors. However, it was discovered that their susceptibility to swelling and creep made them unsuitable for fast reactor applications. After initial testing at the Fast Flux Test Facility (FFTF), ferritic-martensitic steels became the leading candidates for high temperature-high dpa applications. Ferritic-martensitic steels are body-centered cubic, iron-based alloys, with typically 7-15% chromium with a specific steel T91 nominally at 9% chromium. Minor solute elements such as Mo, Ni, Nb, Mn, Si, V, Cu, Ta, Ti and W are common additions to add strength, ductility, or reduce activation of the alloys. Relative to austenitic stainless steels, ferritic-martensitic steels have a very complex microstructure consisting of very small grains, subgrains, laths, precipitates, and a high dislocation line density. The crystal structure along with the complex microstructure of ferritic-martensitic steels provides strong sinks for point defects generated during irradiation to annihilate, increasing the radiation tolerance of the material.

The development of radiation-tolerant materials for current or new nuclear power plants requires extensive research, development and deployment programs. Typically, radiation effects studies are conducted using materials test reactors followed by expensive and time-consuming post-irradiation examination because of the resulting neutron induced radioactivity. A typical damage rate for neutrons is on the order of 10^{-8} dpa/s up to 10^{-6} dpa/s in fast reactors [1]. Therefore

both proton irradiation [2] and heavy ion irradiation [3] (~10^{-5} and ~10^{-3} dpa/s respectively) are being used to emulate neutron damage in a faster and more cost effective manner out to high levels of damage. By virtue of its high damage rate, ion irradiation is the only viable means to study microstructure evolution at high dpa (> 100 dpa) with relatively low cost, no induced radioactivity, and with primary recoil spectra similar to that from neutron irradiation [4,5]. Ion irradiation experiments with damage rates of 10^{-4} to 10^{-3} dpa/s have successfully replicated many of the features of the microstructure observed in fast reactor irradiated materials [3,6]. However, there are still critical gaps in the use of ion irradiation as a surrogate for neutron irradiation [7]. While ion beams can achieve very high damage rates, there are several drawbacks that must be considered. Ion irradiations suffer from a shallow penetration depth into materials, varying damage rate with distance from the surface, lack of transmutation, effects of injected ions as interstitials, and carbon contamination [5,8]. Many of these limitations can be overcome with careful experimental design and appropriate characterization techniques.

One such gap in the use of ion irradiation is the inclusion of helium, which is generated by transmutation reactions in nuclear reactors through (n,α) reactions and is known to play a role in the nucleation and growth of the cavity microstructure [9–13], but can also influence the dislocation microstructure [14–16] and precipitating phases [17–21]. Previous ion irradiation studies on ferritic-martensitic steels have used helium pre-implantation as a method to nucleate cavities for studying high dose microstructure evolution [22] and understanding the role of helium on cavity evolution [23]. However, the swelling behavior under ion irradiation is influenced by the mode of helium injection [24,25]. Additionally, many of the ion irradiation studies on swelling use only high damage rates to compare with the lower damage rates of neutron irradiation with no attempt to bridge the magnitude changes in damage rate. A systematic study of irradiation damage

rates and helium injection rates that captures the evolution of the cavity size distributions is necessary to understand and separate out the effects of helium and damage rate on cavity nucleation. In a reactor the flux of neutrons and gamma rays control the radiation damage rate, temperature, and helium generation rate making the analysis for the underlying mechanisms difficult. Ion irradiation experiments allow for the separation of single variable dependencies to uncover the processes and understand the mechanisms underlying cavity nucleation.

The objective of this thesis is to understand the role of temperature, co-injected helium and high damage rates on the nucleation of cavities in dual ion irradiated T91. A combination of ion irradiation experiments, with careful post-irradiation characterization techniques, coupled with a computational model were used to achieve this objective. Chapter 2 provides a background on ferritic-martensitic steels and the effects of neutron and ion irradiation on the microstructural evolution, with a focus on the effects of helium and irradiation damage rate. Chapter 3 summarizes the objective of the thesis and the approach to achieve the objective. Chapter 4 describes the experimental procedures for the ion irradiation experiments and the techniques used for post irradiation characterization. Chapter 5 summarizes the results gathered from the experiments and analytical techniques. Chapter 6 offers an interpretation and discussion of the experimental results and addresses the objective. Chapter 7 provides the conclusions drawn from this thesis and Chapter 8 suggests future work.

Chapter 2: Background

A large body of literature exists on ferritic-martensitic steels because of their potential as structural materials for high damage applications. This chapter will define the context for the work performed in this thesis by describing the microstructure of ferritic-martensitic steels and the changes induced by neutron and ion irradiation. Existing experimental and theoretical work regarding swelling and other related microstructural developments during irradiation will be considered. Several areas, such as the effects of helium and irradiation damage rate on swelling, will be highlighted and given strong focus as these areas are the topics of this thesis.

2.1 Microstructure of Ferritic-Martensitic Steels

Ferritic-martensitic steels, with a focus on chromium steels, are body centered cubic (bcc) materials with a complex microstructure. These chromium steels are either fully austenitic or have a duplex structure, austenite and δ-ferrite, at austenitizing temperatures in the range 850 to 1200°C. The austenite phase transforms to martensite during air cooling or rapid quenching to ambient temperature, and the steels are subsequently tempered to obtain a good combination of strength, ductility, and toughness. The metallurgical basis and development of high-chromium martensitic steels have been reviewed previously [26–29]. The factors determining the constitution, transformation, and tempering characteristics are briefly reviewed here with similarity to [26].

2.1.1 Physical Metallurgy of Ferritic-Martensitic Steels

The basic composition leading to a ferritic-martensitic steel is iron with varying amounts of chromium with a set amount of carbon. From [30], the figure shown below as Figure 2.1 shows the effect of chromium on the phases in an Fe-Cr-C steel. The γ-Fe loop is closed if the chromium

content exceeds about 12% [30]. However, the austenite-stabilizing elements, such as C, N, Ni, Mn, Cu, and Co, extend the γ-phase field, while the ferrite-forming elements, mainly Cr, Mo, Nb, V, W, Si, Ti, and Al contract it [31–33]. The austenite in low-carbon, low-nitrogen 9 and 12% Cr steels is stable at the normal austenitizing temperatures of 850 to 1200°C and 950 to 1150°C respectively. The tempering resistance of the steels is increased by the addition of the ferrite-forming elements and, consequently, highly alloyed commercial steels may contain some δ-ferrite. The ferrite phase inhibits austenite grain growth, but it adversely influences the strength and, directly or indirectly, the toughness [34–36].

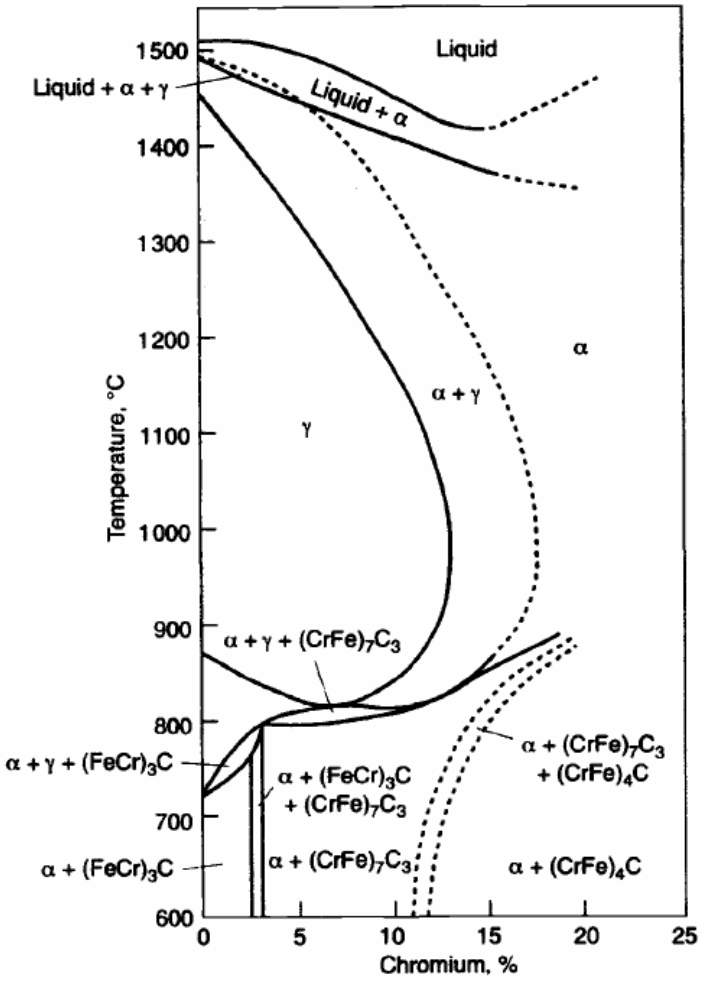

Figure 2.1. Effect of chromium on Fe-Cr-C steels containing 0.1% C from [30], reproduced from [26].

The formation of δ-ferrite can be avoided with the addition of the austenite-forming elements; thus, the balancing of the constitution to ensure 100% austenite at the austenitizing temperature may be effected using the data in [37]. Carbon is the cheapest austenite former, but is not always favored, as it decreases the toughness and impairs the weldability and corrosion resistance [29]. Furthermore, higher austenitizing temperatures are required to dissolve carbides of the MC type, where M is V, Nb, Ti, or Ta, resulting in coarser prior austenite grain sizes and reductions in toughness and creep ductility. Nitrogen can also be utilized as an austenite stabilizer, but the amount required is generally in excess. Nickel, although less effective than carbon and nitrogen, is usually used in steels for non-nuclear applications, as it has fewer adverse effects. Manganese has been considered as an alternative; however, it is inferior to nickel as an austenite stabilizer, and 0.1% C, 12% Cr steels contain some δ-ferrite even with an addition of 6% manganese [26,38]. The high-manganese steels are also prone to embrittlement during thermal aging or irradiation, possibly as a consequence of chi-phase formation [38]. Cobalt may also be employed, but, in common with nickel, has to be minimized in steels for component applications in reactor systems because of the high residual radioactivity induced by neutron irradiation.

The ferrite-forming elements V, Nb, Ta, Ti, and A1 are also effective in removing the austenite formers carbon and/or nitrogen from solution as insoluble carbides and nitrides, thereby indirectly affecting the constitution of the steels [39]. The concentration of the elements that are soluble during austenitizing of the high-chromium steels may be estimated using solubility relationships derived for low-alloy or austenitic steels [40]. The solubility products of Nb(CN), VN, and AlN in austenite have been modified by taking account of the interaction parameters between the alloying element chromium and the interstitials carbon and nitrogen, with details available in [41,42]. The solubility curves for VN, Nb(CN), and AlN in a 11% Cr martensitic steel

at 1100 °C are also found in [41,42]. The solubility of VN is significantly greater than for AlN and Nb(CN), and complete dissolution of the VN in the high-chromium steels is likely at 1100 °C and lower austenitizing temperatures. The AlN may also be completely soluble during the austenitizing treatment as the steels generally contain relatively small amounts of aluminum. However, Nb(CN) may remain undissolved at the usual austenitizing temperatures, and particles of this phase are also effective in preventing excessive austenite grain growth. Cobalt is unusual in that it raises the martensite start temperature as well as being an austenite former capable of balancing the constitution; it is therefore an important addition in steels containing large concentrations of the ferrite-forming elements [43].

The constitution of the steels at ambient temperature following cooling from the austenitizing temperature may be predicted from the Schaeffler-Schneider diagram, found in [26], from [44,45] using the nickel and chromium equivalents of the alloying elements [39,46]. Some of the 9% Cr [EM10, T91, TB9 (NF616) and E911] and 12% Cr [FI, FV448, 1.4914, MANET II, and TRII50] steels are predicted to be fully martensitic, while others are predicted to have duplex martensite plus δ-ferrite [HCM9M, NSCR9, EM12, JFMS, Tempaloy F-9, MANET I, HCMI2, TB12, and HCM12A], duplex martensite plus retained austenite [GE and HR1200], or three-phase martensite plus austenite plus δ-ferrite (HT9) structures on cooling to ambient temperature [26]. The structure of the rapidly cooled HT9 (12Cr-1MoVW) steel is reported to consist of martensite laths with high dislocation densities [47], small amounts of retained austenite in the form of islands, and δ-ferrite grains having low dislocation densities [48]. It has also been established that the δ-ferrite formation in the high-chromium martensitic steels is suppressed by maintaining a Cr equivalent element content of ≤ 9 wt% [49]; the Cr equivalent in this case is given by [50].

The austenite present at the austenitizing temperature should transform fully to martensite on cooling [51] in order to form a martensitic steel. The alloying additions made to balance the constitution or improve the tempering resistance of the steels also lower the martensite start (M_s) and finish (M_f) temperatures, resulting in a tendency for retained austenite to be present if the M_s temperature is close to or below room temperature [37]. The retained austenite increases the toughness of high-chromium transformable steels but, in other respects, it is undesirable as distortion occurs during its transformation and it decreases the strength. It follows that the composition of the steel must be adjusted not only to control the constitution but also to maintain the M_s-M_f temperature range above ambient. The coefficients of the elements in the Ni and Cr equivalent relationships are not the same as those for the effects on the M_s and M_f temperatures. A general indication of the influence of alloying elements on the M_s temperature can, however, be obtained from experimental relations, explained in more detail in [26].

2.1.1.1 Microstructure

The phase transformations and precipitation reactions that occur during anisothermal and isothermal treatments are important in regard to heat treatment and normal fabrication and welding procedures. The continuous cooling transformation (CCT) and isothermal time-temperature-transformation (TTT) characteristics of the high-chromium, 8 to 14%, conventional and reduced-activation ferritic-martensitic steels have been extensively studied using several techniques, including dilatometry, thermoelectric power, and optical and electron microscopy [52–56]. The CCT and TTT, displaying the characteristic C-curve behavior for chromium steels, diagrams for a 12Cr-MoVNb steel are compared in [53], and the CCT diagram for the reduced activation 7.5Cr-2WVTa [F82H] steel is found in [52], and displayed below in Figure 2.2 and in Figure 2.3.

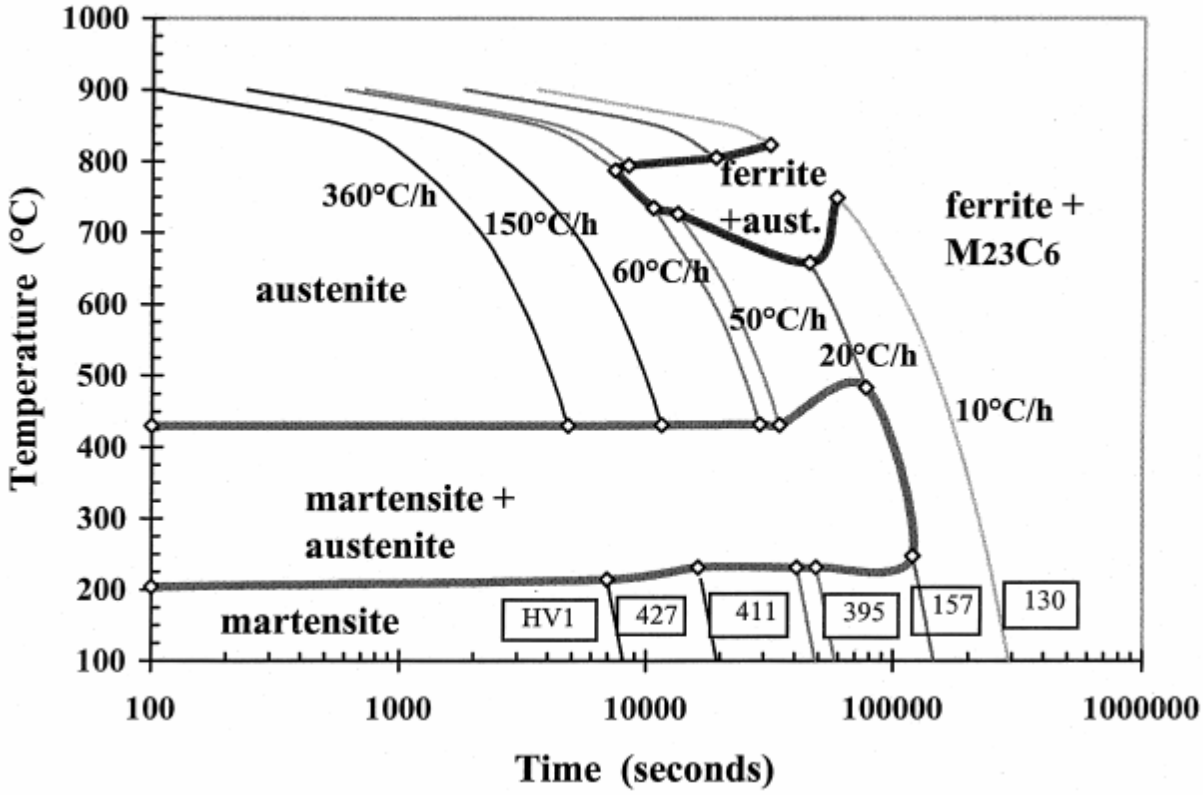

Figure 2.2. CCT diagram of F82H determined after austenitization for 30 min at 1050°C [52]

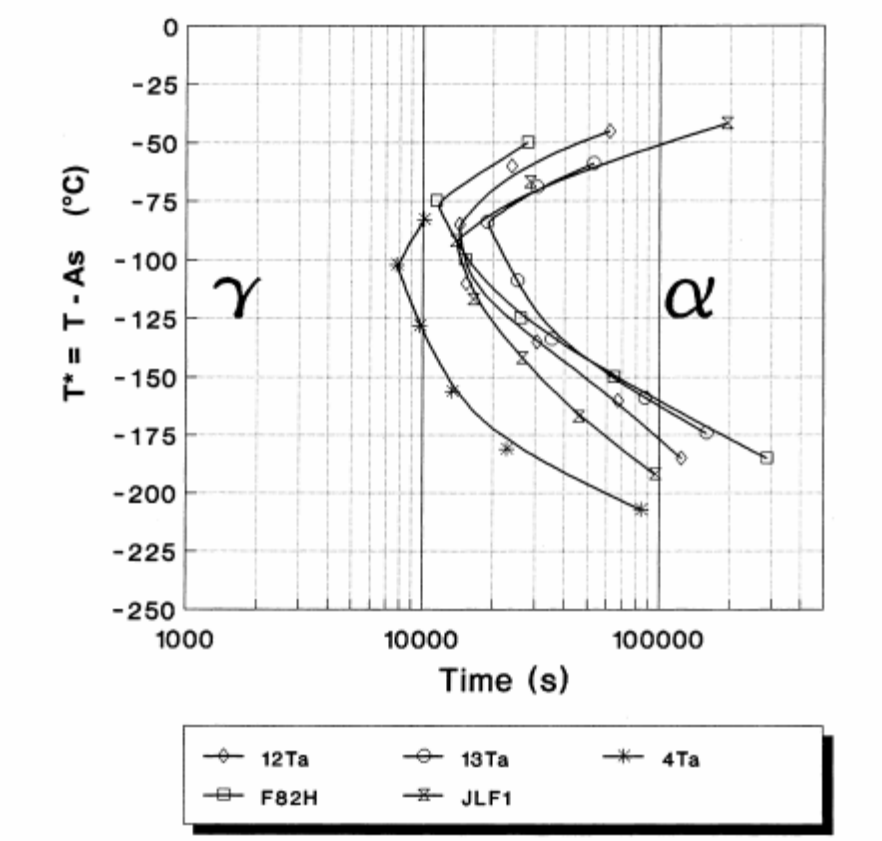

Figure 2.3. TTT diagrams for several low activation martensitic steels showing $t_{99\%}$. T* represents the shift of the temperature of isothermal transformation from starting temperature. [52]

The M_s and M_f temperatures for the high-chromium steels usually range from 250 to 350°C and 80 to 190°C respectively, but much higher $M_s \leq 450$°C and $M_f \leq 260$°C temperatures have been determined for some of the reduced-activation steels [52,53,56]. These observations and the CCT diagrams demonstrate that the steels are air hardenable, with the martensite being formed in thick sections because the pearlite transformation is greatly slowed and bainite is not formed even within extended time periods. The martensite produced is typical low-carbon lath martensite; the hardness of the as-quenched martensite in the high-chromium ferritic-martensitic steels increases linearly with increasing interstitial carbon and nitrogen contents [52,53,57] and is given in [53]. The martensite hardness is not significantly dependent on the chromium, tungsten, vanadium, and

tantalum contents, austenitizing temperature, and microstructural characteristics, and depends mainly on the prior austenite grain size and martensite lath width and length [52].

The tempering of the martensite is performed at temperatures below the Ac1, the temperature at which the α to γ transformation beings on heating, to avoid reaustenitization and thereby achieve the optimum combination of strength and toughness. Nickel, manganese, and, to a lesser extent, copper all lower the Ac1 temperature, while the ferrite-forming elements Si, Mo, V, and Al increase it [37,51]. The difference measured Ac1 and Ac3, the temperature at which the α to γ transformation is complete, temperatures in the ranges 760 to 850°C and 870 to 960°C, respectively, are quoted for conventional and reduced-activation steels [52,53,56]. The respective Ac1 and Ac3 temperatures for a series of 9Cr-0.8WTa reduced-activation steels are comparable and the transformation behavior on heating is not significantly dependent on the interstitial element and tantalum concentrations [52]. Increased chromium, ~11%, and tungsten, ~2 to 3%, contents result in higher transformation temperatures.

Slowed softening occurs during tempering of a simple, low-carbon 12% Cr steel at temperatures up to about 500°C while pronounced softening occurs at 500 to 550°C [29,37]. The rate of softening decreases progressively above 550°C. The hardness changes at different tempering temperatures can be correlated with the microstructural changes as follows [29,58,59]. Below 350°C, a fine dispersion of M_3C (Fe_3C) precipitates forms and grows to a dendritic morphology and then to a plate-like Widmanstätten distribution. The chromium content of the Fe_3C increases to about 20% with the possibility of M_7C_3 being formed *in situ* from the Cr-enriched Fe_3C [60]. Both these effects slow down the growth rate of the Fe_3C and thereby slow softening. At about 450-500°C needles of M_2X [predominantly $Cr_2(CN)$] nucleate primarily on the dislocations within the martensite laths and slow the softening, but the precipitation is not

sufficiently intense to produce secondary hardening. At about 500-550°C M_7C_3 and M_2X phases coarsen, with a resulting rapid decrease in hardness. Greater than 550°C M_7C_3 and M_2X are replaced by Cr-rich $M_{23}C_6$ precipitates, which nucleate on the martensite lath and prior austenite grain boundaries, and the rate of decrease of hardness slows down. The dislocation density decreases relative to that of the "as-quenched" martensite, and sub-structures consisting of low-angle boundaries and dislocation arrays begin to form. At about ≥ 650°C $M_{23}C_6$ precipitates at the tempered lath martensite boundaries grow, leading to a further reduction in dislocation density and pronounced sub-grain formation across the martensite laths. At about ≥ 750°C sub-cells within the martensite laths grow into fairly equiaxed sub-grains with little or no trace of the original lath martensite structure. Growth of the $M_{23}C_6$ precipitates continues, but clearly defined dislocation networks may still be present. Virtually all the carbon in solution in the steels is precipitated as $M_{23}C_6$ on tempering for ≥ 1 h at 700 to 780°C [47].

It follows that over aging during tempering of these steels is associated with the removal of M_2X from within the martensite laths and the growth of the grain boundary $M_{23}C_6$. These processes allow the dislocations to form polygonal networks. Further coarsening results in the sub-boundaries becoming unpinned and growth of equiaxed areas of ferrite occurs with the boundaries being composed of well-defined dislocation arrays. This has been referred to as recrystallization during tempering, but it is also referred to as a form of sub-grain growth [29].

The tempering characteristics of simple high-chromium steels are modified by alloying additions [29,58,59,61]. The presence of 0.02 to 0.03% nitrogen causes the hexagonal Cr_2N (M_2X) phase to form in preference to the rhombohedral M_7C_3 and increases the intensity of the secondary hardening and over aged hardness. Carbon is also effective in promoting secondary hardening by increasing the volume fraction of the M_2X phase. Nickel, which is present in the majority of the

12% Cr steels to balance the constitution, accelerates carbide over aging and thus slightly decreases the tempering resistance. The ferrite formers Mo, W, and V are soluble in the M_2X and increase its lattice parameter and the associated coherency strains, resulting in secondary hardening and increased tempering resistance [62]. However, silicon increases the coherency strains and the tempering resistance by dissolving in the matrix and decreasing its lattice parameter [33]. Vanadium, niobium, tantalum, and titanium form carbides, nitrides, or carbonitrides [VC, VN, Nb(CN), Ta(CN), and TiN/TiC] at higher temperatures than those at which M_2X precipitates. These phases are very stable and increase the resistance to over aging and tempering. Any soluble V, Nb, Ta, and Ti also produce solid solution strengthening and slow recovery and growth of the sub-grains at the highest tempering temperatures. The solubilities of various carbides and nitrides in ferritic steels have been documented and reviewed [41,63] and will not be repeated here.

The development of higher creep-rupture strength 9-12% Cr steels containing various combinations of N, Mo, W, V, Co, Cu, Nb, and Ta is based on optimizing the constitution and δ-ferrite content, increasing the stability of the martensite dislocation structure, and maximizing the solid solution and precipitation hardening. The intensity of the precipitation hardening by carbides and nitrides of the V(CN) and Nb(CN) types is enhanced in steels having the appropriate stoichiometric ratios [64]. The W-containing intermetallic compounds appear to coarsen at a slower rate than the Mo variant, resulting in higher strength, ductility, and toughness.

In summary, the microstructures of the conventional high-chromium martensitic steels in the normalized-and-tempered condition consist of: (a) martensite laths about 1μm wide and ≥ 5μm long [47], containing dislocations with a Burgers vector $1/2a_0<111>$ and a density of approximately 10^{14}-10^{15} m^{-2} [65] and (b) coarse $M_{23}C_6$ particles located at prior austenite and ferrite grain boundaries with finer precipitates within the laths and at the martensite lath and sub-

grain boundaries; M_2X precipitates rich in chromium and isomorphous with $(CrMoWV)_2(CN)$ within the martensite laths and δ-ferrite phase; primary (Nb,Ta)X; and fine secondary (V,Nb,Ta)X.

2.2 Radiation Damage in Ferritic-Martensitic Steels

Radiation damage can occur in ferritic-martensitic steels from nearly any source of radiation, whether it is neutrons, ions, electrons, or gamma rays. All of these forms of radiation have the capability to displace atoms from their lattice sites. The effect of irradiation on materials is rooted in the initial event in which an energetic projectile strikes a target. While the event is made up of several steps or processes, the primary result is the displacement of an atom from its lattice site. The kinetics of the projectile strike on a target lattice atom are discussed in detail in a number of sources [66,67], and will not be reproduced here. Irradiation displaces an atom from its site, leaving a vacant site behind (a vacancy) and the displaced atom eventually comes to rest in a location that is between lattice sites, becoming an interstitial atom. The vacancy-interstitial pair, known as a Frenkel pair, makes up the basis for radiation effects in crystalline solids. Irradiation events can produce many Frenkel pairs as damage from a single event cascade. The accumulation and diffusion of the resulting point defects form the foundation for the observed effects of irradiation on the physical and mechanical properties of materials.

The formation, growth and dissolution of defect aggregates such as voids, dislocation loops, and other features, depend upon the diffusion of point defects and their reaction with the defect aggregates. They also depend upon the concentration of point defects in the solid. The concentration at any point and time is a balance between the production rate, and the loss rate of point defects and is adequately described by the point defect balance equations. The increase in diffusion or enhancement of atom mobility in an irradiated metal is due to two factors: the enhanced concentration of the defects from the damage cascade, and the creation of new defect

species. The development of radiation-induced vacancy and interstitial concentrations occurs due to competing processes. Frenkel defects are created from the collisions between high-energy particles and lattice atoms. These defects can be lost either through recombination of vacancies and interstitials or by reaction with a defect sink, such as void, dislocation, dislocation loop, grain boundary or precipitate. The local change in defect concentration of the various defect species can be written as the net result of the local production rate, reaction with other species, and diffusion into or out of the local volume.

The point defect balance equations can be broken up into four cases [66]: (1) low temperature, low sink density, (2) low temperature, intermediate sink density, (3) low temperature, high sink density, and (4) high temperature. While all of these cases are relevant to the general effects of concentrations of defects on solids, ferritic-martensitic steels, having a complex microstructure of grain boundaries, lath boundaries, precipitates, dislocations, and other features, fall into the third category for most reactor relevant conditions. The main effect of a high sink density is that interstitials find the sinks before they find vacancies. The time relationship with the concentration of defects can be broken into four regions. In the first region, both interstitials and vacancies buildup without reactions. In the second region, the concentration of vacancies continues to increase while the interstitials reach a semi-steady state as they arrive at sinks. The concentration of interstitials decreases when the concentration of vacancies is high enough to lead to mutual recombination in the third region. Eventually, both the interstitial and vacancy concentrations will reach steady states and begin to form extended defects. These extended defects are responsible for many of the macroscopic changes observed from irradiation.

The first of these extended defects is the dislocation. The interactions of dislocations, a line of either interstitials or vacancies that forms a boundary between a region of the crystal that has

slipped and one that has not, with intrinsic point defects are of importance in understanding the processes of plasticity, hardening, and irradiation creep. Plasticity is enabled through the presence of dislocations, which lower the stress needed to deform a material. Additionally, dislocations act as sinks for point defects, affecting dislocation growth and the subsequent swelling of irradiated materials. Although this section is dedicated to dislocation microstructure, the effects of dislocations on ferritic-martensitic steels are important to nearly every radiation induced change in the material. During the early stages of irradiation of ferritic-martensitic steels, defect clusters appear to be rather uniformly distributed within grains, and a saturation density is quickly reached. However, with further irradiation, self-ordering alignment of defect clusters was found in some grains at doses as low as 3 dpa whereas in other grains the defect spatial distribution remained uniform. Once the aligned structure was created, it was stable up to 15 dpa. The stress caused by a high density of loops would be minimized by the regular arrangement of defects clusters. The preferred crystallographic orientation of defect arrays may be driven by the minimization of elastic interaction energy between defect clusters.

Voids in ferritic-martensitic steels are also one of the extended defects that form during irradiation and lead to irradiation induced swelling. In the radiation damage process, equal numbers of vacancies and interstitial atoms are created as Frenkel pairs. The dislocations in most ferritic-martensitic steels have a slightly higher preference for the interstitials, leaving the concentration of vacancies higher in the metallic lattice. The excess vacancies can migrate and form clusters. These clusters are stabilized by the diffusion of gases, such as helium produced by (n,α) transmutation reactions, to form three dimensional cavities with a preferential spherical shape. Austenitic stainless steels, having been heavily used in the nuclear industry extensively, are well researched. The major and minor elemental components in austenitic steels, as well as the

heat treatment, have been shown to influence the incubation and transient doses before swelling continues at a near constant rate of about 1% per dpa, with the length of the transient regime varying. Body centered cubic materials, such as pure iron, iron alloys, ferritic, bainitic, and martensitic steels with varying levels of chromium, have also been researched heavily and show a much greater resistance to void swelling than the austenitic steels, having a face centered cubic structure. The swelling rates for bcc steels are lower than austenitic stainless steels, closer to ~0.1% per dpa or lower compared to 1% per dpa [68].

Another large factor in the microstructural evolution of ferritic-martensitic steels under irradiation is radiation-induced segregation and precipitation. The strong interaction between solutes and the point defects, generated during irradiation, results in coupled transport of the solute atoms by the point-defect fluxes to and away from sinks, such as grain boundaries, free surfaces, dislocations loops, and void surfaces. The magnitude of the solute-point defect binding energy determines whether the solute flow is towards or away from the sinks. A Modified Inverse Kirkendall Effect has been shown to be the primary mechanism for Cr RIS in ferritic-martensitic steels [69]. This segregation also leads to new irradiation induces phases in the ferritic-martensitic steels. These phases are most commonly chromium-rich ferrite (α'), M_6X (η), G phase, and sigma phase (σ). These are primarily formed by the enrichment of chromium (α'), nickel and silicon (G phase), with phosphorus (σ). These changes in phases, along with the growth of dislocations and voids simultaneously, make the evolving microstructure of ferritic-martensitic steels under irradiation complex.

As a result of these microstructural changes, the macroscopic properties of the ferritic-martensitic steels also see alteration. The loss of ductility in ferritic-martensitic steels during irradiation can be caused by many factors, including hydrogen and helium. It has been concluded

from discussions of the mechanisms responsible for the hydrogen embrittlement in the high-chromium martensitic steels that hydrogen is transported to microstructural features and regions of triaxiality during tensile testing by lattice diffusion and mobile dislocation sweeping and is eventually trapped at interfaces and dislocations. The embrittlement then results from either one or a combination of the following processes: the interaction of the hydrogen with dislocations such that plastic flow is localized on specific slip planes, with cross slip possibly being inhibited, and leading to shear modes of failure, and the lowering of the cohesive strength of the interfaces on which the hydrogen has accumulated, thereby promoting brittle modes of fracture. The most widely accepted model of helium embrittlement is based on the stress-induced growth of cavities nucleated from helium bubbles at the grain boundaries. The helium bubbles of a certain radius are initially equilibrium with the internal gas pressure being balanced by the surface tension. The bubbles on the grain boundaries orthogonal to the applied tensile stress become unstable and grow by grain boundary vacancy condensation if the stress exceeds a critical value. Intergranular helium bubbles of nanometer dimensions have been observed to nucleate cavities that enlarge and coalesce to form cracks on the transverse grain boundaries in irradiated austenitic steels and alloys in a manner analogous to the growth of cavities during thermal creep. Irradiation creep, however, involves stress-induced processes that enhance the annihilation of irradiation-produced point defects.

In general, the deformation processes involve the stress-induced absorption of irradiation-produced point defects on dislocations that cause the dislocations to climb, which can subsequently lead to glide of the dislocations. For irradiation creep to occur, the absorption of point defects at dislocations must be asymmetric, for if vacancies and interstitials were partitioned equally, annihilation would occur without climb, and there would be no creep. Proposed mechanisms for

irradiation creep include swelling-driven creep (I-creep), Stress Induced Preferential Absorption (SIPA) creep, and Preferred Absorption Glide (PAG) creep. I-creep involves climb-enabled glide that occurs because dislocations have a slight bias for interstitials, and these interstitials induce dislocation climb; the excess vacancies are incorporated in voids. Under the influence of a stress, pinned dislocations can bow out to give an increment of elastic strain. The bias-driven interstitials at dislocations can cause them to climb around the pinning obstacles and glide until they encounter another obstacle and are again pinned. Each time this process is repeated, an increment of creep strain occurs, with the creep rate depending on the climb velocity. In SIPA creep, dislocations are assumed to be sinks for both vacancies and interstitials, but there is a slight bias for interstitials to be absorbed by dislocations with their Burgers vectors aligned with the stress axis. This preferential absorption due to the stress-induced higher capture efficiency of the dislocations with properly aligned Burgers vectors causes dislocation climb and deformation in the stressed direction. PAG creep is due to climb-enabled glide; that is, first, the dislocations climb around obstacles by the SIPA process, after which the dislocations can glide under the influence of the applied stress until they are again stopped by an obstacle.

In conclusion, the point defects created as part of the radiation damage process provide the basis for the changes of ferritic-martensitic steels under irradiation. The point defects gather to form clusters and from there, agglomerate into extended defects, such as dislocations, voids, precipitates. They can also cause segregation of elements in the material. These extended defects cause macroscopic changes in ductility, creep strength, hardness, tensile behavior, etc. All of these macroscopic and microscopic changes in ferritic-martensitic steels make predicting the full behavior under irradiation complex.

2.3 Swelling in Ferritic-Martensitic Steels

Since the initial observation of voids in irradiated materials [70], they have been the subject of much research. The theory of nucleation and void growth, as well as the thermodynamics of gas containing voids, has been published [71–73] and reviewed [74]. Modeling efforts have also been done to understand the behavior of point defects in ferritic steels [75,76]. The primary objective of this section is to provide a review of the experimental undertakings over the years and the conclusions of these studies. This section follows a similar logic and approach to the work done by Klueh and Harries [26] and Garner et al. [68] with additional material added.

In the radiation damage process, equal numbers of vacancies and interstitial atoms are created as Frenkel pairs. The dislocations in most ferritic-martensitic steels have a slightly higher preference for the interstitials, leaving the concentration of vacancies higher in the metallic lattice. The excess vacancies can migrate and form clusters. These clusters are stabilized by the diffusion of gases, such as helium produced by (n,α) transmutation reactions, to form three dimensional voids with a preferential spherical shape. The formation of these voids is partially influenced by the temperature of the material. At low temperatures, defined as 30% of the melting temperature, T_m, the vacancies are slow to diffuse, allowing for recombination with the relatively more mobile interstitials. At relatively high temperatures, greater than 50% of T_m, the thermal vacancy concentration exceeds that caused by the irradiation environment. Thus, the stability of these three dimensional defects is limited to the temperature range 0.3-0.5 T_m [66].

The swelling to damage relation is typically represented as being composed of three regimes, an incubation regime, a transient regime, and a linear swelling regime. In the incubation regime, the swelling is very low, less than 0.1%, and can be considered negligible up to an incubation dose. In the linear swelling regime, the total swelling can be described by a linear relation with the difference between the total dose and the incubation dose multiplied by a swelling rate. Between

these two regimes is a transient period to merge the incubation and linear swelling regimes into a continuous function [73,77].

2.3.1 Neutron Irradiation of Ferritic-Martensitic Steels

Under neutron irradiation, helium production via (n,α) reactions is controlled by the neutron energy spectrum of the reactor and the energy dependent cross sections based on the elemental components of the material. Typical helium production has been estimated for fast reactors from ~0.1 appm helium/dpa [78] to ~1.0 appm helium/dpa [79] but varies strongly with composition. This section attempts to gather relevant neutron irradiation experiments to elucidate the effect of helium/dpa on the cavity evolution.

Little [80] presents a general overview of the microstructural evolution of ferritic-martensitic steels under irradiation. For swelling, Little describes the viability of using ferritic-martensitic steels for their superior swelling resistance as compared with austenitic steels. Figure 2.4 shows how swelling in ferritic-martensitic steels is much lower compared to swelling in austenitic stainless steels for a given damage level under a variety of irradiation spectrums.

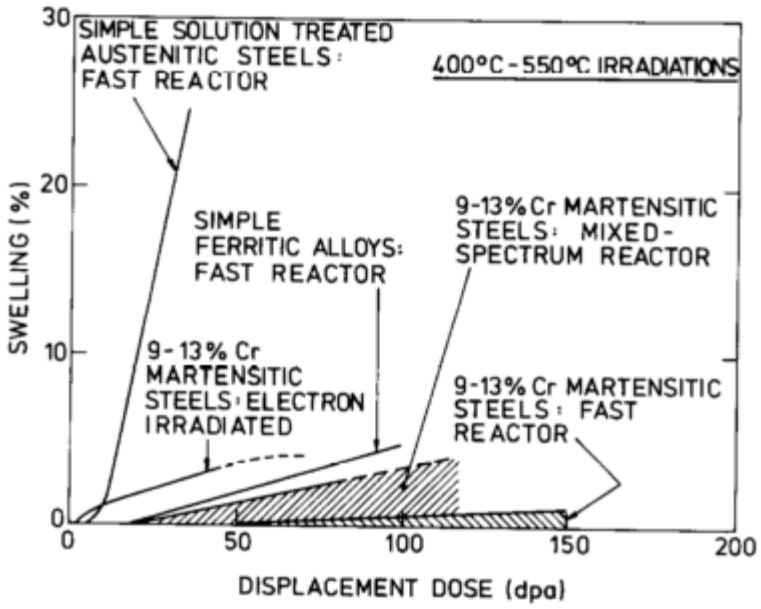

Figure 2.4. Swelling of ferritic-martensitic and austenitic alloys are displayed under a variety of irradiation spectrums.

In general, it is observed that increasing amounts of Cr from pure iron tend to increase the swelling resistance. Little continues to propose that ferritic-martensitic steels with 9-12% Cr exhibit the highest swelling resistance at dpa values >100. However lower levels of swelling (<0.5%) are also observed for higher Cr steels (14-22%). The resistance to swelling is also coupled with a large increase in incubation period.

Vitek *et al.* [79] irradiated a 9Cr-1MoVNb steel in HFIR at 300°C, 400°C, 500°C, and 600°C to about 36 dpa with an estimated helium/dpa ratio of 0.83 appm helium/dpa. Few cavities of roughly 4-6nm in diameter were observed at 300°C, 500°C, and 600°C with a homogenous distribution at 300°C and heterogeneously nucleated at dislocations and lath boundaries at 500 and 600°C. At 400°C, the cavities have an average size of 15 nm with a density of 1.1×10^{21} m^{-3} and swelling of 0.19%.

The work of Wakai *et al.* [81,82] explored the effects of helium on cavity development in the reduced activation ferritic-martensitic steel F82H doped with natural boron, boron-10, nickel-

58, and nickel-60 to produce helium/dpa ratios of ~0.5 to ~10 appm helium/dpa when irradiated in HFIR to 51 dpa at 300°C and 400°C. At the lower temperature, cavities were observed only in the highest helium/dpa ratios of 6.5 and 9.9 appm helium/dpa. At 400°C, however, cavities were observed in nearly all variations of F82H. As the helium/dpa ratio was increased, the average cavity size decreased, but the number density came to a peak in the F82H tailored with boron-10 (6.5 appm helium/dpa).

For comparison to the works presented previously, several studies done in FFTF are presented with an assumed nominal helium/dpa ratio of 0.2 appm helium/dpa. Kai *et al.* [83] irradiated a 9Cr-1MoVNb, 9Cr-2WV, 9Cr-2WVTa, and a 12Cr-1MoVW to about 35 dpa at 420°C resulting in cavity densities ranging from 0.05-6 x 10^{20} m^{-3} and average sizes from 25-30nm. Kimura *et al.* [84] irradiated several Fe9Cr-2(1)W alloys to about 40 dpa at 420°C, resulting in average cavity sizes from 20-31nm and densities from 1.6-8.2 x 10^{20} m^{-3}. Sencer *et al.* [85] examined a duct of HT9 used in the FFTF reactor that reached an estimated 155 dpa at 443°C with an average cavity size of 28nm and density of 2.5 x 10^{20} m^{-3}. Van den Bosch *et al.* [86] examined FFTF irradiated T91 irradiated at about 413°C to 184 dpa resulting in an average cavity size of 29nm and 8.3 x 10^{20} m^{-3}. Finally, T91, HT9, MA 956 and MA 957 were examined in the work of Gelles *et al.* [87] at about 200 dpa. The average cavity sizes ranged from 21-35nm and densities from 1.9-48 x 10^{20} m^{-3}. Examining the data from FFTF there is a little concern that the cavity sizes are all in the same range despite the large differences in damage level. However, as the cavities are influenced by the entire microstructure, there are many complicating factors that cannot be sorted out without additional information.

In a recent paper, Getto *et al.* [22] provided a review of swelling in the ferritic-martensitic steels HT9 and T91 irradiated in-reactor up to 208 dpa at temperatures ranging from 400°C to

443°C, reproduced in Figure 2.5. There is a significant amount of scatter in the swelling reported, but in general as the damage level increases, the amount of swelling also increases. There are also variations in different heats of the same alloy, and single heats undergoing different heat treatments. Up to the high damage level of 208 dpa though, the amount of swelling is still < 3%, highlighting the overall swelling resistance of ferritic-martensitic steels.

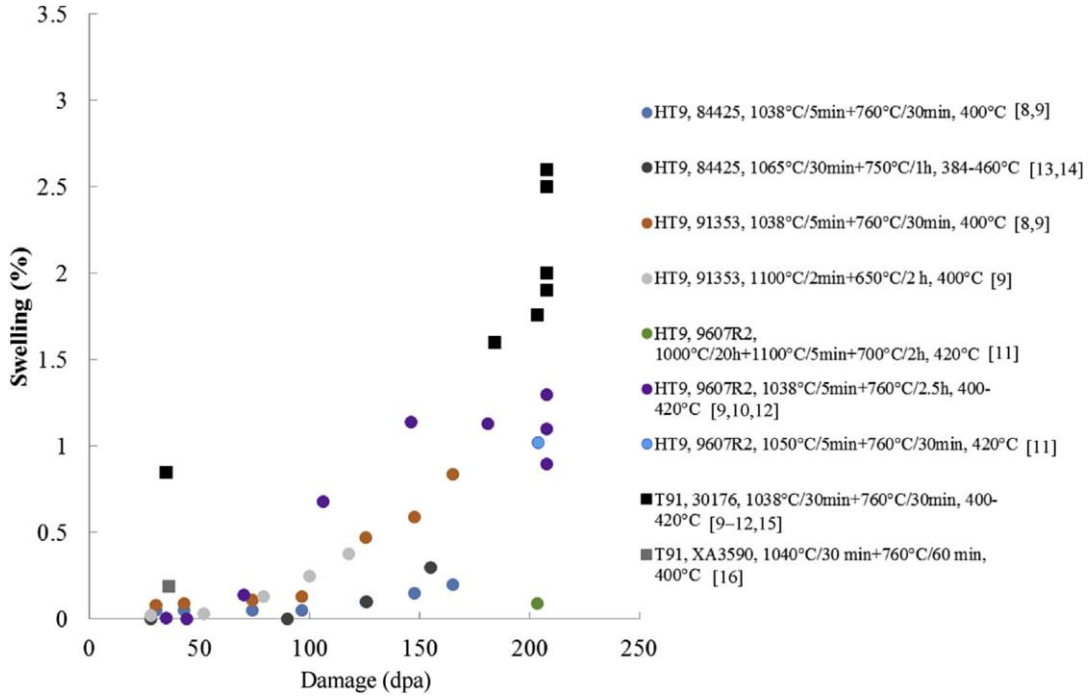

Figure 2.5. Summary of ferritic-martensitic steels irradiated in-reactor up to 208 dpa at temperatures varying from 400°C to 443°C, reproduced from [22].

2.3.2 Heavy Ion Irradiation of Ferritic-Martensitic Steels

In order to understand the radiation responses of material at an accelerated rate compared to neutron irradiation, ion irradiation experiments have been performed at high damage rates to simulate the effects of damage seen in reactor at high damage levels.

A ferritic steel (Fe2.25Cr-1 Mo) was studied by Sindelar *et al.* [88]. The focus of this studying was to determine the microstructural response to irradiation at various damage levels and in different phases of the material. Irradiation was performed up to 350 dpa at 500°C using 14

MeV nickel ions. No cavities were present in any of the samples unless helium was pre-injected at 100 appm.

The ferritic-martensitic alloy T91 was studied by Gigax et al. [89] using 3.5 MeV iron ions at 475°C up to 550 dpa at the region examined. The swelling response indicated low swelling (< 3%) up to 410 dpa but a sudden increase to 22% swelling at 550 dpa for a rate of 0.11%/dpa. Maximum swelling occurred at approximately half of the projected ion range, supposedly due to the defect imbalance effect [90]. Swelling of T91 had an incubation period of swelling of ~400 dpa at the depth of peak swelling, greater than incubation periods from neutron irradiated T91. However, in reactor the production of helium will drive cavity nucleation and therefore, decrease the incubation period for swelling. This ion irradiation study was conducted without considering the effects of helium and this may account for the delay in the incubation period.

The swelling and microstructure evolution of ferritic-martensitic alloys HT9, T91, and T92 were investigated by Getto et al. [22] using iron ions and 10 appm helium pre-implanted to obtain systematic evolution from 75 to 650 dpa. Contrary to the previous study, for the least swelling resistant alloy (HT9), a swelling rate of 0.033%/ dpa was observed from 188 to 650 dpa. Swelling resistance was higher in T91 at a rate 0.007%/ dpa. The decrease in swelling/swelling rate in T91 was primarily due to suppression of cavity nucleation, rather than growth, which proceeded at approximately 0.1 nm/dpa. Swelling resistance was highest in T92, which had not yet reached steady state swelling by 650 dpa due to a low density of small cavities, indicating suppression of both nucleation and growth. Analysis of additional heats of T91 indicated that alloy composition was not the primary factor in determining swelling resistance. In addition to swelling increasing with damage level, the volume fraction of G-phase precipitates and line length of dislocation were found to evolve in the microstructure up to 650 dpa as shown in Figure 2.6. The

use of ion irradiations has been instrumental in determining that the microstructure of ferritic-martensitic steels will continue to evolve with damage level beyond intended reactor lifetimes.

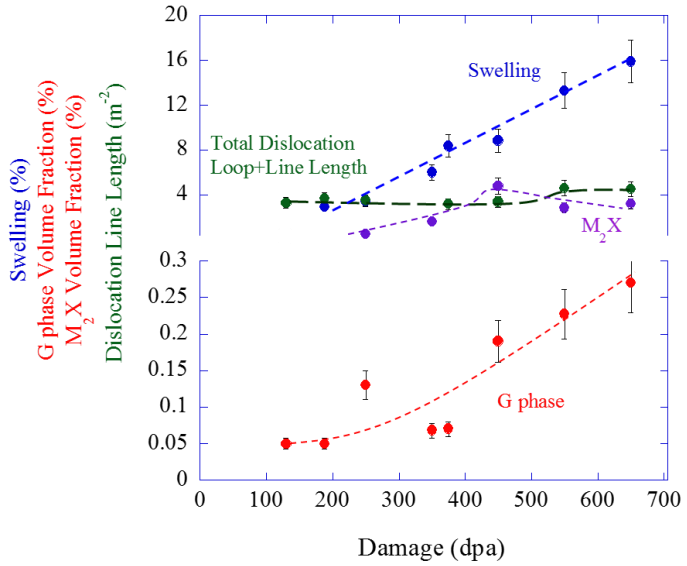

Figure 2.6. Microstructural evolution of HT9 irradiation with 5 MeV iron ions at 460°C from 130 to 650 dpa from [22].

2.4 Factors Affecting Cavity Nucleation and Evolution

2.4.1 Impact of Temperature on Cavity Evolution

Cavity nucleation rate is strongly dependent on the vacancy super-saturation. Therefore, changes in temperature which affect the super-saturation of vacancies will affect the length of the nucleation region as well. Theory has shown that swelling follows a bell-curve temperature dependence based on the melting temperature of the material, T_m [91]. Cavity formation and swelling tends to prevail at irradiation temperatures from about $0.3T_m$ to about $0.5T_m$. Below this temperature range, vacancies are unable to diffuse and cluster together to form cavity embryos. Nucleation of cavities decreases with increasing temperature outside of this range due to a higher emission of vacancies from clusters. In this intermediate temperature range, there is a temperature

where the vacancy flux to a cavity embryo is largest compared to the vacancy emission. Vacancies have limited mobility at these temperatures and will recombine with interstitials before clustering into cavities. This behavior can be described by the number of vacancies required for a critically stable cavity to form [92]:

$$n = \frac{36\pi\gamma^3\Omega^2}{3(kT)^3\left[ln\left(\frac{B_v(n)-B_i(n+1)}{B_v^0(n)}\right)\right]^3}, \quad \text{Eq. 2.1}$$

where $\gamma$is the surface energy, Ω is the atomic volume, k is Boltzmann's constant, T is temperature and $\frac{B_v(n)-B_i(n+1)}{B_v^0(n)}$ represents the vacancy super-saturation. Both temperature and vacancy super-saturation appear in the denominator. At low temperatures and low vacancy super-saturations, the number of vacancies n becomes extremely large, and cavity nucleation is an unlikely event. At high temperatures, the vacancy super-saturation is reduced, from the increase in thermal vacancies and emission of vacancies to be lost to other sinks and therefore $n$will also become prohibitively large.

Dvoriashin and colleagues [93] studied a ferritic-martensitic steel EP-450 after irradiation in a fast reactor. Swelling was studied as a function of temperature in the range of 275ºC - 690ºC. Figure 2.7 shows swelling rate as a function of temperature demonstrating the characteristic bell-curve dependence. A peak is observed around 420ºC. Considering the lower damage data points at 11 dpa have a larger swelling rate than those at either 46 dpa or 89 dpa, it is likely that these swelling rates are representative are more representative of a nucleation rate rather than a growth rate, and therefore demonstrating that nucleation follows a similar bell-curve.

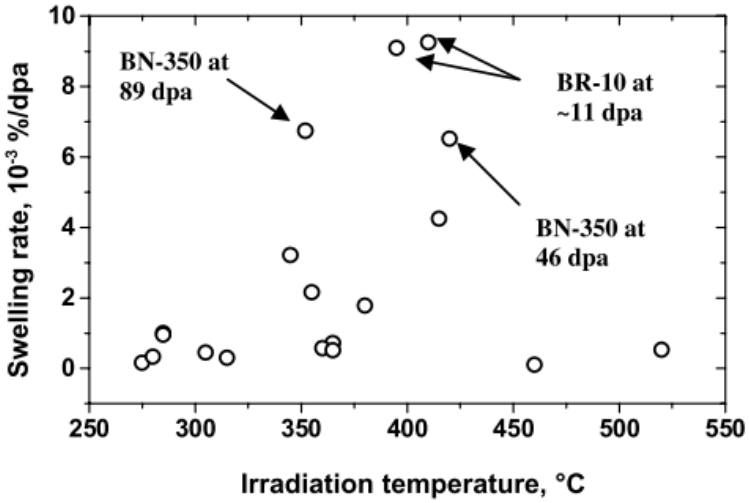

Figure 2.7. Temperature dependence of swelling rate in EP-450 [93].

Ayrault [94] studied the effect of irradiation temperatures above 450°C on a 9Cr-1Mo steel. No swelling peak was found, but the highest swelling occurred at 450ºC. This may suggest that the tail-end of a temperature peak was caught in this study and the peak would appear somewhere close to 450ºC.

Hide *et al.* [95] studied the response to irradiation of six different ferritic alloys with 200keV C^+ and 3 MeV Ni^+: MA957 (an ODS alloy), HT9, Fe-12Cr, 12Cr-2Mo, 9Cr-8Mo-4Ni (solution anneal), 9Cr-8Mo-4Ni (aged). These metals were studied at damage levels ranging from 50 – 200 dpa and temperatures from 425-625°C. All of the samples were pre-injected with helium to a fixed ratio of 0.1 appm/dpa. All alloys exhibited peak swelling at 575°C. Although this value is higher than the previously suggested values between 400-500°C, the higher damage rate is expected to shift the swelling bell-curve to higher temperatures [73,96].

Kai and Kulcinski [97] studied HT9 irradiated with nickel ions at three different temperatures: 400ºC, 500ºC , and 600ºC. Cavities were only observed at 500ºC. The intermediate temperature seemed the only temperature which allowed for cavity nucleation.

Schmidt *et al*. [98] observed a peak swelling temperature of 500ºC in HT9 and 550ºC in EM-12 after irradiation with 2.8 MeV Fe^{+} ions up to 250 dpa. The dependence of swelling as a function of temperature is shown in Figure 2.8.

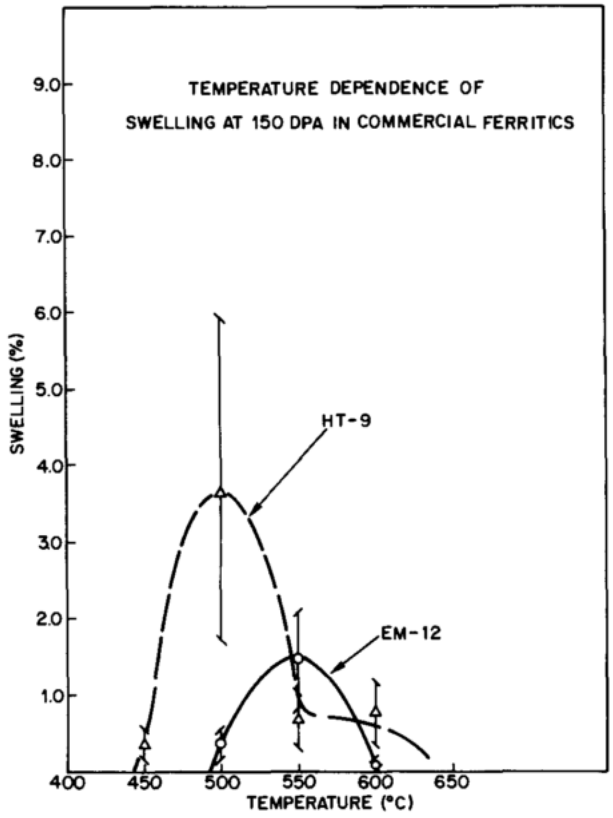

Figure 2.8. Temperature dependence of swelling at 150 dpa for EM-12 and HT9 [98].

Sencer *et al.* [85] irradiated HT9 in FFTF and found a peak swelling temperature at about 443ºC. However, it must be noted that the damage level was also highest at this temperature (155 dpa compared to 28 dpa at 384ºC), which may cloud the effect of temperature.

Wakai *et al*. [99] showed highest swelling at 470ºC, which then decreased with increasing temperature. Ferritic-martensitic steel F82H was irradiated with a triple beam system (Fe^{+}, He^{+}, and H^{+}) at temperatures from 470ºC to 600ºC. It is likely that a peak swelling temperature is present at a temperature lower than that studied in this paper.

Getto *et al.* [6] studied swelling in HT9 at temperatures ranging from 400°C to 480ºC after irradiation up to 375 dpa using Fe^{2+} ions and 10 or 100 appm helium pre-implanted. The peak swelling temperature was determined to be near 460ºC. At lower and higher temperatures 480ºC and 440ºC, it was determined that the onset of swelling was delayed relative to experiments performed at 460ºC. The swelling behavior as a function of temperature at 188 dpa is shown in Figure 2.9. This set of experiments suggested that cavity nucleation was enhanced closer to the peak swelling temperature.

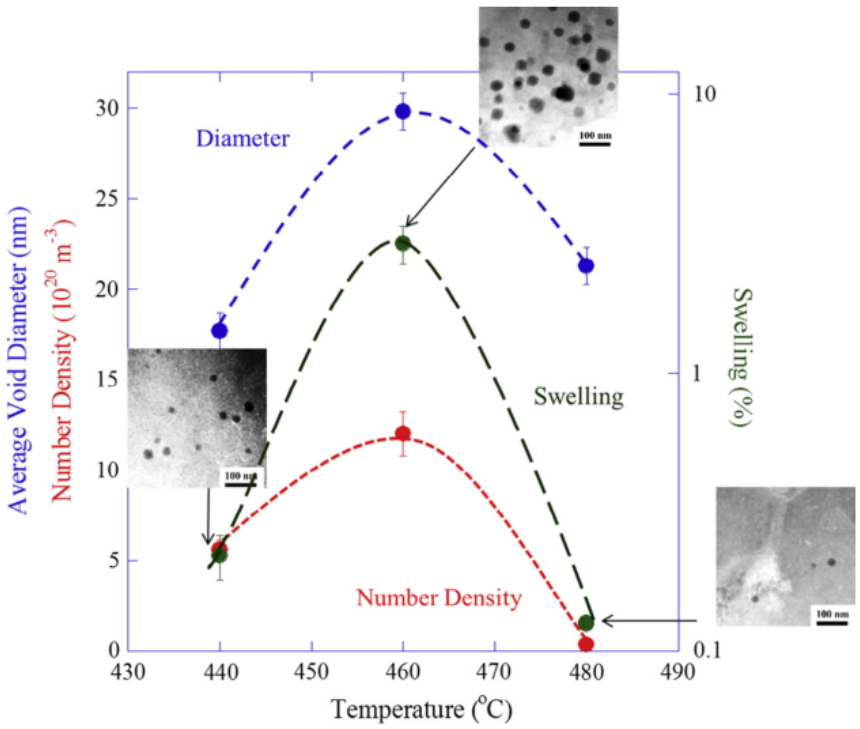

Figure 2.9. Temperature dependence of swelling, diameter, and number density at 188 dpa for HT9 [6].

Toloczko *et al.* [100] performed a study on a MA957 tube up to 500 dpa at a variety of temperatures, 400ºC, 420ºC, 450ºC, and 500ºC. The peak swelling temperature was determined to be near 450ºC. The swelling results are shown in Figure 2.10. The study compared the swelling

behavior at damage levels of 100 and 500 dpa. However, the coarseness of these doses does not allow for the determination whether steady-state swelling was achieved. It does, however, provide further evidence that nucleation was enhanced at doses closer to the peak temperature.

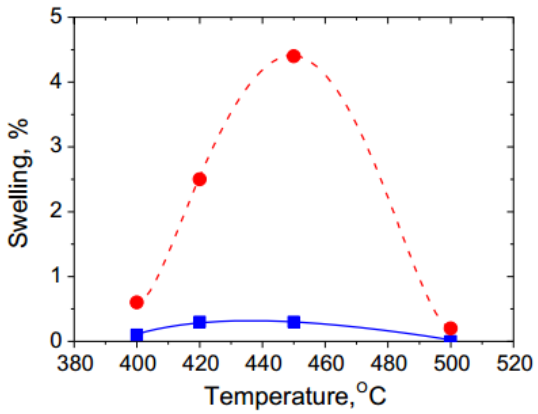

Figure 2.10. The temperature of dependence of swelling is shown for MA 957 at 500 dpa (red curve) and 100 dpa (blue curve) from [100].

The authors compared the swelling behavior of MA-957 to that of HT9 and EP-450. The swelling as a function of dose are shown up through about 500 dpa in Figure 2.11. A steady-state swelling value of 0.2%/dpa was determined for HT9 and EP-450. However, it is important to note that EP-450 was irradiated at a different temperature (480°C) compared to MA-957 and HT9. MA-957 exhibited the lower swelling up to 500 dpa and the achievement of steady-state has not yet been confirmed. This is further supported by the cavity size distributions in the paper, which are skewed to smaller sizes.

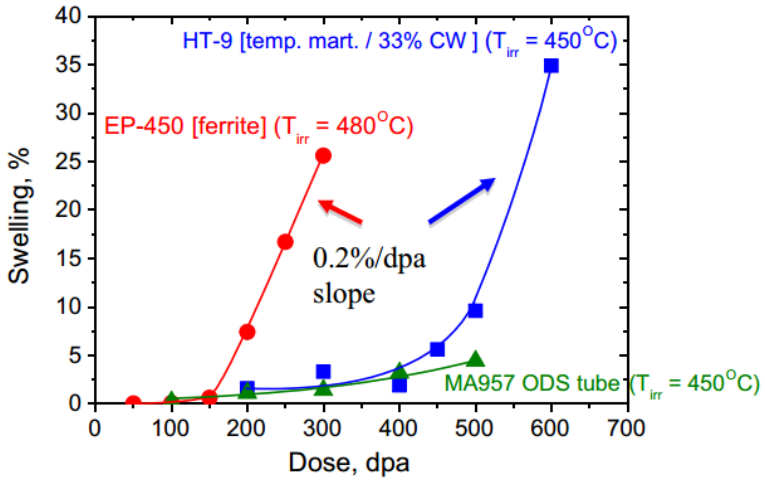

Figure 2.11. The swelling dependency for MA 957, HT9, and EP-450 are shown through ~600 dpa from [100].

Per both theory and the studies described here; a swelling peak is expected at an intermediate temperature range. For neutron irradiations, this peak may be approximately centered at 420°C-440ºC. For ion irradiations, it may be higher from ~460ºC-500ºC. This swelling peak is usually referred to as occurring at steady state, however since the processes affecting the growth of cavities also govern nucleation behavior (i.e. super-saturation of vacancies), these concepts can also be extended to cavity nucleation. Therefore, the swelling at low damage levels would also be expected to have a peaked behavior at an intermediate temperature.

Qualitatively, there is evidence that swelling follows the expected bell-curve behavior, and so it is reasonable to assume that nucleation behavior will follow, due to its large role in determining overall swelling behavior. However, there is a very little direct experimental evidence that suggests this is the case. This is due to the difficulty in determining the transition from nucleation to growth dominated behavior. Garner [68] postulated that there exists a "universal steady-state swelling rate" independent of temperature, but this has not been experimentally confirmed. A systematic set of experiments at incremental temperatures and incremental damage

levels would be required to identify the location of the peak swelling temperature and possible changes during the transition from nucleation to growth dominated swelling.

2.4.2 Helium Effect on Cavity Evolution

Neutron Irradiation of Ferritic-Martensitic Steels

Under neutron irradiation, helium production via (n,α) reactions is controlled by the neutron energy spectrum of the reactor and the energy dependent cross sections based on the elemental components of the material. Typical helium production has been estimated for fast reactors from ~0.1 appm helium/dpa [78] to ~1.0 appm helium/dpa [79] but varies strongly with composition. This section attempts to gather relevant neutron irradiation experiments to elucidate the effect of helium/dpa on the cavity evolution.

Vitek *et al.* [79] irradiated a 9Cr-1MoVNb steel in HFIR at 300°C, 400°C, 500°C, and 600°C to about 36 dpa with an estimated helium/dpa ratio of 0.83 appm helium/dpa. Few cavities of roughly 4-6nm in diameter were observed at 300°C, 500°C, and 600°C with a homogenous distribution at 300°C and heterogeneously nucleated at dislocations and lath boundaries at 500 and 600°C. At 400°C, the cavities have an average size of 15 nm with a density of 1.1×10^{21} m^{-3} and swelling of 0.19%.

Complimenting the previous study, Hashimoto *et al.* [101] irradiated a 9Cr-1MoVNb steel and 9Cr-2WVTa and additional alloys with 2Ni added to increase helium generation during irradiation in HFIR to about 12 dpa at 400°C with about 2-2.5 appm helium/dpa in the base alloys and 12-13 appm helium/dpa in the nickel doped alloys. Irradiation of the nickel doped alloys resulted in smaller cavities on average and a larger density of cavities compared to the non-nickel doped alloys. However, the amount of swelling was still small in both cases with the largest swelling occurring in the 9Cr-1MoVNb at 0.17%.

The work of Wakai *et al.* [81,82] explored the effects of helium on cavity development in the reduced activation ferritic-martensitic steel F82H doped with natural boron, boron-10, nickel-58, and nickel-60 to produce helium/dpa ratios of ~0.5 to ~10 appm helium/dpa when irradiated in HFIR to 51 dpa at 300°C and 400°C. At the lower temperature, cavities were observed only in the highest helium/dpa ratios of 6.5 and 9.9 appm helium/dpa. At 400°C, however, cavities were observed in nearly all variations of F82H. As the helium/dpa ratio was increased, the average cavity size decreased, but the number density came to a peak in the F82H tailored with boron-10 (6.5 appm helium/dpa).

For comparison to the works presented previously, several studies done in FFTF are presented with an assumed nominal helium/dpa ratio of 0.2 appm helium/dpa. Kai *et al.* [83] irradiated a 9Cr-1MoVNb, 9Cr-2WV, 9Cr-2WVTa, and a 12Cr-1MoVW to about 35 dpa at 420°C resulting in cavity densities ranging from 0.05-6 x 10^{20} m^{-3} and average sizes from 25-30nm. Kimura *et al.* [84] irradiated several Fe9Cr-2(1)W alloys to about 40 dpa at 420°C, resulting in average cavity sizes from 20-31nm and densities from 1.6-8.2 x 10^{20} m^{-3}. Sencer *et al.* [85] examined a duct of HT9 used in the FFTF reactor that reached an estimated 155 dpa at 443°C with an average cavity size of 28nm and density of 2.5 x 10^{20} m^{-3}. Van den Bosch *et al.* [86] examined FFTF irradiated T91 irradiated at about 413°C to 184 dpa resulting in an average cavity size of 29nm and 8.3 x 10^{20} m^{-3}. Finally, T91, HT9, MA 956 and MA 957 were examined in the work of Gelles *et al.* [87] at about 200 dpa. The average cavity sizes ranged from 21-35nm and densities from 1.9-48 x 10^{20} m^{-3}. Examining the data from FFTF there is a little concern that the cavity sizes are all in the same range despite the large differences in damage level. However, as the cavities are influenced by the entire microstructure, there are many complicating factors that cannot be sorted out without additional information.

Dual Ion Irradiation of Austenitic Steels and FCC Alloys

Although ferritic-martensitic steels are the focus of this work, the studies of Katoh *et al.* [102,103] combined together experimental and modeling information on dual ion irradiated solution annealed Type 316 stainless steel to examine the effects of the helium/dpa ratio on the cavity density (separated into bubbles and voids), cavity radius, and swelling. For the voids shown in Figure 2.12, designated in this work as large cavities, the number density exhibited a bell curve behavior with regards to the helium/dpa ratio with a peak near 15 appm helium/dpa at 25 dpa. For the same level of damage, the average void size decreased with increasing helium/dpa ratio. For bubbles observed at 25 dpa, the density increased with increasing helium/dpa ratio. This study also examined the effect of the damage rate dependence of the helium/dpa ratio on swelling using a rate theory model. For the same temperature, see Figure 2.13, the model predicts as the damage rate is increased, the helium/dpa ratio needed for peak swelling also increased. However, there is no experimental data presented to validate this prediction.

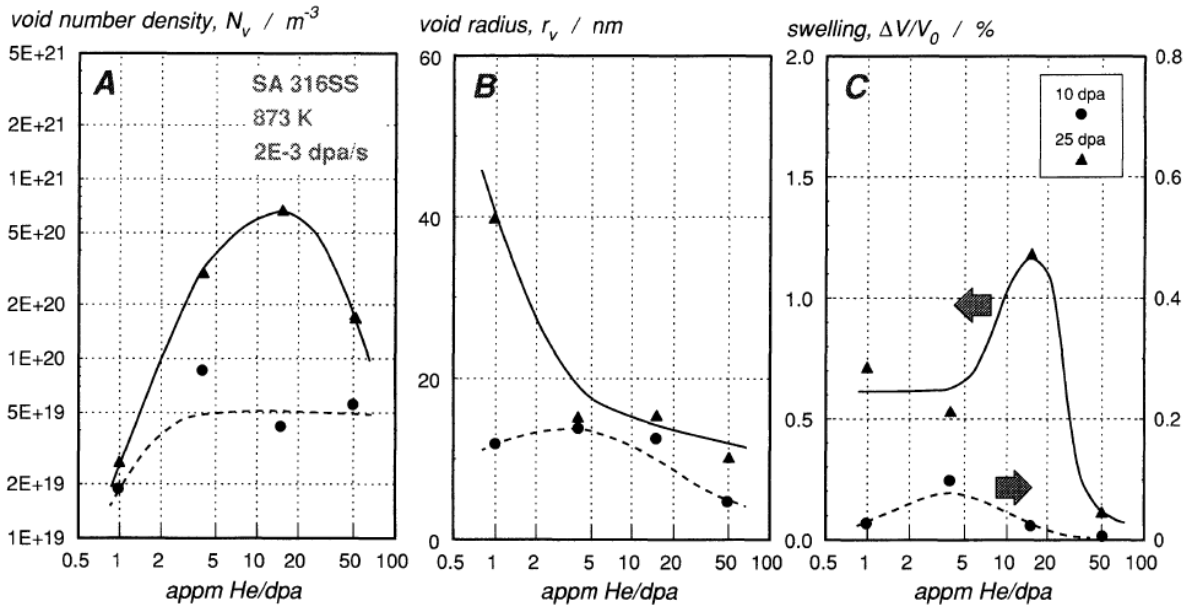

Figure 2.12. He/dpa dependence of (A) void number density, (B) mean void radius and (C) swelling in dual-ion irradiated 316 stainless steel from [102,103].

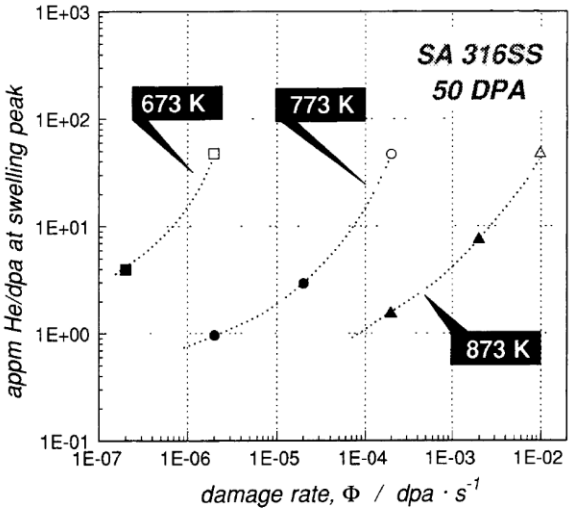

Figure 2.13. Predicted damage rate dependence of the He/dpa ratio at which peak swelling occurs from [102].

The effects of helium and its relationship with damage rate have been presented in [104] and discussed in a review by Abromeit [105]. Using dual ion irradiation, the effects of the He/dpa ratio on swelling across a range of damage rates from 10^{-4} to 10^{-2} dpa/s were investigated. As shown in Figure 2.14, increasing the helium/dpa ratio increased the swelling overall. However, for the same He/dpa ratio, as the damage rate increased, the amount of swelling decreased. The exact reasons for this decrease are not discussed as no microstructural information is presented. Speculation could suggest an increase in the density of cavities and lower growth of any individual cavity as the damage rate is increased.

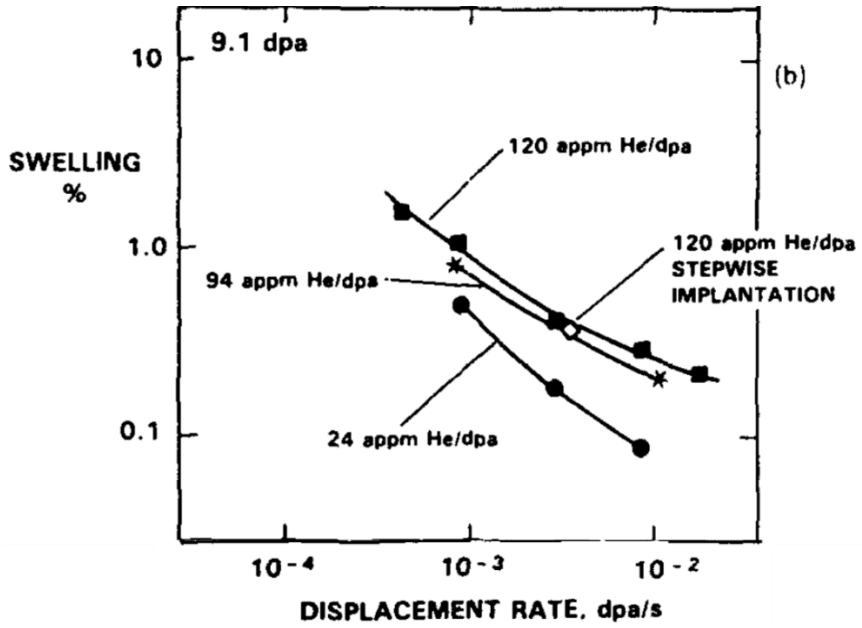

Figure 2.14. The influence of helium and displacement rate on nickel-ion induced swelling from [104], reproduced in [105].

Similar behavior can be found in other austenitic stainless steels [15,21,106–109] and in simple FCC materials such as copper [110,111] and nickel [112,113]. In these materials, a monotonic increase in cavity density and corresponding decrease in cavity size with increasing He/dpa ratio at a given irradiation temperature and damage was observed. The peak cavity swelling has been reported to occur near 10-30 appm He/dpa in neutron-irradiated FCC metals, such as copper in Figure 2.15 from references [110,114–119].

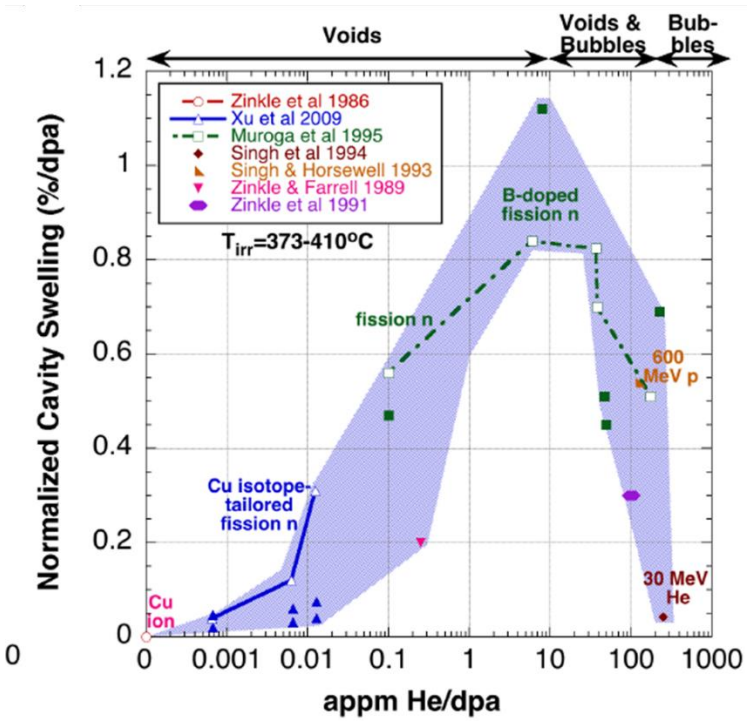

Figure 2.15. Normalized cavity swelling as a function of He/dpa ratio for copper irradiated between 373 and 410°C. Figure produced by S. Zinkle from [110,114–119].

Dual Ion Irradiation of Ferritic-Martensitic Steels

Asano *et al.* [12] performed a study on the ferritic-martensitic steel HT9 using dual ion irradiation to 25 dpa with 15 appm helium/dpa at several temperatures (350°C, 410°C, 470°C, 530°C, and 600°C), and up to 100 dpa with 5 appm helium/dpa or 15 appm helium/dpa. At 25 dpa, the highest swelling occurred at 470°C with a bimodal cavity size distribution. At higher temperatures of 530°C and 600°C, the cavities were associated with dislocations and grain boundaries. For the HT9 irradiated to 100 dpa at 450°C, a helium/dpa ratio of 15 appm helium/dpa resulted in a bimodal cavity distribution while the lower helium/dpa ratio of 5 appm helium/dpa formed only small cavities.

In the work of Kupriiyanova *et al.* [120], the ferritic-martensitic steel EP-450 was dual ion irradiated at 480°C up to 200 dpa with up to 160 appm helium/dpa. At 50 dpa, as the helium/dpa ratio was increased from zero, the average size decreased and number density of cavities increased

resulting in increased swelling with increased helium/dpa ratio. However at 200 dpa, the swelling decreased with increasing helium/dpa ratio from the decrease in cavity size. Similar trends at 200 dpa were observed in other ferritic-martensitic steels F82H and EK181 also studied in this work.

Ogiwara *et al.* [121] dual ion irradiated two reduced activation ferritic-martensitic steels JLF-1 and JLS-1 from 40-100 dpa with 15 appm helium/dpa at 470°C and 550°C. Significant swelling was observed only at 470°C in both alloys.

The work of Wakai *et al.* [122] irradiated the ferritic-martensitic F82H to 50 dpa with 18 appm helium/dpa at 470°C, 510°C, and 600°C. With increasing temperature the cavity density was reduced but not significantly, such as 5.2×10^{21} m^{-3} at 470°C to 4.6×10^{21} m^{-3} at 600°C and average cavity sizes ranging from 5.2 to 6.7 nm. From this information, it is likely that all of the cavities observed are stabilized by the co-injected helium and have limited growth from the high temperature.

The work of Hiwatashi *et al.* [123] explored the effects of dual ion irradiation on several reduced activation ferritic-martensitic steels JLF1, JLF3, JLF4, JLF5, and two model alloys Fe9Cr2Mo and Fe2.25Cr1Mo up to 125 dpa and 0, 1, and 15 appm helium/dpa at 450°C. In both JLF4 and the model alloy Fe2.25Cr1Mo, the average cavity size decreased and density increased with increasing helium/dpa ratio with the highest swelling occurring at the intermediate value of 1 appm helium/dpa.

Yamamoto *et al.* [124] performed several dual ion irradiations on a ferritic-martensitic alloy, F82H3 and two nanostructured ferritic alloys MA957 and 14YWT-PM2 at 500°C and 650°C from 15-55 appm helium/dpa with significant characterization at 10 dpa and 26 dpa in F82H3 and MA 957. This work found no significant systematic trend in the cavity density, average cavity

density, or swelling with helium/dpa, but found a systematic increase in average cavity diameter with increasing helium content.

Although the materials used in the work of Bhattacharya *et al.* [125] were not commercial ferritic-martensitic steels, the model iron-chromium alloys (Fe, Fe3Cr, Fe5Cr, Fe10Cr, Fe12Cr, Fe14Cr) dual ion irradiated to 128 dpa with 13 appm helium/dpa at 500°C provided insight into the effect of chromium addition on swelling. The Fe10Cr alloy displayed the highest amount of swelling, primarily from its increased cavity density, as the sizes for all model alloys had similar cavity sizes.

The study of Brimbal *et al.* [126] performed dual ion irradiation on Fe and Fe5Cr to 100dpa with 0, 2.5, and 26 appm helium/dpa at 500°C to examine the effects of helium and chromium on swelling. As the helium/dpa ratio was increased in the pure iron, the average cavity size decreased and the cavity density increased. However, cavities were only observed in the Fe5Cr at the highest helium/dpa ratio of 26 appm helium/dpa with a very high density of cavities and small average size.

2.4.3 Effects of Damage Rate and Helium Co-Injection Rate

From the neutron and dual ion irradiated ferritic-martensitic steels, a picture of the overall effect of the helium/dpa ratio can be attempted. Several assumptions have been made going into this picture, such as the assumption that any FFTF irradiated material had a helium/dpa ratio of about 0.2 appm helium/dpa and the assumption that materials irradiated in the same reactor have the same nominal damage rate. Consolidating all of the available cavity information from neutron irradiations performed between 400-500°C and 12-200 dpa [78,79,81–87,101] and dual ion irradiations from 10-125 dpa between 360-600°C [12,120–126], the trends of cavity density, Figure 2.16b, average cavity size, Figure 2.16a, and swelling, Figure 2.16c with the helium/dpa

ratio can be obtained. Because of the high sink density in ferritic-martensitic steels, the damage rate and the vacancy concentration are expected to be linearly dependent, and thus Figure 2.16 an also be viewed as the helium/vacancy ratio.

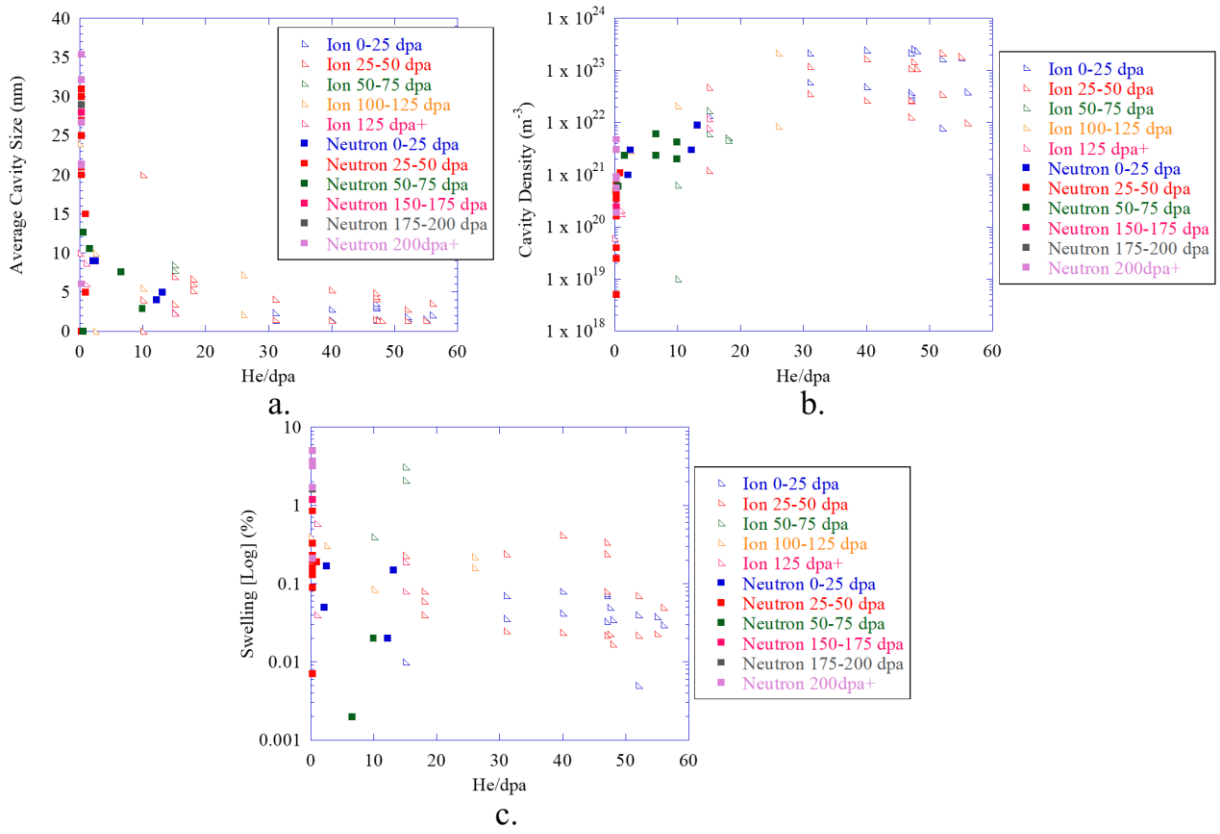

Figure 2.16. Compilation of literature data to show the effect of the helium/dpa ratio on (A) average cavity size, (B) average cavity density, and (C) swelling.

As the helium/dpa ratio increases, the average cavity diameter appears to decrease. The cavity density also appears to increase with increasing helium/dpa ratio up to about 30 appm helium/dpa. The swelling appears to decrease with increasing helium/dpa ratio. Although the trends are visible, there is still significant scatter in the available data. Given the possible variations in cavity evolution with temperature, material composition, heat treatment, and across damage rates, these trends have still emerged. Graphing the same set of cavity data as a function of the

irradiation damage rate, Figure 2.17, similar trends do not emerge. While the cavity densities can be considered similar between the low damage rates of neutron irradiation and the high damage rates of ion irradiation, the significant differences in the helium/dpa ratio, and therefore helium/vacancy ratio, make the comparison questionable. The dependence of damage rate on cavity evolution is not discernable from the literature included in this review. This is likely in part from the lack of reporting on the damage rate for many of the neutron irradiation studies.

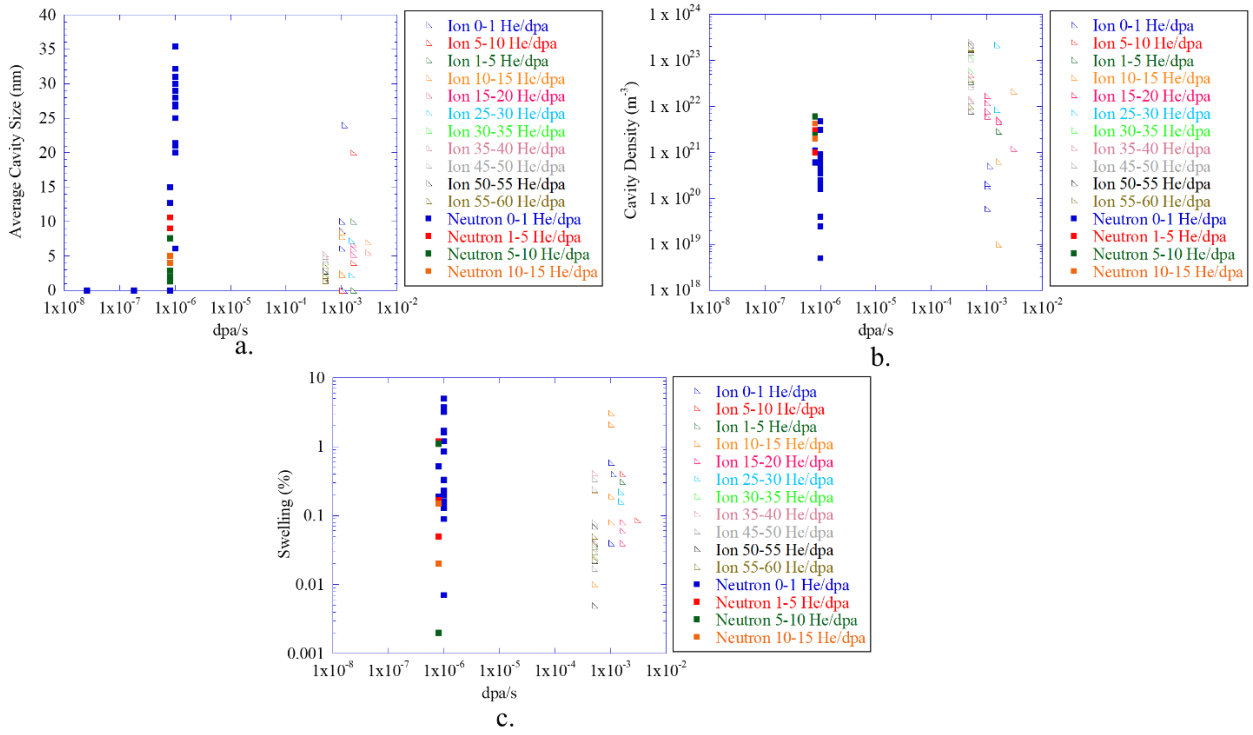

Figure 2.17. Compilation of literature data to show the effect of the damage rate on (A) average cavity size, (B) average cavity density, and (C) swelling.

2.4.4 Theoretical Considerations

Russell [71,72,127] presents the thermodynamics of voids and gas-containing cavities in metals. For the cavity to be in equilibrium with the solid around it, the external pressure of the solid on the cavity must be equal to the internal pressure from the gas atoms with the surface energy taken into account as well. This theory presents that the size of the cavity is proportional

to the density of the gas occupying the cavity, and the volume of the cavity itself. The internal pressure of a gas in any individual cavity is difficult to measure, but has been estimated by using Electron Energy Loss Spectroscopy [128], as done in [129–132] for helium bubbles in aluminum and ferritic-martensitic alloys.

The production of inert gas atoms in reactors acts to stabilize subcritical cavities, and from this process, encourage nucleation of stable cavities. Helium is the focus of many inert gas studies as it is commonly produced in reactor materials through nuclear transmutation reactions. Helium is thought to enhance the nucleation of cavities by lowering the free energy requirement to create a critical cavity embryo. The free energy equation for voids without any gas is driven by the supersaturation of vacancies (S_v) and countered by the energy required to form an interface in the material:

$$\Delta G = -nkT\, ln(S_V) + (36\pi\Omega^2)^{1/3}\gamma n^{2/3}. \qquad \text{Eq. 2.2}$$

In the presence of helium, the free energy equation for cavities becomes:

$$\Delta G = -nkT\, ln(S_V) + (36\pi\Omega^2)^{\frac{1}{3}}\gamma n^{\frac{2}{3}} - xkT\, ln\left(\frac{MHn\Omega}{xkT}\right), \qquad \text{Eq. 2.3}$$

where *x* corresponds to the number of helium atoms in the cavity, *M* is the concentration of helium atoms in the solid (usually in atoms/cm^3 or equivalent), and *H* is the Henry's Law constant for the dissolution of helium in the metal. From comparing Equations 2.2 and 2.3, the presence of helium lowers the free energy required to form a stable cavity, with the added term being the free energy required to move the helium from the solid into the cavity. This lower free energy results in a smaller critical cavity nucleus, and thus enhancing nucleation relative to a gas-free environment.

Hishinuma [92] and Mansur [133] discuss the effect of helium in terms of a critical radius required for a cavity to stabilize and grow. These works highlight a derivation of the critical radius, the radius at which the net flux of vacancies to the cavity is zero, to include the functional

dependences on gas pressure, dislocation and cavity capture efficiencies, temperature, damage rate, and other variables. By examining the critical radius, the emergence of a bimodal cavity size distribution is discussed with one distribution around the radius of a gas-stabilized bubble and the other distribution arising from cavities with a large enough inward flux of vacancies to grow.

To investigate the importance of helium to cavity nucleation, Stoller and Odette [134] studied the effect of the cluster composition (helium vs. vacancy) on the nucleation path of cavities. Two paths emerge to limit cavity formation: one limited to growth by helium accumulation alone, the other limited by stochastic fluctuations in the vacancy cluster population. The accumulation of gas seemed to be the generally dominant mechanism. Specific cluster compositions and distributions are not analyzed, however. This work was also analyzed in the context of austenitic stainless steels, and its applicability to ferritic-martensitic steels has still not fully emerged.

Stoller and Osetsky [135] evaluated the behavior of helium in bcc iron using molecular dynamics. This work found that when a helium bubble is in mechanical equilibrium with the iron lattice, the helium/vacancy ratio decreases as the bubble increases in size. The compressibility of the helium also decreases with increasing bubble size, leading to ideal gas behavior for the helium. However, the bubbles presented in these simulations are less than 5 nanometers in size and would result in barely visible structures under TEM. The simulations found that the helium to vacancy ratio for equilibrium bubbles large enough to be visible is in the range of 0.3-1.0, consistent with electron energy loss spectroscopy results in ferritic-martensitic steels [129,130].

One mechanism of helium related to swelling is the generation of Frenkel pairs via a loop punching mechanism [136–138]. Small clusters of helium atoms produce lattice distortions and lead to lattice atoms being pushed into interstitial sites. In BCC materials, the helium interstitial activation energy is lower than in FCC materials. Since the binding energies of helium interstitials

to each other in BCC materials are even greater than in FCC, self-trapping of helium will also occur. The concentration of helium–helium clusters increases in the initial evolution phase under irradiation but decreases to a negligible amount at longer times. The concentration of helium–vacancy clusters shows three distinct stages of evolution [139,140]. At lower times, the helium–vacancy cluster concentration increases, it remains fairly constant for several orders of magnitude of time and then decreases at higher time scales. The initial increase is due to very small helium–vacancy clusters. Once the free helium is depleted, the size of the clusters grows by incorporating more vacancies. At longer time scales, point defects dissociate from smaller clusters and form larger clusters. These large clusters serve as sinks to absorb point defects and grow into cavities.

2.4.5 The Critical Bubble Model of Cavity Nucleation

Many aspects of cavity formation have been modeled approximately using the critical bubble model (CBM) concept [141,142]. A critical bubble is one that has grown to a radius (r^*) and helium (m^*) content such that upon the addition of a single helium atom or vacancy, the bubble immediately transforms into an unstably growing cavity without the need for statistical nucleation. More generally, the CBM is one of the possible solutions to the cavity growth rate equation when the growth rate is equal to zero:

$$\frac{dr}{dt} = \frac{\Omega}{r}\left[D_v C_v - D_i C_i - D_v C_{v,T} \exp\left(\frac{2\gamma}{r} - p_g\right)\right]. \qquad \text{Eq. 2.4}$$

The three major terms of the equation are the growth of the cavity through the arrival of vacancies to the cavity ($D_v C_v$), the reduction in cavity radius from interstitial arrival to the cavity ($D_i C_i$), and the thermal emission of vacancies using the capillary approximation to account for the gas pressure inside the cavity ($D_v C_{v,T} \exp\left(\frac{2\gamma}{r} - p_g\right)$). In general, the roots of the cavity growth rate equation strongly depend on the helium gas pressure and can result in four possible states with

increasing helium concentration in the cavity, illustrated in Figure 2.18. Without helium, there is only one root (r_v^*) and it corresponds to when a cavity embryo becomes large enough through statistical fluctuations in the number of vacancies in the cavity to grow through bias driven growth. With some helium atoms in the cavity and below the critical helium content, the growth rate equation has two roots corresponding to the stable bubble radius (r_b^*) and the size to convert from a bubble to an unstably growing cavity (r_v^*). With the critical amount of helium, as described previously for the CBM, there is only one root (r^*) and it corresponds to the critical bubble radius. With a helium content greater than the critical number of helium atoms, there are no roots to the growth rate equation and all cavities and bubbles grow unstably.

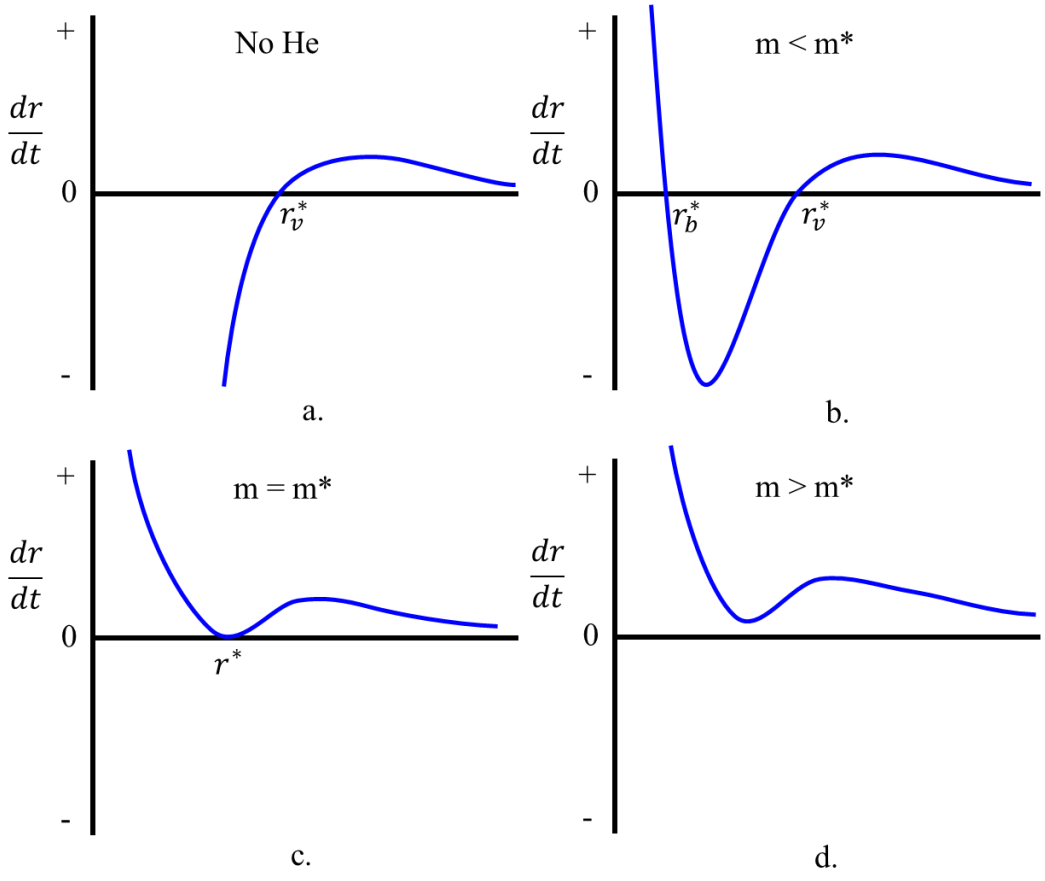

Figure 2.18. A schematic showing solutions to the cavity growth rate equation with (a) no helium, (b) less than the critical amount of helium (m < m*), (c) the critical amount of helium (m=m*) and (d) in excess of the critical amount of helium (m > m*).

A significant advantage of the CBM and the cavity growth rate equation is that it requires a relatively modest number of parameters, and parameter combinations, that are generally reasonably well known including for defect production, recombination, dislocation bias, sink strengths, interface energy, and defect diffusion rates. One key prediction of the CBM is the prediction of a bimodal cavity size distribution, composed of growing cavities and stable bubbles. It is with this prediction and advantage that the cavity growth rate equation used with the CBM is the primary context for the discussion around cavity nucleation.

2.4.6 Summary of Background

From a theoretical view, the effect of helium is to lower the free energy necessary to create a stable cavity embryo. The free energy depends on both the number of vacancies involved in the embryo and the amount of gas atoms in the cavity embryo. For any stabilization point, where the change in free energy is zero, there are many combinations of these two parameters to satisfy this requirement. As the damage rate is changed the number of vacancies will increase in some proportionality to the damage rate depending on the dominant mode of point defect loss through either recombination of interstitials and vacancies or loss to sinks. In order to maintain the same free energy for a stable cavity, the amount of helium must be modified in proportion to the vacancy population for each damage rate. Once a cavity is stable, its growth is driven by the flux of vacancies in the case of voids, or a combination of helium and vacancy fluxes in the case of bubbles. Thus, a key parameter of cavity nucleation and growth is the ratio of available helium in the matrix and available vacancies.

From the experimental and theoretical work presented previously, there are two potential paths to discuss for the helium to vacancy ratio: the effects of helium through the helium co-injection rate independently of the damage rate, and the effects of the vacancy population through

the damage rate. Without helium, cavity nucleation begins instantaneously with radiation damage, nucleating vacancy defect clusters that transition to embryos and grow large enough to become cavities. Eventually these self-stabilizing cavities will grow with increasing radiation damage and swell the irradiated material. When a small amount of helium is co-injected into the microstructure, the helium binds to vacancy clusters with a certain amount of energy and lowers the free energy necessary for the cavity to stabilize. The helium stabilized clusters can achieve growth faster than the vacancy clusters lacking helium, and thus achieve growth dominated swelling at a lower level of damage. Ideally, the density and sizes of clusters would be directly measured at this stage of nucleation and stabilization, but this information is beyond most measurement techniques. These cavity embryos continually nucleate and grow to resolvable sizes as the material experiences more radiation damage. The resulting size distribution becomes bimodal with cavities above a critical size threshold stable enough to grow with only vacancy accumulation and cavities below this threshold stabilized only through the amount of gas pressure from helium.

Chapter 3: Objective

The objective of this work is to determine the mechanisms that control cavity nucleation in dual ion irradiated T91 steel over a range of temperature, helium injection rates, and damage rates. A hypothesis for the behavior of cavities as a function of helium co-injection rate and damage rate is presented as follows:

Dual ion irradiated T91 will exhibit monotonically increased bubble and void density as the helium-to-vacancy ratio is increased through the helium co-injection rate for the same level of damage and same temperature. This is due to the stabilization of vacancy clusters as bubbles and voids from the increased helium pressure inside the cavity which is directly proportional to the number of helium atoms in the cavity and injected in the matrix.

For a fixed helium-to-vacancy ratio, bubbles will transition to voids at the same void radius independent of damage rate implying the same transition process across damage rates with the growth of cavities decreasing with increasing damage rate.

To test the hypotheses a combination of ion irradiation experiments with careful characterization of the microstructure was used.

To achieve the main objective, two sub-objectives were identified. The first sub-objective is aimed at determining *the effects of temperature, helium, and damage rate* on the cavity size distributions. To complete this sub-objective, a series of experiments were performed in the laboratory with varying conditions. This required the establishment of a well-defined and consistent process to perform the experiments, analyze the results, and process the experimental

data. The development of the following techniques was essential in acquiring the relevant experimental data:

- A method for consistent and controlled ion irradiation experiments with and without simultaneous helium co-injection
- A post-characterization technique utilizing TEM (transmission electron microscopy) and STEM (scanning transmission electron microscopy) to image the microstructure
- A method for consistent quantification of the microstructure features (bubbles, cavities, dislocations)

Through these methods, the magnitude and shape of the size distributions of cavities and dislocation loops with changes in the temperature, helium co-injection rate and damage rate were determined. These size distributions provided a comprehensive picture of the microstructure evolution with increasing temperature for the same helium co-injection rate and damage rate, and increased helium co-injection rate and damage rate for the same level of damage and temperature. Together, these results answered the question of *what* happened to the cavity behavior as a function of temperature, helium co-injection rate and damage rate.

The second sub-objective is aimed at determining *why* a change in the temperature, helium co-injection rate or damage rate resulted in the observed changes in the cavity evolution. A detailed analysis of the cavity size distributions and dislocation loop size distributions accomplished this sub-objective. The results from this work were applied to existing cavity nucleation theories and compared with other available experimental results. This analysis ultimately provided insight into the role of the temperature, helium co-injection rate and damage rate on the nucleation of cavities.

Completion of these two sub-objectives demonstrated the roles of temperature, helium co-injection rate, and irradiation damage rate on the nucleation of cavities.

Chapter 4: Experimental procedures and Methodology

This chapter presents the experimental procedures used to prepare, irradiate, and characterize the T91 samples explored in this dissertation. Additionally, the analysis framework for the cavity growth rate equation is described.

4.1 Alloy and Sample Preparation

Alloy T91 heat 30176 was used for the work in this thesis. The composition in weight percent is reported in Table 4.1. The composition designated PNNL was provided by PNNL and has been reported in several publications using this archival heat [86,87,143]. An independent chemical analysis was performed by Luvak Inc. using combustion infrared detection to measure carbon and sulfur content (ASTM E1019 [144]), inert gas fusion to measure oxygen and nitrogen content (ASTM E1019 [144]) and direct current plasma emission spectroscopy to measure all other elements (ASTM E1097 [145]). As discussed previously, T91 is a nominally 9Cr ferritic-martensitic steel and considered to be a candidate for fast reactor applications because of its high swelling resistance. The as-received T91 samples were encapsulated in a quartz tube that was evacuated twice and then backfilled with 0.25 atmosphere of argon. The samples were then normalized at 1038°C for 30 minutes and air cooled. Tempering was performed at 760°C for 30 minutes and then air cooled. The timer for each step of the heat treatment process began when the temperature of a thermocouple touching the quartz tube read within 5°C of the target temperature.

The resulting microstructure was a tempered martensitic material. Figure 4.1 shows the microstructure of the non-irradiated, heat treated T91 imaged using bright field scanning transmission electron microscopy (BF STEM). The unirradiated microstructure of T91 in the as-

tempered condition as reported in [146] consisted of prior austenite grain boundaries, packets, laths, coarse chromium carbides, fine V,Cr-nitrides, and network dislocations. Chromium carbides were mainly $M_{23}C_6$ type and were mostly on the prior austenite grain boundaries (PAGBs) or lath boundaries. Fine V,Cr-nitrides were observed in the matrix and sometimes were found adjacent to the Cr-carbides. The average size of $M_{23}C_6$ was estimated to be ~100 nm while the average size for (V,Cr)N was approximately 40 nm. Both Cr carbides and V,Cr-nitrides had an estimated number density between 10^{18} m^{-3} and 10^{19} m^{-3}. The dislocation density varied from area-to-area and was estimated to be ~5 $\times 10^{14}$ m^{-2}.

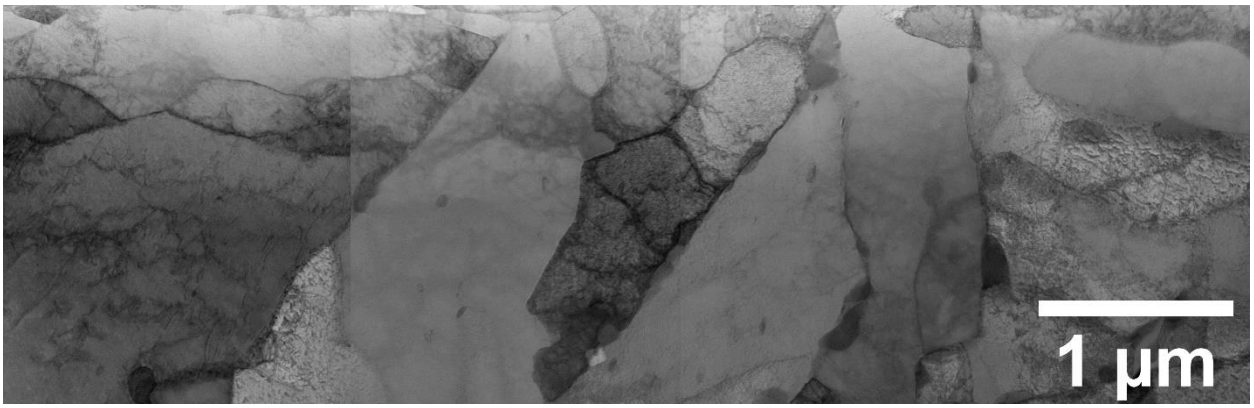

Figure 4.1. Bright field scanning transmission electron microscopy image of T91 heat 30176 in the as-received, as-tempered state.

Table 4.1. Chemical compositions (wt%) of T91 heat 30176 provided by PNNL and Luvak, from [146].

	Fe	Cr	Mn	Nb	Mo	Ni	Si	V	C	N	Al	S	P	Ti	Cu	W
PNNL	Bal.	8.6	0.37	0.072	0.89	0.09	0.11	0.21	0.08	0.054	-	-	-	-	-	-
Luvak	Bal.	8.76	0.44	0.086	0.86	0.10	0.25	0.23	0.091	0.052	0.004	0.002	0.007	0.003	0.062	0.004

Prior to ion irradiation, samples of T91 were cut in the form of 1.5 × 1.5 × 20mm bars using electrical discharge machining (EDM). EDM utilizes rapid current discharge through two electrodes to break down material and effectively cut the metallic sample. The desired cuts of the material can be programmed into the machine and can result in a geometric precision on the order of 1μm.

The bar samples were then mechanically polished using successively finer grits of silicon carbide grinding paper. The samples were mounted on a metal puck using Crystalbond™ adhesive resin. The puck was heated on a hot plate to melt a thin layer of adhesive. The T91 bar samples were then arranged on the adhesive in the center of the puck, side-by-side, as they would be on the irradiation stage. Additional bars of spare ferritic-martensitic steel samples, called guide bars, were added to the puck to bookend the irradiation samples. The guide bars allowed for more consistent polishing and a welding point for thermocouples on the irradiation stage. It was necessary to ensure that the samples were adhered flat to the puck and at the same height. The puck was then removed from the hot plate and allowed to cool, with deionized water sprayed at the base of the puck to reduce the temperature quickly and harden the adhesive. The samples were then hand-polished using a variable speed grinding wheel overlaid with silicon carbide grinding paper. Grits of 600, 800 and 1200 were used to polish the sample. The polishing direction was rotated 90 degrees between each grit step so that it would be easy to identify when the damage induced by the previous polishing step had been removed. The samples were also rinsed with deionized water between grinding steps to remove stray particles. After the 1200 grit grinding step, the puck was re-heated to melt the adhesive and the samples were flipped to the opposite side, while maintaining the same relative orientation. The grinding process was repeated for the opposite face. The to-be-irradiated surface was further polished with a cloth pad and diamond slurries of 3μm, 1μm and 0.25μm to provide a mirror-like finish. The samples were then removed from the puck by heating once again. To remove any residual adhesive, the samples were allowed to rest in a beaker of acetone until the adhesive completely dissolved. They were then successively cleaned with methanol then ethanol and allowed to dry in air.

To remove any damage layer induced by mechanical polishing, the samples were then electropolished. The electropolishing solution consisted of a 10% perchloric acid, 90% methanol solution which was cooled to between -40 and -50°C using a methanol bath with dry ice or liquid nitrogen. The sample was completely submerged in a 1000 mL beaker containing approximately 500 mL of electropolishing solution. A magnetic stirrer rotating at ~300 rpm was used to create a vortex in the electropolishing solution which impacted the surface of the sample head on. The to-be-irradiated surface of the sample was oriented to face the cathode, a 25 x 25mm square platinum wire mesh, which was also submerged in the solution. The sample itself served as the anode. A diagram of electropolishing set-up is shown in Figure 4.2. The samples were electropolished at an applied voltage of -40V for approximately 20 seconds. During the electropolishing, the sample was agitated within the vortex to refresh the flow of solution at the surface. This procedure was estimated to remove about 2μm of material based on the polishing curve presented in [147]. As the final mechanical polish utilized 0.25μm particles, removal of 2μm was deemed more than sufficient for removal of a remaining damage layer.

Prior to irradiation in the BOR-60 nuclear reactor, Slices of thickness of 0.4 mm were cut from the heat-treated T91 samples using wire EDM and were thinned down to 0.25 mm by double sided diamond lapping to a 0.25 μm finish. 3-mm diameter disks were then punched out from the thinned slices using a Gatan TEM disc punch system. Each of the disks was then laser engraved for identification before they were loaded into capsules for BOR-60 irradiation.

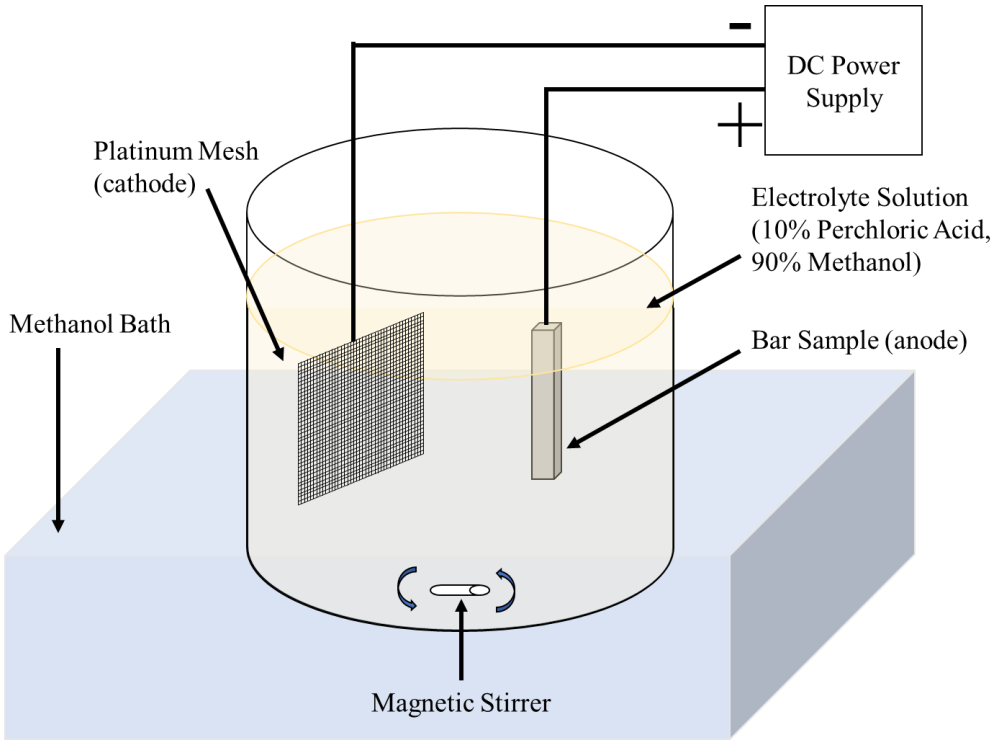

Figure 4.2. A schematic of the electropolishing setup used for samples prior to ion irradiation.

4.2 Dual Ion Irradiations

4.2.1 Ion Irradiation Experiments and Characterization Performed

For clarity, the ion irradiation campaigns will be divided into three: the temperature series to determine starting conditions for the other series, the helium co-injection series, and the damage rate series. A total of fourteen dual ion irradiation experiments were performed for this thesis. Each irradiation consisted of one sample of as-tempered T91 heat 30176. The temperature series was performed at damage rates of 5-8 × 10^{-4} dpa/s with a helium co-injection rate of about 4 appm He/dpa to a total damage of 14.6-16.6 dpa at temperatures of 406°C, 420°C, 432°C, 445°C, 460°C, 480°C, 520°C, and 570°C with one irradiation conduced to a total damage of 35 dpa by adding 18.4 dpa to the previous 16.6 dpa sample at a temperature of 445°C. The temperature histograms recorded by a thermocouple calibrated FLIR® thermal imager are included in Appendix A - . The

helium co-injection series was performed with damage rates of 7-8 x 10^{-4} dpa/s at 445°C to a total damage of 16.6 dpa with helium co-injection rates of 0, 0.02, 0.22, and 4 appm He/dpa. The damage rate series was performed with a helium co-injection rate of about 4 appm He/dpa to a total damage of 16.6 dpa at 445°C with damage rates of 5×10^{-5} dpa/s, 1×10^{-4} dpa/s, 7.1×10^{-4} dpa/s, and 3×10^{-3} dpa/s. After the irradiation was performed, at least two TEM specimens were extracted for characterization of cavities and dislocation loops. Table 4.2 summarizes the experimental details of the irradiations.

Table 4.2. The experimental details for ion irradiations conducted as part of this thesis.

Date of Completion	Damage (Kinchin-Pease dpa)	Temperature (°C)	Damage Rate (dpa/s)	Helium Co-Injection Rate (He appm /dpa)	He Injected (appm)
Nov. 4, 2015	16.6	406	6.0×10^{-4}	4.3	72
Jan. 23, 2017	16.6	420	5.4×10^{-4}	4.3	72
Oct. 10, 2016	16.6	432	5.4×10^{-4}	4.3	72
Sept. 27, 2017	16.6	445	7.1×10^{-4}	4.3	72
Sept. 29, 2017	16.6	460	7.5×10^{-4}	4.3	72
Jan. 25, 2017	16.6	480	5.8×10^{-4}	4.3	72
Oct. 26, 2017	14.6	520	6.5×10^{-4}	4.3	63
Nov. 1, 2017	15.4	570	6.7×10^{-4}	4.3	67
May 30, 2018	35.0 (16.6+18.4)	445	7.6×10^{-4}	4.3	150
May 13, 2017	16.6	445	7.0×10^{-4}	0	0
Dec. 17, 2018	16.6	445	8.1×10^{-4}	0.02	0.36
Dec. 07, 2018	16.6	445	7.2×10^{-4}	0.22	3.6
Jan. 20, 2019	16.6	445	5.0×10^{-5}	4.3	72
Aug, 22, 2017	16.6	445	1.0×10^{-4}	4.3	72
Feb. 26, 2019	16.6	445	3.0×10^{-3}	4.3	72

The T91 samples were irradiated using the dual-beam configuration at the Michigan Ion Beam Laboratory at the University of Michigan [148]. Dual ion beam irradiations were conducted with the stage facing Beamline 4 (BL4). BL4 delivered a 5 MeV iron ion beam from the 3 MV NEC Pelletron accelerator and is normal to the sample surface. Beamline 7 delivered the helium ion beam from the 1.7 MV General Ionex Tandem Accelerator for dual beam irradiations and is +60° from BL4. The configuration of the sample stage and a description of the multi-beam chamber used for these irradiations are described later in Sections 4.2.4 and 4.2.5. These accelerators, along with a series of diagnostic instruments allowed for the performance of well-

controlled experiments. 5.0 MeV iron ions from the NEC Pelletron provided an adequate penetration depth to analyze the irradiated microstructure using a focused ion beam lift out technique (detailed later in Section 4.4.1).

4.2.2 SRIM Damage and Helium Implantation Calculations

Stopping and Range of Ions in Matter (SRIM) [149] was used to provide a depth-dependent estimation of the damage caused by an ion, given the ion energy and the target material composition in atomic percent. The SRIM damage calculations were performed using the quick Kinchin-Pease mode using the displacement energies for each element from Table 1 in [150]. A displacement energy of 40 eV was used for Fe, Cr, Ni, V, and Mn, and 60 eV for Nb and Mo. For all other elements, a displacement energy of 25 eV was used. The composition for the SRIM calculation was the PNNL composition of the target material and detailed in Table 4.1. The simulation was run for 100,000 ions to obtain smooth damage and implantation curves with adequate counting statistics. Figure 4.3 shows the SRIM calculated profiles for how the damage rate and injected interstitials change with depth for 5 MeV Fe^{2+} ions in T91. As is clear in image, the damage varies with depth. The damage level at 600 nm depth was used as the nominal damage level for any given experiment as this region is far from the surface and avoids the profile of the injected ions [7]. The damage rates provided by SRIM for the relevant experiments performed is 0.348 displacements / Å-ion for the 5.0 MeV Fe^{2+} ion beam. The damage rate from the energy degraded helium ions was determined to be several orders of magnitude lower than the damage rate for 5.0 MeV Fe^{2+} and considered negligible.

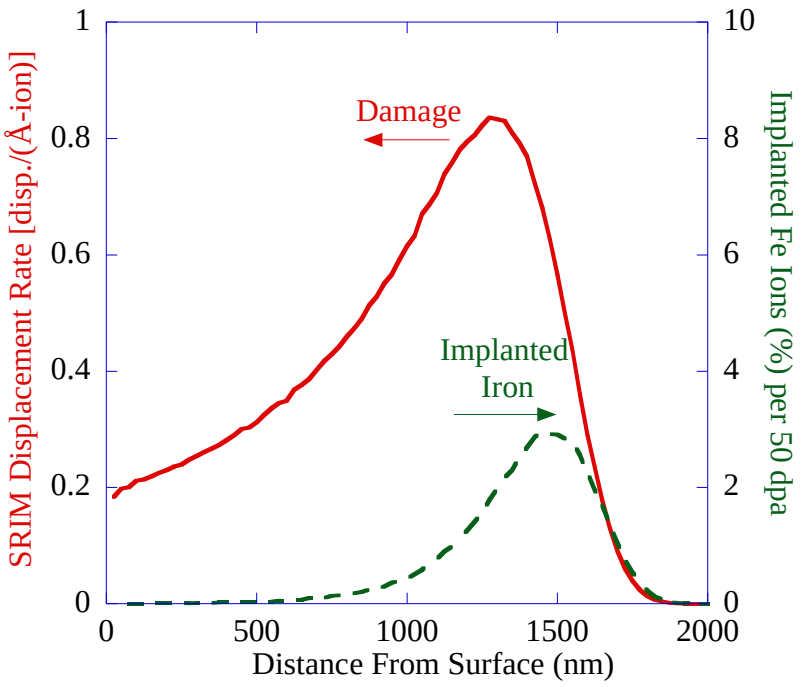

Figure 4.3. The damage rate and implanted ion concentration as a function of depth for 5 MeV Fe^{2+} in T91 as calculated by SRIM.

The SRIM damage rate was used to estimate the total irradiation time required to reach any given damage level. By making periodic measurements of the beam current, and integrating it over the time of irradiation, an estimation of the total ion fluence was made. The equations below, Eq. 4.1 and Eq. 4.2, estimated the total dpa for a given condition (the units for each input and appropriate conversions are also given):

$$dpa = \frac{(SRIM\ Damage\ Rate)\sum(ion\ beam\ current{*}time)}{(Number\ Density)(Ion\ Charge)(Specimen\ Area\ Irradiated)}, \quad \text{Eq. 4.1}$$

$$\frac{disp.}{atom} = \frac{\left(\frac{disp.}{Å{*}ion}\right)\sum\left(\frac{\mu C}{s}{*}s\right)\left(\frac{10^8\ Å}{cm}\right)}{\left(\frac{atom}{cm^3}\right)\left(\frac{C}{ion}\right)\left(\frac{10^6\ \mu C}{C}\right)(cm^2)}. \quad \text{Eq. 4.2}$$

Using the measured thickness of the aluminum foil in the foil degrader in the multi-beam chamber described in Section 4.2.5, SRIM was used to calculate the energy, *E*, position vector in three dimensions, ***r***, and direction vector, ***φ***, in three dimensions for each ion exiting the foil and for each angle of foil rotation, ***θ***, in one degree increments. Individual ions were then propagated

from the foil to the sample surface following the direction vectors calculated with SRIM without any additional forces to alter the beam trajectory. A schematic of this description is available in Figure 4.4. This resulted in a “plume” of ions forming a curved distribution. To ensure an even distribution of ions across the sample surface, the effects of raster scanning the beam were considered. The plume of ions was copied and added to itself with a small change (0.5 mm) in the raster scanned direction. This process was repeated until the entire raster scanned distance along the x and y directions of scanning were covered. The same variation in position would be used for a defocused ion beam passing through the foil and would be used for this simulation. The position and direction of each ion were then rotated to match the geometry between the ion beam’s original direction and the irradiation stage. For this dual ion beam setup, the helium ion beam impinge on the sample surface at 60° to the normal of the stage surface. SRIM was used after this geometric adjustment to calculate the implantation distribution of the energy degraded ions for each angle of foil rotation. Although the foil can rotate to higher angles beyond 60°, the increased amount of scattering from the apparent thickness significantly reduces the ion beam current density at the irradiation stage and makes these angles impractical for multi-ion beam irradiations.

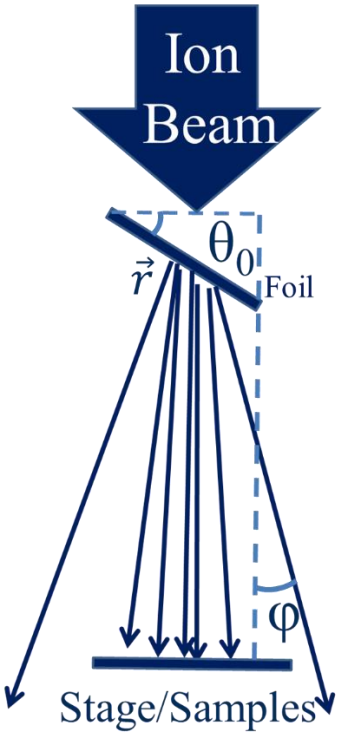

Figure 4.4. A schematic of the foil degrader geometry considered for SRIM based calculations based on the foil rotation angle, $\boldsymbol{\theta}$, position of the ions after degradation, $\boldsymbol{r}$, and direction of ions from the original trajectory, $\boldsymbol{\varphi}$.

The resulting profiles for displacement damage in dpa, injected iron interstitial concentration in at% and helium concentration in atomic parts per million (appm) are displayed in Figure 4.5 for 4 appm He/dpa. Due to an error in the original helium foil degrader calculation methodology, the He/dpa ratio is non-uniform and not expected to significantly impact the results in the area of interest 500-700 nm from the surface. For the damage rate series of ion irradiations, the helium concentration and flux were scaled linearly with the same shape as this helium concentration profile to limit potential confounding factors in the analysis.

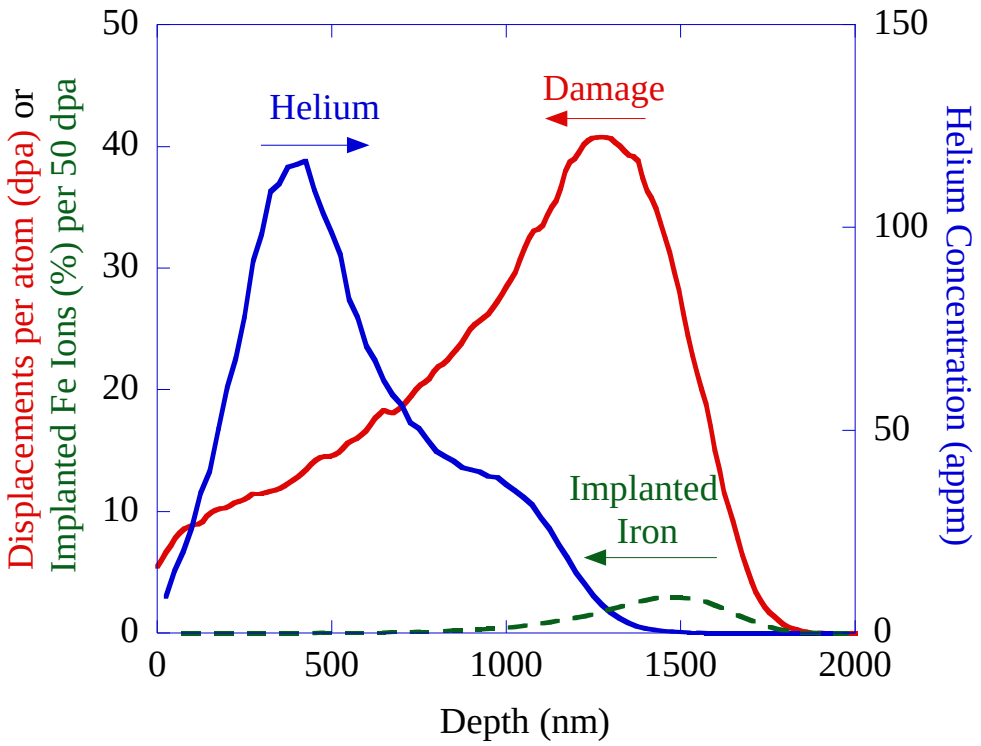

Figure 4.5. Iron and helium depth profiles for dual ion irradiations using 5 MeV defocused Fe^{2+} ions and degraded He^{2+} ions in alloy T91 to 16.6 dpa at 600 nm for 4 appm He/dpa.

4.2.3 Conditions for Each Ion Beam

To define the irradiated area, a slit aperture system was used for each beamline. The aperture system for each beamline consisted of four independently controlled and electrically isolated slits that could be moved into and out of the beam path via digital control. The slit apertures also measured the unsuppressed current incident on each individual slit. With this system, the area of irradiation from each ion beam was directly determined using the geometry of the stage relative to the beamline. For example, with the iron ion beam, if a 6mm × 6mm irradiation area was desired, both X slits were set to a distance of 3mm and the Y slits were set to a distance of 3mm, resulting in a total area between the slits of 6mm x 6mm. However, for the helium ion beam which impacted the stage at a 60° angle relative to the Fe^{2+} beam, the X slits were adjusted by the cosine of the angle. For example, the X slits were set to a distance of 2.5mm and the Y slits were set to a distance

of 5mm, the total area hit on the stage was 10mm × 10mm. To achieve a uniform damage profile, the Fe^{2+} beam needed to be defocused such that it completely covered the area defined by the slit aperture system.

4.2.4 Irradiation Stage

An irradiation stage was used to hold the samples in place and provide the necessary heating and cooling avenues. A schematic of the stage is shown in Figure 4.6. The ion irradiation stage consists of a thermally conductive copper or nickel alloy head attached to a stainless-steel tube welded onto a 6" CF flange for use with the high vacuum system. The length of the stage was machined to match the distance from the flange to the intersection point of ions beams from the irradiation beamlines in the multi-beam chamber. The stage head has channels machined for pressurized air cooling and a hole machined into the non-vacuum side of the stage head for a resistive cartridge heater. A 0.25mm thick square of copper foil was placed on the stage head to facilitate heat conduction from the back of the stage to the samples. The samples, along with the guide bars, were then arranged on the copper foil side-by-side to-be-irradiated side facing upward. Specimens were held down with a notched plate and notched hold down bars for a typical multi-beam ion irradiation with a photograph of a typical irradiation stage presented in Figure 4.7. The notches are 1 mm in width and spaced 1 mm apart to aid in the alignment of the samples to the intersection point of the ion beams. Type J thermocouples custom built for each experiment using 0.001mm diameter iron and constantan wires were spot-welded to samples placed just outside of the irradiation area. The wires were connected to a feedthrough which led to the back of the stage flange and would eventually be connected to the cold junction (digitally controlled). These thermocouples are used to calibrate a 2D infrared thermal pyrometer viewing the irradiation stage through a Ge window. Figure 4.7 presents a photograph of a completely built stage.

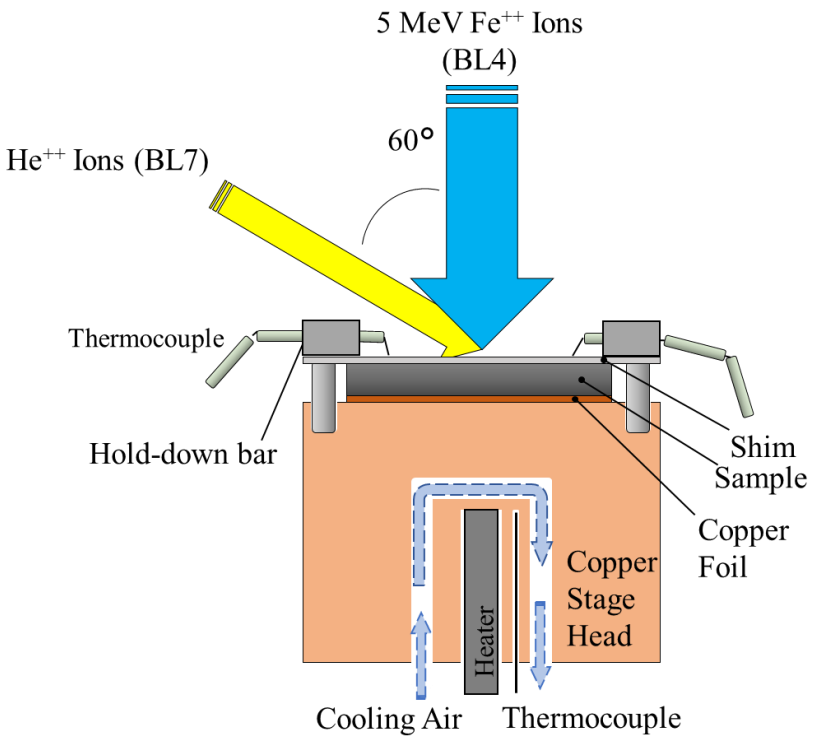

Figure 4.6. Schematic drawing of the stage used for dual ion irradiations in this work.

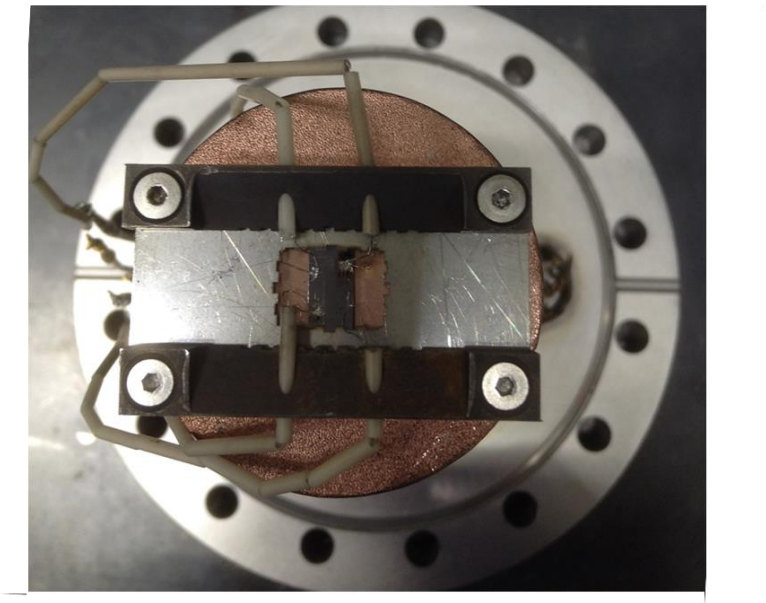

Figure 4.7. A photograph of a fully assembled ion irradiation stage.

4.2.5 The Multi-Beam Chamber

After assembling the stage, it was mounted into the Multi-Beam Chamber (MBC). The MBC was designed to provide a fixed intersection point for each of the three accelerators at the Michigan Ion Beam Laboratory. A schematic of the MBC is provided in Figure 4.8. A custom-built half-cylinder shape was chosen for the chamber to provide radially directed ports, allowing direct access to the irradiation stage for the accelerators and monitoring equipment, and a flat back panel for easy access while minimizing the chamber volume, which is necessary for high vacuum. Two back panels were made for the MBC each with a 6" Conflat Flange (CF) for the irradiation stage. The angle of the 6" CF is different between the two panels to provide the stage at either 0° to face Beamline 5 (BL5) or 30° to face either Beamline 4 (BL4) or Beamline 7 (BL7). The dual ion beam irradiations for this thesis were conducted with the stage facing BL4. BL4 delivers an iron ion beam from the 3 MV Pelletron accelerator and is normal to the ion irradiation stage. BL7 delivers the helium ion beam from the 1.7 MV General Ionex Tandem Accelerator and is +60° from BL4 and in the same horizontal plane. The stage was mounted to the back panel of the chamber using a copper gasket and tightened down with nuts and bolts. Once mounted a resistive cartridge heater was inserted into the back of the stage. The cartridge heater was approximately 4cm long and 1cm in diameter, with a temperature rating of up to 760°C. Additionally, a contact Type J thermocouple was inserted into the back of the stage into an approximately 1mm diameter hole to monitor the temperature close to the heater. Cables from a computer readout were attached to thermocouple feedthroughs, and the airlines for cooling the stage were also attached.

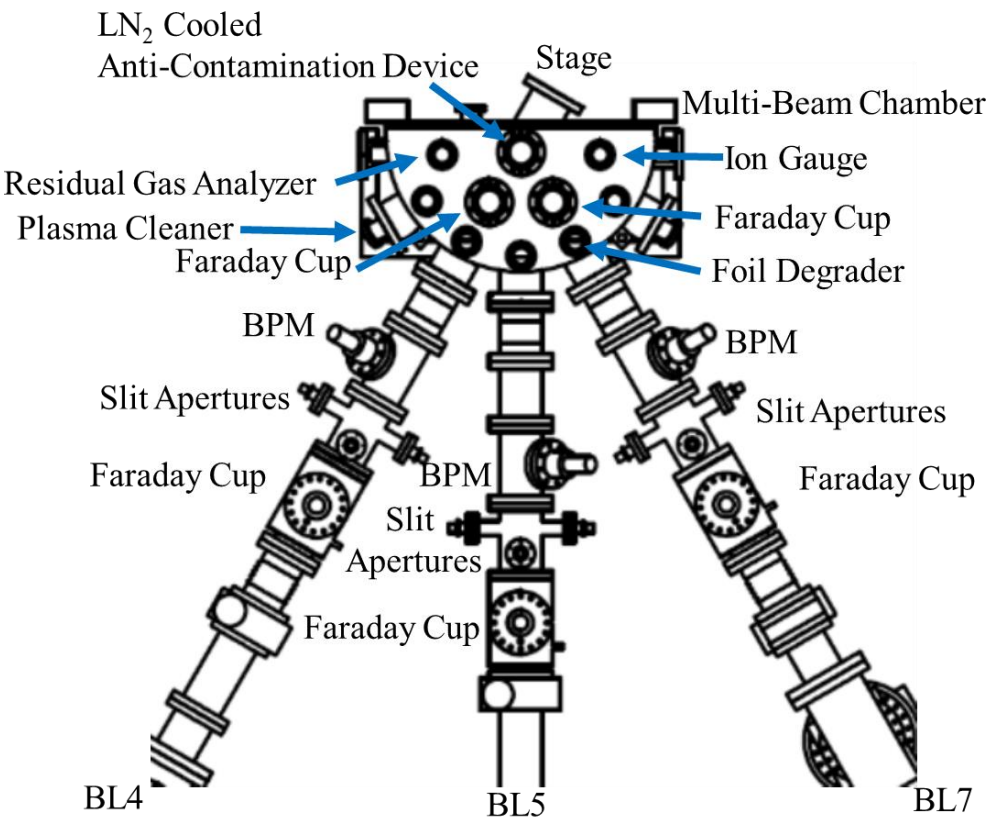

Figure 4.8. Multi-beam chamber with connecting beamlines. Each beamline is equipped with Faraday cups to record the ion beam current, slit apertures to define the irradiation area, and a beam profile monitor (BPM) to assess the beam shape.

The MBC contains many diagnostic instruments to monitor the status of the irradiation chamber before, during, and after an ion irradiation experiment. The pressure in the vacuum chamber is monitored using an InstruTech Inc. model IGM402 hot cathode ionization vacuum gauge. The partial pressure of each gas specie in the vacuum is monitored using an Inficon Transpector® MPS Residual Gas Analyzer. The chamber is equipped with an Evactron EP Series Plasma De-Contaminator to plasma clean the chamber. A large copper piece in the MBC acts as a liquid nitrogen cooled cold trap that encircles the stage to prevent contamination during irradiation [8]. The vacuum chamber pressure for each irradiation was maintained below 10^{-7} torr ($< 1.3 \times 10^{-5}$ Pa). The MBC also has several quartz windows to allow live viewing of the irradiation stage using a Nikon digital camera interfaced through the internal laboratory network. A 2D FLIR®

infrared thermal pyrometer viewing the irradiation stage through a germanium window. The pyrometer records surface temperatures on user-defined regions of interest on the specimens at a rate of 3.125 Hz throughout the experiment. All of these diagnostics provided digital outputs to networked computer systems, which recorded and displayed the information using custom built LabView™ programs.

After the appropriate diagnostic connections were made, the slit aperture system discussed previously in Section 4.2.3 was set to the desired area. The alignment of the stage was then checked with a laser which had been previously aligned with the beam path for BL4. The laser was mounted at the end of a bending magnet near the accelerator. A plastic film was placed in front of the laser to diffuse the beam and simulate the effect of a defocused ion beam. The alignment of the laser illuminated area was checked via the camera on the samples to-be-irradiated. Figure 4.9a shows an image of samples mounted on the beamline and aligned with the laser. Following laser alignment to the samples, a gridded piece of alumina was slid in front of the irradiation stage using a linear motion feedthrough. The alumina fluoresces when struck with ion beams and verified the alignment of the laser, Figure 4.9b and the iron ion beam from BL4, Figure 4.9c. The alumina piece is retracted prior to irradiation.

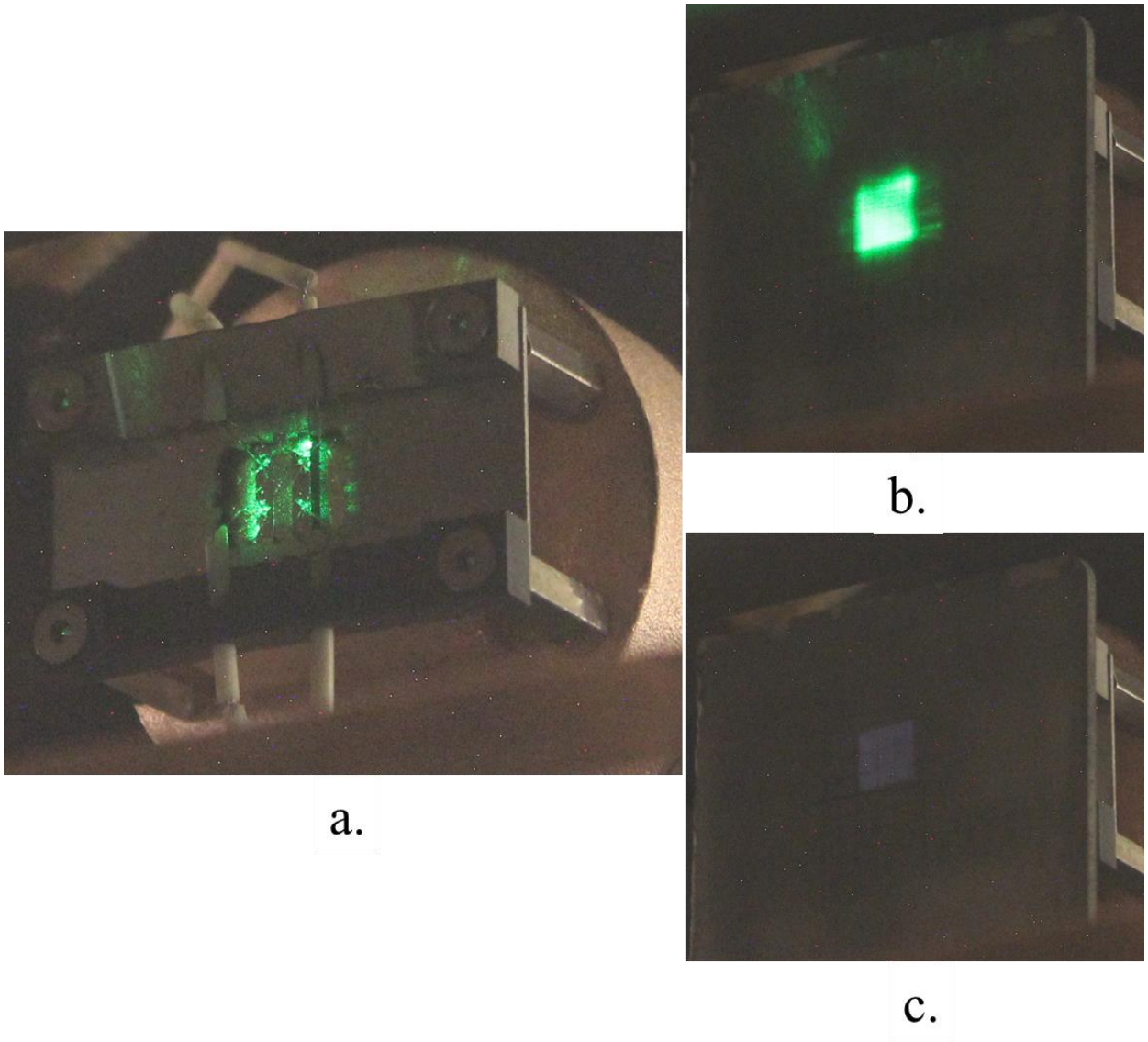

Figure 4.9. Photographs of the alignment verification process showing (a) the diffuse laser on the irradiation stage, (b) the same diffuse laser on an alumina piece in front of the irradiation stage, (c) fluorescence of the alumina piece from the 5 MeV Fe^{2+} ions.

Once the stage is mounted, the irradiation chamber was pumped down, starting with an oil-free scroll pump. Pumping with the rough pump for about 10 minutes allowed the chamber to reach a pressure of approximately $1x10^{-1}$ torr. At this point to prevent possible carbon contamination, the samples, sample stage and vacuum chamber were plasma cleaned using the Evactron EP Series Plasma De-Contaminator using a forward power of 15W for 2 hours. Following the plasma cleaning, the scroll pump was allowed to pump the chamber to $< 10^{-2}$ torr,

at which the gate valve to a cryopump directly underneath the chamber was then opened and the valve to the scroll pump was closed. This cryopump almost immediately brought the chamber pressure to about 1×10^{-5} torr. Once the chamber vacuum was less than 10^{-6} torr, the gate valves were opened up to the rest of the beamlines, which were maintained at $\sim 5 \times 10^{-8}$ torr to provide additional pumping power. The stage was then left to pump for at least 12 hours, usually overnight, to achieve a pressure in the range of $0.8\text{-}1 \times 10^{-7}$ torr.

As the sources were started for the day, the liquid nitrogen tank was opened to allow the cold trap to cool. A series of automated valves pulled the liquid nitrogen from a large dewar into a dewar on the MBC with a large copper surface. The large copper surface acted to transfer heat from the copper cold trap in the MBC to the liquid nitrogen through conduction. The cooling process started approximately two hours prior to the ion beams being ready to allow for the cold trap to reach a steady state temperature near the boiling point of liquid nitrogen. When the ion beams were confirmed ready, the stage was heated to the irradiation temperature by applying a voltage to the cartridge heater in the back of the stage. No outgassing was performed on the samples and the heat up to temperature was done as quickly as possible. This resulted in a temporary increase in the pressure near the stage to about $3\text{-}4 \times 10^{-7}$ torr. The thermocouples were carefully monitored during heat-up to ensure that the samples exhibited uniform heating behavior. The entire heat up process typically took about 20-30 minutes. As soon as the desired irradiation temperature was reached, the thermal imager was calibrated against the thermocouple measurements for user-defined areas of interest (AOI) by adjusting the emissivity of each AOI until agreement is reached. In the thermal imaging program, three AOIs were placed on each sample in the irradiated region and monitored for the duration of the irradiation. Figure 4.10 shows a typical thermal image with square AOIs on a heated irradiation stage. As soon as the irradiation

stage was at temperature and calibrated, the ion beams were allowed pass to the samples to begin the experiment.

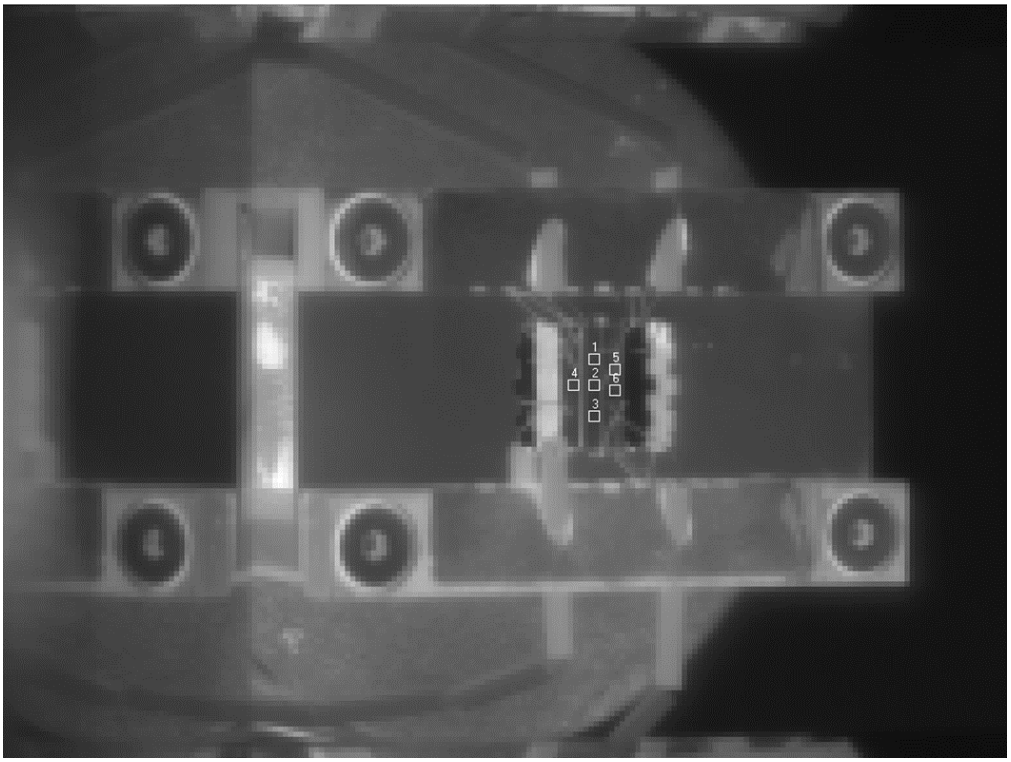

Figure 4.10. A typical thermal image with square AOIs on a heated irradiation stage. AOIs 1, 2, and 3 are in the ion irradiation area struck by both the 5 MeV Fe^{2+} ions and energy degraded He^{2+} ions.

4.2.6 Running the Irradiations

While the experiment was running, it was monitored continuously to ensure all of the irradiation parameters remained within specifications. All irradiations were maintained within ±10°C of the desired target temperature and in many cases with a 2σ less than ±7°C. While the thermocouples were still monitored, the AOIs from the FLIR® imager were used to monitor the temperature throughout the experiment. The imager provided the spatial dependence on temperature and could be used to see if all samples were experiencing a uniform temperature. The LabView™ program interfacing with the FLIR® imager would sound an alarm if any of the AOIs deviated more than ±10°C of the target temperature. If fluctuations were observed, changes were made to the voltage on the cartridge heater to compensate and keep the temperature as close to the

desired temperature as possible. For a 5 MeV Fe^{2+} beam, only a small amount of beam heating was observed, ranging from 1-10°C depending on the ion flux. Similarly, for the He^{2+} beam, only a small amount of beam heating was observed, ranging from 1-2°C depending on the ion flux and the rotation of the thin foil energy degrader. The cooling lines for air flow were not typically used during the experiments, since the heater cartridge could stably maintain the temperature on its own.

The pressure near the stage and in the beamlines was also monitored digitally during irradiation using InstruTech Inc. model IGM402 hot cathode ionization vacuum gauges. The target starting pressure before heating the sample was below $1x10^{-7}$ torr. With the combination of heating up and putting the beam on the samples, the stage pressure at the very beginning of irradiation spiked to the 5-8 × 10^{-7} range but recovered to ~1 × 10^{-7} in about an hour. It was important to always make sure the pressure was below 10^{-6} torr during irradiation to minimize the possibility of oxidizing the samples.

The current for each ion beam was also monitored at all times during the experiment. As mentioned in Section 4.2.3, the iron beam was defocused to have the beam spread across the sample surfaces and impacting the slit apertures. The helium beam was raster-scanned across the opening of slit apertures and passed through a thin foil energy degrader before reaching the samples. A suppressed Faraday cup was periodically inserted in front of the stage for each beam to measure the current of each ion beam that was impacting the samples. For irradiations lasting longer than three hours, a time interval of 30-45 minutes was used between insertions while a shorter time period of 15 minutes was used for irradiations lasting shorter than three hours. The Faraday cups for each beam had to be inserted at the same time as electrons emitted from the stage due to either ion beam would hit the back of the inserted Faraday cup, causing a false modification to the measured current value from the Faraday cup. A continuous current measurement was not

possible because the entire stage and irradiation chamber could not be suppressed. However, the slit apertures were used to continuously measure the presence of current and the alignment of the beam. If the balance of current the slits shifted, the bending magnet could be used to realign the beam. Additionally, while the current values on the slits were not quantitatively accurate, they could still be used to measure the relative stability of an ion beam (i.e. if the beam was increasing or decreasing in current). They would therefore provide an indication of whether the stage Faraday cup needed to be inserted to capture a change in either the Fe^{2+} or He^{2+} ion beams.

If at any point during the irradiation the pressure, current, or temperature were compromised (due to a power outage, accelerator or source malfunction, etc.) priority was given to maintain the integrity of the samples. If for example, the beam was lost for a period longer than 15 minutes, the samples would be quickly cooled to room temperature. This would be achieved by shutting off the cartridge heater voltage and applying high pressure air to the air-cooling lines. Typically, this would allow the samples on the stage to reach below 100°C within 10 minutes. Once the issue had been resolved, the samples would be heated like start-up, the AOIs for the thermal imager would be recalibrated, and the irradiation would resume.

Once the target damage level was achieved, the irradiation was complete. The irradiation was terminated by blocking each ion beam with a Faraday cup and rapidly cooling the stage. The heater voltage was turned off and the air-cooling lines were opened to high pressure. The stage was cooled to room temperature and the irradiation chamber was left under vacuum to allow for the liquid nitrogen cooled cold trap to warm up enough to reduce water condensation on the cold trap when the MBC was vented.

4.3 Irradiation with Neutrons in the BOR-60 Reactor

The TEM capsules were inserted into the BOR-60 reactor in 2013 at different reactor core positions to achieve various irradiation temperatures. The targeted irradiation temperatures were 370, 400, 450 and 525°C and the targeted doses were 20 and 40 dpa. All the TEM capsules went through multiple irradiation cycles in the BOR-60 reactor. Actual sample temperatures were calculated based on the coolant temperature reported during each irradiation cycle and the calculated temperature rise through the capsule to the TEM samples. The individual cycle histories were provided by Terrapower, LLC from the Research Institute of Atomic Reactors (RIAR) to relay to researchers through a personal communication [151] and are not publicly available. The irradiation conditions for the BOR-60 irradiated T91 is included in Table 4.3 with reported damage levels of 14.6-35 dpa at rates of 6-9 × 10^{-7} dpa/s in a temperature range of 376°C to 524°C. The estimated uncertainty on the temperature histories is reported as ±23°C. The helium generation rate of T91 irradiated in BOR-60 was estimated using SPECTER (0.20 appm He/dpa) [152] and FISPACT-II (0.22 appm He/dpa) [153] using ENDF libraries [154] in both programs. The value of 0.22 appm He/dpa was assumed to be constant throughout the irradiation campaign in the BOR-60 reactor.

Table 4.3. The experimental details for BOR-60 reactor irradiations conducted as part of this thesis.

Irradiation Capsule	Damage (Kinchin-Pease dpa)	Temperature (°C)	Damage Rate (dpa/s)	Helium Generation Rate (He appm /dpa)	He Generated (appm)
P027	17.1	376	6-9 × 10^{-7}	0.22	3.76
P033	18.6	415	6-9 × 10^{-7}	0.22	4.09
P037	14.6	460	6-9 × 10^{-7}	0.22	3.21
P042	15.4	524	6-9 × 10^{-7}	0.22	3.39
P028	35	445	6-9 × 10^{-7}	0.22	7.70

4.4 Post Irradiation Characterization Methods

The following section details the preparation and analysis methods used to examine the microstructure of T91 after it was irradiated. It consists of TEM sample preparation, imaging with TEM and STEM, and the characterization and analysis of the images.

4.4.1 TEM Specimen Preparation

Due to the shallow penetration depth of the Fe^{2+} and He^{2+} ions (see Figure 4.5) in the dual ion irradiated T91 and the residual radioactivity of the BOR-60 irradiated T91, the FIB (focused ion beam) lift-out method was needed to prepare TEM samples. This method allowed for the extraction of cross-sectional slices of material just a few microns into the surface. Additionally, T91 is highly magnetic, and large samples would cause magnetic distortion in the electron beam during TEM imaging. The FIB lift-out method allowed for microstructural analysis and avoided magnetic issues during imaging.

The TEM foils were prepared using a dual beam FIB. This instrument utilizes an electron beam (normal to a horizontal surface) for imaging, and a gallium ion gun (52° from the electron beam) for imaging and milling. The currents and energies of these beams could be varied according to user specifications. The ion beam operated at energies up to 30keV and currents of about 21nA. Energies of 30keV were used for most preparation steps. The specific instruments used in this thesis were FEI Helios NanoLab™ Dual Beam™ and Nova NanoLab™ DualBeam™ focused ion beam workstations for the dual ion irradiated T91 and FEI Versa NanoLab™ Dual Beam™ and Quanta NanoLab™ DualBeam™ for the BOR-60 irradiated T91 at the Low Activation Materials Development Analysis (LAMDA) laboratory [155] at Oak Ridge National Laboratory.

The FIB liftout method was utilized as follows. The irradiated specimen was mounted irradiated-side up on an SEM mount and placed in the FIB chamber, which was then pumped down. The stage was tilted 52° to be perpendicular to the ion beam. An appropriate area on the

sample was chosen in the irradiated region. A gas injector was inserted and the gallium beam was used to deposit a small layer of platinum on the target surface, in dimensions of approximately 20 × 2 micron surface area with a 3 micron height, using a current of about 0.4 nA and an ion energy of 16 keV. Using a higher current of ~21nA and energy of 30 keV, the gallium beam was used to create trenches using a regular cross section pattern about 4 microns deep on the long sides of platinum deposition. The long sides of the deposition were cleaned up using lower current (~3nA) and the cleaning cross section pattern. The stage was then tilted back to 7° so that the gallium beam could provide an undercut of the sample in a U-cut shape. The undercut was done to both sides of the samples to leave the sample attached to the bulk T91 piece by two small pieces. A micromanipulator (called an Omniprobe™ needle) was inserted and slowly positioned such that it made contact with the corner of the platinum deposition. A small amount of platinum (~1 micron) was used to weld the Omniprobe™ needle to the sample. The final connecting edges were then cut with the gallium beam to free the specimen from the metal bulk. The Omniprobe™ needle was then carefully raised a safe distance away from the irradiated sample and the stage was moved to the location of a mounted Omniprobe™ grid. The needle with the attached sample was lowered to a position in a valley of a chevron post where the two lower corners of the liftout sample were in contact. The gallium beam was used to weld the specimen to the post with about 1 micron of platinum on each corner. The needle was then cut free from the sample and retracted from the chamber. The stage was then rotated 180° to add an additional 1 micron of platinum on each corner to secure the sample to the chevron post. At this point, the specimen was still ~2 microns in thickness.

To achieve the target thickness of 100 nm, successive thinning needed to be done. The sample was tilted to 52° and the current was lowered to 0.23 nA. A cleaning cross section was used to

create even surfaces on each side and thin the liftout to 1 micron in thickness. Two windows were created by placing the cleaning cross section with a length of about 6 microns inside the platinum coating and using a Z height of 0.1 micron to create a window slowly. The bar at the bottom and the resulting frame provided support for the liftout to minimize chances of a bent or twisted liftout. The sample was alternately tilted ±2° about 52° to thin the sample in a wedge shape. This method was used to minimize the amount of material milled from the top of the sample to preserve the surface, while still thinning the entire specimen. The current was successively lowered as needed, while alternating the angle until the specimen was measured in the SEM to be less than 200nm thick. The energy of the ion beam was reduced in successive steps of 5 keV and 2 keV to thin the foil to a final thickness of about 100 nm. The low energy milling was found to effectively eliminate TEM-visible damage induced by the FIB process at higher ion beam energies. The chamber was then vented and the sample attached to the grid was placed in a labelled membrane box for safe keeping. Figure 4.11 highlights the key steps summarizing the FIB lift-out process.

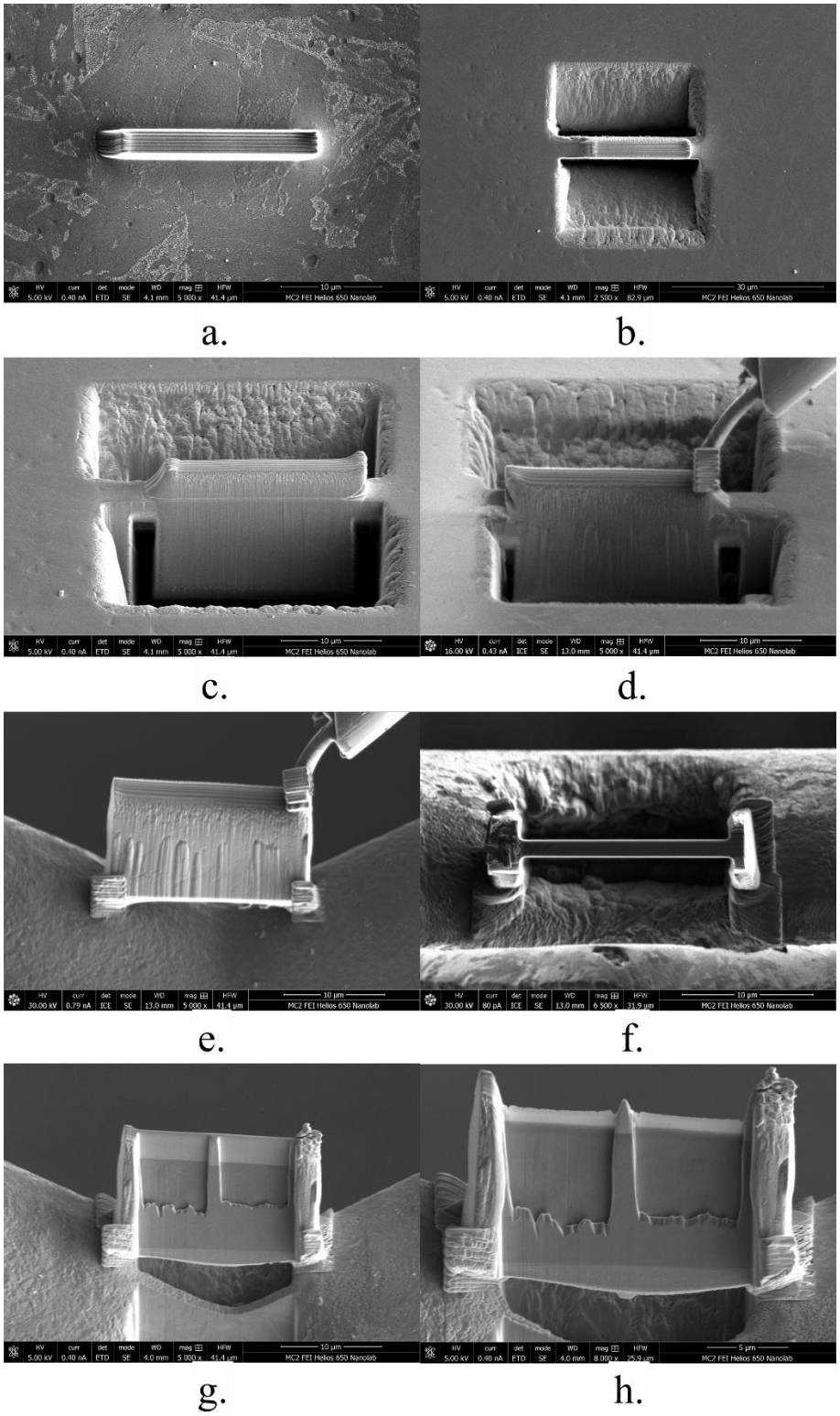

Figure 4.11. A schematic of the FIB process, showing a) platinum deposition on the surface, b) trenching around the platinum deposition, c) undercut of the sample at 52°, d) attaching of the Omniprobe to the sample, e) attaching of the sample to the copper grid, f) thinning the specimen prior to window formation, g) after window formation, and h) after final thinning.

4.4.2 Cavity Imaging

Imaging of the TEM specimens in this thesis was performed using a JEOL 2100F Cs Corrected Analytic Electron Microscope (AEM) and a JEOL 2010F AEM at the Michigan Center for Materials Characterization $(MC)^2$. The JEOL 2100F is a 200keV microscope that operates mainly in scanning TEM (STEM) mode. The JEOL 2010F is a 200keV microscope that can operate in both conventional TEM and STEM modes with a Gatan OneView 16-megapixel CCD camera capable of 4k resolution with 0.25 nm point to point resolution. Both microscopes also maintained the capability for XEDS using an EDAX® detector, with EDAX® acquisition software. Additionally, a Gatan® Imaging Filter (GIF) allowed for the capability to perform electron energy loss spectroscopy (EELS). A software suite called DigitalMicrograph® was used to acquire the images. The TEM specimen was mounted on a JEOL Single-tilt or Double-tilt stage and inserted into the microscope.

To determine the size and density of cavities, imaging of the entire liftout was performed using STEM mode on the JEOL 2100F, capturing a high angle annular dark field (HAADF) image and a bright field (BF) image simultaneously. The contrast in STEM HAADF images arises mainly from thickness and "Z-contrast," which is dependent on the atomic number of the material. Cavities, which lack both thickness and any atomic number appear as distinct, dark areas under these imaging conditions with well-defined boundaries. The HAADF images are typically free from contrast caused by dislocation networks and FIB damage allowing for accurate and convenient imaging of cavities. Example images of a typical HAADF image and its corresponding BF image is shown in Figure 4.12.

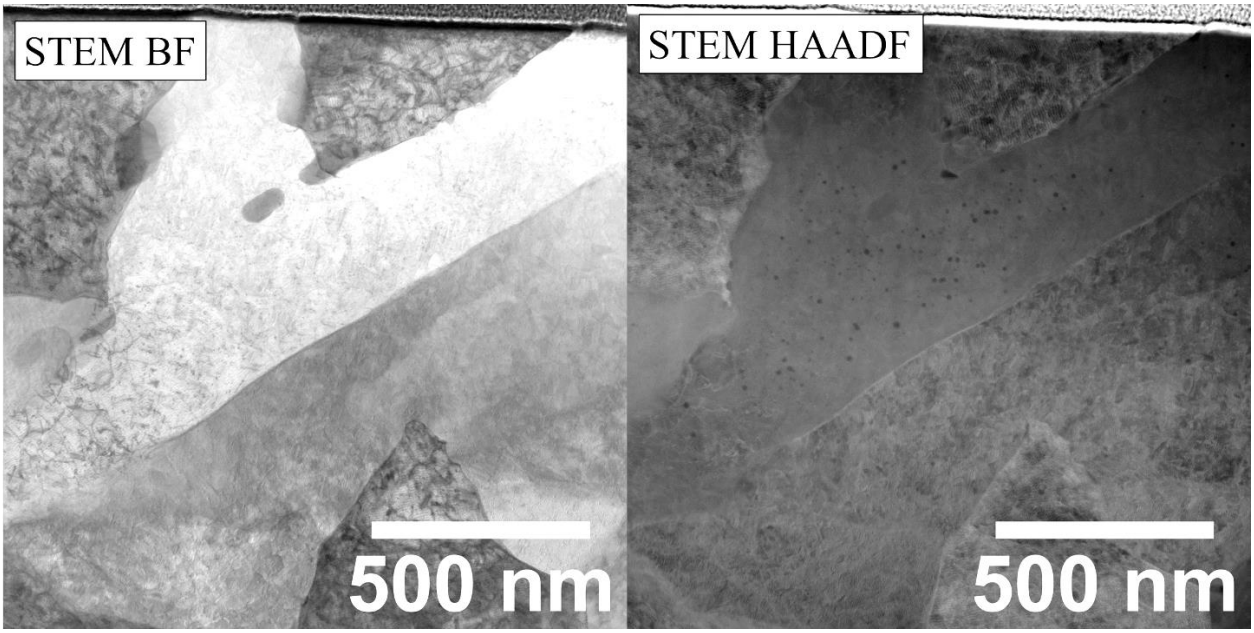

Figure 4.12. STEM BF (left) and STEM HAADF (right) micrographs of the same area on a T91 specimen irradiated to 16.6 dpa at 445°C with 4 appm He/dpa and 7.1×10^{-4} dpa/s.

A standard procedure for consistent imaging of cavities across all samples was used. Images were taken at approximately 100kx magnification, which allowed for a field of view of about 1.4 x 1.4 microns. Successive images were taken across the length of the sample with minimal overlap until a complete set of HAADF and BF images covering the entire specimen were taken. In many cases, higher magnification images were taken to acquire more detailed views smaller cavities and microstructural features. The point resolution for these images is about 0.68 nm [156].

Typically, conventional TEM (CTEM) images have been used to image cavities. In this work, CTEM BF images were collected to determine the size and density of cavities smaller than 5 nm in diameter using the 4k resolution of the Gatan OneView camera. A standard procedure for consistent imaging of these small cavities across all samples was used. A series of underfocused and overfocused images were collected sequentially from a focus value of - 2 μm and +2 μm in 0.2 μm steps. When the image is in focus, the cavities do not exhibit any noticeable contrast. In

underfocused images, cavities appear as lighter features with a darker fringe around them, and in overfocused images, the cavities appear as darker features with a lighter rim around them. However, the diameter of such small cavities is not reliable for focus values less than -1 μm or greater than +1 μm [157]. Therefore, the underfocused images collected closest to the focal value of +0 μm were used to estimate the size of a cavity and the remaining images were used to confirm the feature being measured is indeed a cavity. Example images of underfocused and overfocused cavities are shown in Figure 4.13. Images were taken at approximately 150kx magnification in CTEM mode, which allowed for a field of view of about 0.3 × 0.3 microns and a point resolution of 0.23 nm [156]. At least three areas centered at 600 nm from the surface of the TEM specimen were imaged per irradiation condition.

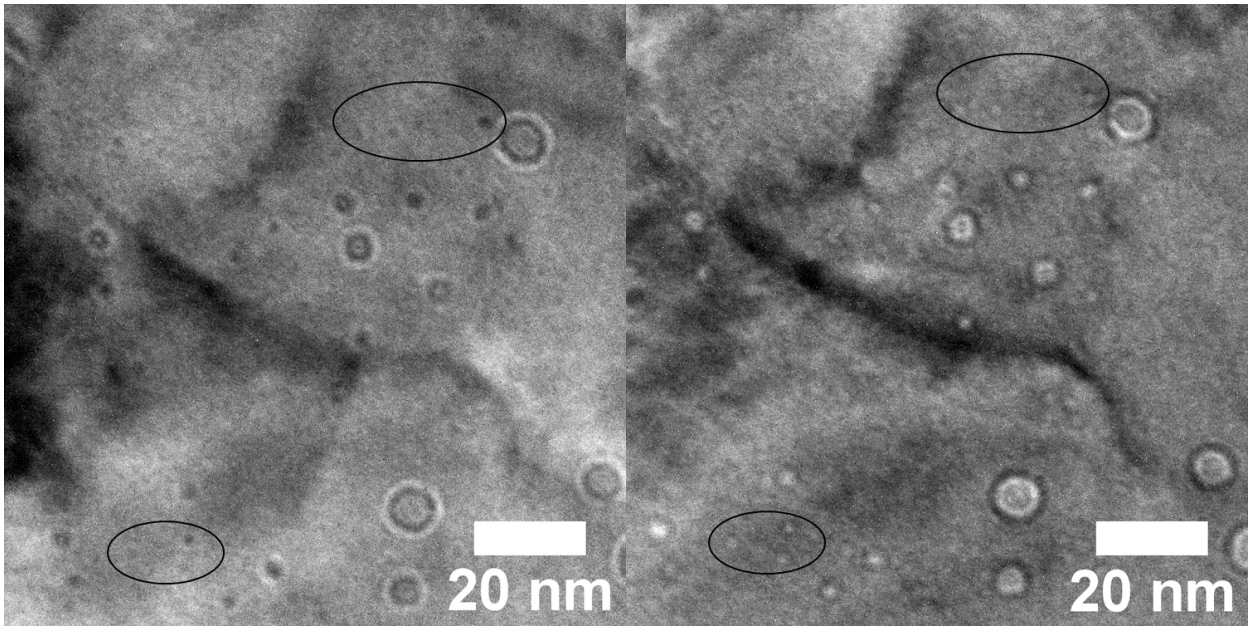

Figure 4.13. CTEM BF overfocused (left) and CTEM BF underfocused (right) micrographs of the same area on a T91 specimen irradiated to 16.6 dpa at 445°C with 4 appm He/dpa and 7.1×10^{-4} dpa/s. The circled areas highlight some of the small cavities observed with CTEM.

The thickness of the TEM specimen was measured using EELS (electron energy loss spectroscopy). This method estimated the thickness of the sample by measuring the amount of electron energy loss as the beam passed through the sample. The electron beam was set to probe

size of ~1nm and the camera length was set to 2cm (for a corresponding collection angle of about 38mrad). A zero-loss spectrum was taken in an area without going through the sample to calibrate the beam. Then an EELS spectrum map was taken on at least six areas of the sample (within the 500-700nm depth region). The DigitalMicrograph® software included an algorithm to calculate the thickness by calculating the error in a logarithmic fit of the inelastic mean free path of the electrons through the sample. The error in this calculation is estimated to be around 10% [158]. The average of these thickness measurements taken from the EELS map was used as the nominal thickness of the TEM specimen.

4.4.3 Cavity Characterization

Characterization of the cavities after the images were taken was performed using a freely available image processing suite FIJI [159]. For each HAADF image, the cavities were counted and measured with the diameter and the position of center of the cavities being recorded and stored separately from the image. During counting, the HAADF images were cross-referenced with the BF images to ensure the cavities being counted were actually cavities and not precipitates, contrast from dislocations, or other microstructural features. After the counting of an image was complete, the next sequential image was examined for any overlapping regions and marked to avoid double counting cavities in the overlapping regions. When the entire TEM specimen was counted, the resulting information was fed into a custom script written in MATLAB®. This script reads in the length of all counted regions (excluding the overlapped regions) to tally the total length of the specimen. The script also reads in the cavity diameter and position from the measurement files and sorts them into 100nm depth bins, starting at the surface of the sample. Taking this length into account, the 100nm depth of the bin, and the average thickness of the specimen a total volume of the bin, V_{bin}, was calculated. The volume of each cavity was calculated assuming the cavity was a

sphere. The sum of the volume of each cavity was tallied for each bin. This value was effectively the change in volume, ΔV, in the bin. Swelling was then calculated as the change in volume divided by the original volume. Therefore, the swelling of any particular depth bin could be expressed as a percentage:

$$\text{Swelling (\%)} = \frac{\Delta V}{V_{bin}-\Delta V} * 100\% = \frac{\frac{\pi}{6}\sum_{i=1}^{N} d_i^3}{l*w*\delta-\frac{\pi}{6}\sum_{i=1}^{N} d_i^3} * 100\%, \qquad \text{Eq. 4.3}$$

where l is the length of the bin, w is the width of the bin, and δ is the thickness of the TEM specimen, N is the number of cavities in the bin, and d_i is the diameter of the individual ith cavity. For the nominal swelling value within the 500-700 nm depth region, the volume change calculation included cavities from both the 500-600 nm and the 600-700 nm bins. Average cavity diameter and number densities were also determined as a function of depth. Additionally, a cavity size distribution with number density plotted as a function of size was also determined.

For the cavities of smaller sizes, nominally smaller than 5 nm in diameter, on each underfocused BF CTEM image near the +0 μm focal point, the cavities were counted and measured with the diameter of the cavities being recorded and stored separately from the image. During counting, the underfocused BF images were cross-referenced with the overfocused BF images to ensure the cavities being counted were cavities. After the counting of an image was complete, the next sequential image was examined for any overlapping regions and marked to avoid double counting cavities in the overlapping regions. When the entire image set for the TEM specimen was counted, the cavity sizes were collected into one file. The average cavity size from these images and number densities were also determined. The cavity size distribution with number plotted as a function of size was also determined and spliced into the cavity size distribution from the HAADF images to create size distributions for the full range of cavity sizes.

The sink strength of the total cavity size distribution was determined by summing over the size distribution with the following equation from [4]:

$$k_{cav}^2 = 2\pi \sum_{i=0}^{D} d_i N_i, \quad \text{Eq. 4.4}$$

where N_i is the density of cavities of diameter d_i, and D is the maximum cavity size observed. Density bins in the size distribution were calculated with a resolution of 0.5 nm per bin from 0 to 5 nm and 1 nm per bin for cavities greater than 5 nm in diameter. An example of the results of depth profiling cavities from HAADF images with size, number density, and swelling, along with the combined HAADF STEM and BF CTEM size distribution is shown in Figure 4.14.

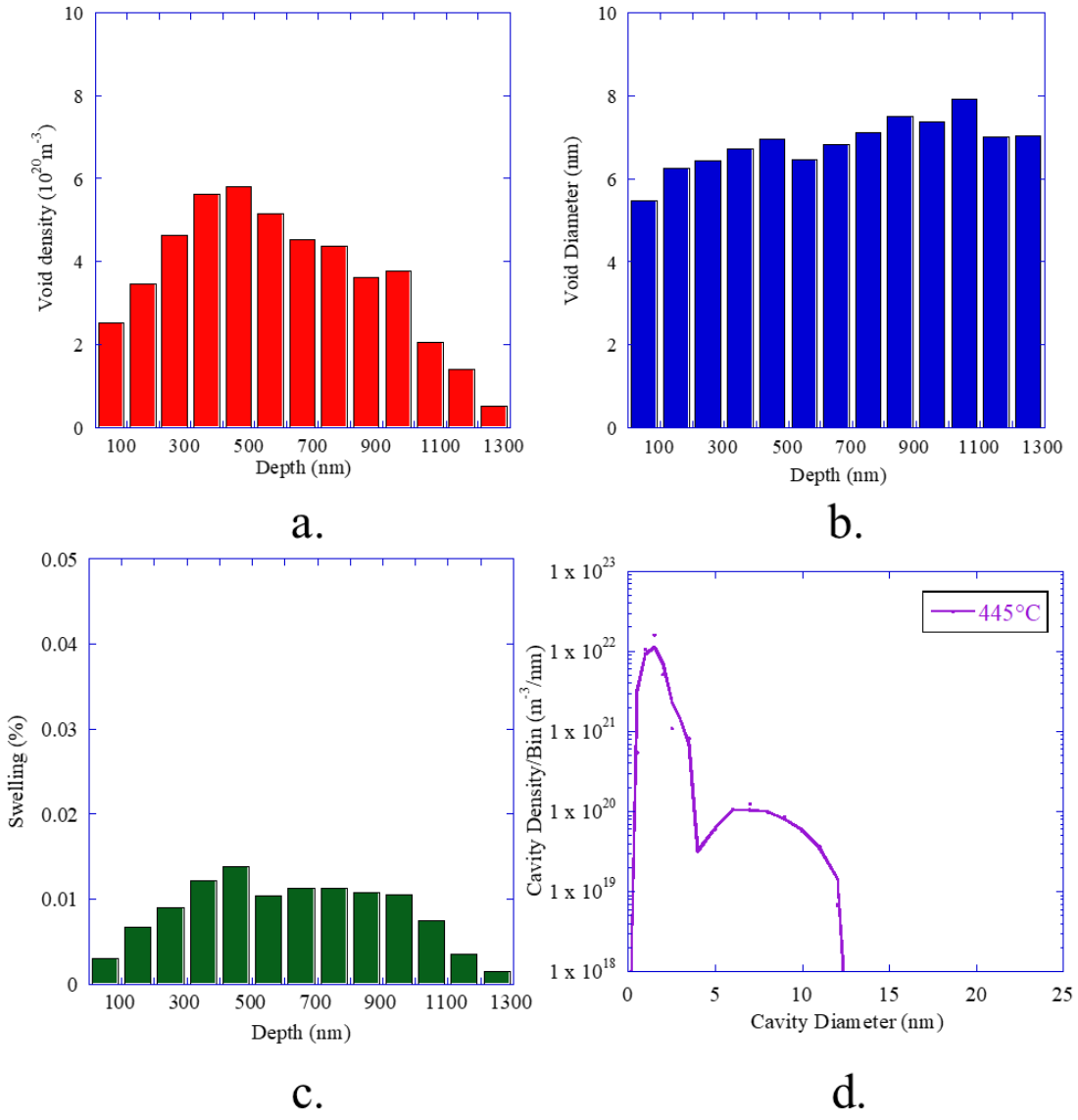

Figure 4.14. An example of profiling cavities through depth in T91 irradiated to 16.6 dpa at 445°C with 4 appm He/dpa at 7.1 × 10^{-4} dpa/s for (a) number density, (b) average diameter and (c) swelling from STEM imaging. The resulting combined STEM and CTEM cavity size distribution from the 500-700 nm region is shown in (d).

4.4.4 Determination of Valid Region of Analysis

As seen in the SRIM profile in Figure 4.5, the damage rate changes as a function of depth, so the calculation of a damage level for a particular experiment is not straightforward. As mentioned previously, a depth of 600 nm in the SRIM profile was used as the nominal damage level for each experiment. This depth was chosen as it adequately avoids the effects of injected interstitials at the higher depths and avoids effects of the free surface. Zinkle and Snead [7]

determined the valid depths of analysis for a Fe-10Cr system for 5 MeV iron ions which takes into account diffusion of interstitials from higher depths and the void-denuded surface effects. For the T91 system, which is close to the model system as a nominally Fe-9Cr alloy, at 50 dpa and 450°C, the valid depth regions remain within a range of 350 – 900 nm, which adequately avoids surface and interstitial effects. A similar depth range was determined as valid by Getto et al. [6] in HT9. Thus, using a depth of 500-700 nm in the SRIM profile as the region of analysis avoids complicating artefacts from the shallow penetration depth of ion irradiation.

4.4.5 Error Analysis

For all conditions in this thesis, an effort was made to minimize the error due to counting statistics, to ensure the accuracy of the cavity size distribution measurements. A similar error analysis presented in [147,160] is followed here. At least two TEM specimens for each condition were extracted, which was nominally equivalent to 2.5 μm^2 of material about 100nm thick (for the 500-700nm region). However, errors due to instrument limitations, such as TEM resolution needed to be considered. The two types of error that needed to be accounted for were error due to TEM resolution, and error due to EELS thickness measurements.

The resolution for the HAADF images taken was 0.7nm/pixel. This would mean that the error on each end of a measurement would be less than 1nm, regardless of the size of the measurement. The error in the measurement of the size of the feature (cavity, precipitate, or dislocation), would then depend on the size of the measurement. The fractional error could then be represented for the STEM images by:

$$\mu_{res} = \frac{1nm}{L}, \qquad \text{Eq. 4.5}$$

where L is the size of the measurement.

The resolution for CTEM BF underfocused and overfocused images was 0.07nm/pixel for the magnification used for imaging. However, the imaging resolution of the instrument for CTEM is 0.10 nm for lattice resolution and 0.25 nm for point-to-point resolution. Therefore, 0.25 nm was assumed to be the error in the CTEM BF measurements of cavities. The fractional error could then be represented for the CTEM BF images by:

$$\mu_{res} = \frac{0.25nm}{L}, \quad \text{Eq. 4.6}$$

where *L* is the size of the measurement. Figure 4.15 shows how the error due to TEM resolution changes as a function of cavity size. This measurement error would also contribute to any calculation which depends on the cavity size, such as the calculation of swelling.

As mentioned previously, the fitting of the EELS zero loss method exhibits an error of 10%. This thickness measurement affects the calculation of number density but is not dependent on any other factors. Therefore, error in number density at all times is estimated to be 10%. This is depicted as a flat line in Figure 4.15. The calculation of swelling includes both diameter and thickness measurements, therefore the contributions of error in both TEM resolution and EELS thickness measurements both contribute to the swelling error. Cavity swelling is directly proportional to the number density and proportional to the cube of the diameter, as shown below:

$$\frac{\Delta V}{V} \propto N_v \propto \left(\frac{d}{2}\right)^3. \quad \text{Eq. 4.7}$$

The propagation of error for multiplicative quantities and quantities raised to a power is shown below:

$$\mu_{mult} = \frac{\sigma_u}{u} = \sqrt{\left(\frac{\sigma_x}{x}\right)^2 + \left(\frac{\sigma_y}{y}\right)^2}, \quad \text{Eq. 4.8}$$

$$\mu_{power} = n * \left(\frac{\sigma_x}{x}\right), \quad \text{Eq. 4.9}$$

where n is the exponent in the original equation. For swelling, these two propagations can be combined, resulting in the following calculation for swelling error:

$$\mu_{swelling} = \sqrt{\left(\frac{\sigma_{N_d}}{N_d}\right)^2 + \left(n\frac{\sigma_d}{d}\right)^2} = \sqrt{\left(\mu_{N_d}\right)^2 + (3 * \mu_d)^2} \qquad \text{Eq. 4.10}$$

where N_d is the number density, d is the cavity diameter, and μ_{N_d} and μ_d are the fractional errors in the number density and diameter respectively. The swelling error therefore depends on errors in the number density and diameter. The dependence of the error with swelling on cavity size is also shown in Figure 4.15.

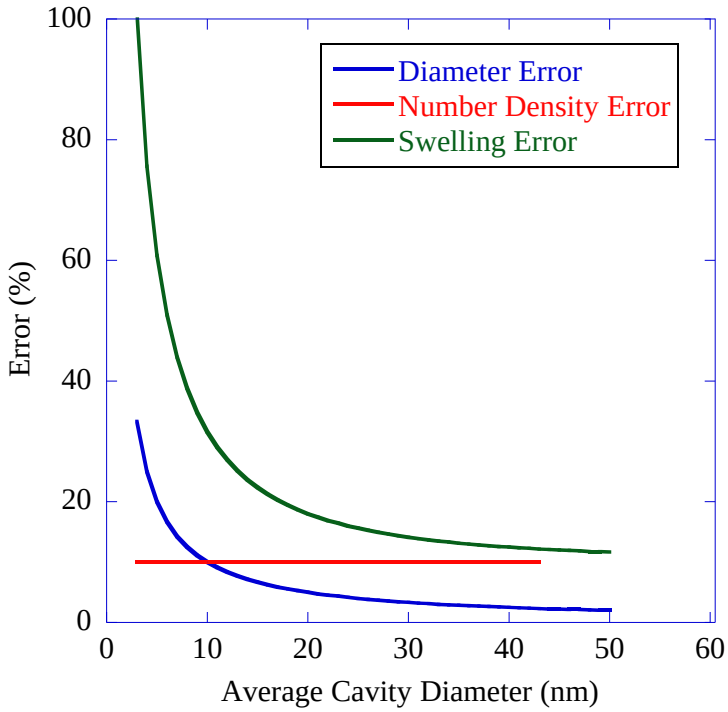

Figure 4.15. The error in diameter, number density and swelling is plotted as a function of cavity diameter.

It is also important to consider the high degree of inhomogeneity inherent to ferritic-martensitic steels. Grain-to-grain variation in the microstructure contributes additional uncertainty to the swelling measurements, as cavity nucleation and growth can vary extensively in adjacent grains. To minimize this uncertainty, multiple TEM specimens were extracted for each condition

from different regions of the irradiated sample. At least two TEM specimens were made per condition, encompassing an area of approximately 2.5 μm^2, with foil thicknesses less than 100 nm.

4.4.6 Dislocation Imaging and Characterization

Imaging of dislocation loops in ferritic-martensitic steels requires careful imaging conditions and sample preparation. The TEM specimens which were used for cavities were also used for dislocations. Two types of loops exist in FM alloys: sessile **b**<100> loops aligned on the [100] planes and glissile ½ **b**<111> loops. The ratio between these loops typically favors a higher population of **b**<100> loops. Typically, CTEM has been used to investigate the presence of these loops using the weak two-beam condition. However, such a method requires a sequence of images in the same area using varying diffraction vectors **g** to satisfy the dislocation loop **g·b** invisibility criterion. This is especially difficult in ferritic-martensitic steels which typically exhibit small grains with limited orientations. Methods to image dislocation loops using STEM mode have been used to more easily characterize these loops [71]. STEM imaging of loops also smears out thickness-dependent contrast that may be present in CTEM, resulting in a cleaner image. On-zone STEM imaging allows for the simultaneous imaging of all possible diffraction vectors, allowing for viewing of **b**<100>, ½ **b**<111> loops and dislocation lines all in the same image. When imaging along the [100] zone axis, **b**<100> loops appear circular or as perpendicular lines aligned with the [002] directions, while the ½ **b**<111> loops appear as ellipses aligned with the [011] direction. When imaging along the [110] zone axis, **b**<100> loops appear as ellipses or perpendicular lines aligned with the [002] directions, while the ½ **b**<111> loops as ellipses or perpendicular lines aligned with the [110] or [112] directions. A schematic of loop orientations when imaged along the [100] and [110] zone axes is shown in Figure 4.16 adapted from [161]. In practice, the loops were imaged in STEM mode just slightly off of the [100] zone axis or [110] zone axis so that

perpendicular loops did not appear as lines, and the inside-outside contrast was seen. An example micrograph showing **b**<100> loops, ½ **b**<111> loops, and dislocation lines of T91 irradiated to 16.6 dpa at 445°C and a damage rate of 7.1 × 10^{-4} dpa/s is shown in Figure 4.17.

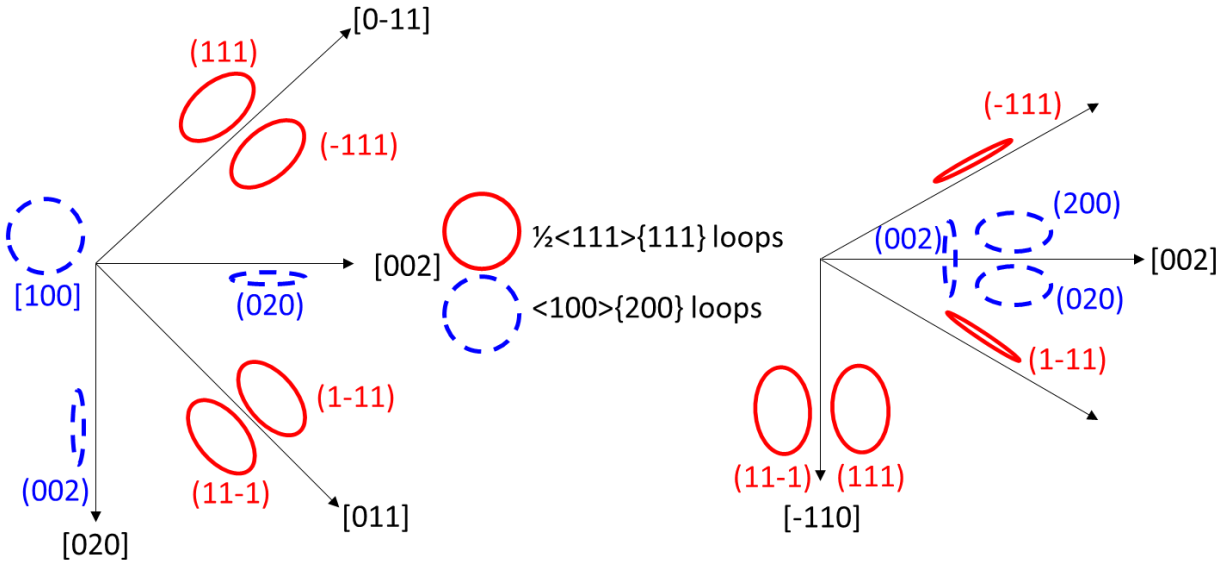

Figure 4.16. Schematic of dislocation loop orientations when observing down the [100] zone axis (left) and [110] zone axis (right) without considering ***g*·*b*=0** invisibility criterion, adapted from [161].

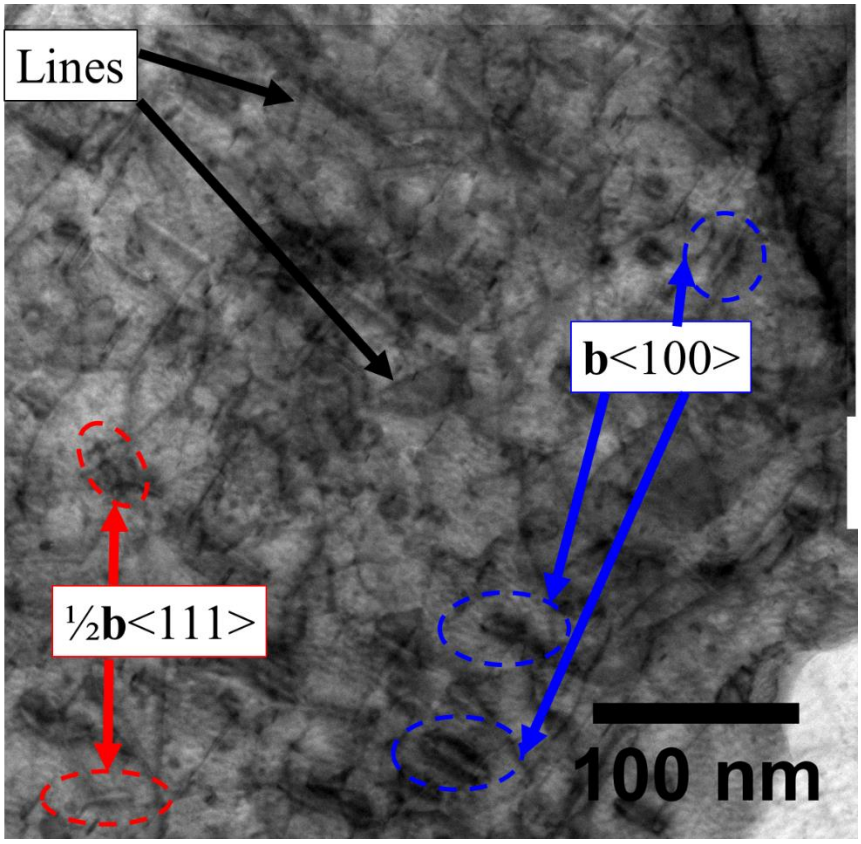

Figure 4.17. BF STEM image taken down the [100] zone axis showing **b**<100> loops, ½ **b**<111> loops and dislocation lines in T91 irradiated to 16.6 dpa at 445°C.

Images of loops were taken from at least three different grains for every condition within the 500-700nm depth region. Using FIJI, loops were counted and sized in a single orientation (for example along the [001] direction for **b**<100> loops with a [110] zone axis) or along two orientations (for example along the [001] and [010] directions for **b**<100> loops with a [001] zone axis). EELS thickness measurements were used as were used with the cavity number densities to calculate a loop density. The density was then multiplied by 3 for images along the [110] zone axis or multiplied by 1.5 for images along the [100] zone axis to account for the loops in the other directions which were not counted. Additionally, a dislocation loop size distribution with number density plotted as a function of size was also determined. From the values of diameter and density

a total loop line length (or sink strength) was calculated. The sink strength of the dislocation loops was calculated using the following equation:

$$k_{loop}^2 = \pi \sum_{i=0}^{N} d_i \rho_i, \quad \text{Eq. 4.11}$$

where ρ_i is the number density of dislocation loops of diameter d_i in the dislocation loop size distribution. The dislocation network density was calculated for this heat of T91, heat 30176, in previous work done by Jiao et. al [146] and estimated to be 10^{14}-10^{15} m^{-2}. A nominal value of 5×10^{14} m^{-2} was assumed for the dislocation network density.

4.5 Numerical Solutions to the Cavity Growth Rate Equation

Before discussing the results of the irradiation experiments, it is helpful to describe a common analytical framework in this section to be used in the analysis. Many aspects of cavity formation have been modeled approximately using the critical bubble model (CBM) concept [141,142] as described in Section 2.4.5 previously and follow from the growth rate equation:

$$\frac{dr}{dt} = \frac{\Omega}{r}\left[D_v C_v - D_i C_i - D_v C_{v,T} \exp\left(\frac{2\gamma}{r} - p_g\right)\right]. \quad \text{Eq. 4.12}$$

The cavity growth rate equation depends on several parameters from the microstructure, the irradiation conditions, and the material properties. Determination of the cavity growth rate involves two principle calculations: 1) the steady state point defect concentrations, and 2) the helium gas pressure inside a cavity. To calculate the point defect concentrations a standard rate equation for the change in defect concentration of either interstitials and vacancies with time was used from [4]:

$$\frac{dC_{(i,v)}}{dt} = K_0 - K_{iv} C_i \left(C_v + C_{v,T}\right) - K_{(i,v)s} C_{(i,v)} C_s. \quad \text{Eq. 4.13}$$

The first term on the right side of the equation is the production rate of defects, K_0,. The second term, $K_{iv} C_i \left(C_v + C_{v,T}\right)$, is the annihilation of the point defects due to mutual recombination

and includes the loss of interstitials recombining with thermally produced vacancies. The final term in the equation is the loss of point defects to sinks and is dependent on the concentration of sinks, C_s, the concentrations of point defects, and the interaction rate for either interstitials or vacancies with sinks, $K_{(i,v)s}$. To input the measured sink strengths of the microstructure, the point defect rate equations can be rewritten as:

$$\frac{dC_{(i,v)}}{dt} = K_0 - K_{iv}C_i\left(C_v + C_{v,T}\right) - k^2_{(i,v)}D_{(i,v)}C_{(i,v)}, \quad \text{Eq. 4.14}$$

where $k^2_{(i,v)}$ is the sink strength for either vacancies or interstitials and $D_{(i,v)}$ is the diffusion coefficient for the point defect specie.

The recombination parameter for defects was taken from [4]:

$$K_{iv} = \frac{z_{iv}\Omega(D_i+D_v)}{a^2},\ z_{iv}\sim 500, \quad \text{Eq. 4.15}$$

where z_{iv} is the combinatorial factor, Ω is the atomic volume, and a is the lattice parameter.

The sink strengths for interstitials and vacancies will be calculated for each irradiation condition using the microstructure measured in Chapter 5: . For each specie, the total sink strength is the sum of the sink strengths of the individual measured sinks:

$$k_v^2 = k_{dis}^2 + k_{cav}^2 + k_{gb}^2, \quad \text{Eq. 4.16}$$

$$k_i^2 = k_{dis}^2(1 + bias) + k_{cav}^2 + k_{gb}^2, \quad \text{Eq. 4.17}$$

where k^2_{cav} is the sink strength from cavities and bubbles, k^2_{gb} is the grain boundary sink strength, and the dislocation sink strength, k^2_{dis}, is multiplied by an interstitial bias factor.

The diffusion of interstitials and vacancies was assumed to have an Arrhenius dependence:

$$D_{i,v} = \alpha_{i,v}\omega_{i,v}exp\left(\frac{-E_m^{i,v}}{kT}\right), \quad \text{Eq. 4.18}$$

where α is 1/6 for interstitials and 1 for vacancies, ω is the jump frequency for either vacancies or interstitials, k is the Boltzmann constant, T is the temperature, and E_m is the migration energy for the point defect specie.

Finally, the thermal vacancy concentration was estimated using:

$$C_{v,T} = \frac{1}{\Omega} exp\left(\frac{S_f}{k}\right) exp\left(\frac{-E_f^v}{kT}\right), \quad \text{Eq. 4.19}$$

where S_f is the entropy of formation, and E_f^v is the vacancy formation energy. The thermal interstitial concentration was assumed to be negligible.

All of the previously described equations were used with the time derivative in Eq. 4.14 set to zero to solve for the steady state concentration of interstitials and vacancies using a numerical solver in MATLAB®. The pressure of helium gas inside a cavity was calculated using a modified form of the ideal gas law to include a hard sphere equation of state for helium, as used in previous work on cavity nucleation [141,162]:

$$p_g = \frac{n_g k_{bolt} T Z_{comp}}{V}, \quad \text{Eq. 4.20}$$

where V is the volume of the spherical cavity, n_g is the number of gas atoms with a factor for the compressibility of the helium gas:

$$Z_{comp} = \frac{1+y+y^2+y^3}{(1-y)^3}, \quad \text{Eq. 4.21}$$

where

$$y = \pi * n_g \frac{d_g^3}{6V}, \quad \text{Eq. 4.22}$$

and

$$d_g = 0.3135\left(0.8542 - 0.03996 * \ln\left(\frac{T}{9.16}\right)\right), \quad \text{Eq. 4.23}$$

where d_g is the hard sphere diameter of helium.

These equations were used to solve for the pressure of the gas numerically using MATLAB®. The default parameters used for the calculation of the cavity growth rate equation are included in Table 4.4. The dislocation bias for interstitials has been reported in literature in the range of 1% to 25% using analytic solutions [163–166] and 1 to 5% using rate theory approaches [167–171]. A value of 5% was chosen for this analysis to include the largest effect in the range of both approaches.

Table 4.4. Table of input parameters for calculating the cavity growth rate equation.

Parameter	**Value**	**Reference**
Temperature, T	Input Variable	This work
Damage Rate, K_0	Input Variable	This work
Helium Co-Injection Rate	Input Variable	This work
N	8.34×10^{22} at/cm^3	[69]
Lattice parameter (a)	0.288 nm	[69,160]
Sink strength	From microstructure	This work
ω_i	2.9×10^{12} s^{-1}	[69]
ω_v	1.6×10^{13} s^{-1}	[69]
Γ	1.75 J/m^2	[160]
E_{vm}	0.63 eV	[160]
E_{vf}	1.6 eV	[69]
E_{im}	0.35 eV	[69]
S_f	2.17k	[4]
Dislocation Bias	5%	See text.

Chapter 5: Results

This chapter presents the results of the characterization of the reactor and ion irradiation experiments described in Chapter 4: . The results are segregated into four sections based on the irradiation campaigns undertaken. The first section pertains to ion irradiations conducted with a fixed damage rate range, same levels of damage, same helium co-injection rate, and uses temperature as the altered variable. The second section focuses on ion irradiations conducted with a fixed damage rate range, a fixed level of damage, a fixed temperature determined to have the features of interest and uses the helium co-injection rate as the scaled variable. The third section features the ion irradiations performed at a fixed level of damage, temperature and helium co-injection rate and uses the irradiation damage rate as the independent variable. The fourth section features the irradiations conducted in BOR-60 nuclear reactor. For clarity and brevity, the first series of experiments will be referred to as the Temperature Series, the second series will be referred to as the Helium Rate Series, the third series will be referred to as the Damage Rate Series, and the fourth series will be referred to as the BOR-60 Series. The results of the Temperature Series are presented first as this series determined the starting conditions for the other two ion irradiation series. The Helium Rate Series is presented second and the Damage Rate Series is presented third. Finally, the BOR-60 Series is presented last. The nomenclature adopted for discussion is based on the experimental cavity size distributions. The term “bubbles” is used for cavities in the smaller of the size distributions in the bimodal cavity distribution while the term “voids” is used for those in the larger of the size distributions in the bimodal cavity distribution.

The cutoff between the two is determined based on the valley between the size distributions for each irradiation condition but can generally be estimated as 4-5 nm in diameter.

5.1 Microstructure Evolution with Variable Temperature for Fixed Helium Co-injection Rate and Damage Rate

5.1.1 Cavity Results

Voids were observed at all temperature conditions except the lowest (406°C) and highest (570°C) temperatures. STEM-HAADF images of cavities in dual ion irradiated T91 under different irradiation conditions at 4 appm He/dpa are shown in Figure 5.1. The temperature dependence of void diameter and number density are displayed in Figure 5.2a-b and tabulated in Table 5.1. The average void diameter tended to increase from 4.5±1.1 nm at 420°C to 7.5±1.1 nm at 510°C. Although voids were observed at 520°C, there were too few to obtain a reasonable average for the diameter. The void number density exhibited a bell-shaped behavior with temperature at 14.6-16.6 dpa with a maximum of 5.8×10^{20} m^{-3} at 460°C. Bubbles were observed in all examined conditions. The bubble number density exhibited no obvious trend with temperature at 14.6-16.6 dpa and did not increase significantly at 35 dpa. The combined observations of bubbles and voids resulted in a bimodal cavity size distribution, as displayed in Figure 5.3 for 14.6-16.6 dpa as a function of temperature and Figure 5.4 for a function of damage at 445°C. Void swelling was small at all conditions with values between 0.0008%±0.0004% at 432°C and 0.017%±0.004% at 460°C, as shown in Figure 5.2c. An increase in damage from 16.6 dpa to 35 dpa at 445°C resulted in a modest increase of the average void diameter and almost doubling of the void density. The bubble density remained fairly constant with dpa. The bubble number density, average void diameter, void number density, and void swelling are included for each condition in Table 5.1. Cavities exhibited large area-to-area variation both on a lath-to-lath basis and in different areas within the same lath.

Not all areas showed the presence of cavities when imaged with STEM-HAADF at 100kx or TEM BF at 200kx. Due to the inhomogeneous nature of the ion irradiation damage curve, no attempt was made to quantify the percentage of laths with nucleated cavities and bubbles as the laths frequently extend through multiple 100 nm wide bins.

Table 5.1. Summary of characterization results for cavities in dual ion irradiated T91 with 4.3 appm He/dpa. N.O. indicates that the feature was not observed. N.M. indicates the condition was not characterized for this feature. Negl. indicates the feature was observed but not in a large enough quantity to characterize for a representative value.

Temperature (°C)	Damage (dpa)	Damage rate (10^{-4} dpa/s)	Number of Bubbles Examined	Bubble Density (10^{20} m^{-3})	Average Bubble Diameter (nm)	Number of Voids Examined	Void Density (10^{20} m^{-3})	Average Void Diameter (nm)	Swelling (%)	Total Cavity Sink Strength (10^{14} m^{-2})
406	16.6	6.0	26	250	0.7	0	N.O.	N.O.	Negl.	1.9
420	16.6	5.4	22	280	1.3	54	1.1	4.5±1.1	0.001	3.1
432	16.6	5.4	178	540	1.6	27	1.2	5.0±1.1	0.0008	7.4
445	16.6	7.1	131	178	1.3	423	5.4	6.6±1.1	0.012	2.3
460	16.6	7.5	161	120	1.6	657	5.8	7.1±1.1	0.017	1.8
480	16.6	5.8	190	320	1.1	52	1.5	7.5±1.3	0.0044	2.5
520	14.6	6.5	176	140	2.2	1	Negl.	Negl.	Negl.	2.3
570	15.4	6.7	334	170	1.7	0	N.O.	N.O.	N.O.	2.3
445	35	7.6	573	140	1.0	426	9.4	7.5±1.1	0.036	2.7

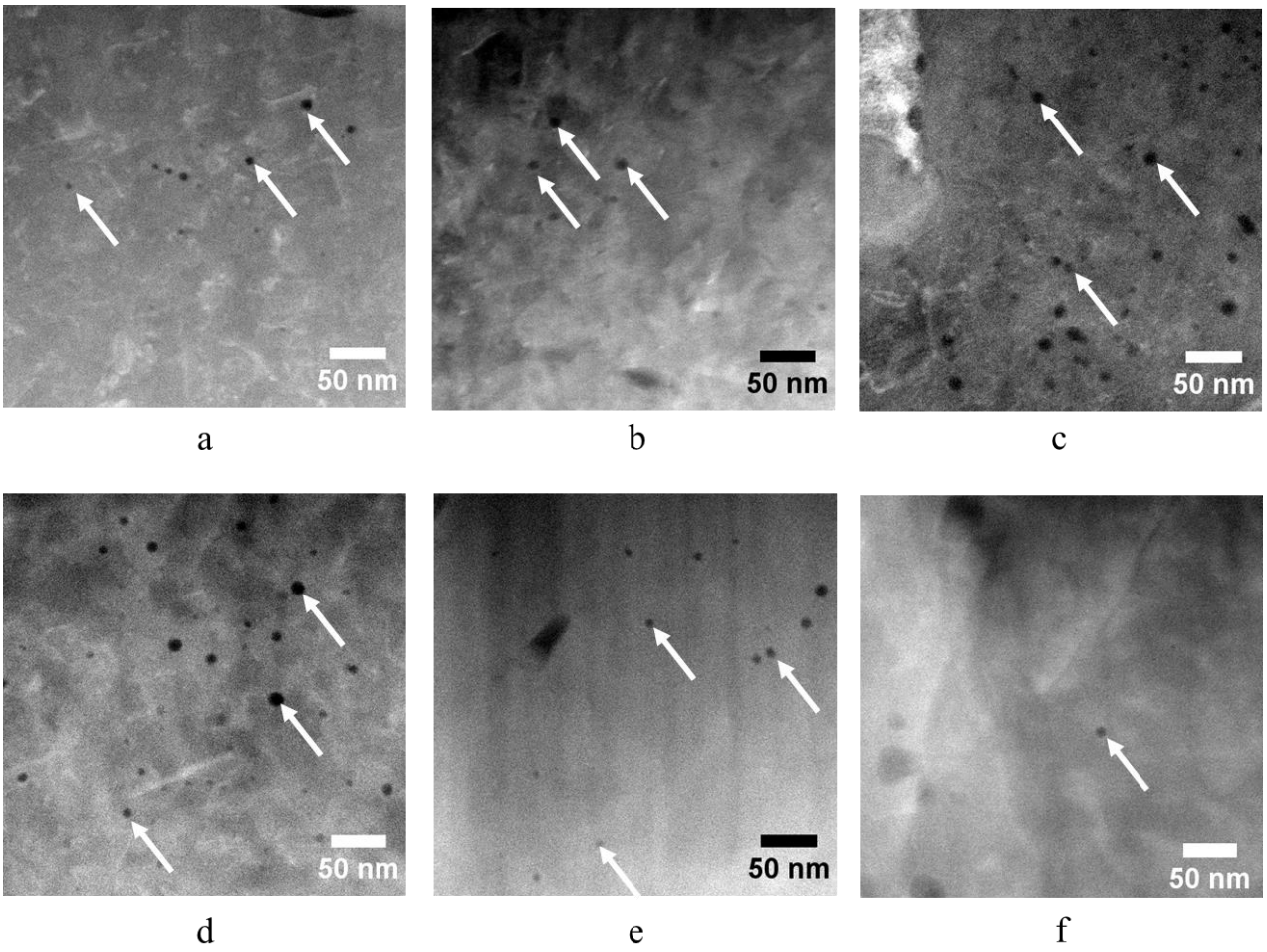

Figure 5.1. STEM HAADF images showing cavity evolution in dual ion irradiated T91 with 4 appm He/dpa from 14.6-16.6 dpa at different temperature conditions: (a) 420°C, (b) 432°C, (c) 445°C, (d) 460°C, (e) 480°C, and (f) 520°C. Some cavities are indicated with arrows.

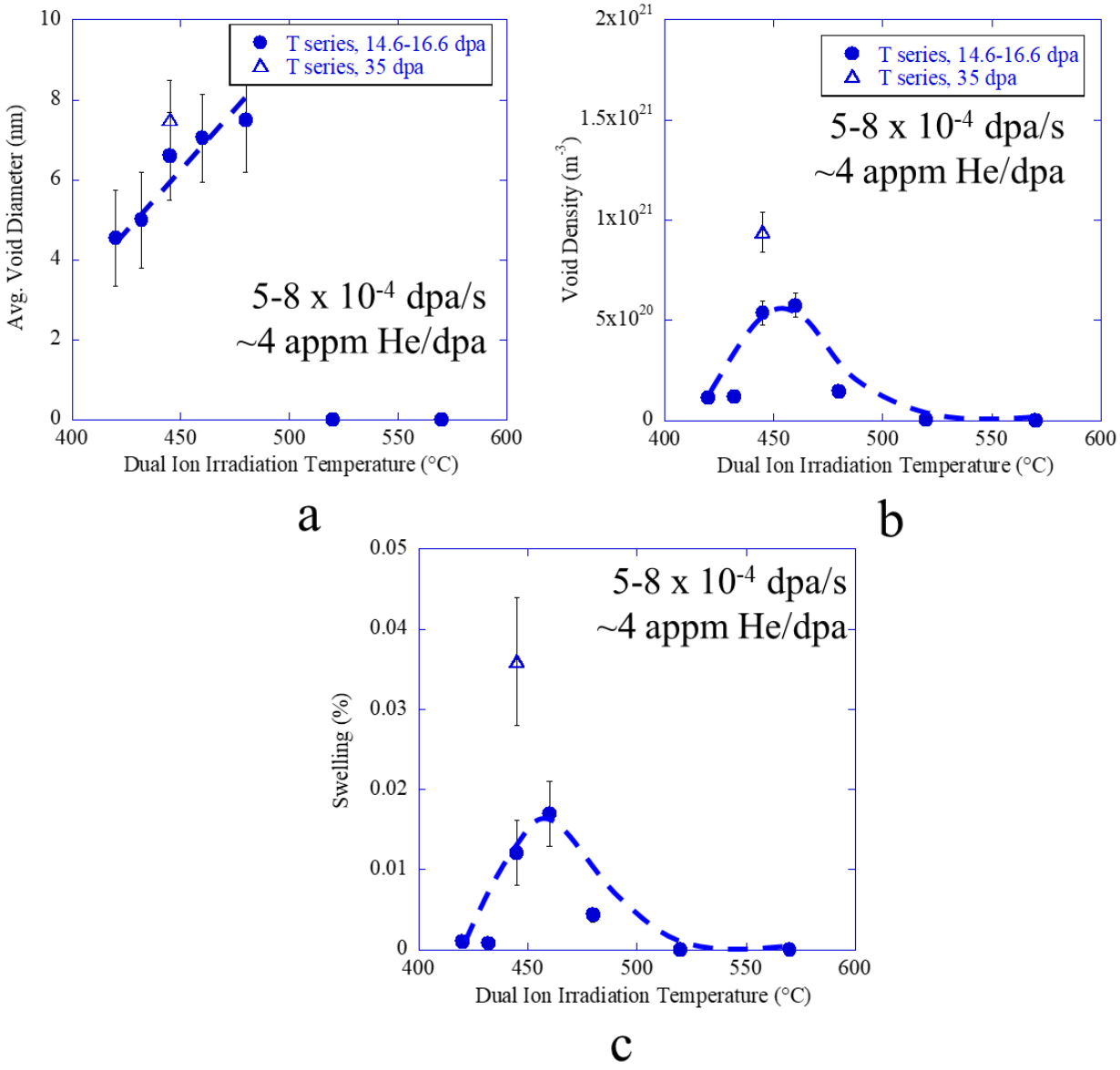

Figure 5.2. Average void diameter (a), density (b) and swelling (c) for voids in dual ion irradiated T91 with 4 appm He/dpa as a function of temperature.

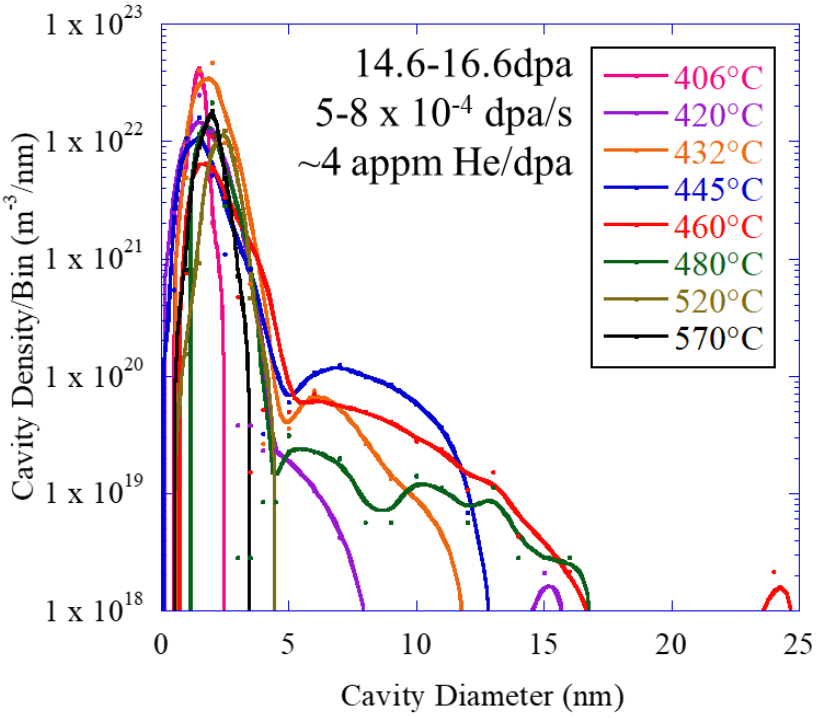

Figure 5.3. Cavity size distributions for dual ion irradiated T91 to 14.6-16.6 dpa with 4 appm He/dpa as a function of temperature.

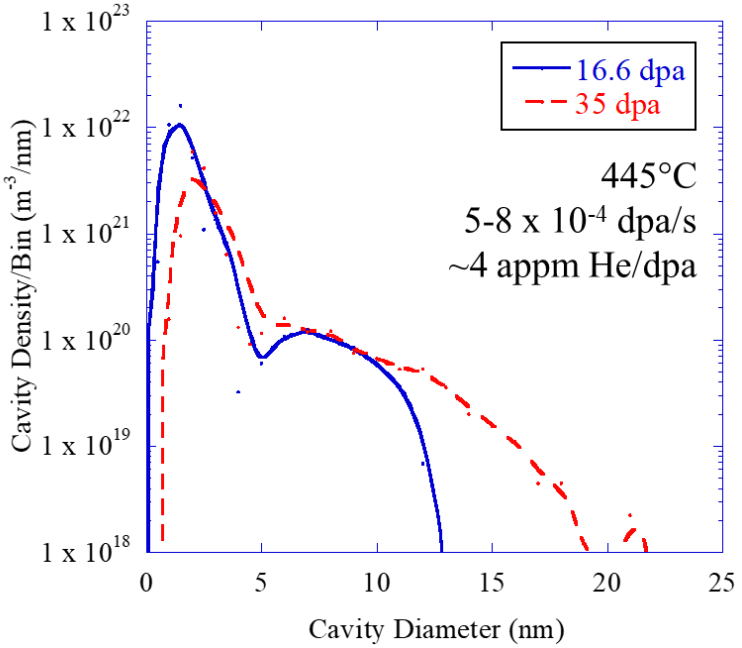

Figure 5.4. Cavity size distributions for dual ion irradiated T91 at 445°C with 4 appm He/dpa as a function of damage.

5.1.1.1 Low Temperature Regime

In a low temperature range (406°C-432°C), the cavity size distributions consist of a high density of bubbles with very little growth of voids as shown in Figure 5.5. Density increased with increasing temperature in this regime from a negligible density at 406°C to 1.2 × 10^{20} m^{-3} at 432°C. while the cavities that did grow grew to similar average sizes of 4.5±1.1 nm at 420°C and 5.0±1.1 nm at 432°C. Swelling was correspondingly low at 0.001% or less for this temperature regime.

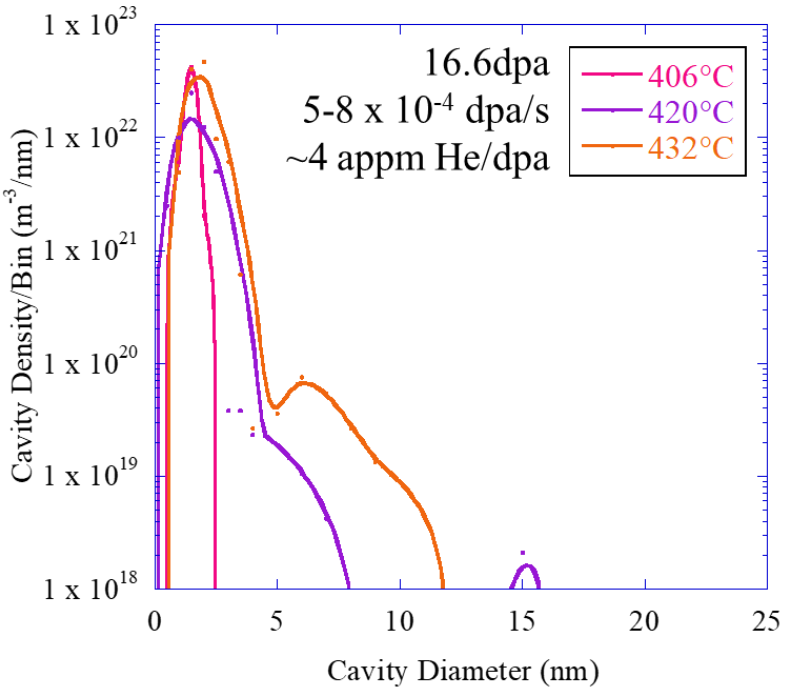

Figure 5.5. Cavity size distributions for dual ion irradiated T91 to 16.6 dpa with 4 appm He/dpa in the low temperature regime.

5.1.1.2 Intermediate Temperature Regime

At the intermediate temperatures of 445°C, 460°C, and 480°C, the cavity size distributions consistent of a high density of small bubbles and exhibit clear growth of voids as shown in Figure 5.6. The tail of the cavity diameter to larger sizes increased with increasing temperature, with the average cavity diameter following the same trend from 6.6±1.1 at 445°C to 7.5±1.1 at 480°C. However, the cavity density showed a peaked behavior with a maximum of 5.8 × 10^{20} m^{-3} at 460°C.

Primarily following from this density behavior is the peaked behavior of swelling with a maximum of 0.017% at 460°C.

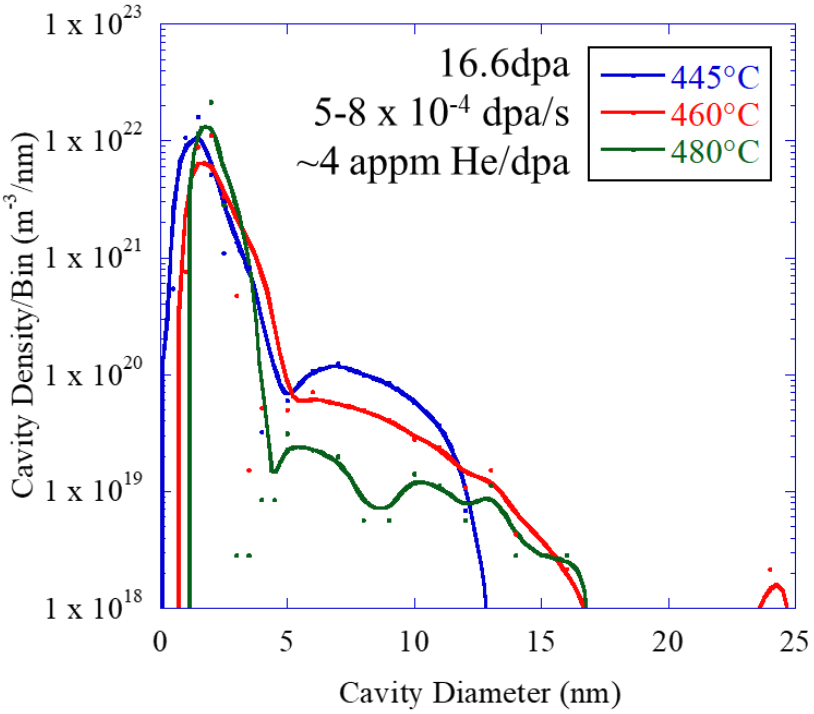

Figure 5.6. Cavity size distributions for dual ion irradiated T91 to 16.6 dpa with 4 appm He/dpa in the intermediate temperature regime.

5.1.1.3 High Temperature Regime

At higher temperatures of 520°C and 570°C, the cavity size distributions are similar to the low temperature distributions in that they consist only of bubbles, shown in Figure 5.7. Although some larger cavities were observed at 520°C, there are not enough to generate a size distribution or estimate a representative average diameter. However, the density of bubbles is lower at high temperature compared to the low temperature regime. The high temperature conditions had negligible swelling.

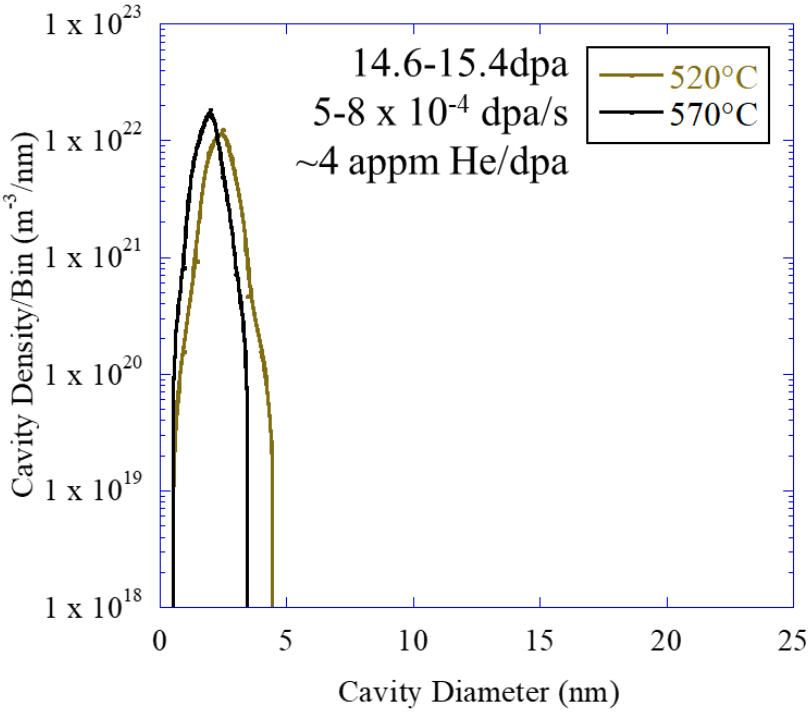

Figure 5.7. Cavity size distributions for dual ion irradiated T91 to 15 dpa with 4 appm He/dpa in the high temperature regime.

The cavity size distributions in all temperature regimes were further examined for the locations of the local extrema in each distribution. At low temperatures of 406°C and 420°C and high temperature of 520°C and 570°C, only bubbles were observed and therefore only one extremum existed in the cavity size distribution. In the intermediate temperature range, three local extrema were observed in each cavity size distribution: two peaks and one valley. The cavity radii associated with extrema did not change significantly with temperature. A summary of the cavity extrema is included in Table 5.2.

Table 5.2. Table of the extrema in the cavity size distributions in the Temperature Series of ion irradiations. N.O. indicates the feature was not observed.

Extrema (radius, nm)	406°C, 16.6 dpa	420°C, 16.6 dpa	432°C, 16.6 dpa	445°C, 16.6 dpa	460°C, 16.6 dpa	480°C, 16.6 dpa	520°C, 14.6 dpa	570°C, 15.4 dpa	445°C, 35 dpa
Peak 1 (bubbles)	~0.75±0.25	~0.75±0.25	~1.0±0.25	~0.75±0.25	~1.0±0.25	~1.0±0.25	~1.25±0.25	~1.0±0.25	~1.0±0.25
Valley	N.O.	N.O.	~2.0±0.25	~2.0±0.25	~2.5±0.25	~2.25±0.25	N.O.	N.O.	~2.25±0.25
Peak 2 (voids)	N.O.	N.O.	~3±0.25	~3.5±0.25	~3±0.25	~3±0.25	N.O.	N.O.	~3±0.25

5.1.2 Dislocation Loop Results

STEM-BF images of dislocation loops under different dual ion irradiation conditions at 4 appm He/dpa are shown in Figure 5.8 with a summary of the average dislocation loop diameter and number density tabulated in

Table 5.3 and shown graphically in Figure 5.9. The dislocation loop size distributions are included in Figure 5.10. Loops with a Burgers vector of **a**<100> on either (010) or (001) planes appeared as nearly edge-on in the images, while the **a**/2<111> loops residing on (111) planes appeared at an angle of approximately 54° relative to the (001) plane. The primary dislocation loops observed at each temperature from 406°C to 480°C were **a**{100} dislocation loops. Very few **a**/2{111} dislocation loops were observed across all temperatures examined and comprised less than 10% of the total loop number density. Several **a**/2{111} dislocation loops are visible in Figure 5.8 for the conditions of 432°C, 445°C, and 460°C. At a higher temperature of 520°C, very few dislocation loops were observed and there were not enough to have statistical significance. At the highest temperature of 570°C, only dislocation lines were observed. The average dislocation loop diameter increased monotonically with temperature up through 460°C and the dislocation loop number density decreased monotonically with irradiation temperature as shown in Figure 5.9. The trends in the averages stem from the dislocation size distributions in Figure 5.10 where distributions decrease in density and shift to larger sizes with increasing temperature. Dislocation

lines were observed at all temperatures and no significant alteration of the existing network dislocation density was noted compared to the as-tempered condition.

Table 5.3. Summary of characterization results for dislocation loops in dual ion irradiated T91 with 4.3 appm He/dpa. N.O. indicates that the feature was not observed. N.M. indicates the condition was not characterized for this feature. Negl. indicates the feature was observed but not in a large enough quantity to characterize for a representative value.

Temperature (°C)	Damage (dpa)	Damage rate (10^{-4} dpa/s)	Number of Dislocation Loops Examined	Dislocation Loop Density (10^{21} m^{-3})	Average Dislocation Loop Diameter (nm)	Dislocation Loop Line Density (m^{-2})	Total Dislocation Loop Sink Strength (10^{14} m^{-2})
406	16.6	6.0	50	12.0	10.1±1.2	3.8	3.8
420	16.6	5.4	61	5.4	13.1±1.6	2.2	3.1
432	16.6	5.4	55	4.7	19.8±2.4	2.9	2.9
445	16.6	7.1	103	3.5	25.3±3.0	2.8	2.5
460	16.6	7.5	59	1.6	29.5±3.5	1.5	1.8
480	16.6	5.8	33	0.46	29.0±3.8	0.42	0.4
520	14.6	6.5	4	Negl.	Negl.	Negl.	Negl.
570	15.4	6.7	0	N.O.	N.O.	N.O.	N.O.
445	35	7.6	139	2.8	19.0±2.2	1.7	2.1

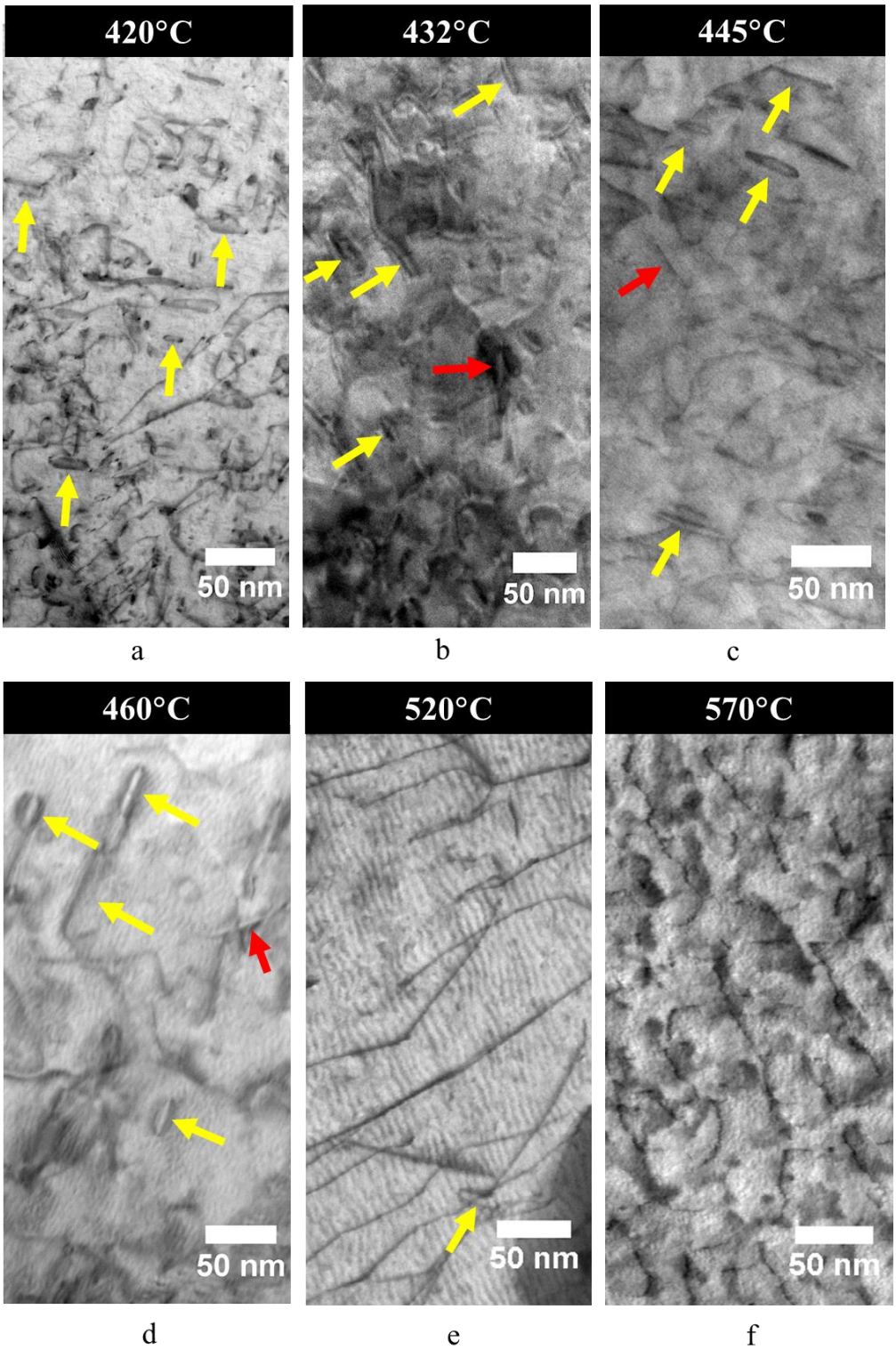

Figure 5.8. STEM-BF images showing dislocation evolution in T91 in the Temperature Series of irradiations to 14.6-16.6 dpa at 4 appm He/dpa under different irradiation conditions: (a) 420°C, (b) 432°C, (c) 445°C, (d) 460°C, (e) 520°C, and (f) 570°C. Some near-edge on **a**<100> type dislocation loops are indicated with yellow arrows and **a**/2<111> type dislocation loops indicated with red arrows.

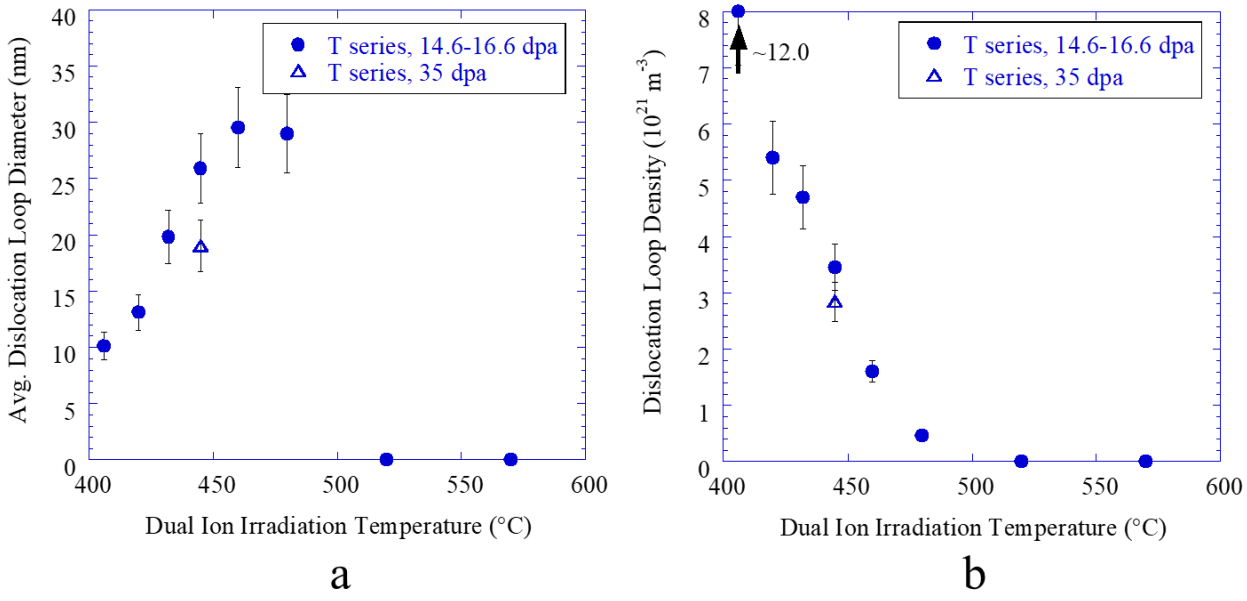

Figure 5.9. Average dislocation loop diameter (a) and dislocation loop density (b) as a function of temperature for dual ion irradiated T91 with 4 appm He/dpa.

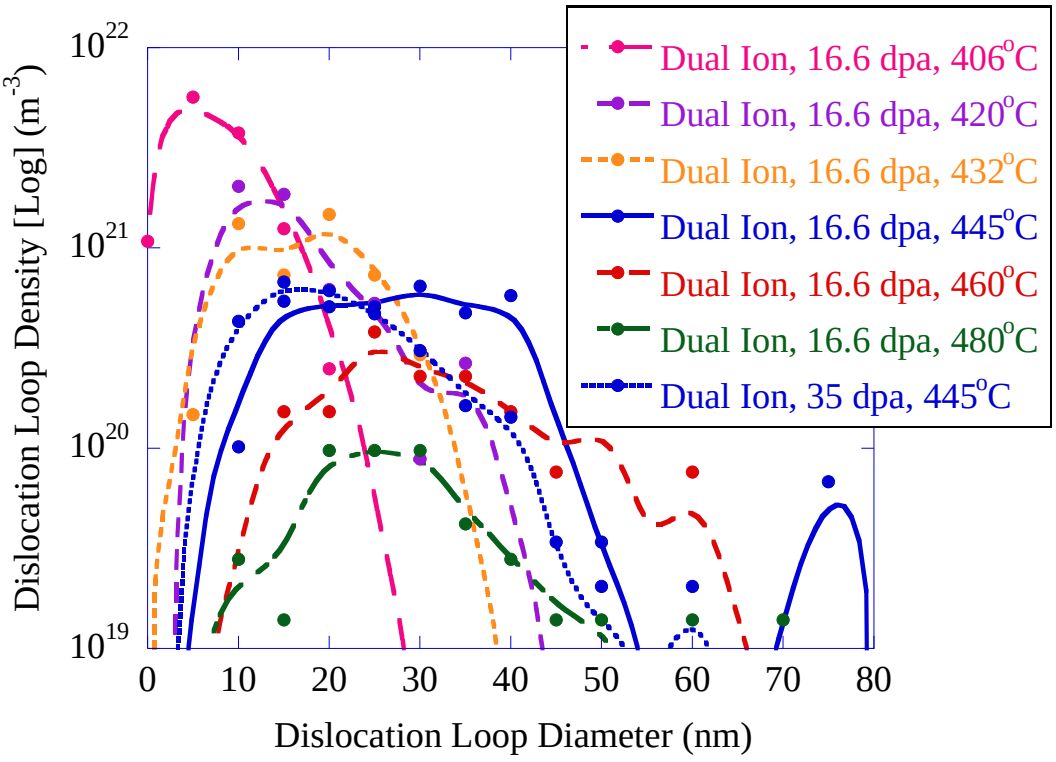

Figure 5.10. Dislocation loop size distributions as a function of temperature for dual ion irradiated T91 with 4 appm He/dpa.

5.2 Microstructure Evolution with Variable Helium Co-Injection Rate for Fixed Temperature and Damage Rate

5.2.1 Cavity Results

Cavities were observed across all helium conditions, as shown with STEM HAADF images in Figure 5.11. The dependence of void diameter and number density are displayed in Figure 5.12a-b and tabulated in Table 5.4. Overall the average void diameter across this range of helium co-injection rates did not change significantly with a range of 5.8±1.1 nm to 6.9±1.1 nm. Small cavities consistent with bubbles were only observed when helium was co-injected. Both the void density and bubble density increased with increasing helium co-injection rates, included in Figure 5.12b-c. The combined observations of bubbles and voids with helium co-injection resulted in bimodal cavity size distributions, as displayed in Figure 5.13. Both lobes of the distribution increased in density with increasing helium co-injection rate. Cavity swelling increased with increasing helium co-injection rate from a negligible amount of swelling with no helium co-injection to 0.012%±0.004% at 4 appm He/dpa, as shown in Figure 5.12d. The bubble number density, average void diameter, void number density, and void swelling are included for each condition in Table 5.4.

Table 5.4. Summary of characterization results for cavities in dual ion irradiated T91 at 445°C to a damage level of 16.6 dpa. N.O. indicates that the feature was not observed. N.M. indicates the condition was not characterized for this feature. Negl. indicates the feature was observed but not in a large enough quantity to characterize for a representative value.

Helium Co-Injection Rate (appm /dpa)	Damage rate (10^{-4} dpa/s)	Number of Bubbles Examined	Bubble Density (10^{20} m^{-3})	Average Bubble Diameter (nm)	Number of Voids Examined	Void Density (10^{20} m^{-3})	Average Void Diameter (nm)	Swelling (%)	Total Cavity Sink Strength (10^{14} m^{-2})
4.3	7.1	131	178	1.3	423	5.4	6.6±1.1	0.012	2.3
0.22	8.1	32	7.0	2.5	238	3.4	5.9±1.1	0.0051	0.29
0.02	7.2	27	3.0	3.1	37	0.57	5.8±1.1	0.0007	0.09
0	6.6	0	N.O.	N.O.	4	Negl.	6.9±1.3	Negl.	Negl.

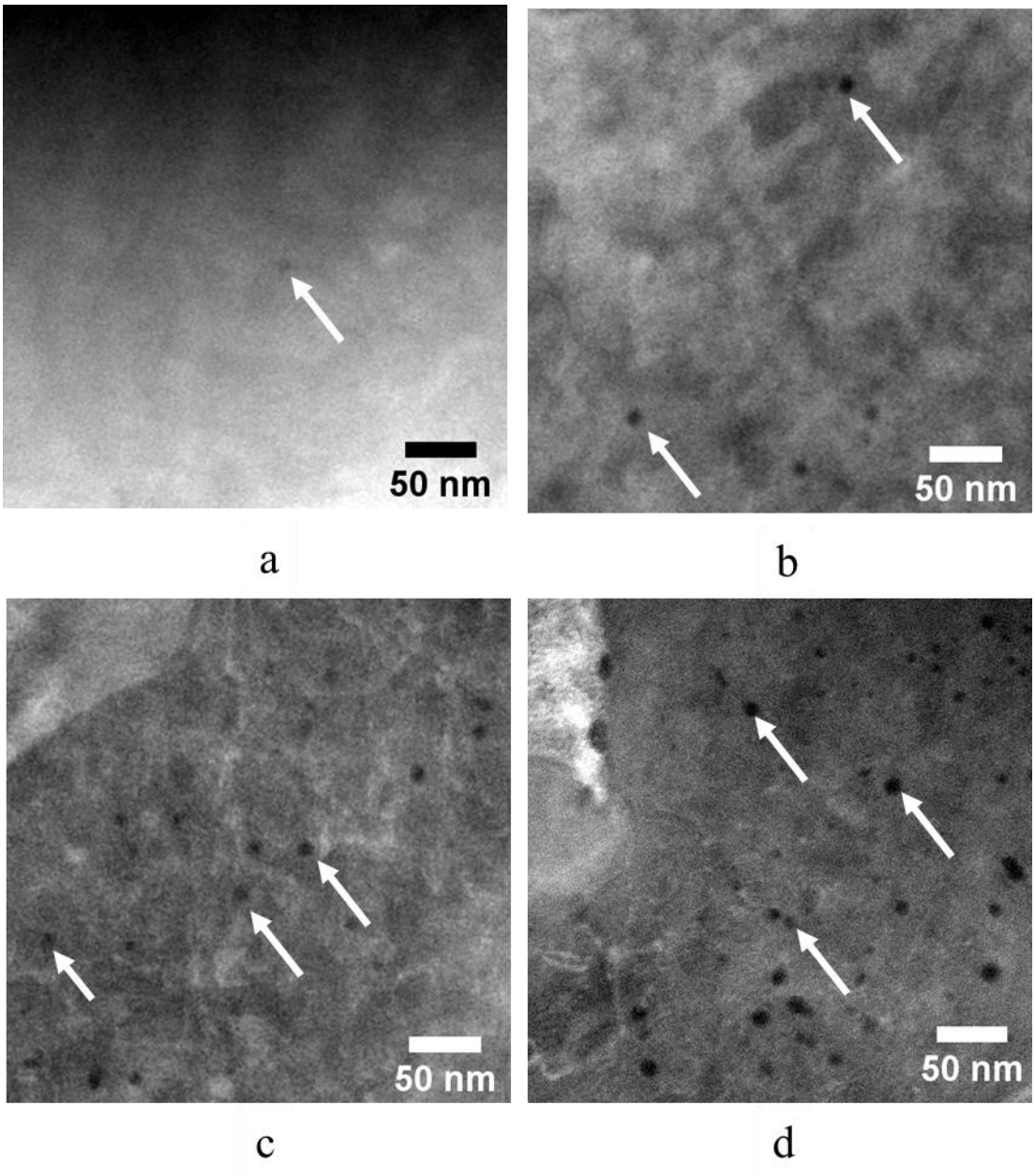

Figure 5.11. STEM HAADF images showing cavity evolution in dual ion irradiated T91 to 16.6 dpa at 445°C with (a) 0 He/dpa, (b) 0.02 appm He/dpa, (c) 0.22 appm He/dpa, and (d) 4 appm He/dpa. Some cavities are indicated with arrows.

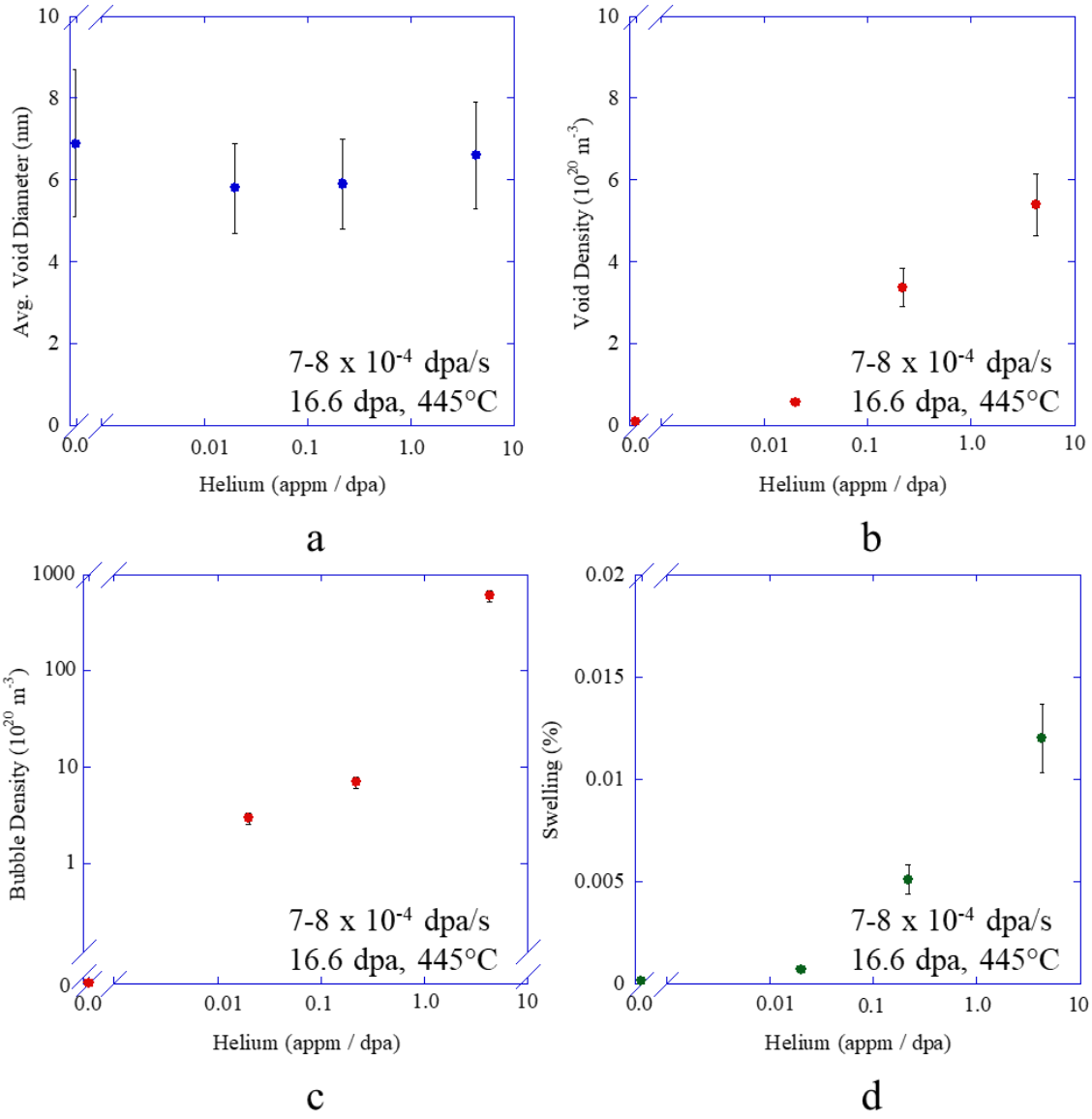

Figure 5.12. Average void diameter (a), void density (b), bubble density (c) and swelling (d) for cavities in dual ion irradiated T91 at 445°C to 16.6 dpa as a function of He/dpa.

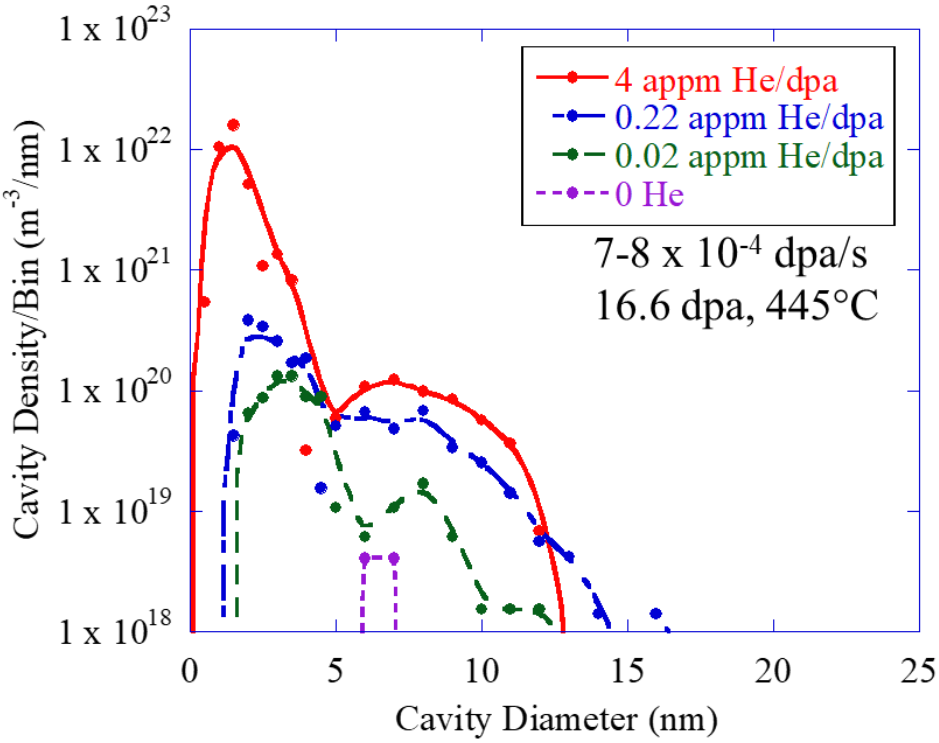

Figure 5.13. Cavity size distributions for dual ion irradiated T91 to 16.6 dpa at 445°C as a function of He/dpa ratio.

The cavity size distributions were examined for local extrema in the distribution. Without helium, only one peak was observed. With an increase in helium to 0.02 appm He/dpa, the distribution is bimodal in nature and contains three extrema: two peaks and one valley. With increasing He/dpa, the valley and the larger of the two peaks shifted to smaller cavity radii. A summary of the extrema for each distribution is included in Table 5.5.

Table 5.5. Table of the extrema in the cavity size distributions in the Helium Rate Series of ion irradiations. N.O. indicates the feature was not observed.

Extrema (radius)	0 He/dpa	0.02 appm He/dpa	0.22 appm He/dpa	4 appm He/dpa
Peak 1 (bubbles)	N.O.	~1.625±0.25 nm	~1.125±0.25 nm	~0.75±0.25 nm
Valley	N.O.	~3.0±0.25 nm	~2.25±0.25 nm	~2.0±0.25 nm
Peak 2 (voids)	~3.25±0.25 nm	~4.0±0.25 nm	~4.0±0.25 nm	~3.5±0.25 nm

5.2.2 Dislocation Loop Results

STEM-BF images of dislocation loops under different helium co-injection rates irradiated at 445°C to 16.6 dpa are shown in Figure 5.14 with a summary of the average dislocation loops

diameter and number density tabulated in Table 5.6 and shown graphically in Figure 5.15. The dislocation loop size distributions are included in Figure 5.16. Loops with a Burgers vector of **a**<100> on either (010) or (001) planes appeared as nearly edge-on in the images, while the **a**/2<111> loops residing on (111) planes appeared at an angle of approximately 54° relative to the (001) plane. The primary dislocation loops observed at each helium co-injection rate were **a**{100} dislocation loops with very few **a**/2{111} dislocation loops observed. The average dislocation loop diameter did not change significantly with helium co-injection rate from 17.5±3.2 nm to 25.3±3.0 nm. The dislocation loop density did not significantly change with helium co-injection rate in the range of $3.1\pm0.5 \times 10^{21}$ m^{-3} to $3.9\pm0.5 \times 10^{21}$ m^{-3}. Consequently, the dislocation loop size distributions, shown in Figure 5.16, showed strong similarity with the helium co-injection rate range. Dislocation lines were observed at all helium co-injection rates and no significant alteration of the existing network dislocation density was noted compared to the as-tempered condition.

Table 5.6. Summary of characterization results for dislocation loops in dual ion irradiated T91 at 445°C to a damage level of 16.6 dpa. N.O. indicates that the feature was not observed. N.M. indicates the condition was not characterized for this feature. Negl. indicates the feature was observed but not in a large enough quantity to characterize for a representative value.

Helium Co-Injection Rate (appm /dpa)	Damage rate (10^{-4} dpa/s)	Number of Dislocation Loops Examined	Dislocation Loop Density (10^{21} m^{-3})	Average Dislocation Loop Diameter (nm)	Dislocation Loop Line Density (10^{14} m^{-2})	Total Dislocation Loop Sink Strength (10^{14} m^{-2})
4.3	7.1	103	3.5	25.3±3.0	2.8	2.5
0.22	8.1	104	3.9	17.5±2.2	2.1	2.7
0.02	7.2	141	3.1	18.8±2.4	1.8	2.3
0	6.6	156	3.8	18.9±2.4	2.3	2.8

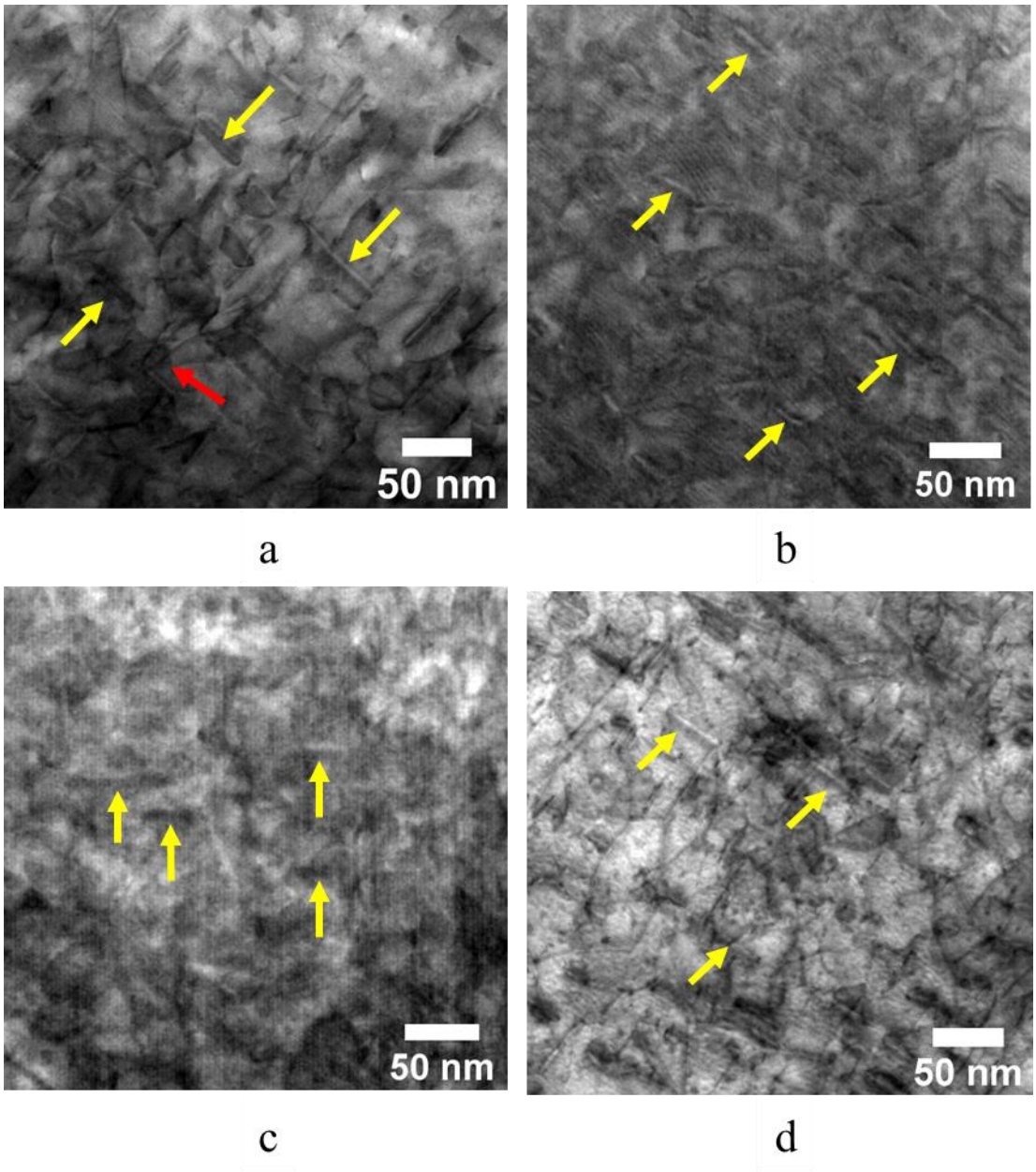

Figure 5.14. STEM-BF images showing dislocation evolution in T91 in the Helium Rate Series of irradiations to 16.6 dpa at 445°C under different irradiation conditions: (a) 0 He/dpa, (b) 0.02 appm He/dpa, (c) 0.22 appm He/dpa, and (d) 4 appm He/dpa. Some near-edge on **a**<100> type dislocation loops are indicated with yellow arrows and **a**/2<111> type dislocation loops indicated with red arrows.

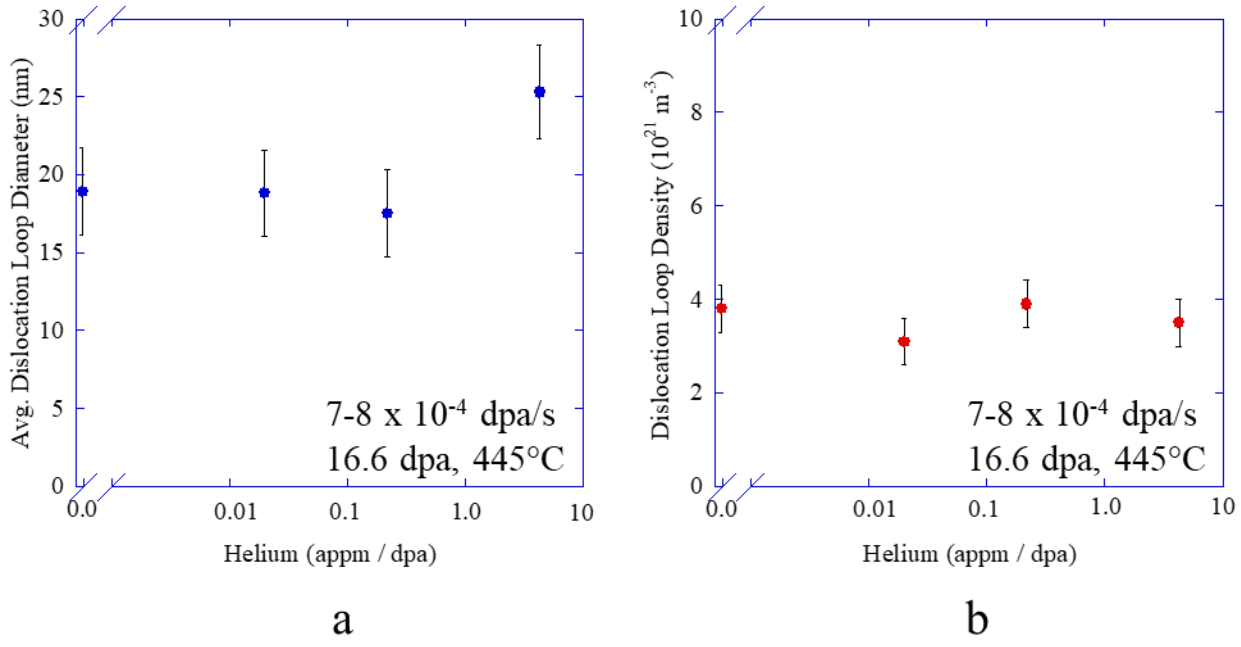

Figure 5.15. Average dislocation loop diameter (a) and dislocation loop density (b) as a function of He/dpa ratio for dual ion irradiated T91 at 445°C at 16.6 dpa.

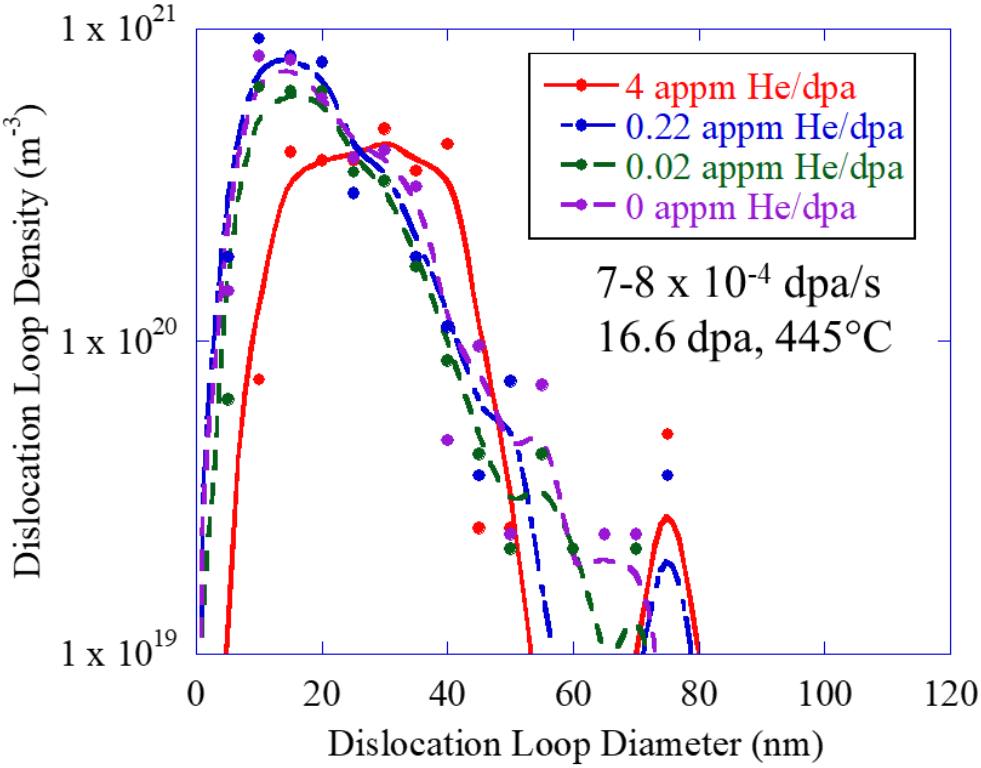

Figure 5.16. Dislocation loop size distributions as a function of He/dpa ratio for dual ion irradiated T91 at 445°C to 16.6 dpa.

5.3 Microstructure Evolution with Variable Damage Rate for Fixed Temperature and Helium Co-Injection Rate

5.3.1 Cavity Results

Cavities were observed across all damage rate conditions, as shown with STEM HAADF images in Figure 5.17. The dependence of void diameter and number density are displayed in Figure 5.18a-b and tabulated in Table 5.7. The average void diameter held nearly constant near 6.8±1.1 nm except for the highest damage rate condition where the average void diameter dropped to 4.7±1.1 nm. The void density appeared to decrease with increasing damage rate almost monotonically as shown in Figure 5.18b. Small cavities consistent with bubbles were observed at all damage rates. The bubble density showed no significant trend with damage rate, included in Figure 5.18c. The combined observations of bubbles and voids with helium co-injection resulted in bimodal cavity size distributions, as displayed in Figure 5.19. The size distribution of bubbles was consistent across damage rates, but the cavity distribution appeared to have a smaller tail to higher cavity diameters as the damage rate increased. Cavity swelling decreased with increasing damage rate from 0.023%±0.005% at the lowest damage rate to 0.0024%±0.0008% at the highest damage rate, as shown in Figure 5.18d. The bubble number density, average cavity diameter, cavity number density, and cavity swelling are included for each condition in Table 5.7.

Table 5.7. Summary of characterization results for cavities in dual ion irradiated T91 at 445°C to a damage level of 16.6 dpa. N.O. indicates that the feature was not observed. N.M. indicates the condition was not characterized for this feature. Negl. indicates the feature was observed but not in a large enough quantity to characterize for a representative value.

Helium Co-Injection Rate (appm /dpa)	Damage rate (dpa/s)	Number of Bubbles Examined	Bubble Density (10^{20} m^{-3})	Average Bubble Diameter (nm)	Number of Voids Examined	Void Density (10^{20} m^{-3})	Average Void Diameter (nm)	Swelling (%)	Total Cavity Sink Strength (10^{14} m^{-2})
4.3	3×10^{-3}	283	45	1.7	236	3.2	4.7±1.1	0.00244	0.8
4.3	7.1×10^{-4}	131	178	1.3	423	5.4	6.6±1.1	0.012	2.3
4.3	1×10^{-4}	380	55	1.8	182	5.2	7.2±1.1	0.0154	1.2
4.3	5×10^{-5}	160	30	1.9	598	9.4	6.8±1.1	0.0225	0.9

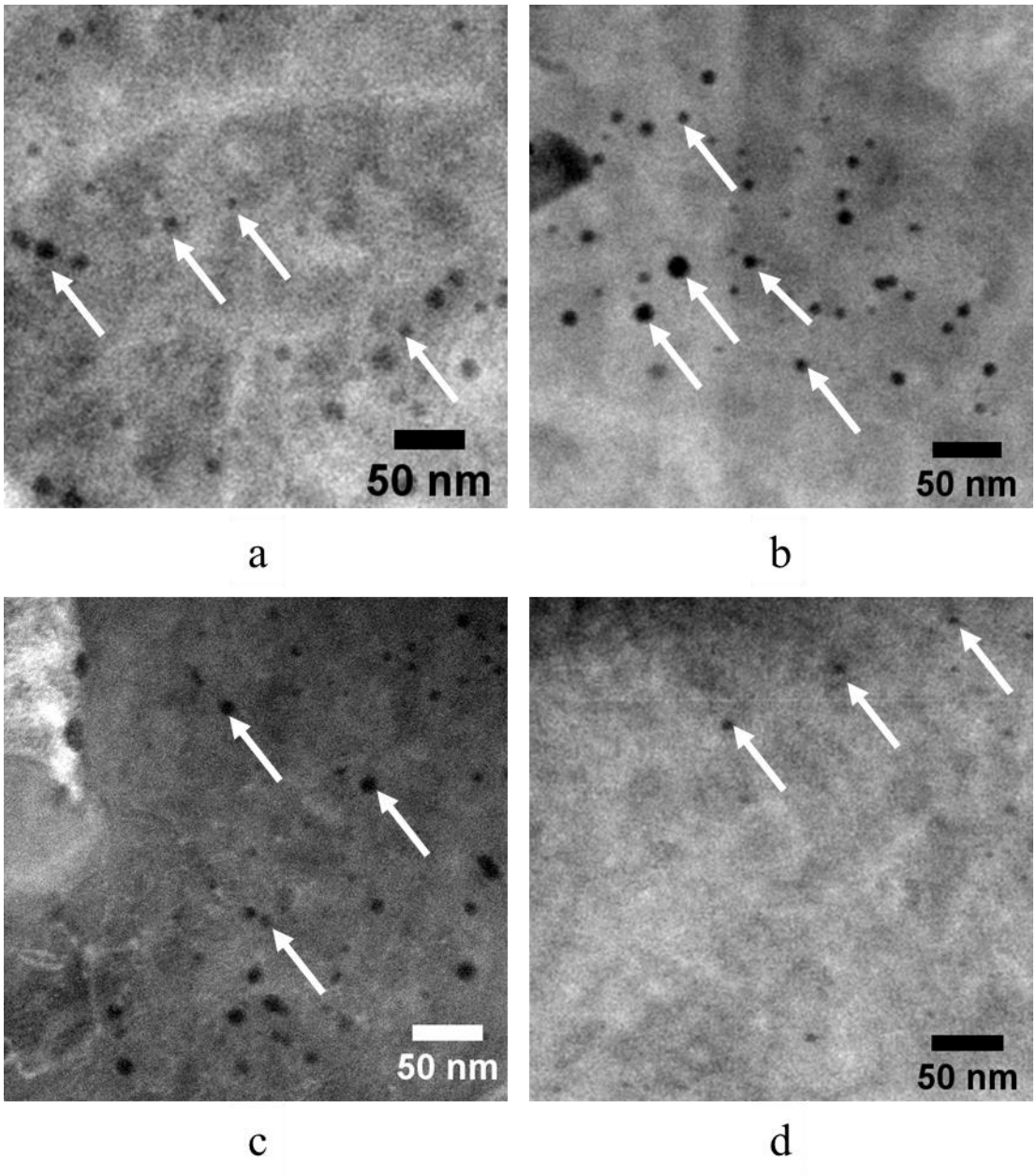

Figure 5.17. STEM HAADF images showing cavity evolution in dual ion irradiated T91 to 16.6 dpa at 445°C with 4 appm He/dpa irradiated with damage rates of (a) 5×10^{-5} dpa/s, (b) 1×10^{-4} dpa/s, (c) 7.1×10^{-4} dpa/s, and (d) 3×10^{-3} dpa/s. Some cavities are indicated with arrows.

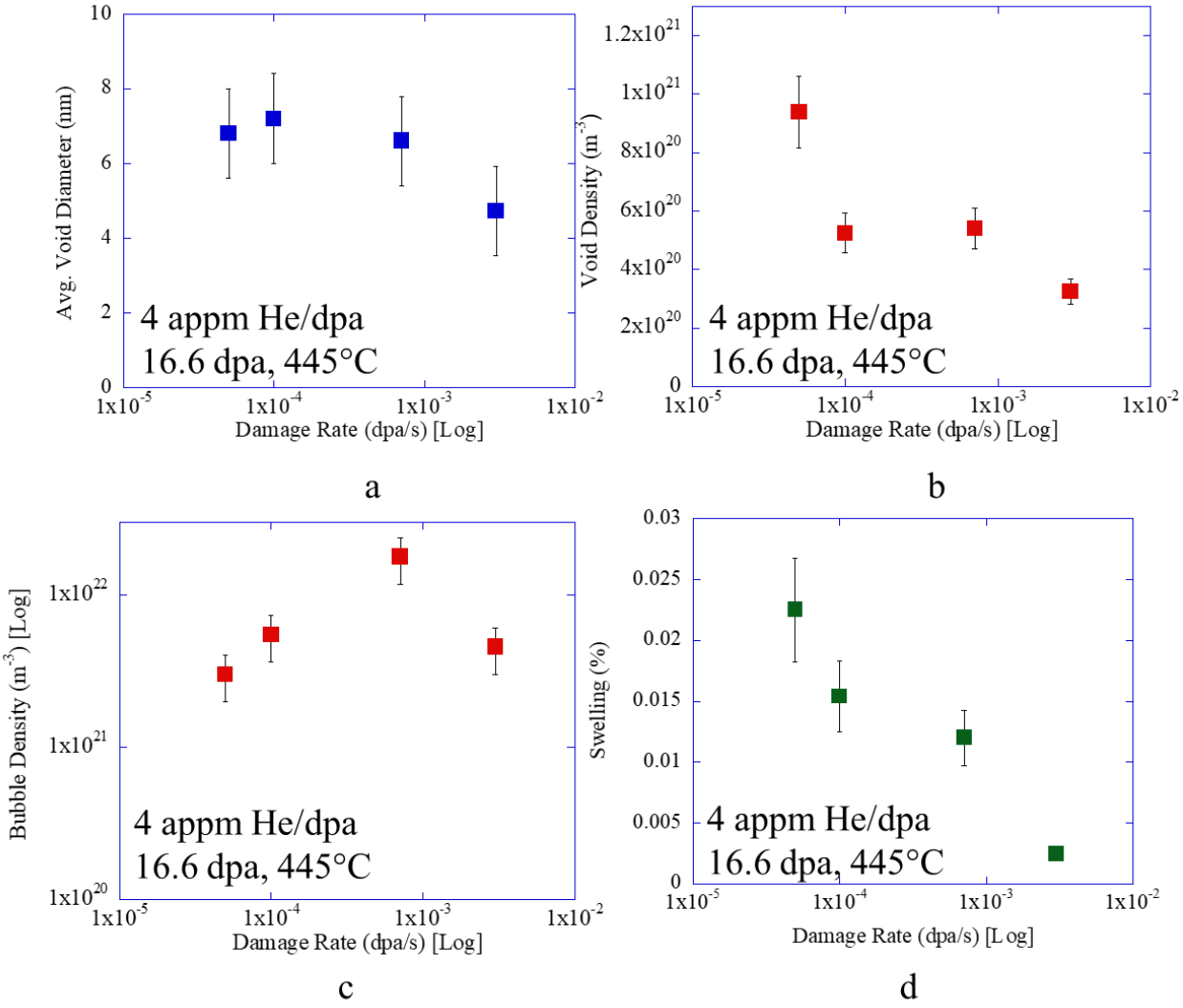

Figure 5.18. Average void diameter (a), void density (b), bubble density (c) and swelling (d) for cavities in dual ion irradiated T91 at 445°C to 16.6 dpa as a function of damage rate.

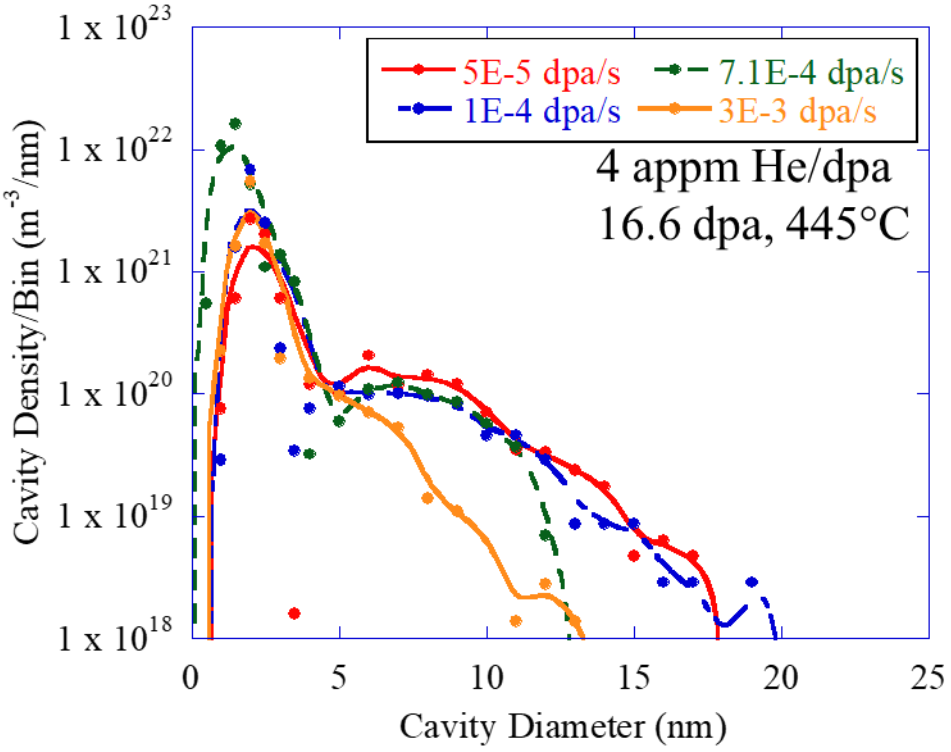

Figure 5.19. Cavity size distributions for dual ion irradiated T91 to 16.6 dpa with 4 appm He/dpa as a function of damage rate.

The cavity size distributions were examined for local extrema in the distributions. In each bimodal cavity size distribution, three local extrema were observed corresponding to two peaks and one valley in the distribution. There was no significant change in the locations of the peaks and valleys with irradiation damage rate in this series of experiments. A summary of the cavity size distribution extrema is included in Table 5.8.

Table 5.8. Table of the extrema in the cavity size distributions in the Damage Rate Series of ion irradiations. N.O. indicates the feature was not observed.

Extrema (radius)	5 x 10^{-5} dpa/s	1 x 10^{-4} dpa/s	7.1 x 10^{-4} dpa/s	3 x 10^{-3} dpa/s
Peak 1 (bubbles)	~1.0±0.25 nm	~1.0±0.25 nm	~0.75±0.25 nm	~1.0±0.25 nm
Valley	~1.75±0.25 nm	~1.75±0.25 nm	~2.0±0.25 nm	~1.75±0.25 nm
Peak 2 (voids)	~3.0±0.25 nm	~3.5±0.25 nm	~3.5±0.25 nm	~3.0±0.25 nm

5.3.2 Dislocation Loop Results

STEM-BF images of dislocation loops from dual ion irradiated T91 irradiated at 445°C to 16.6 dpa across a range of damage rates are shown in Figure 5.20 with a summary of the average dislocation loops diameter and number density tabulated in Table 5.9 and shown graphically in Figure 5.21. The dislocation loop size distributions are included in Figure 5.22. Loops with a Burgers vector of **a**<100> on either (010) or (001) planes appeared as nearly edge-on in the images, while the **a**/2<111> loops residing on (111) planes appeared at an angle of approximately 54° relative to the (001) plane. The primary dislocation loops observed at each damage rate were **a**{100} dislocation loops with very few **a**/2{111} dislocation loops observed. The average dislocation loop diameter did not change significantly with damage rate from 24.7±3.0 nm to 27.2±3.0 nm except at the highest damage rate condition of 3×10^{-3} dpa/s where the average dislocation loop diameter decreased to 10.5±2.2 nm. The dislocation loop density increased with increasing damage rate from $1.7\pm0.2 \times 10^{21}$ m^{-3} at the lowest damage rate to $4.7\pm0.6 \times 10^{21}$ m^{-3} at the highest damage rate. The dislocation loop size distributions, shown in Figure 5.16, showed a shift to smaller sizes with increasing damage rate with the tail of the size distribution becoming smaller with increasing damage rate. Dislocation lines were observed at all damage rates and no significant alteration of the existing network dislocation density was noted compared to the as-tempered condition.

Table 5.9. Summary of characterization results for dislocation loops in dual ion irradiated T91 at 445°C to a damage level of 16.6 dpa as a function of damage rate. N.O. indicates that the feature was not observed. N.M. indicates the condition was not characterized for this feature. Negl. indicates the feature was observed but not in a large enough quantity to characterize for a representative value.

Helium Co-Injection Rate (appm /dpa)	Damage rate (dpa/s)	Number of Dislocation Loops Examined	Dislocation Loop Density (10^{21} m^{-3})	Average Dislocation Loop Diameter (nm)	Dislocation Loop Line Density (10^{14} m^{-2})	Total Dislocation Loop Sink Strength (10^{14} m^{-2})
4.3	3×10^{-3}	93	4.7	10.5±1.2	1.6`	2.3
4.3	7.1×10^{-4}	103	3.5	25.3±3.0	2.8	2.5
4.3	1×10^{-4}	40	2.2	24.7±2.6	1.7	2.1
4.3	5×10^{-5}	121	1.7	27.2±3.1	1.5	1.7

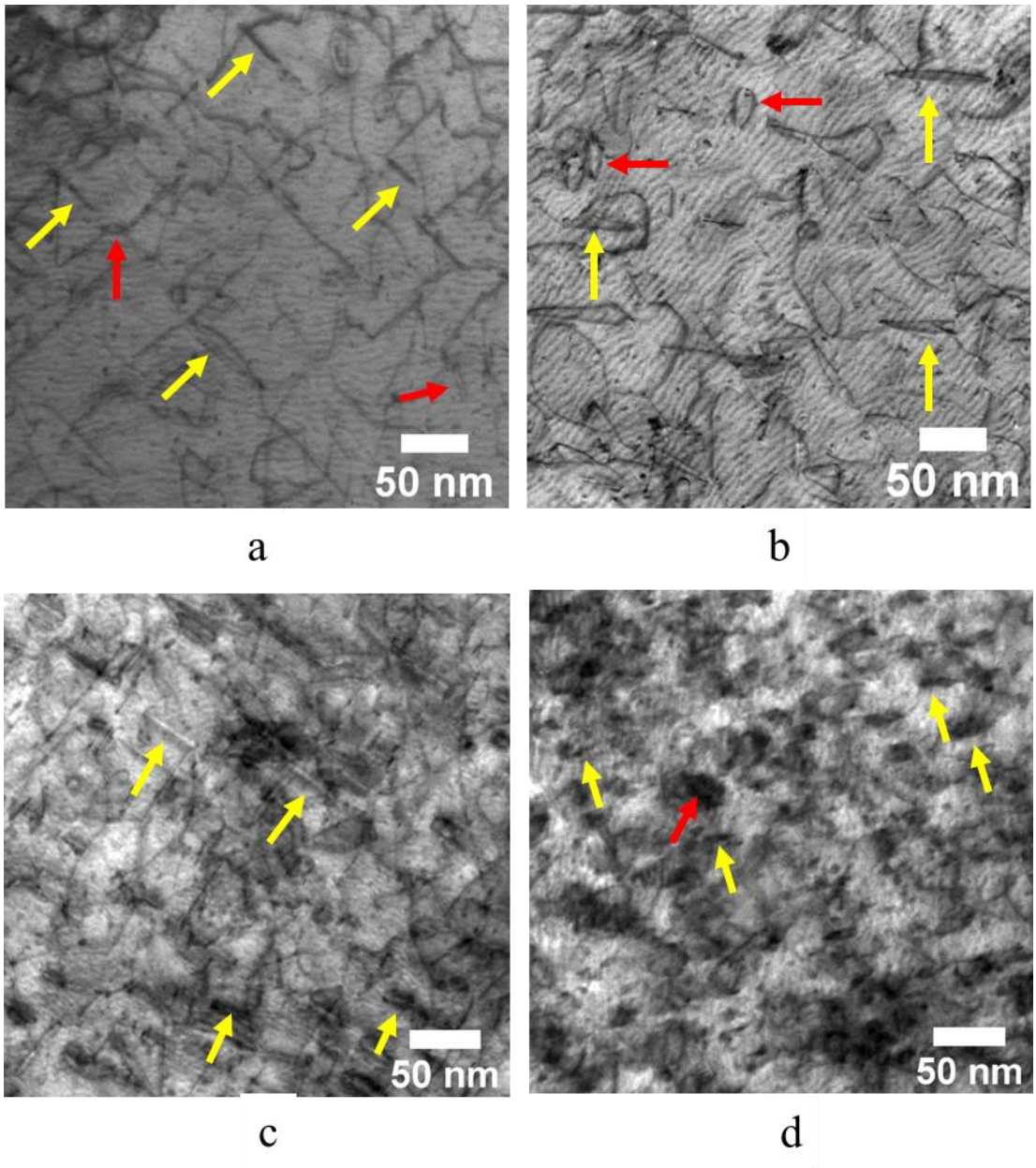

Figure 5.20. STEM-BF images showing dislocation evolution in T91 in the Damage Rate Series of irradiations to 16.6 dpa at 445°C with 4 appm He/dpa at damage rates of: (a) 5×10^{-5} dpa/s, (b) 1×10^{-4} dpa/s, (c) 7.1×10^{-4} dpa/s, and (d) 3×10^{-3} dpa/s. Some near-edge on **a**<100> type dislocation loops are indicated with yellow arrows and **a**/2<111> type dislocation loops indicated with red arrows.

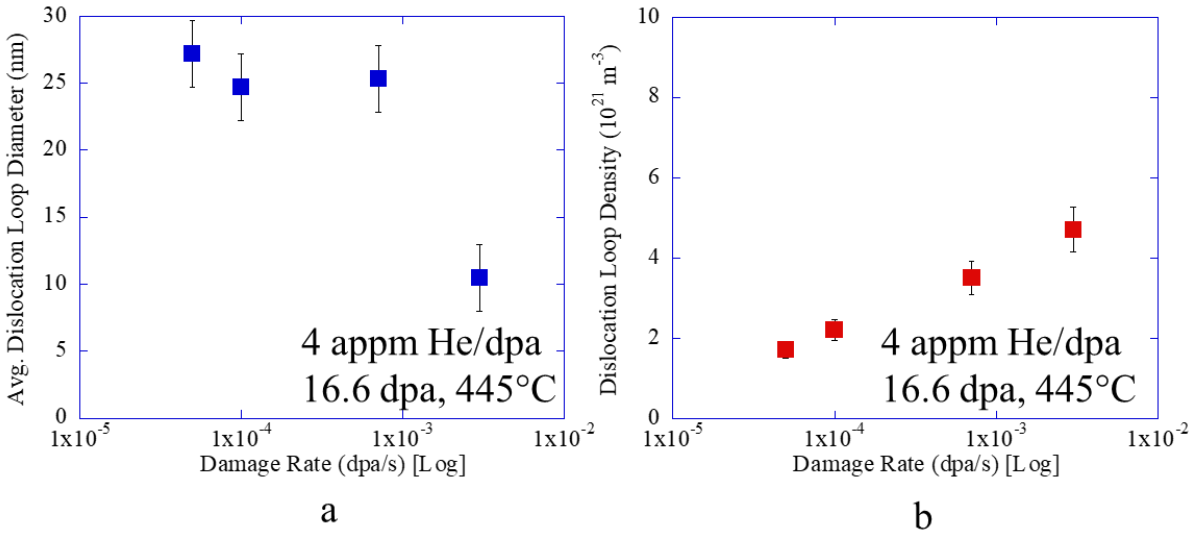

Figure 5.21. Average dislocation loop diameter (a) and dislocation loop density (b) as a function of damage rate for dual ion irradiated T91 at 445°C at 16.6 dpa.

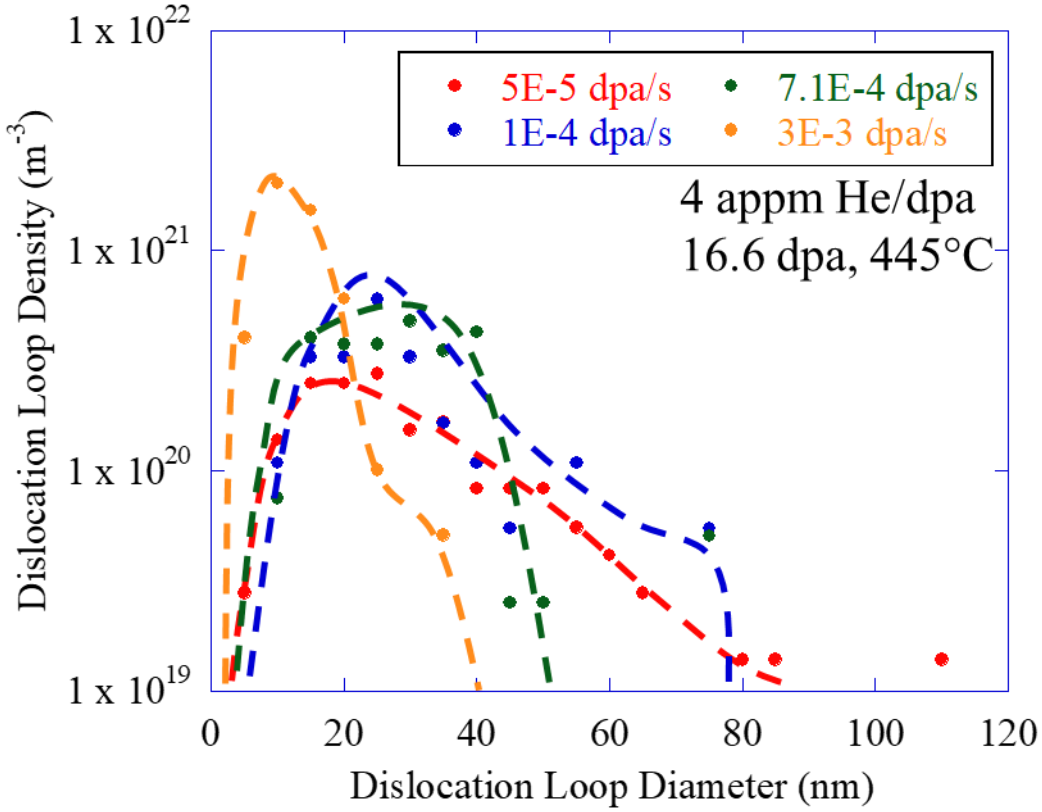

Figure 5.22. Dislocation loop size distributions as a function of damage rate for dual ion irradiated T91 with 4 appm He/dpa to 16.6 dpa at 445°C.

5.4 Microstructure Evolution in the BOR-60 Nuclear Reactor

5.4.1 Cavity Results

Voids were observed in some BOR-60 irradiation conditions, shown with STEM HAADF images in Figure 5.23. Only bubbles were observed at the high temperatures of 460°C and 524°C. The dependence of void diameter and number density are displayed in Figure 5.24 and tabulated in Table 5.10. At 15-19 dpa, voids decreased in density with increasing temperature until no voids remained at high temperatures. The average void diameter did not change significantly with temperature or damage level. With an increase in dpa from 17 to 35 dpa, the density of voids nearly doubled while maintaining a consistent average diameter. Small cavities consistent with bubbles were observed at all damage rates. The bubble decreased with increasing temperature and appeared to levels off to a floor at higher temperatures, consistent with the void densities. The combined observations of bubbles and voids resulted in bimodal cavity size distributions, as displayed in Figure 5.25. Increasing the dpa from 17 dpa to 35 dpa resulted in a small decreased in the bubble density and an increase in the void distribution to larger diameters, an indication of growth. Swelling remained small in all BOR-60 conditions with a maximum swelling of 0.033% at 35 dpa and 378°C as shown in Figure 5.24d.

Table 5.10. Summary of characterization results for cavities in BOR-60 irradiated T91 at a damage rate of 6-9 × 10^{-7} dpa/s. N.O. indicates that the feature was not observed. N.M. indicates the condition was not characterized for this feature. Negl. indicates the feature was observed but not in a large enough quantity to characterize for a representative value.

Irradiation Capsule	Damage (dpa)	Temperature (°C)	Number of Bubbles Examined	Bubble Density (10^{21} m^{-3})	Average Bubble Diameter (nm)	Number of Voids Examined	Void Density (10^{20} m^{-3})	Average Void Diameter (nm)	Swelling (%)	Total Cavity Sink Strength (10^{14} m^{-2})
P027	17.1	376	254	120	1.0	549	7.3	6.9±1.1	0.016	16.4
P033	18.6	415	218	16	0.9	240	6.5	5.6±1.1	0.0058	2.6
P037	14.6	460	47	3.2	1.0	N.O.	N.O.	N.O.	Negl.	0.5
P042	15.4	524	103	3.3	1.1	N.O.	N.O.	N.O.	Negl.	0.6
P028	35	445	240	22	0.9	893	14.7	6.5±1.1	0.033	3.8

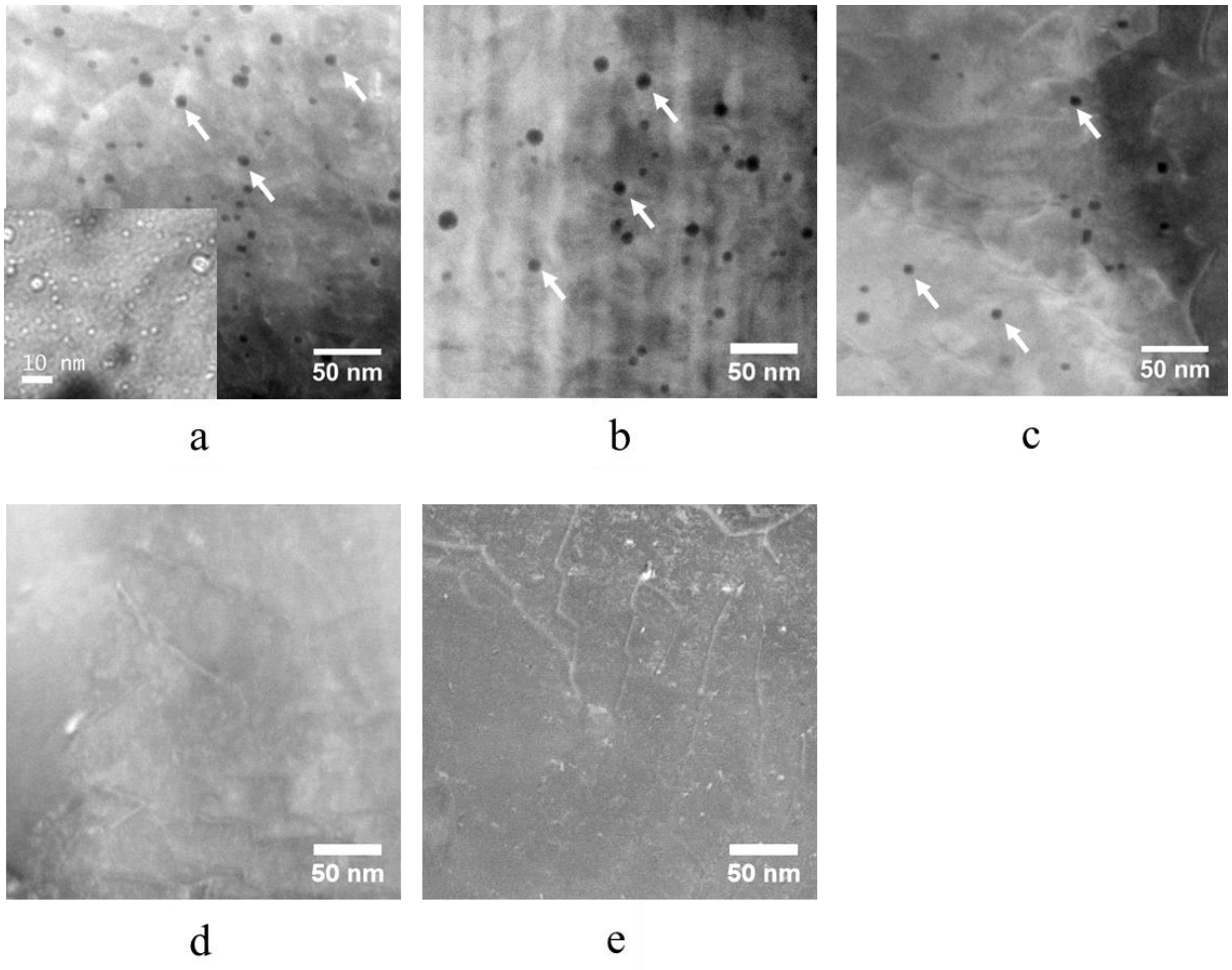

Figure 5.23. STEM HAADF images showing cavity evolution in T91 irradiated in BOR60 under different irradiation conditions: (a) 17.1 dpa at 376°C; (b) 35.1 dpa at 378°C; (c) 18.6 dpa at 415°C; (d) 14.6 dpa at 460°C; and (e) 15.4 dpa at 524°C. Some cavities are indicated by arrows. The inset in (a) is an under focus TEM BF image showing a high density of small bubbles.

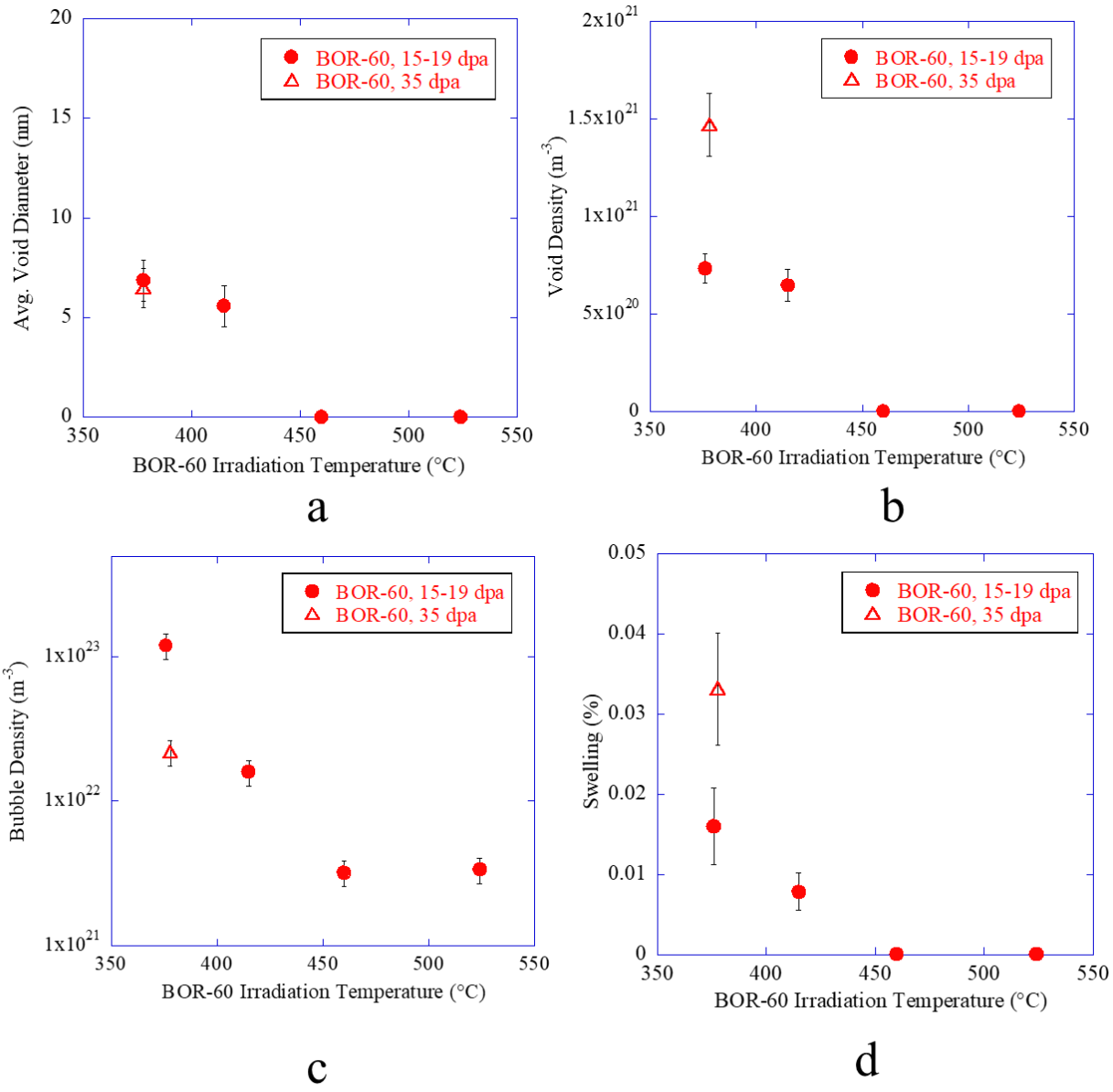

Figure 5.24. Average void diameter (a), void density (b), bubble density (c) and swelling (d) for cavities in BOR-60 irradiated T91.

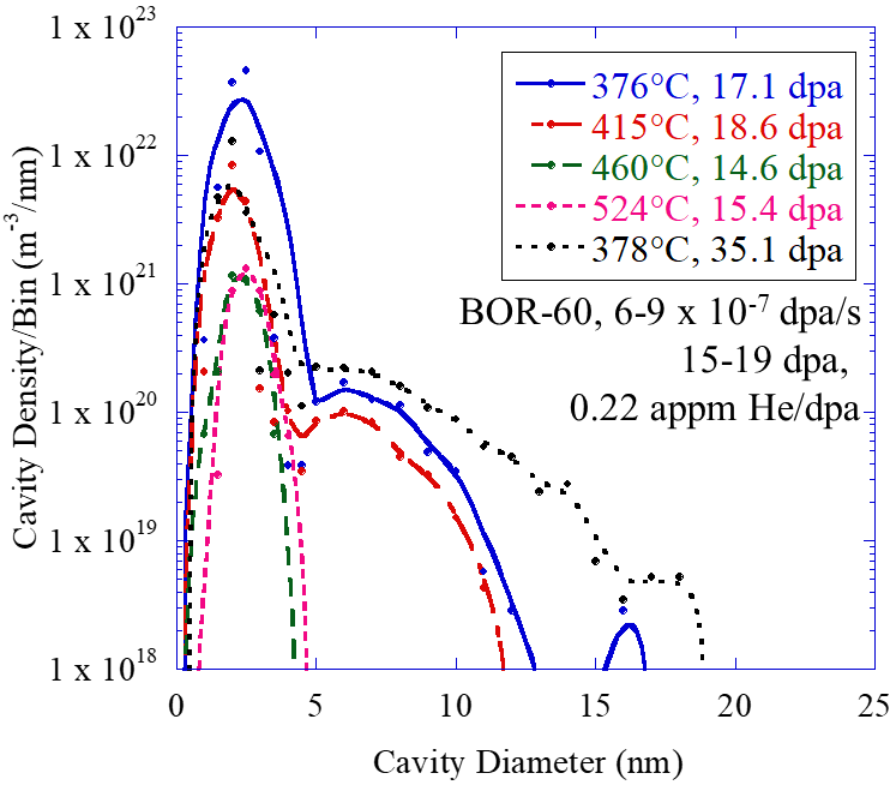

Figure 5.25. Cavity size distributions for BOR-60 irradiated T91.

The cavity size distributions were examined for local extrema in the distributions. In each bimodal cavity size distribution, three local extrema were observed corresponding to two peaks and one valley in the distribution. There was no significant change in the locations of the first peak with increasing irradiation temperature in this series of experiments. A summary of the cavity size distribution extrema for the BOR-60 Series is included in Table 5.11.

Table 5.11. Table of the extrema in the cavity size distributions in the BOR-60 Series of irradiations. N.O. indicates the feature was not observed.

Extrema (radius)	376°C, 17.1 dpa	415°C, 18.6 dpa	460°C, 14.6 dpa	524°C, 15.4 dpa	378°C, 35 dpa
Peak 1 (bubbles)	~1.25±0.25 nm	~1.0±0.25 nm	~1.0±0.25 nm	~1.25±0.25 nm	~1.0±0.25 nm
Valley	~2.0±0.25 nm	~2.25±0.25 nm	N. O.	N. O.	~2.25±0.25 nm
Peak 2 (voids)	~3.0±0.25 nm	~3.0±0.25 nm	N. O.	N. O.	~3.0±0.25 nm

5.4.2 Dislocation Loop Results

This portion of the dislocation loop characterization was performed and analyzed primarily by Dr. Zhijie Jiao at the University of Michigan. It is included in this dissertation as the information

is presented in literature in Ref. [146]. STEM-BF images of dislocation loops from BOR-60 irradiated T91 are shown in Figure 5.26 with a summary of the average dislocation loops diameter and number density tabulated in Table 5.12 and shown graphically in Figure 5.27. The dislocation loop size distributions are included in Figure 5.28. Loops with a Burgers vector of **a**<100> on either (010) or (001) planes appeared as nearly edge-on in the images, while the **a**/2<111> loops residing on (111) planes appeared at an angle of approximately 54° relative to the (001) plane. The primary dislocation loops observed at each damage rate were **a**{100} dislocation loops with very few **a**/2{111} dislocation loops observed. The average dislocation loop diameter at 17 dpa increased with temperature from 21.8±0.5 nm to 25.8±0.9 nm and remained a consistent diameter of about 22.9±1.2 nm when increasing from 17 dpa to 35 dpa. The dislocation loop density showed no change in the temperature range of 376°C to 415°C at 15-19 dpa with a density of about 2.0±0.3 $\times 10^{21}$ m^{-3}, very few dislocation loops at 460°C, and no dislocation loops at 524°C. The dislocation loop density did not change significantly with increasing damage indicating a steady state dislocation loop microstructure. increased with increasing damage rate from 1.7±0.2 $\times 10^{21}$ m^{-3} at the lowest damage rate to 4.7±0.6 $\times 10^{21}$ m^{-3} at the highest damage rate. The dislocation loop size distributions, shown in Figure 5.28, showed similar shapes and densities at 17 dpa and 35 dpa at either temperature. Dislocation lines were observed in all BOR-60 irradiation conditions and no significant alteration of the existing network dislocation density was noted compared to the as-tempered condition.

Table 5.12. Summary of characterization results for dislocation loops in BOR-60 irradiated T91 at a damage rate of 6-9 × 10^{-7} dpa/s. N.O. indicates that the feature was not observed. N.M. indicates the condition was not characterized for this feature. Negl. indicates the feature was observed but not in a large enough quantity to characterize for a representative value.

Irradiation Capsule	Damage (dpa)	Temperature (°C)	Dislocation Loop Density (10^{21} m^{-3})	Average Dislocation Loop Diameter (nm)	Dislocation Loop Line Density (10^{14} m^{-2})	Total Dislocation Loop Sink Strength (10^{14} m^{-2})
P027	17.1	376	2.0	21.8±0.5	2.0	2.0
P033	18.6	415	2.0	25.8±0.9	1.0	1.6
P037	14.6	460	Negl.	Negl.	Negl.	Negl.
P042	15.4	524	N.O.	N.O.	N.O.	N.O.
P028	35	445	1.9	22.9±1.2	1.4	1.3

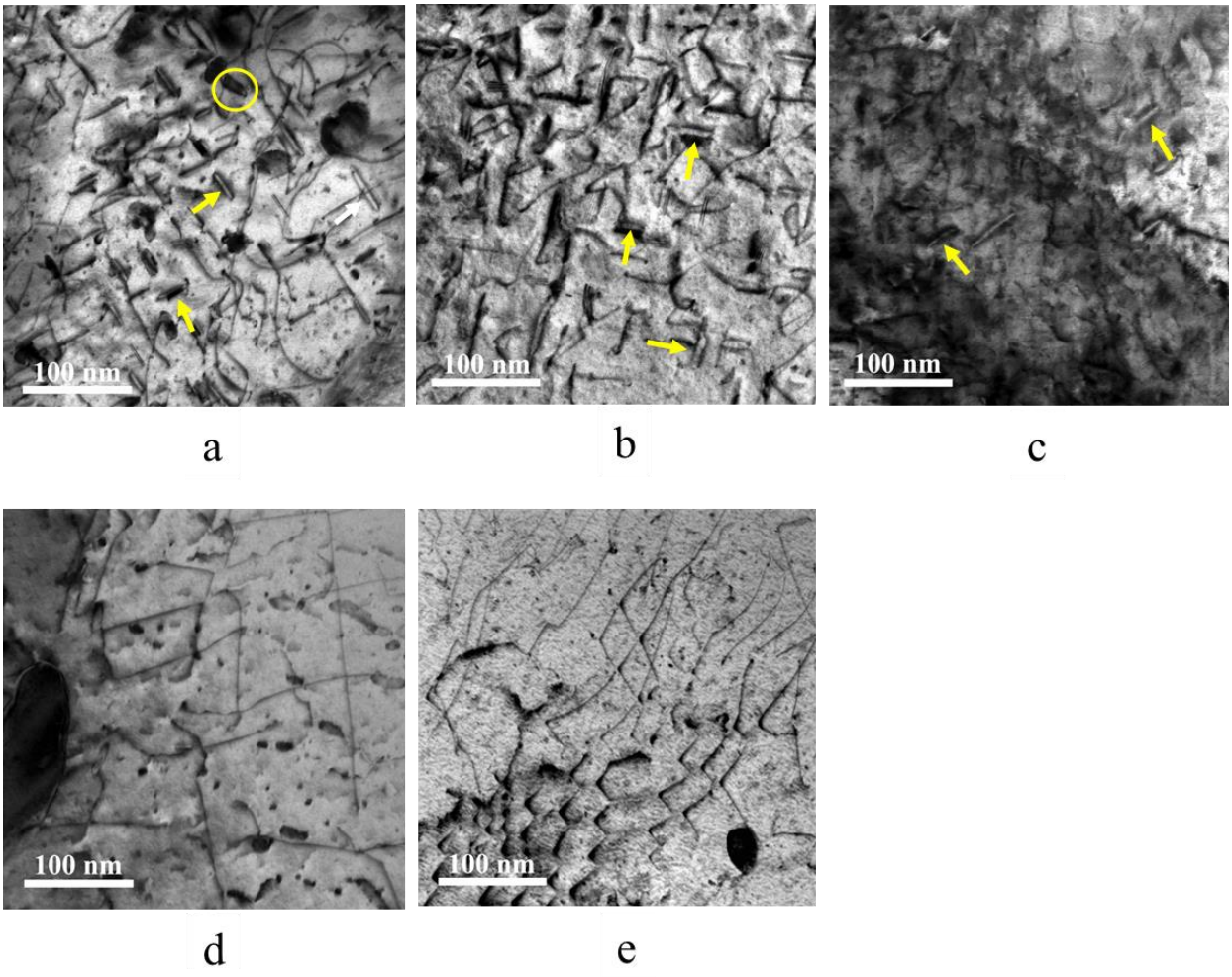

Figure 5.26. STEM-BF images showing dislocation evolution in T91 irradiated in BOR60 under different irradiation conditions: (a) 17.1 dpa at 376°C; (b) 35.1 dpa at 378°C; (c) 18.6 dpa at 415°C; (d) 14.6 dpa at 460°C:14.6 dpa; and (e) 15.4 dpa at 524°C; Some near edge-on dislocation loops are indicated by arrows. A possible 1/2**a**<111> type dislocation loop is circled in (a)).

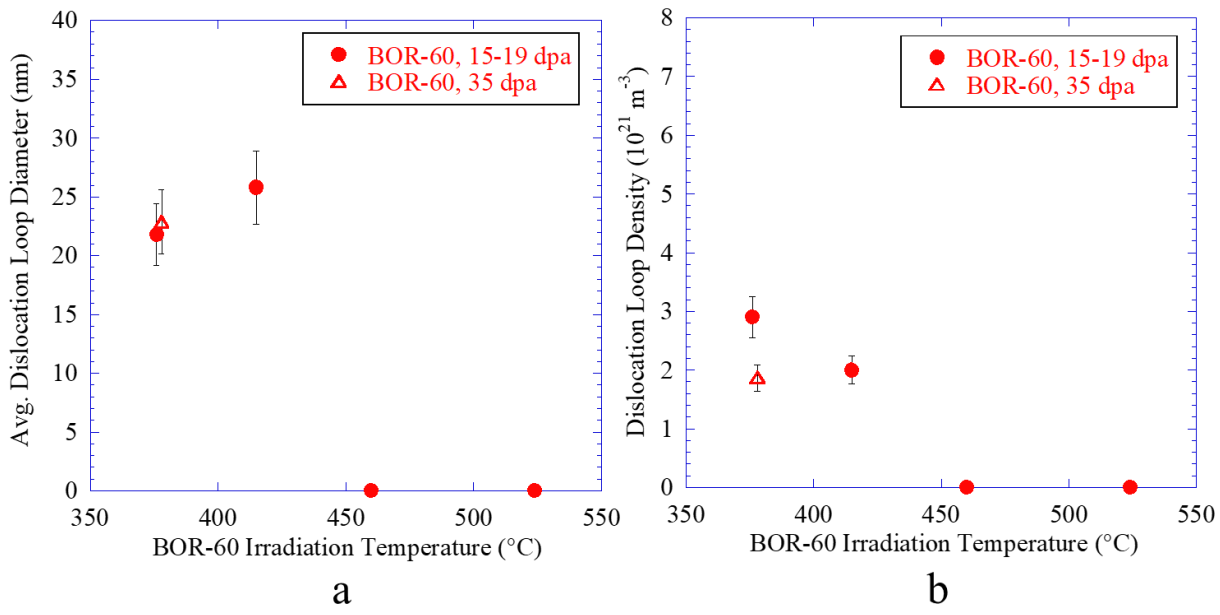

Figure 5.27. Average dislocation loop diameter (a) and dislocation loop density (b) as a function of damage rate for BOR-60 irradiated T91.

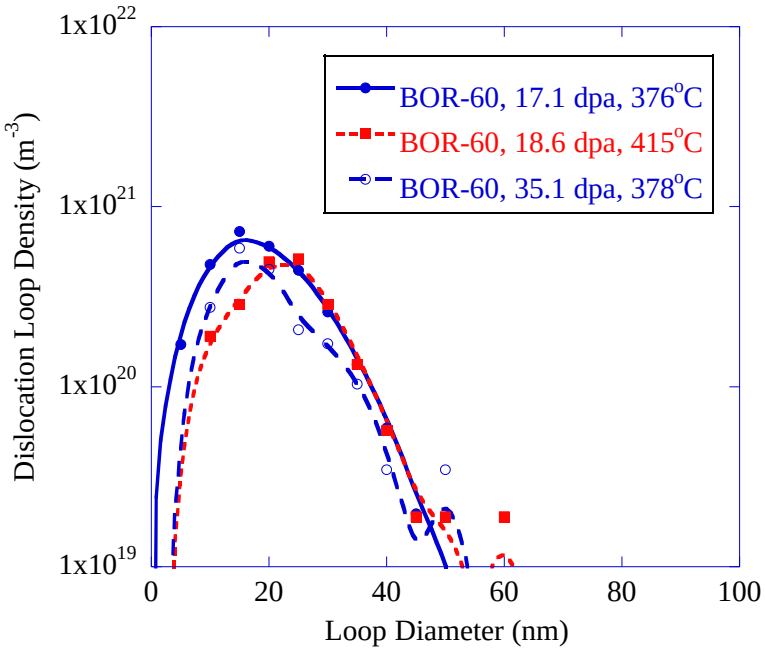

Figure 5.28. Dislocation loop size distributions for BOR-60 irradiated T91.

Chapter 6: Discussion

The discussion of the results presented in Chapter 5 will be divided into three main sections. The first two sections are the role of helium on bubble nucleation and the mechanisms of void nucleation across damage rates in dual ion irradiated T91 and directly address the objective of determining the mechanisms that control cavity nucleation in dual ion irradiated T91 steel over a range of damage rates. The third section extrapolates the mechanisms determined using dual ion irradiated to reactor irradiation, and from this discussion examines the suitability of the cavity growth rate equation to bubbles and voids in reactor. The cavity growth rate equation, as presented in Section 2.4.5, will be used to explain the nucleation of bubbles and the transition from bubbles to voids according to the critical bubble model. As the level of dpa in this work is low for void swelling in ferritic-martensitic steels [22], this discussion will focus only on cavity nucleation and not the growth of cavities. Prior to the discussion on bubble and voids, a sensitivity analysis of the cavity growth rate equation is presented to identify the key parameters affecting bubble and void behavior.

Sensitivity is defined as the derivative of an individual root of the cavity growth rate equation with respect to an input parameter, similar to the methodology presented in [69] for the sensitivity of grain boundary composition via radiation induced segregation. For calculational purposes, the sensitivity was approximated as the ratio of the change in a root of the cavity growth rate equation with respect to a change in an input parameter, $\frac{\partial\left(\frac{dr}{dt}=0\right)}{\partial P}$, when the input parameter was varied by a factor of 10^{-4} about its reference value. The sensitivity was expressed as:

$$\frac{\partial\left(\frac{dr}{dt}=0\right)}{\partial P} \approx \frac{\delta\left(\frac{dr}{dt}=0\right)}{\delta P} = \frac{\left(\frac{dr}{dt}=0\right)' - \left(\frac{dr}{dt}=0\right)_{reference}}{P' - P_{reference}}, \qquad \text{Eq. 6.1}$$

where $\left(\frac{dr}{dt}=0\right)_{reference}$ is a root of the cavity growth rate equation calculated at $P_{reference}$ and $\left(\frac{dr}{dt}=0\right)'$ is the resulting root of the cavity growth rate equation calculated with the modified input parameter, P'.

The sensitivity can be expressed as the fractional change in a root of the cavity growth rate equation relative to the fractional change in the input parameter, or the significance, $S_P^{\left(\frac{dr}{dt}=0\right)}$. The significance of $\left(\frac{dr}{dt}=0\right)$ given P is defined as:

$$S_P^{\left(\frac{dr}{dt}=0\right)} = \frac{\left(\frac{dr}{dt}=0\right)' - \left(\frac{dr}{dt}=0\right)_{reference}}{P' - P_{reference}} * \frac{P_{reference}}{\left(\frac{dr}{dt}=0\right)_{reference}}. \qquad \text{Eq. 6.2}$$

It follows then, that the variable of interest, the roots of the cavity growth rate equation, will be most sensitive to those parameters that have the largest magnitude of significance. In general, there will be two roots, one corresponding to the stable bubble radius, r_b^*, and one corresponding to the critical radius for unstably growing voids, r_v^*.

Significance was calculated for three ion irradiation temperatures (420°C, 445°C, 480°C) at high damage rates, three helium co-injection rates (0.02 appm He/dpa, 0.22 appm He/dpa, and 4.34 appm He/dpa), three damage rates (5×10^{-5} dpa/s, 1×10^{-4} dpa/s, and 7×10^{-4} dpa/s) at 445°C. The results of these calculations are included in

Table 6.1 for the significance related to temperature, Table 6.2 for the significance related to the helium co-injection rate, and

Table 6.3 for the significance related to irradiation damage rate with ion irradiation.

Table 6.1. Table containing significance related to irradiation temperature of several input parameters on the roots of the cavity growth rate equation. The irradiation damage rate and helium co-injection rate are fixed at 7×10^{-4} dpa/s and 4 appm He/dpa, respectively.

	420°C		**445°C**		**480°C**	
Input Parameter (below)	r_b^*	r_v^*	r_b^*	r_v^*	r_b^*	r_v^*
a	0	0	-1.33	1.30	-0.063	1.118

Bias	0	0	0.77	-0.75	0.036	-0.63
γ	0	0	-2.88	2.27	-0.22	1.004
ω_i	0	0	0.015	-0.018	0	-0.0
ω_v	0	0	-0.75	0.72	-0.036	0.620
r_i	0	0	0	0	0	0
Grain size	0	0	0.10	-0.10	0	-0.10
E_m^i	0	0	-0.099	0.092	-0.009	0.075
E_m^v	0	0	7.63	-7.47	0.34	-6.03
E_f^v	0	0	20.6	-20.23	0.92	-16.1
T	-0.80	14.93	-2.95	17.05	-0.98	24.04
He/dpa	0	0	1.617	-0.42	0.42	-0.013
dpa/s	0.027	-0.42	0.084	-0.4	0.027	-0.70

Table 6.2. Table containing significance related to helium co-injection rate of several input parameters on the roots of the cavity growth rate equation. The damage rate and temperature are fixed at 7×10^{-4} dpa/s and 445°C respectively.

	0.02 appm He/dpa		**0.22 appm He/dpa**		**4.34 appm He/dpa**	
Input Parameter (below)	r_b*	r_v*	r_b*	r_v*	r_b*	r_v*

a	-0.084	0.63	-0.084	0.63	-1.33	1.30
Bias	0.056	-0.40	0.056	-0.40	0.77	-0.75
Γ	-0.35	1.25	-0.35	1.25	-2.88	2.27
ω_i	0.014	-0.013	0.014	-0.013	0.015	-0.018
ω_v	-0.042	0.38	-0.042	0.38	-0.75	0.72
r_i	0	0	0	0	0	0
Grain size	0.014	-0.072	0.014	-0.072	0.10	-0.10
E_m^i	0	0.072	0	0.072	-0.099	0.092
E_m^v	0.53	-3.88	0.53	-3.88	7.63	-7.47
E_f^v	1.48	-10.86	1.48	-10.86	20.6	-20.2
T	-2.71	13.93	-2.71	13.93	-2.95	17.05
He/dpa	0.52	-0.045	0.52	-0.045	1.61	-0.42
dpa/s	0.073	-0.38	0.073	-0.38	0.084	-0.48

Table 6.3. Table containing significance related to damage rate of several input parameters on the roots of the cavity growth rate equation. The helium co-injection rate and temperature are fixed at 4 appm He/dpa and 445°C, respectively.

	5 x 10^{-5} dpa/s		**1 x 10^{-4} dpa/s**		**7.1 x 10^{-4} dpa/s**	
Input Parameter (below)	r_b*	r_v*	r_b*	r_v*	r_b*	r_v*
a	-0.16	1.52	-0.22	1.31	-1.33	1.30

Bias	0.083	-0.75	0.11	-0.65	0.77	-0.75
Γ	-0.31	1.11	-0.43	1.14	-2.88	2.27
ω_i	0	-0.0032	0	-0.005	0.015	-0.018
ω_v	-0.083	0.77	-0.11	0.67	-0.75	0.72
r_i	0	0	0	0	0	0
Grain size	0.017	-0.14	0.021	-0.11	0.10	-0.10
E_m^i	0	0.013	-0.005	0.02	-0.099	0.092
E_m^v	0.85	-7.93	1.20	-6.88	7.63	-7.47
E_f^v	2.19	-20.3	3.10	-17.8	20.6	-20.2
T	-1.76	28.63	-1.80	26.46	-2.95	17.05
He/dpa	0.40	-0.046	0.48	-0.062	1.61	-0.42
dpa/s	0.059	-0.82	0.056	-0.75	0.084	-0.48

The roots of the cavity growth rate equation were most sensitive to the vacancy migration energy and vacancy formation energy for all irradiation experiment series and several different input parameters in each irradiation experiment series. The first root, corresponding to r_b^*, is most sensitive to temperature at low temperatures, surface energy (γ) and helium co-injection rate at intermediate temperatures, and temperature at high temperatures. The significance of the helium co-injection rate on r_b^* also increased with increasing helium co-injection rate. The second root, corresponding to r_v^*, is most sensitive to the irradiation temperature at all temperatures, helium co-injection rates, and damage rate. The roots of the cavity growth rate equation were relatively insensitive to the other input parameters examined. This sensitivity analysis serves as the foundation to examine the experimental cavity size distributions with the cavity growth rate equation by identifying the helium co-injection or generation rate, the vacancy migration energy, and the vacancy formation energy as key parameters of interest.

6.1 The Role of Helium on Bubble Nucleation

The sensitivity analysis performed previously identified the helium co-injection rate as one of the primary factors influencing the roots of the cavity growth rate equation. In the cavity growth rate equation, Eq. 2.4 in Section 2.4.5, the helium co-injection rate enters the equation through the gas pressure inside the cavity, repeated for convenience as:

$$\frac{dr}{dt} = \frac{\Omega}{r}\left[D_v C_v - D_i C_i - D_v C_{v,T} \exp\left(\frac{2\gamma}{r} - p_g\right)\right]. \quad \text{Eq. 6.3}$$

The gas pressure stabilizes the cavity from evaporation through thermal vacancy emission. Therefore, determining the number of gas atoms inside a cavity is crucial to determine the stability of bubbles. Helium has an extremely low solubility in the matrix and a low migration energy as an interstitial atom, on the order of 0.06 eV [172]. When injected into the matrix, helium will diffuse rapidly and subsequently bind to various sinks in the microstructure. This section will determine the impact of helium partitioning on the stable bubble radius by examining the conditions under which helium resides in the matrix using the cavity growth rate equation, comparing the cavity growth rate equation to the experimental cavity size distributions and through a discussion of the binding energies associated with common microstructural features.

As a first approximation of the fate of helium in the microstructure, it is assumed that all helium is in cavities. As shown in Figure 5.3, the bubble density is significantly higher than the void density and thus the assumption can be made that the helium is only in bubbles. Furthermore, since the bubble size distribution is so narrow that it is assumed all bubbles are of the same size with a radius of 1 nm. The pressure of helium gas in the bubbles was calculated using a modified form of the ideal gas law to include a hard sphere equation of state for helium, as used in previous work on cavity nucleation [141,162]:

$$p_g = \frac{n_g k_{bolt} T Z_{comp}}{V}, \quad \text{Eq. 6.4}$$

where V is the volume of the spherical cavity of radius r, n_g is the number of gas atoms with a factor for the compressibility of the helium gas:

$$Z_{comp} = \frac{1+y+y^2+y^3}{(1-y)^3}, \quad \text{Eq. 6.5}$$

where

$$y = \pi * n_g \frac{d_g^3}{6V}, \quad \text{Eq. 6.6}$$

and

$$d_g = 0.3135\left(0.8542 - 0.03996 * \ln\left(\frac{T}{9.16}\right)\right), \quad \text{Eq. 6.7}$$

where d_g is the hard sphere diameter of helium. The number of helium atoms, n_g^{cav}, can be estimated using:

$$n_g^{cav} = \frac{\frac{appm\ He}{dpa} * dpa * N_{bcc}}{N_{bub} 10^6}, \quad \text{Eq. 6.8}$$

where N_{bcc} is the density of iron atoms in the iron matrix, $\frac{appm\ He}{dpa}$ is the helium co-injection or helium generation rate during the irradiation experiment, dpa is the final damage level of the irradiation experiment, and N_{bub} is the density of bubbles. Physically, the roots in the cavity growth rate equation manifest themselves in the cavity size distributions as the local extrema; the peaks and valleys. By comparing the roots of the cavity growth rate equation with the peaks (r_b^*) and valleys (r_v^*) in the cavity size distributions for each experimental series in Chapter 5, the cavity growth rate can be assessed quantitatively. This comparison is made in Figure 6.1a for the Temperature Series of ion irradiation experiments, Figure 6.1b for the Helium Series, and Figure 6.1c for the Damage Rate Series. The stable bubble radius is presented in these figures as r_b^* and corresponds to the first root in the cavity growth rate equation. Each irradiation series will be

discussed separately in the following paragraphs. The y-axis of this figure is scaled to match other figures presented later in the discussion.

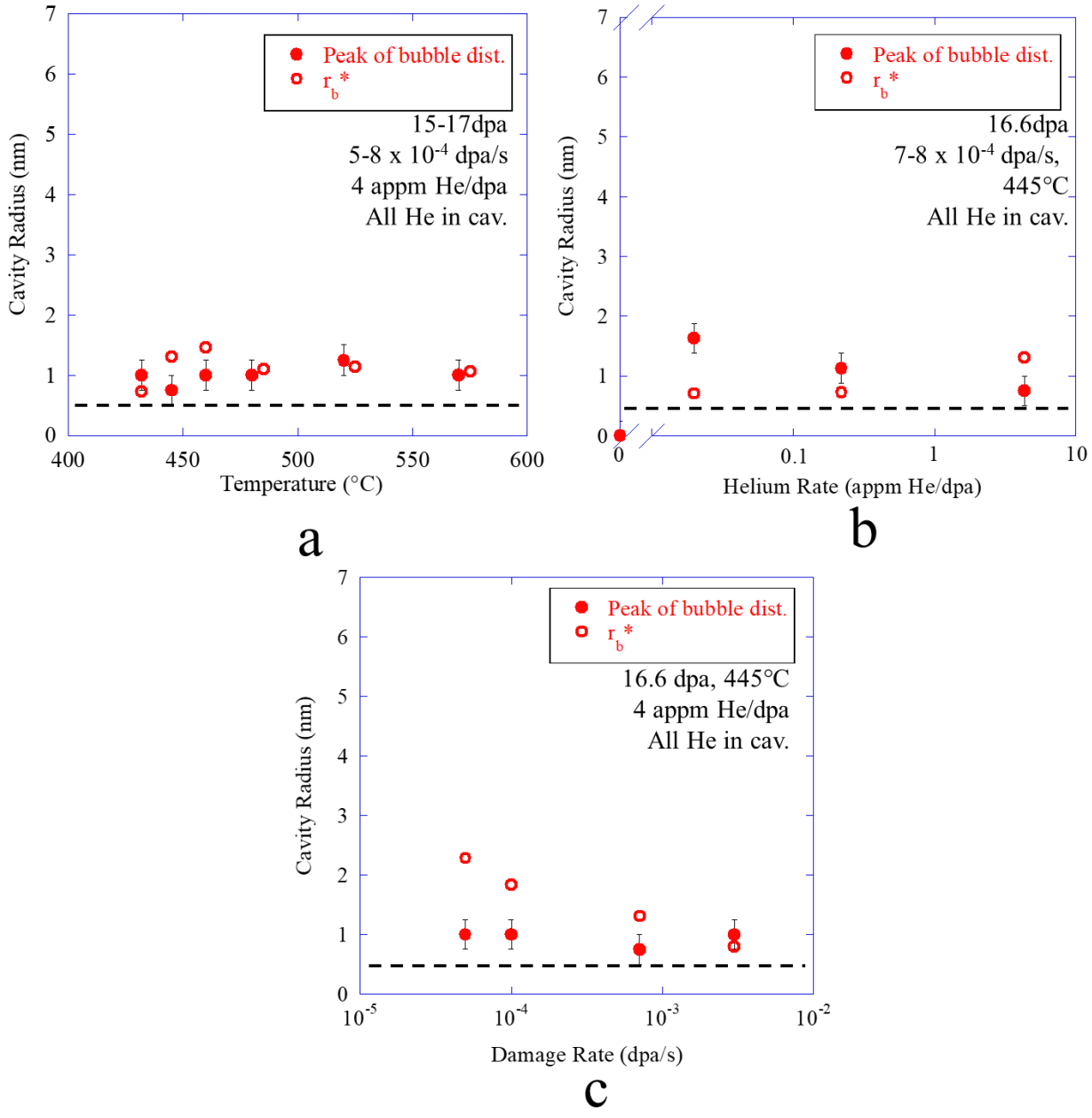

Figure 6.1. Comparison of the experimentally determined bubble peak in the cavity size distributions for the a) Temperature Series of ion irradiations, b) Helium Series of ion irradiations, c) Damage Rate Series of irradiations and the first root of the cavity growth rate equation for each series assuming all helium is in cavities. The dashed line is the smallest size bin used for analysis. Some open points are displaced along the x-axis slightly to avoid overlap.

Temperature Series: With increasing ion irradiation temperature, the experimental results suggest that the stable bubble radius, r_b^*, does not change significantly. The cavity growth rate equation provides a similar picture where the calculated r_b^* is within 0.5 nm of the experimental value across all ion irradiation temperatures. This consistency is not surprising as each ion irradiation was performed with the same helium co-injection ratio.

Helium Series: With all the helium in the cavities, the calculated stable bubble radius increases weakly with increasing helium co-injection rate. At low helium co-injection levels of 0.02 appm He/dpa and 0.22 appm He/dpa, the measured bubble peaks are larger than the calculated stable bubble size indicating that the observed bubbles are likely stable. However, at the highest helium co-injection rate, the calculated r_b^* is larger than the measured bubble peak suggesting the observed bubbles should not be stable and should grow to the calculated stable bubble radius.

Damage Rate Series: With increasing damage rate the stable bubble radius shifts to smaller values, indicating an expectation of increased bubble stability at higher damage rates. However, the experimental radii did not vary significantly with damage rate. At the highest damage rate, the calculated stable bubble radius converges to about 1 nm and appears to coincide with the peak of the bubble distribution, but the agreement worsens as the damage rate is reduced.

From the comparison of r_b^* and the measured peak in the bubble size distribution, some of the measurements agreed with the calculated roots in the cavity growth rate equation but many did not. One of the potential reasons for disagreement is the assumption in the model that all the helium is in the cavities. Helium is known to become trapped at precipitate interfaces [173], dislocation cores [174], and grain boundaries [175–179]. Ideally, the fate of helium could be estimated using EELS to measure the concentration of helium in cavities [129,180] or using Thermal Helium Desorption Spectroscopy (THDS) to correlate the release of trapped helium to groups of

microstructure features [181–184]. The other microstructural features such as dislocation lines, dislocation loops, precipitates, and grain boundaries will act as sinks for helium according to their point defect sink strength. To refine the analysis using the cavity growth rate equation, the assumption of the fate of helium was revised to proportion among the sinks by sink strength. We will consider only the sink strength of cavities compared to the total sink strength in the sample. The number of helium atoms, n_g^{sink}, arriving at cavities by the calculated sink strength of the cavities is:

$$n_g^{sink} = \frac{\frac{appm\ He}{dpa} * dpa * N_{bcc}}{(N_{void} + N_{bub})10^6} * \frac{k_{cav}^2}{k_{total}^2}, \quad \text{Eq. 6.9}$$

where k_{cav}^2 is the cavity sink strength with voids and bubbles combined, and k_{total}^2 is the total sink strength of the microstructural features. The percentage of the total sink strength belonging to cavities and a revised estimate of the concentration of helium atoms in cavities are displayed in

Table 6.4 for the Temperature Series, Table 6.5 for the Helium Rate Series, and Table 6.6 for the Damage Rate Series. For the Temperature Series, the cavities make up between 20-30% of the total sink strength in the microstructure with an exception at 432°C caused by the high bubble density. With increasing helium co-injection rate, the increased density of cavities increases the cavity sink strength from 0 to about 23% of the total sink strength. With increasing damage rate, the sink strength follows primarily from the bubble density and thus increases with damage rate until the highest damage rate condition. The comparison between the experimental extrema in the cavity size distributions and the calculated roots of the cavity growth rate equation with helium

partitioning by sink strength is shown in Figure 6.2. As done in Figure 6.1, the y-axis is scaled to be consistent with figures further in the discussion.

Table 6.4. Table containing the concentration of helium co-injected with and without partitioning by sink strength for the Temperature Series of irradiations.

Temperature (°C)	Total Helium Injected (appm)	Cavity Sink Strength / Total Sink Strength (%)	Helium in cavities assuming sink strength partitioning (appm)
432	72	47	34
445	72	22	16
460	72	20	15
480	72	30	22
520	64	30	19
570	67	30	20

Table 6.5. Table containing the concentration of helium co-injected with and without partitioning by sink strength for the Helium Rate Series of irradiations.

Helium Co-Injection Rate (appm He/dpa)	Total Helium Injected (appm)	Cavity Sink Strength / Total Sink Strength (%)	Helium in cavities assuming sink strength partitioning (appm)
0	0	0	0
0.02	0.332	1.2	0.004
0.22	3.65	3.5	0.13
4.34	72	23	16

Table 6.6. Table containing the concentration of helium co-injected with and without partitioning by sink strength for the Damage Rate Series of irradiations.

Damage Rate (dpa/s)	Total Helium Injected (appm)	Cavity Sink Strength / Total Sink Strength (%)	Helium in cavities assuming sink strength partitioning (appm)
5×10^{-5} dpa/s	72	12	8.5
1×10^{-4} dpa/s	72	14	9.7
7×10^{-4} dpa/s	72	23	16
3×10^{-3} dpa/s	72	9.0	6.6

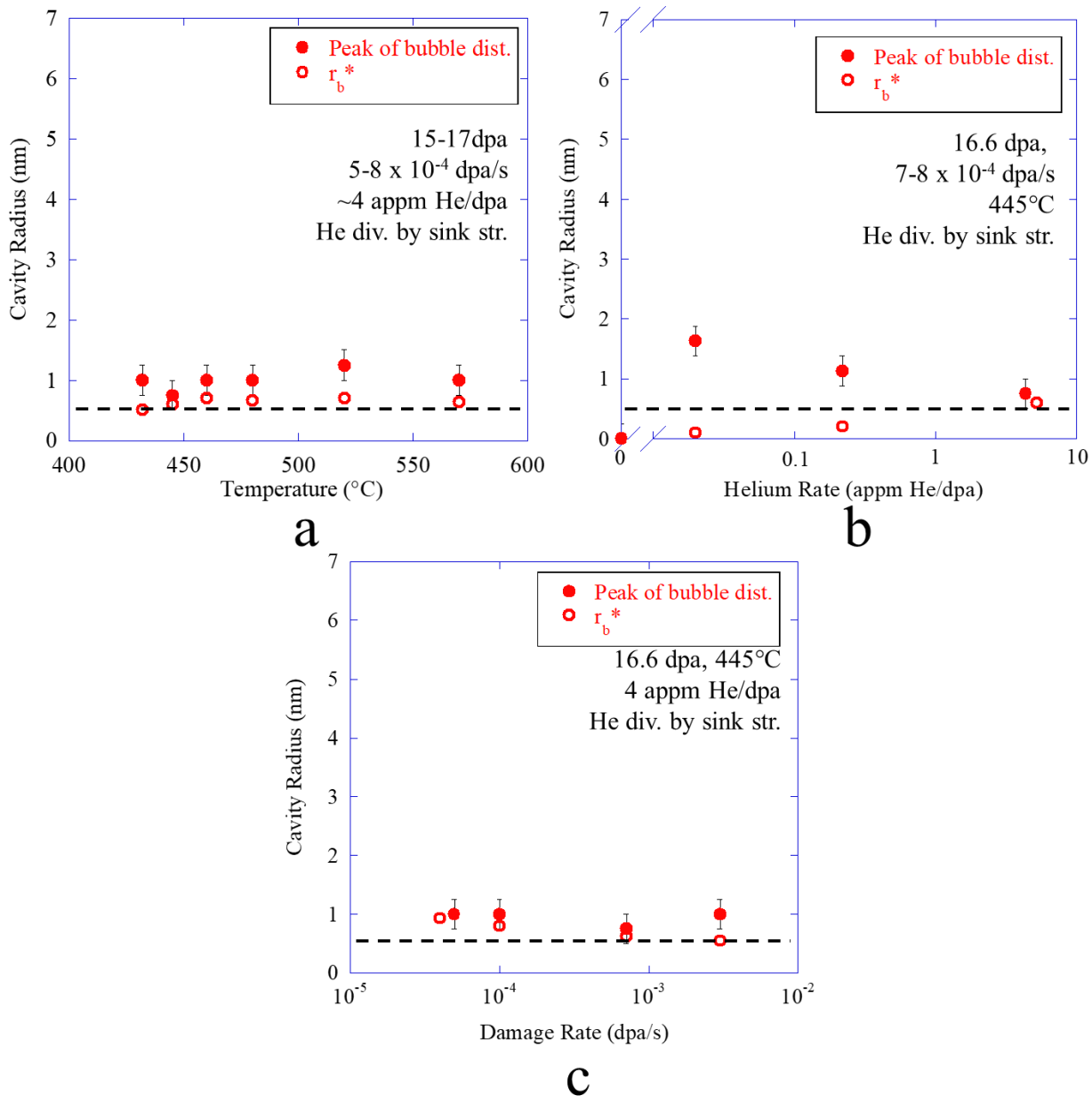

Figure 6.2. Comparison of the experimentally determined bubble peak in the cavity size distributions for the a) Temperature Series of ion irradiations, b) Helium Series of ion irradiations, c) Damage Rate Series of irradiations, d) BOR-60 irradiations and the first root of the cavity growth rate equation for each series assuming helium is divided in the microstructure by sink strength. The dashed line is the smallest size bin used for analysis. Some open points are displaced along the x-axis slightly to avoid overlap.

The partitioning of helium according to sink strength modified the calculated stable bubble radii, r_b^* primarily by reducing it in all irradiation series. In general, the calculated stable bubble radii did not change significantly with ion irradiation temperature and are within the experimental error of the measured bubble peak location in the cavity size distributions. For the Temperature

Series, the agreement between the calculated stable bubble radius and the experimental peak was better for the case of all helium in cavities only at high temperatures of 520°C and 570°C. For the Helium Series, the helium partitioning by sink strength brings the measured bubble peak and the calculated stable bubble size into agreement for the highest helium co-injection rate. However, at the lower helium co-injection rates, the values for the stable bubble radii are well below experiment. The calculated stable bubble radii in the Damage Rate Series now show a negligible dependence on the irradiation damage rate and within error of the experimentally measured bubble peak location in the cavity size distributions. From the comparison of the experimental peaks and valleys and the critical bubble model calculated using these two helium partitions schemes, several conclusions can be drawn.

At low helium co-injection rates (0.02 and 0.22 appm He/dpa) helium is likely bound only to cavities. At high helium co-injection rates such as that used for the Temperature Series and Damage Rate Series, the implanted helium atoms become bound to other features in the microstructure along with cavities until reaching a high enough temperature at which all helium is in cavities. The calculations of the roots of the cavity growth rate equation from Eq. 6.3 which were presented in Figure 6.1 and Figure 6.2 suggest a shift from helium being bound only to cavities at low helium co-injection rates to being distributed throughout the microstructure at high helium co-injection rates.

The assumption that all helium atoms are in cavities at low He/dpa values is supported by the binding energy of helium to He_mV_n clusters that ranges from 0.78 eV to 3.16 eV [185] using ab initio methods and has been measured to be about 3.6 eV [182] for bubbles in iron using Thermal Helium Desorption Spectroscopy (THDS). However, the binding energies of interstitial helium to other microstructure features are comparable with an edge dislocation such as an **a**<100>

dislocation loop at about 2.3 eV [174], about 1.0 eV for a screw dislocation line with **a**/2<111> character [186], and a range of 0.55-2.6 eV for grain boundaries [187]. To examine the possibility of helium trapping at microstructure features other than cavities, first consider the maximum number of helium atoms that can be placed in a cavity of radius r. Starting with the modified ideal gas law in Eq. 4.20 and assuming the pressure in the cavity to be the equilibrium pressure $\frac{2\gamma}{r}$, and substituting in Eq. 4.21 for the compressibility factor and rearranging the equation results in:

$$\frac{\frac{2\gamma}{r}V}{n_g kT} = \frac{1+y+y^2+y^3}{(1-y)^3}, \qquad \text{Eq. 6.10}$$

where y is defined in Eq. 4.22 with V as the volume of the cavity, and further defined through Eq. 4.23 for the hard sphere diameter. Solving for the number of gas atoms, n_g, per cavity of volume V as a function of the cavity radius, r, for a temperature of 445°C and a surface energy of 1.75 J/m^2 (as used in previous calculations for the Helium Series of ion irradiations) results in the plot shown in Figure 6.3.

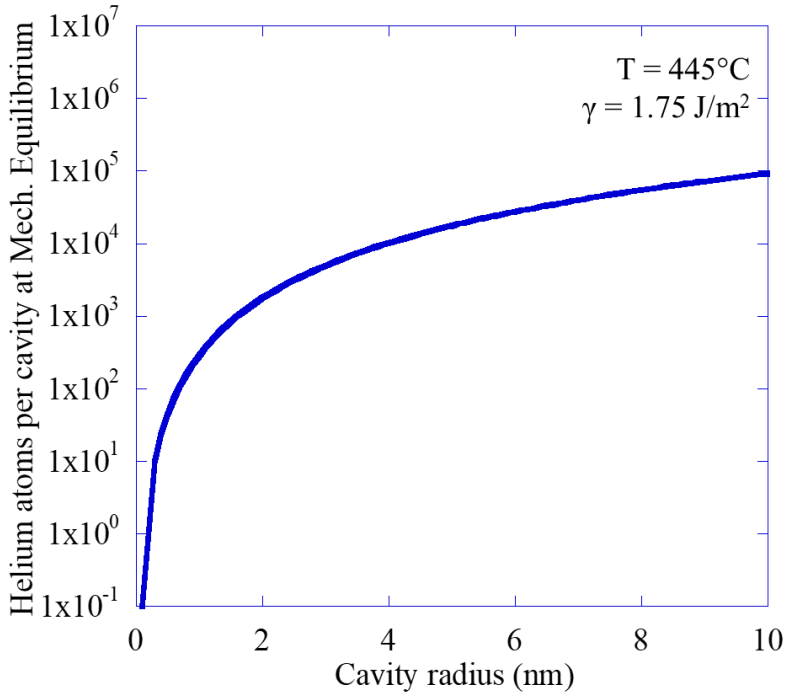

Figure 6.3. Calculation of the helium atoms per cavity at mechanical equilibrium for a nominal ion irradiation temperature of 445°C.

The number of gas atoms per cavity is then multiplied by the density of observed bubbles, a factor of 10^6, and divided by the atomic density of the iron matrix to estimate the total concentration of helium that could be stored in the observed cavities in atomic parts per million. As a conservative estimate, the highest bubble density measured in this work was used to estimate the upper bound of the helium concentration that could be contained in bubbles. The bubble density was chosen as it is the largest contribution to the overall density of cavities and have similar size distributions across the experimental conditions. The estimation of the concentration of injected helium contained in bubbles is displayed in Figure 6.4. From this calculation, all the helium injected at the lower helium rates of 0.02 appm He/dpa and 0.22 appm He/dpa, as well as the BOR-60 case, can be contained in the observed bubbles. However, at the highest helium injection rate, there is more helium than could be contained in all the observed bubbles without exceeding mechanical equilibrium. Therefore, either the bubbles are over pressurized or some of the injected helium is trapped at other features in the microstructure. Over pressurized bubbles were observed in nickel and nickel alloys [188,189] irradiated with very high He/dpa (up to 25000 appm He at 80 dpa) or with a high concentration of helium implanted prior to irradiation [190]. Over pressurized bubbles induce a tensile stress on the surrounding lattice, which increases the capture radius for vacancies. Thus, if the bubbles are over pressurized, then the bubbles will gather additional vacancies to return to mechanical equilibrium. This process requires a surplus of vacancies such as the high supersaturation of vacancies during ion irradiation. Such a supersaturation is not available with helium pre-implantation or with the low damage rates in a thermal reactor (10^{-7} dpa/s). Thus, the bubbles observed in this study for 4 appm He/dpa are likely in mechanical equilibrium as there is always a high vacancy supersaturation from the 7-8 × 10^{-4} dpa/s damage rates and helium must be trapped at other features in the microstructure.

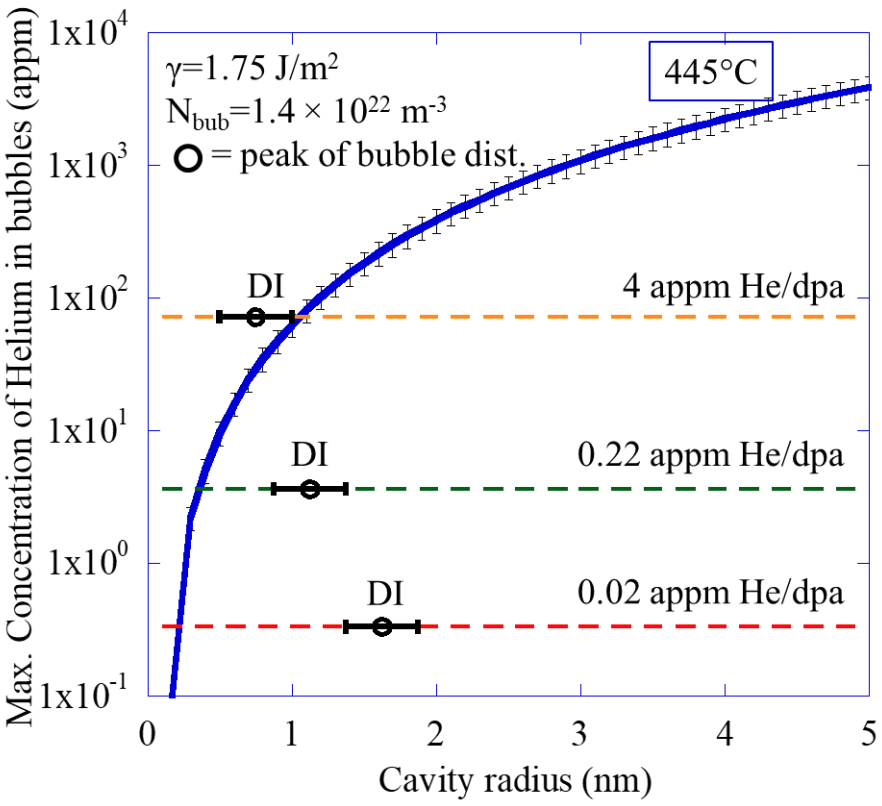

Figure 6.4. The maximum concentration of helium allowed in bubbles according to the hard sphere equation of state as a function of cavity radius. The concentrations of co-injected helium in the Helium Series of ion irradiations are included for reference with the bars showing the peak of the bubble distribution from the experimentally measured cavity size distributions.

Although the previous calculation of bubble saturation provides the conditions under which helium is trapped in the microstructure, it does not provide the amount of helium trapped in bubbles or at other microstructure features. Helium partitioning by sink strength made a significant difference in the calculated stable bubble radius for the dual ion irradiations. To examine the steady state trapping of helium, the trapping and detrapping rates of microstructure features must be considered. As stated earlier, helium has an extremely low solubility in the matrix and a low migration energy as an interstitial atom, on the order of 0.06 eV [172]. When injected into the matrix, helium will diffuse rapidly and subsequently bind to various sinks in the microstructure. Therefore, the helium de-trapping rate will limit the mobility of helium and determine its fate. The helium de-trapping rate of a trap i is proportional to the number of helium atoms bound to it, n_g^i,

and the attempt frequency, ν_0, and is assumed to have an Arrhenius dependence on the binding energy of the microstructure feature, E_b^i:

$$\tau_{detrap}^{i} \propto n_g^i \nu_0 e^{\left(\frac{-E_b^i}{kT}\right)}. \quad \text{Eq. 6.11}$$

From this relationship, a feature with a stronger binding energy for helium will act as a stronger sink for helium and gather more helium with time. Binding energies for helium-vacancy clusters of various compositions calculated using ab initio methods are included in

Table 6.7 along with several reactions for dislocations and grain boundaries.

During the irradiation damage cascade event, vacancy and interstitial clusters are generated in high density relative to the pre-existing microstructure traps [191]. Thus, the first features helium encounters in the microstructure is a vacancy or interstitial cluster. Interstitials clusters form the precursors to dislocations either in the form of edge dislocations like **a**<100> loops or **a**/2<111> lines. Additionally, alloy T91 contains a high density of dislocation lines from the heat treatment process prior to irradiation. Vacancy clusters act as precursors to cavities. From the relative binding energies presented in

Table 6.7 helium will bind to the feature it first encounters. With increasing irradiation time, the helium is likely to be released at a faster rate from screw dislocations compared to other features and become trapped at He_mV_n clusters and edge dislocations which serve as stronger traps with higher sink strength. With time, the helium will continue to trap and release in proportion to the binding energy, eventually resulting in the flow of helium to larger vacancy clusters. However,

the previous section demonstrated that bubbles are likely saturated with helium at high helium co-injection rates and from this, the larger vacancy clusters will also become saturated.

Table 6.7. Table containing the binding energies of helium for He_mV_n clusters from [185], dislocations from [174,186] and a CSL boundary from [187]

Reaction	Binding Energy (eV)	Reaction	Binding Energy (eV)	Reaction	Binding Energy (eV)	Reaction	Binding Energy (eV)
HeV→He+V	2.3	He-Edge Dis.→He_i+Edge Dis.	2.3	He-Screw Dis.→He_i+Screw Dis.	1.0	He-Σ3(112)GB	0.55
He_2V→HeV+He	1.84	He_2V_2→HeV_2+He	2.75	He_2V_3→HeV_3+He	2.96	He_2V_4→HeV_4+He	3.12
He_3V→He_2V+He	1.83	He_3V_2→He_2V_2+He	2.07	He_3V_3→He_2V_3+He	2.91	He_3V_4→He_2V_4+He	3.16
He_4V→He_3V+He	1.91	He_4V_2→He_3V_2+He	2.36	He_4V_3→He_3V_3+He	2.57	He_4V_4→He_3V_4+He	3.05

As an estimation of helium partitioning with time, a simple model of helium trapping and de-trapping was constructed from a mass balance approach as a set of differential equations consisting of the generation of helium, the trapping of helium at a feature in proportion to the sink strength, and the thermal de-trapping of helium from a feature:

$$\frac{dC_{He}}{dt} = G_{He} - \sum_i^{loops,bub,line} k_i^2 D_{He} C_{He} + \sum_i^{loops,bub,line} N_i \Omega n_g^i \nu_0 exp\left(-E_b^i/kT\right), \quad \text{Eq. 6.12}$$

where C_{He} is the concentration of helium in the matrix, G_{He} is the helium injection rate, k_i^2 is the sink strength of a group of microstructure features such as dislocation loops, bubbles, and dislocation lines, N_i is the density of a group of microstructure features, k is the Boltzmann constant, T is the irradiation temperature, Ω is the inverse of the atomic density for iron, and E_b^i is the binding energy of helium to a group of microstructure features. The diffusivity of helium, D_{He} is assumed to have an Arrhenius form with a migration energy of 0.064 eV and a pre-factor, d_0 of 28 nm^2/s from [192]. The remaining term in the equation is the number of helium atoms per

microstructure feature, n_g^i, which can be described as a separate mass balance rate equation for each feature using:

$$\frac{dn_g^i}{dt} = \frac{k_i^2 D_{He} C_{He}}{N_i \Omega} - n_g^i \nu_0 \exp\left(\frac{-E_b^i}{kT}\right). \quad \text{Eq. 6.13}$$

The rate equations in Eq. 6.12 and Eq. 6.13 were solved for two helium injection rates where the dislocation loop microstructure was found to be experimentally identical: dual ion irradiation to 16.6 dpa at 445°C with either 0.22 appm He/dpa or 4.34 appm He/dpa The time dependent solutions are displayed in Figure 6.5. The sink strengths from the characterized microstructure were included as static, time independent features with binding energies of 1.0 eV for dislocation lines, 2.3 eV for dislocation loops and 3.6 eV for bubbles. The matrix of the material is defined as the bcc microstructure where there are no traps for helium.

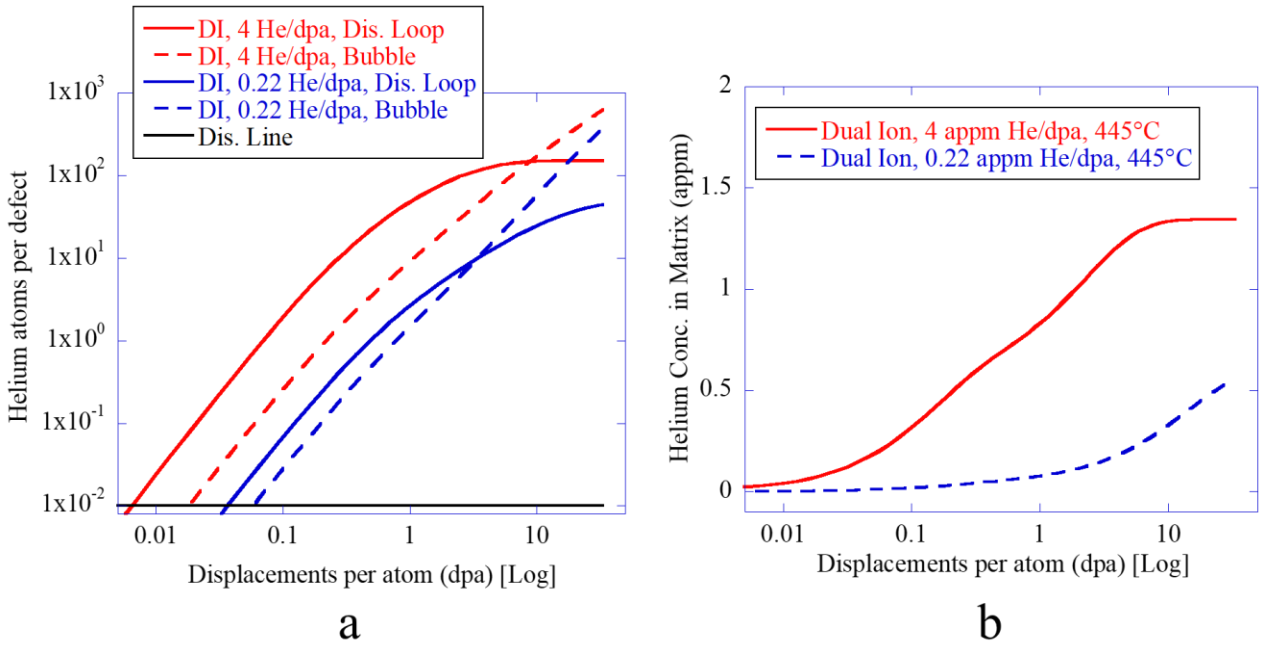

Figure 6.5. Solutions to a trapping-detrapping process consisting of dislocation loops, bubbles, and dislocation lines showing a) the concentration of helium in the matrix, and b) the number of helium atoms per defect as a function of displacement per atom.

In both cases shown in Figure 6.5a, the dislocation lines saturate with helium quickly as these features have the lowest binding energy for helium. Early in the damage process, the

dislocation loops and bubbles quickly begin to accumulate helium. The amount of helium in dislocation loops reaches a steady state at about 3 dpa and helium continues to flow to bubbles beyond this point. The time at which bubbles accumulate more helium than dislocation loops increases with increasing helium injection rate. Thus, helium can be assumed to be in bubbles only with a lower helium injection rate and can be assumed to be divided by sink strength at higher helium injection rates. The dominant traps for helium transition between microstructure features based on the binding energy of helium in the order of weakest to strongest traps. From Figure 6.5b, the saturation concentration of helium in the matrix is on the order of about 1 appm for dual ion irradiation.

The number of helium atoms accumulating at these traps may be physically unreasonable. From a comparison of Figure 6.3 and Figure 6.5, the number of helium atoms per cavity would not exceed the hard sphere equilibrium limit for bubbles of 1 nm radius. With cavities, helium accumulates inside the empty space. However, dislocation loops do not have this empty space. Instead helium accumulates around the dislocation. Within about 2 Burgers vectors of the core on the tension side of the dislocation, interstitial He atoms relax to <111> crowdion configurations in atom rows perpendicular to the dislocation, along the direction of the Burgers vector [174,193]. For a dislocation loop, the tensile strain affected volume can be approximated as a half volume of a torus with the radius of revolution as the radius of the dislocation loop, r_{dis}, and the tube radius being about two Burgers vector length, about 0.6 nm. As the atomic packing factor of a bcc lattice is 0.68, then the maximum volume available for helium trapping is 32% of the volume around the torus. The hard sphere equation of state can then be used to estimate the number of helium atoms able to fit into this available volume, V_{free}. However, as helium accumulates it induces a strain on the lattice counteracting the tensile strain from the dislocation. Thus, the maximum number of

helium atoms trapped at a dislocation loop can be approximated when the pressure of helium is equal to the outward tensile volume from the dislocation loop. Starting with the modified ideal gas law in Eq. 4.20 and substituting in Eq. 4.21 for the compressibility factor and rearranging the equation results in:

$$\frac{\frac{2\pi r_{dis} E_l}{0.5 * V_{torus}} V_{free}}{n_g kT} = \frac{1+y+y^2+y^3}{(1-y)^3}, \quad \text{Eq. 6.14}$$

where y is defined in Eq. 4.22 with V_{free} as the maximum volume available for helium trapping, and further defined through Eq. 4.23 for the hard sphere diameter. The energy of the dislocation loop per unit length is defined by [4]:

$$E_l = \frac{\mu b^2}{4\pi(1-\nu)} ln\left(\frac{R}{r_c}\right) + \varepsilon_c, \quad \text{Eq. 6.15}$$

where b is the length of the Burgers vector, R is the average distance between dislocation loops, ν is the Poisson ratio of about 0.3, r_c is the radius of the dislocation core, taken to be $5b$, and ε_c is the energy of the dislocation core, estimated to be $\frac{\mu b}{10}$ [4] and

$$\mu = \frac{E}{2(1+\nu)}, \quad \text{Eq. 6.16}$$

where E is the elastic modulus of T91, estimated as about 186 GPa from ASTM standard A213 for T91 at 450°C [194]. Based on the dislocation loop density of about 10^{21} m^{-3} (see Table 5.3, Table 5.6, and Table 5.9), the average distance between dislocation loops is about 100 nm. Solving for the number of gas atoms, n_g, per dislocation loop as a function of the dislocation loop radius, r_{dis}, for a temperature of 445°C results in the plot shown in Figure 6.6. Given the average

dislocation loop diameter of 20-25 nm for dual ion irradiated T91, it is possible for the dislocation loop microstructure to accommodate the helium accumulation presented in Figure 6.5

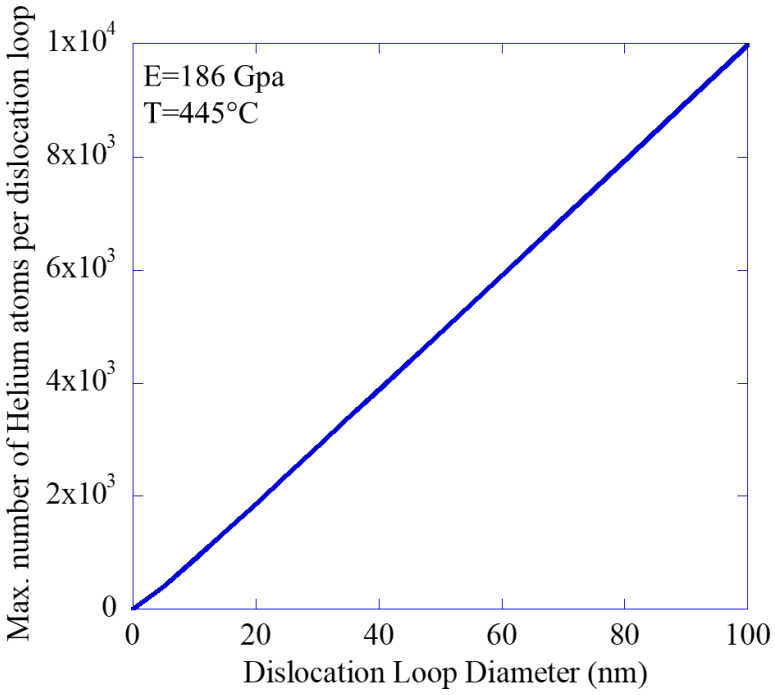

Figure 6.6. Calculation of the maximum number of helium atoms per dislocation loop for a nominal ion irradiation temperature of 445°C.

In this simple model, the traps, including cavities, are assumed not to vary in density or size with time and have binding energies independent of the amount of helium trapped at the microstructure feature. These assumptions is not true over the course of an irradiation as the microstructure continually evolves. As shown in

Table 6.7, as the m/n ratio of a He_mV_n cluster becomes greater than unity, the binding energy becomes less than that of edge dislocations. Helium will then flow from the vacancy clusters to dislocations until the vacancy cluster is able to grow and accommodate more helium. Thus, depending on the growth rate of a cavity, helium will be divided among the vacancy clusters,

bubbles, and dislocations in proportion to the density of these clusters and their relative strength for defects. Therefore, the assumption made in the previous calculations that the helium will partition in the microstructure based on sink strength is indeed a valid assumption at high helium co-injection rates. The helium partitioning shifts from helium being trapped in bubbles at low helium rates to helium being partitioned in the microstructure by sink strength as the cavities become saturated with helium. Shifting the partitioning from a division by sink strength to helium being bound only to cavities with increasing temperature at high helium rates is supported by the strongest sink in the microstructure besides cavities being the population of **a**<100> dislocation loops. The dislocation loop population decreased monotonically with temperature until only dislocation lines remained in the microstructure. This reduction in the dislocation loop density explains the shift in partitioning with increasing temperature.

In this section the role of helium partitioning on the stable bubble radius was determined. Calculations using the cavity growth rate equation were compared to the experimental cavity size distributions accounting for the binding energies associated with common microstructural defects. At low helium injection rates all helium is in vacancy clusters that evolve into bubbles or voids. At high helium injection rates, bubbles become saturated with helium resulting in accumulation of helium at other traps such as dislocation loops. At high enough temperatures, helium is only in bubbles as other strong helium traps, such as **a**<100> dislocation loops, did not nucleate, as expected for high temperatures [195]. The stable bubble radius is determined by the fate of helium in the microstructure. Helium partitioning stems from the sink strength for helium and binding energy of helium to bubbles relative to other traps regardless of damage rate.

6.2 Void Nucleation Across Damage Rates

This section will demonstrate how void nucleation shifts from being driven by the accumulation of helium to the critical bubble at low damage rates to being driven by stochastic vacancy fluctuation at high damage rates. First, the barrier to transition from bubbles to voids will be identified and discussed with pathways to overcome this barrier. Second, the impact of variation in the vacancy migration energy will be discussed and evaluated to identify active transition pathways. Finally, a parameter for spontaneous void nucleation will be calculated and discussed for dual ion irradiation of T91.

The cavity growth rate equation, Eq. 2.4 in Section 2.4.5 and repeated for convenience:

$$\frac{dr}{dt} = \frac{\Omega}{r}\left[D_v C_v - D_i C_i - D_v C_{v,T} \exp\left(\frac{2\gamma}{r} - p_g\right)\right], \qquad \text{Eq. 6.17}$$

has two main competing processes, the net absorption of vacancies, $D_v C_v - D_i C_i$. and the thermal emission of vacancies, $D_v C_{v,T} \exp\left(\frac{2\gamma}{r} - p_g\right)$. The individual components of the cavity growth rate equation are presented in Figure 6.7 for select temperature conditions of 432°C, 460°C, and 520°C: at low temperature primarily bubbles were observed; at intermediate temperature both bubbles and voids were observed; and at high temperature only bubbles were observed. The shape of the net vacancy absorption curve is independent of temperature but changes in magnitude; however, thermal emission changes with increasing temperature. The crossover points for each of temperature corresponds to the roots of the cavity growth rate equation and forms the void nucleation barrier. As stated previously the first root corresponds to the stable bubble radius and the second root corresponds to the size at which a void can grow through bias driven growth. At 460°C the void nucleation barrier is smaller than at 432°C. At a high temperature of 520°C, the void nucleation barrier becomes extremely large because thermal emission is dominant. Thus, the main "barrier" to transition from bubbles to voids is the thermal emission of vacancies.

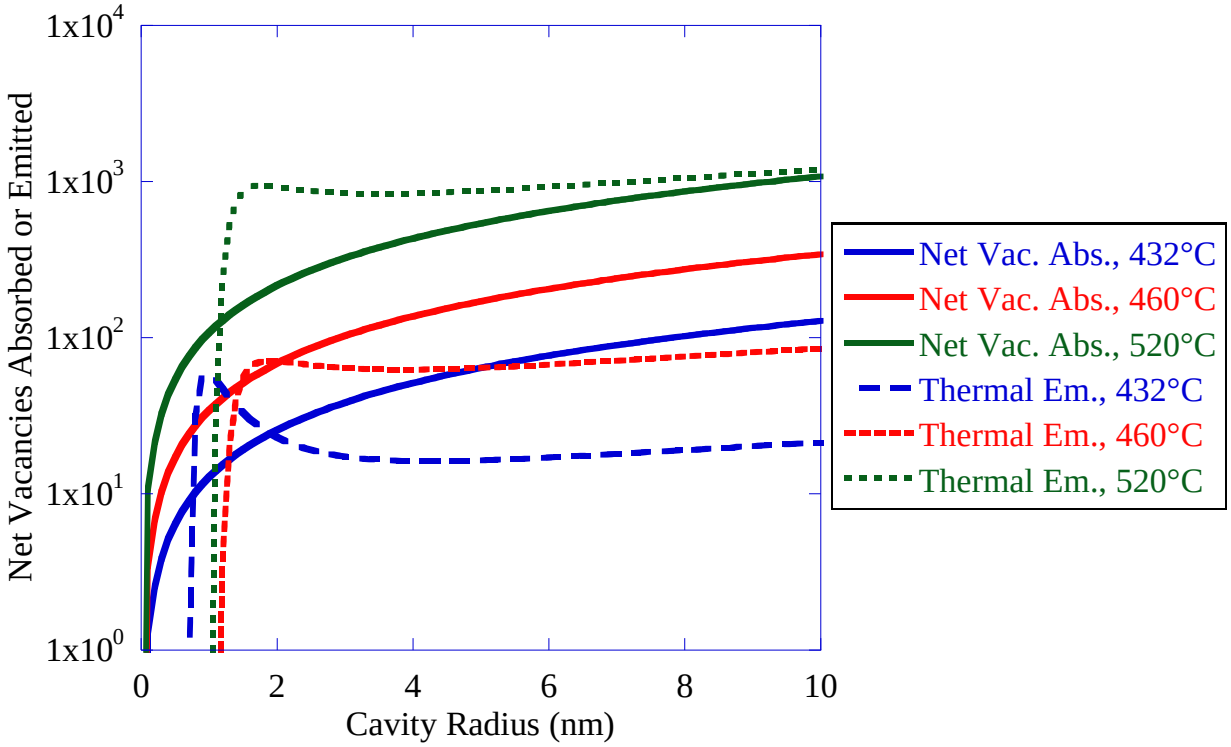

Figure 6.7. Individual components of the cavity growth rate equation using select ion irradiation conditions of 432°C, 460°C, and 520°C and the associated microstructure assuming an equal distribution of all helium in cavities.

6.2.1 Investigation of Individual Variables on Void Nucleation

To investigate the importance of helium to cavity nucleation, Stoller and Odette [134] studied the effect of the cluster composition (helium vs. vacancy) on the nucleation path of cavities. Two paths emerge to limit void formation: one is to limit growth of the critical bubble by helium starvation [141,142], the other is to limit growth of the critical bubble by vacancy starvation [71,72,127]. In the cavity growth rate equation, the helium accumulation pathway corresponds to a solution with helium containing a singular root, r^*, and the stochastic vacancy fluctuation pathway to accumulate vacancies corresponds to the larger root, r_v^*, in the two-root solution, see Figure 6.8. The stochastic fluctuation of vacancies may explain the occurrence of voids without helium as seen in the cavity size distributions for the Helium Series, Figure 5.13.

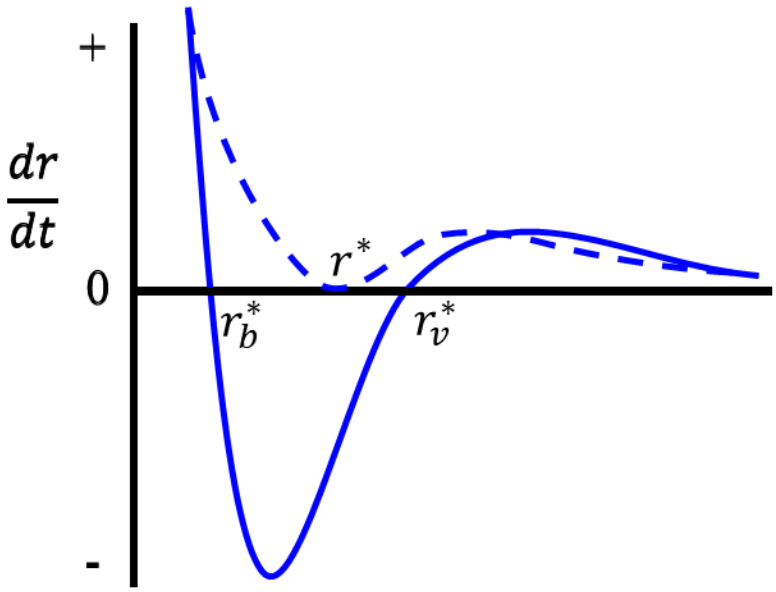

Figure 6.8. Schematic of solutions to the cavity growth rate equation showing the two-root solution for underpressurized cavities (solid line) and the single root solution for the critical bubble through helium accumulation (dashed line).

A comparison of the calculated r^* and r_v^* values and the valleys of the experimental cavity size distributions is shown in Figure 6.9 using the helium partitioning schemes best matching the bubble peak and r_b^* from Section 6.1. Overall, the valleys of the cavity size distributions are greater than r^* or r_v^*, indicating both helium accumulation and vacancy accumulation are active nucleation paths. However, whenever the vacancy absorption becomes small compared to thermal emission, the calculated r^* and r_v^* become unreasonably large.

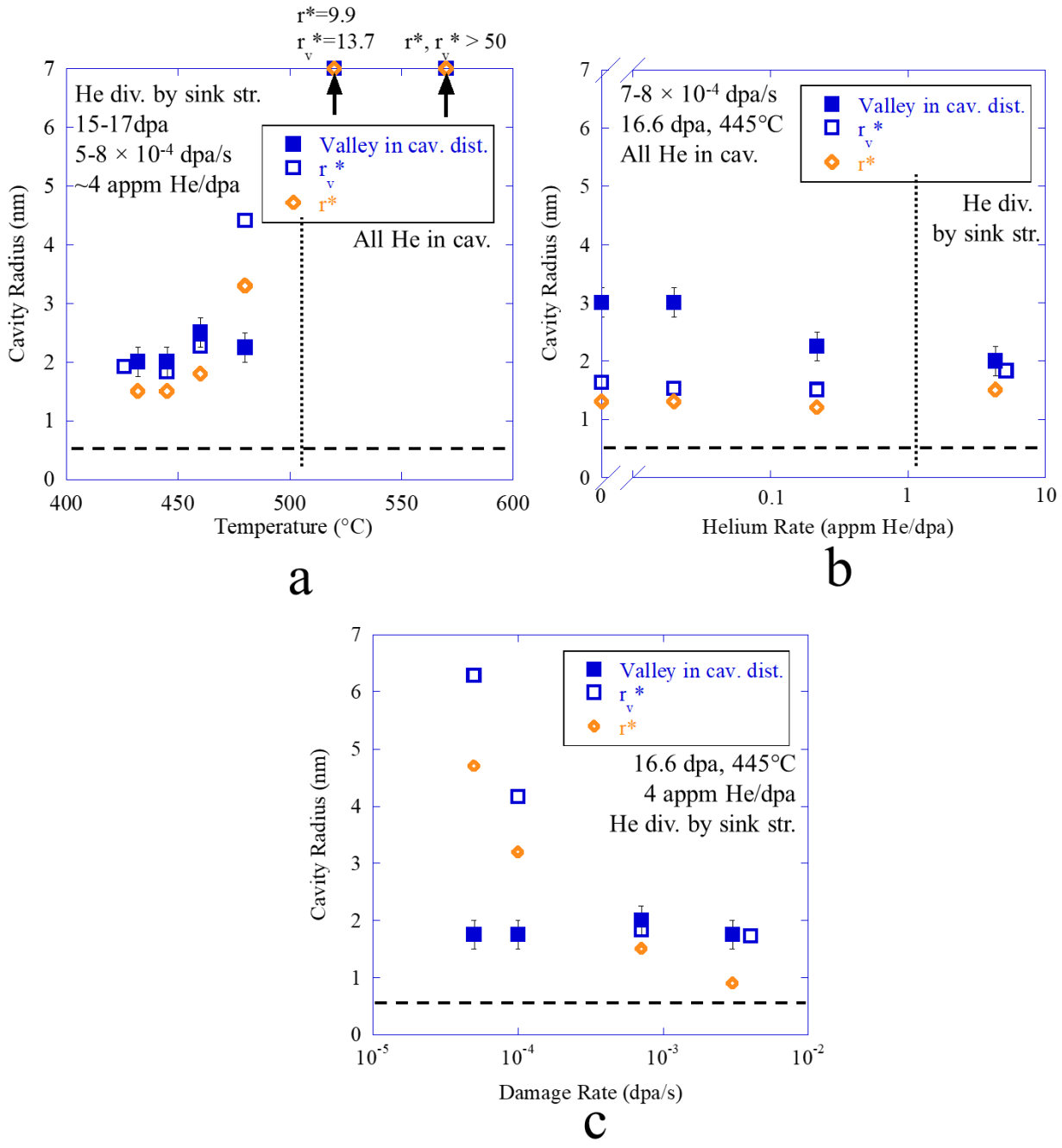

Figure 6.9. Comparison of the experimentally determined valley in the cavity size distributions for the a) Temperature Series of ion irradiations, b) Helium Series of ion irradiations, c) Damage Rate Series of irradiations, and the calculated $r^*$and r_v^*, from the cavity growth rate equation for each series using the helium partitioning schemes identified previously. The dashed line is the smallest size bin used for analysis. Some open points are displaced along the x-axis slightly to avoid overlap.

Now that the effect of helium on void nucleation is included, other parameters can be explored. The sensitivity analysis performed previously in Chapter 6 identified vacancy migration energy, surface energy, and vacancy formation energy as significant parameters impacting void

nucleation in all experimental series. The diffusion of point defects is crucial to the nucleation process as it affects the arrival of point defects to bubbles and voids and appears in the cavity growth rate equation, Eq. 6.3, as $D_i C_i$ and $D_v C_v$. Therefore, at high damage rates changes in diffusion will modify the cavity growth rate equation significantly. Thus, an investigation of the vacancy migration energy is warranted and done first.

The calculations and comparisons thus far have assumed an interstitial migration energy of 0.35 eV and a vacancy migration energy of 0.63 eV for iron vacancies from the work on radiation induced segregation in Fe-Cr alloys by Wharry and Was [69]. This work also surveyed the literature and found a range for the interstitial migration energy of 0.35±0.04 eV and 0.63±0.06 eV for the vacancy migration energy using ab initio methods [196–199]. Using the sensitivity for E_m^v calculated previously, the effect on r_v^* can be estimated for the dual ion irradiation variable series of temperature, helium co-injection rate, and damage rate. This analysis focuses on the conditions where the calculated r^* or r_v^* were greater than the valley in the cavity size distribution to determine whether a reasonable change in the vacancy migration energy (within the limits of the reported range) results in a better agreement. The results of this variation in the migration energy are displayed in Figure 6.10. Increasing the vacancy migration energy reduces vacancy absorption and thus, increases r^* and r_v^*. Because the sensitivity is very high, the range of the calculated r^* and r_v^* extend to include the valley in the cavity size distributions for the dual ion irradiations meaning both helium accumulation and vacancy accumulation are possible nucleation paths. Based on the lower and upper bounds in Figure 6.10, there is likely no singular vacancy migration energy that can accommodate all of the dual ion irradiation conditions.

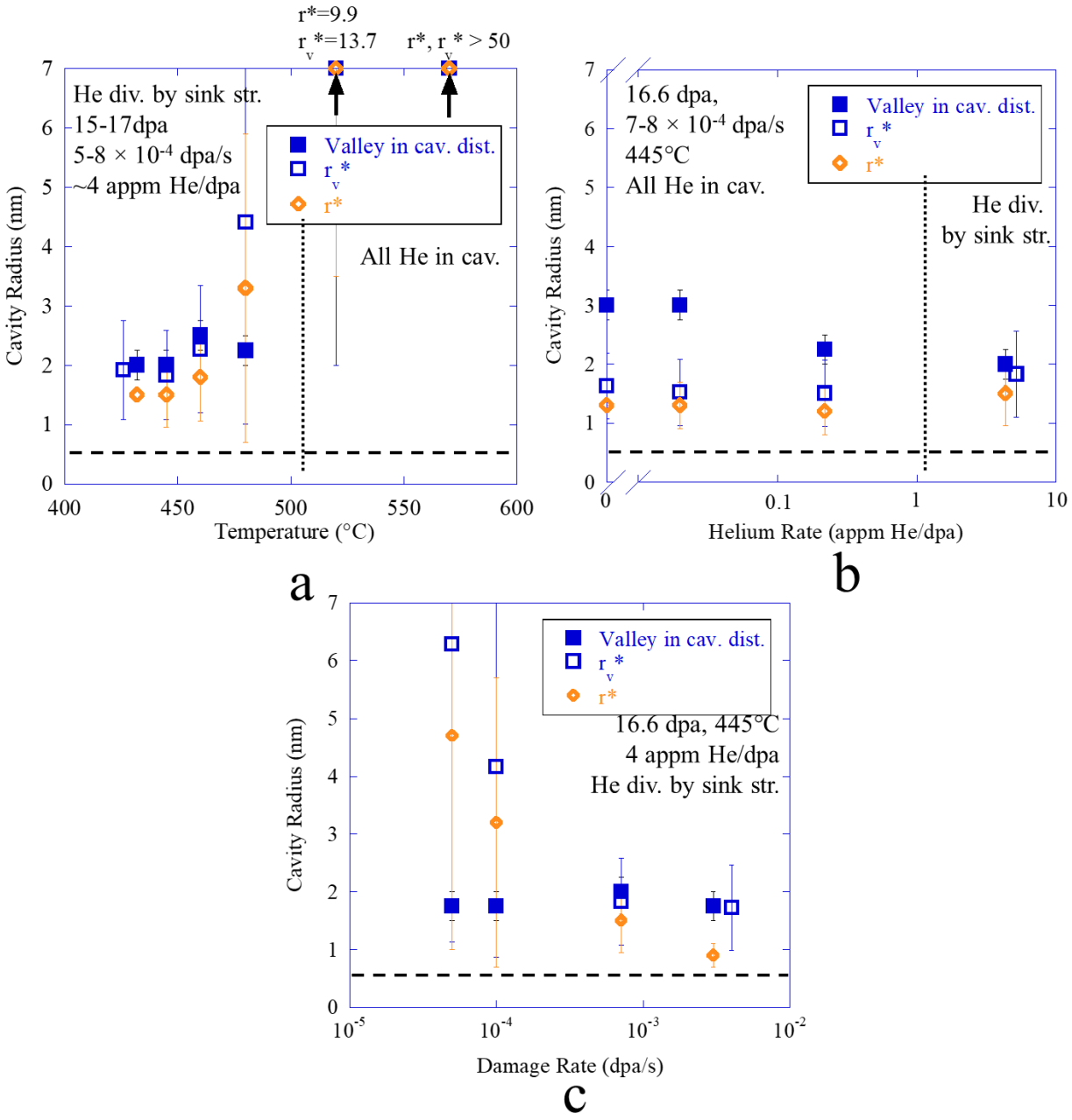

Figure 6.10. Comparison of the experimentally determined valley in the cavity size distributions for the a) Temperature Series of ion irradiations, b) Helium Series of ion irradiations, c) Damage Rate Series of irradiations, and the calculated r^* and r_v^* with bounds for the vacancy migration energy, from the cavity growth rate equation for each series using the helium partitioning schemes identified previously. The dashed line is the smallest size bin used for analysis. Some open points are displaced along the x-axis slightly to avoid overlap.

The remaining highly significant parameters identified are the surface energy and vacancy formation energy. The reported surface energy for bcc iron ranges from 1.75 J/m^2 (used in this work) to 2.62 J/m^2 [200–204]. A larger surface energy makes it harder for voids to stabilize and

would not bring the calculated r^* or r_v^* closer to the valley size distributions. Thus, while the surface energy is a highly sensitive parameter, it is not useful to investigate currently. The vacancy formation energy was measured to be about 1.60±0.1 eV from positron annihilation spectroscopy [205,206] with 1.6 eV used in this work. As the valleys and calculated points already agree with each other from variations in the vacancy migration energy, variation of the vacancy formation energy will further the agreement between the experiments and model. Thus, the critical bubble model of cavity nucleation is likely part of the mechanism of void nucleation in dual ion irradiated T91 steel across damage rates.

6.2.2 The Effect of Stochastic Vacancy Fluctuation at High Damage Rates

The thermal barrier to void nucleation can also be overcome by the stochastic fluctuation of vacancies, as evidenced by the formation of voids without helium at high damage rates. Russell [127] used statistical thermodynamics to create a general theory of void nucleation. One of the specific subcases examined in this work is the spontaneous void nucleation driven by a small amount of inert gas. Prior to void formation, spontaneous nucleation will occur when the void nucleation parameter, ψ, is greater than unity and will stop when the void sink strength overcomes the dislocation sink strength. The void nucleation parameter is written as:

$$\psi = \frac{9C_x^0(kT)^2\ln\left[S_v\left(1-\frac{\beta_i^0}{\beta_v^0}\right)\right]K_x^T}{(36\pi\Omega^2)^{2/3}\gamma^2a^2k^2K_x^C} = \frac{9C_x^0(kT)^2\ln\left[S_v\left(1-\frac{k_v^2}{k_i^2}\right)\right]K_x^T}{(36\pi\Omega^2)^{2/3}\gamma^2a^2k^2K_x^C} \qquad \text{Eq. 6.18}$$

where C_x^0 is the concentration of the inert gas in the matrix, k is the Boltzmann constant, T is the temperature, S_v is the supersaturation of vacancies defined as the concentration of radiation induced vacancies divided by the thermal concentration of vacancies, k_v^2 is the sink strength for vacancies, k_i^2 is the sink strength for interstitials, K_x^T is the de-trapping rate of the inert gas from traps in the matrix, Ω is the atomic volume, γ is the surface energy, a is the lattice parameter, k_2

is the total sink strength in the microstructure, and K_x^C is the de-trapping rate of the cavities. For this calculation, the de-trapping rate of inert gas uses Eq. 6.11 with a binding energy of 2.3 eV assuming the majority of traps in the matrix are dislocation loops and 3.6 eV for the binding energy of cavities, resulting in a ratio of $\frac{K_x^T}{K_x^C} = \frac{\exp\left(\frac{-2.3}{kT}\right)}{\exp\left(\frac{-3.6}{kT}\right)} = 1.3 \times 10^9$ at 445°C. The concentration of inert gas atoms was considered based on Figure 6.5b to be about 1 appm helium similar to the saturation concentration of helium in the matrix in the dual ion irradiation. The results of calculating the void nucleation parameter for each irradiation series described in this work is shown in Figure 6.11.

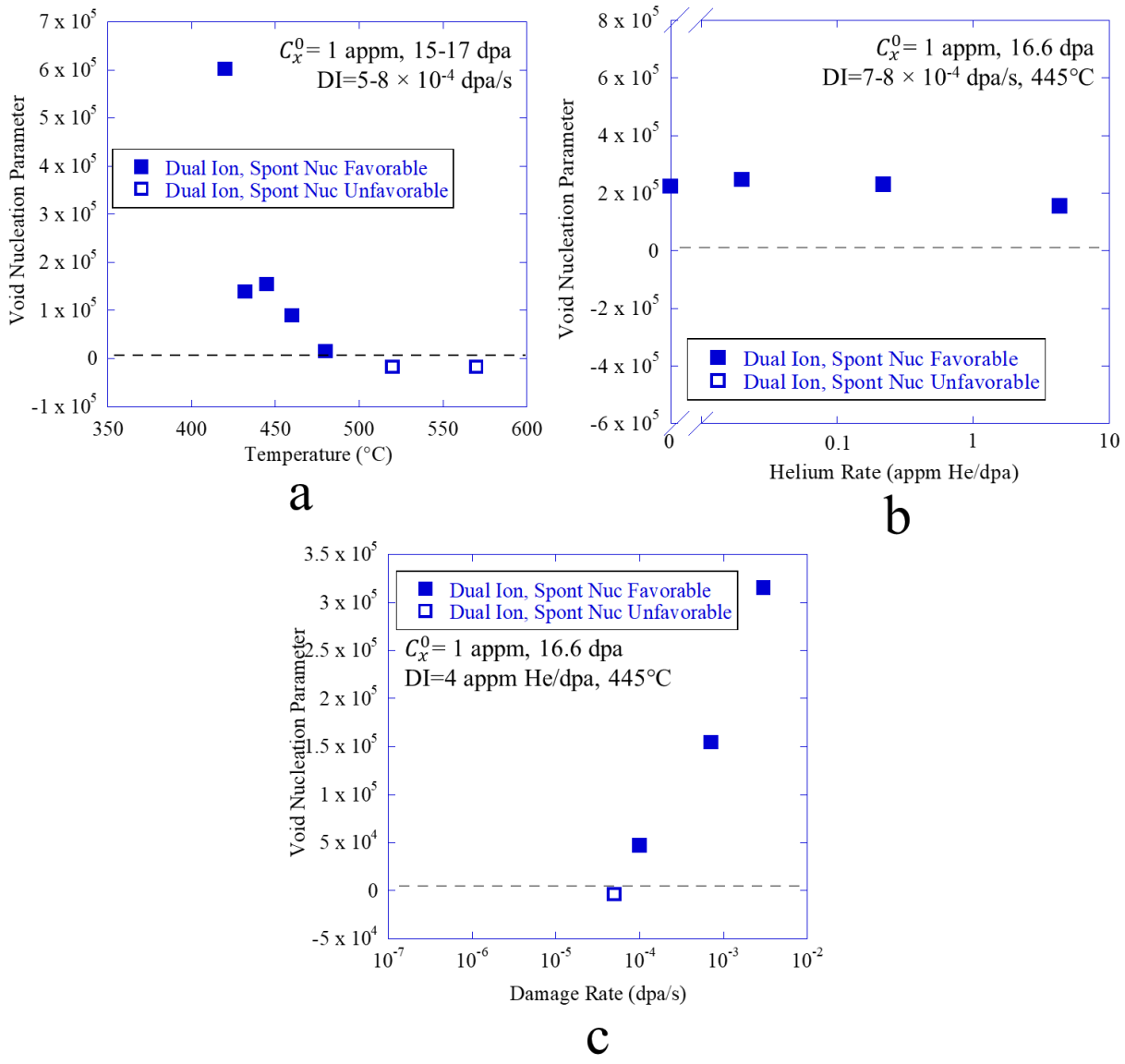

Figure 6.11. Calculation of the void nucleation parameter using the irradiation parameters for the experiments in this work with a matrix concentration of helium at 1 appm. Solid points indicate spontaneous nucleation is favorable and unfilled points indicate spontaneous nucleation is unfavorable.

Several trends can be assessed from the void nucleation parameter presented in Figure 6.11. With increasing damage rate, the void nucleation parameter increases from the increased vacancy supersaturation. Without spontaneous nucleation or vacancy fluctuations, the only path to void nucleation is the accumulation of helium in bubbles to reach the critical bubble. All irradiations below a damage rate of 1×10^{-4} dpa/s should not nucleate voids spontaneously. Yet, the density of

voids decreases with increasing damage rate, see Figure 5.18 and repeated here as Figure 6.12 for reference. So, the amount of helium arriving at cavities must decrease with damage rate to account for the decreased void nucleation rate. Helium accumulation can be assessed using the same helium trapping-detrapping process outlined in Section 6.1, using Eq. 6.12 and Eq. 6.13 for the Damage Rate Series of ion irradiations and their associated microstructure from Section 5.3. Helium accumulation on dislocation loops and cavities is displayed in Figure 6.13. Similar to Figure 6.5, the dislocation lines saturated early in the damage process with a low helium concentration and therefore, were not included in Figure 6.13.

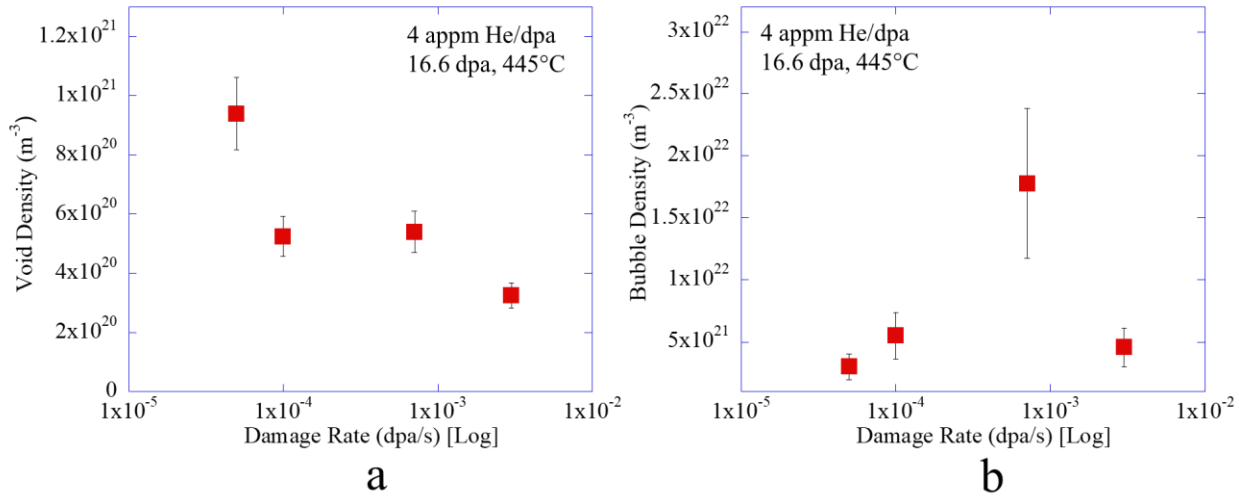

Figure 6.12. Void densities (a) and bubble densities (b) for the Damage Rate Series of dual ion irradiations.

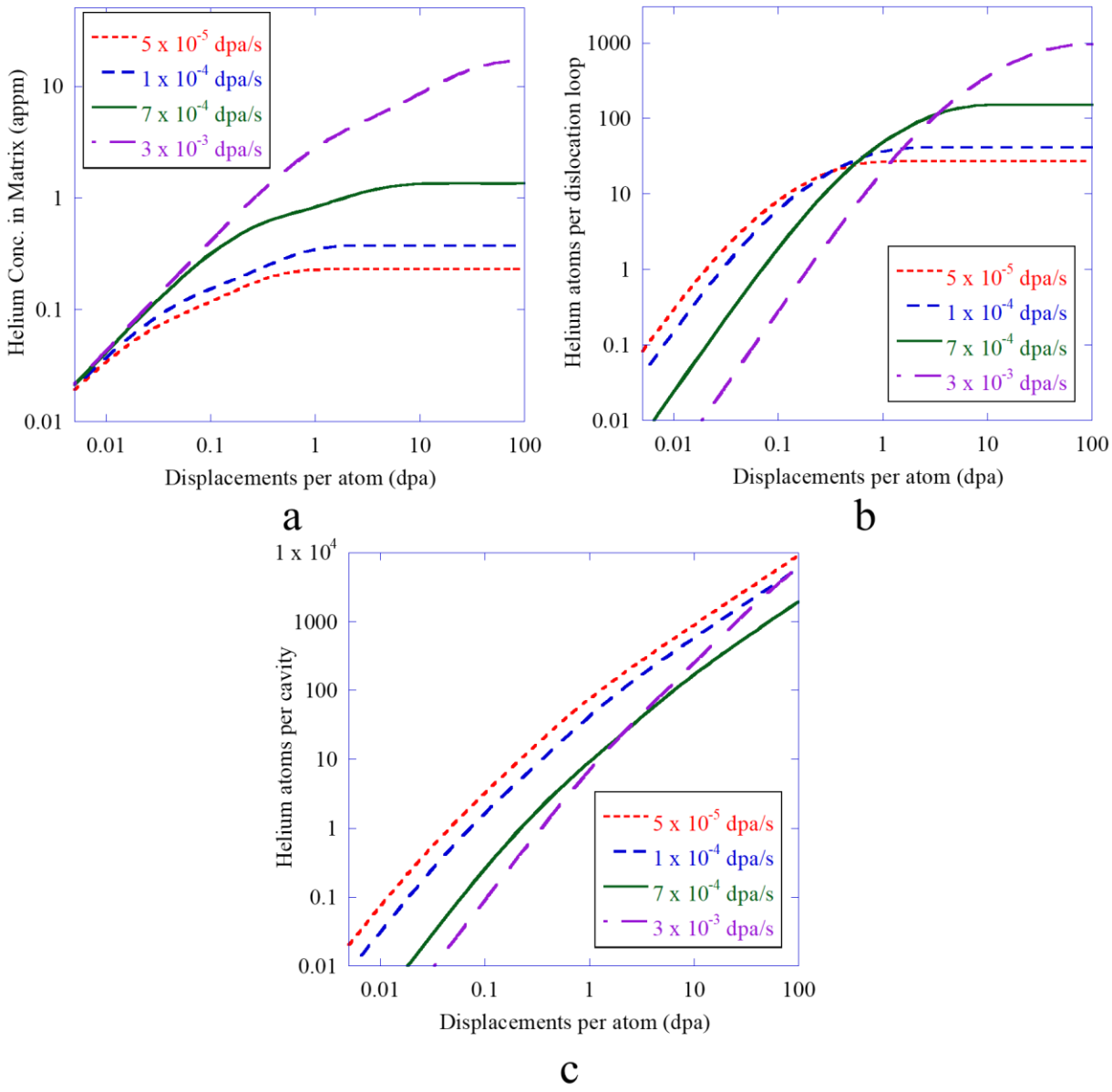

Figure 6.13. Solutions to a trapping-detrapping process consisting of dislocation loops, bubbles, and dislocation lines for the Damage Rate series of ion irradiations up to 100 dpa showing a) the concentration of helium in the matrix, b) the number of helium atoms per dislocation loop, and c) the number of helium atoms per cavity as a function of displacement per atom.

With increasing damage level, the helium concentration in the matrix and at dislocation loops begins to level off between 1 to 10 dpa, saturating with helium. However, the cavities continue to accumulate helium, leading to the continual nucleation of bubbles. Evidence for this comes from the increase in void density with dpa while maintaining a constant average diameter,

Figure 5.2. With increasing damage rate, helium concentration in the matrix and trapped on dislocation loops increases significantly (Figure 6.13a-b), therefore reducing helium available for cavities (Figure 6.13c) at a given damage level. This is likely from the lack of time for helium to de-trap from the weaker traps and flow to the bubbles and voids. The decreased helium per cavity favors a population of bubbles over voids because bubbles are stabilized with less helium than voids.

To assess helium driven void nucleation, the void nucleation rate per dpa for each dual ion irradiation damage rate can be estimated using:

$$\frac{voids}{vol-dpa} = \frac{\partial}{\partial dpa}\left(\frac{n_g^{cav}(dpa)N_{bub}}{m^*}\right), \quad \text{Eq. 6.19}$$

where n_g^{cav} is the helium trapped per cavity as a function of dpa from Figure 6.13c, m^* is the amount of helium to form a stable 2 nm radius critical bubble (as observed in the valley of the distribution, Figure 6.10c), and N_{bub} is the density of bubbles observed. The void nucleation rate for helium driven void nucleation through the critical bubble model is displayed in Figure 6.14. From these nucleation rates, as the damage rate increases, the helium driven void nucleation rate decreases for any given damage level until all arrive at a plateau. Therefore, for a fixed dpa, the density of voids decreases with increasing damage rate. This agrees with the data on void density with increasing damage rate, shown in Figure 6.15. Similarly, the bubble nucleation rate would follow the same trend with a replacement of m^* with the amount of helium necessary to form a stable bubble.

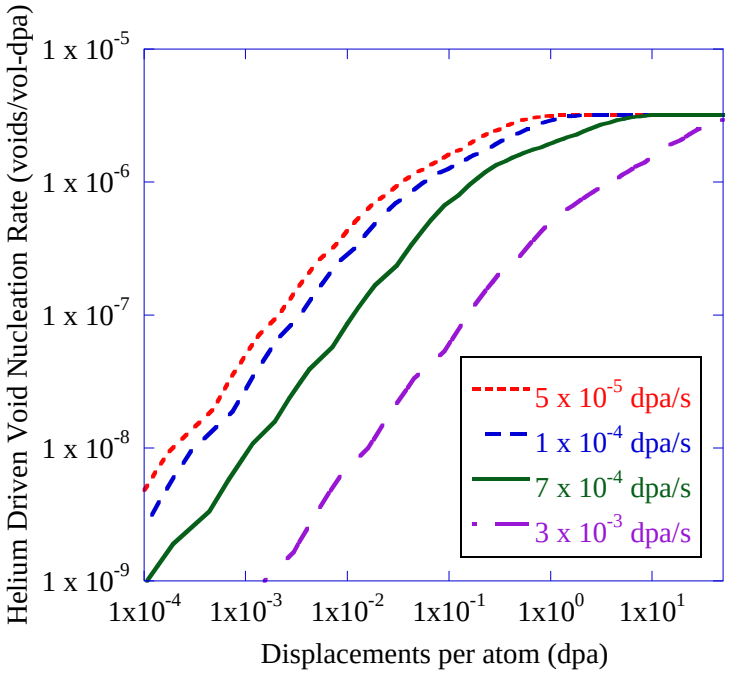

Figure 6.14. Estimated void nucleation rates for helium driven void nucleation through the critical bubble model for the Damage Rate Series of dual ion irradiation.

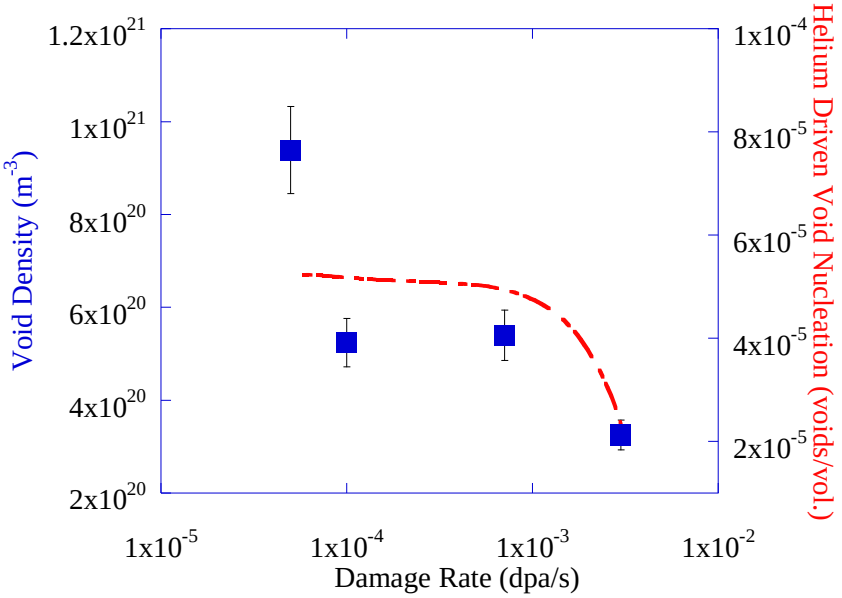

Figure 6.15. Estimated void nucleation rates for helium driven void nucleation through the critical bubble model for the Damage Rate Series of dual ion irradiation compared to the experimental void densities.

The decrease in the helium per cavity with increasing damage rate also implies that as the void density decreases, the bubble density increases as it takes less helium to form a stable bubble

than a stable void. The measured increase in bubble density with damage rate is shown in Figure 6.12b. The relative promotion rate of bubbles into voids is represented by the ratio of the void density over bubble density, Figure 6.16. As the damage rate increases, the ratio decreases until a damage rate of 7×10^{-4} dpa/s is reached, consistent with the decrease in helium per cavity. However, the ratio increases at the highest damage rate. One possibility is spontaneous nucleation which requires both a high vacancy supersaturation and high helium concentration. The helium concentration in the matrix, Figure 6.13a, is at its highest at the highest damage rate, and therefore should have the highest likelihood of spontaneous void nucleation based on Eq. 6.18.

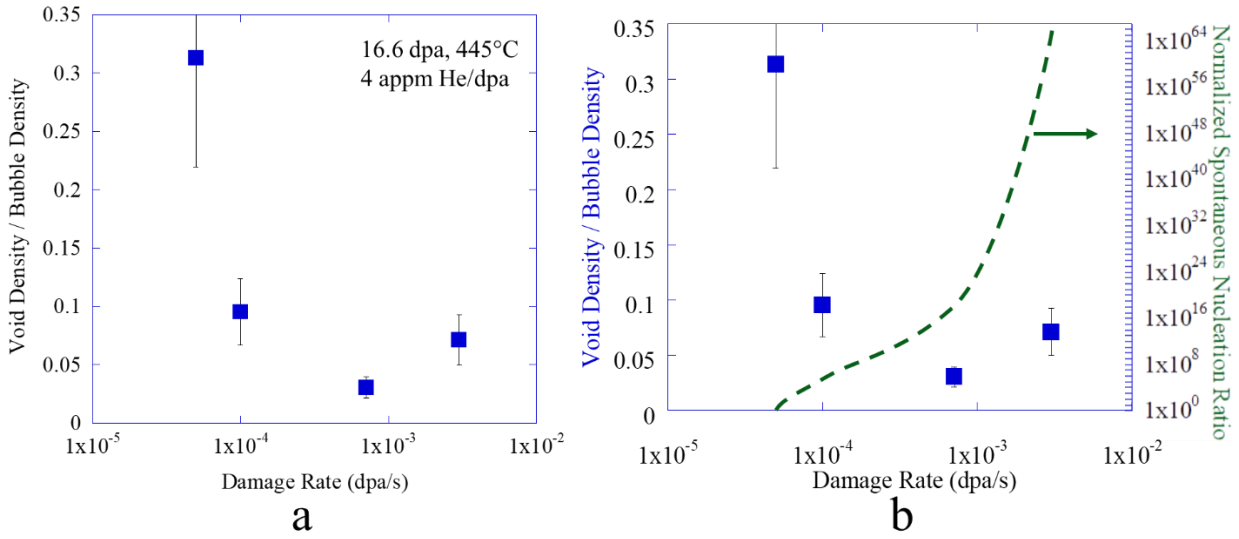

Figure 6.16. Ratio of void to bubble densities as a function of damage rate in the Damage Rate Series of dual ion irradiation (a) without an overlay and (b) overlaid with the normalized to the lowest damage rate.

From the work of Russell [127], the void nucleation rate from spontaneous nucleation can be estimated using:

$$J_s \simeq \frac{K}{\Omega} \exp\left(\frac{-16\pi\Omega^2\gamma^3}{3(kT)^3\{\ln S_v\}^2}\right), \qquad \text{Eq. 6.20}$$

where K is the damage rate, Ω is the atomic volume, γ is the surface energy, kT is the thermal energy, and S_v is the vacancy supersaturation. The calculated nucleation rate ratios for the Damage Rate Series of dual ion irradiations is shown in Figure 6.16b normalized to the lowest dual ion

irradiation damage rate. The spontaneous nucleation rate increases dramatically with increasing damage rate. However, the calculated values seem physically unrealistic. Nevertheless, the trend is consistent with the expectation of increased spontaneous nucleation with irradiation damage rate. Therefore, the mechanism of bubble to void transition shifts from being driven by helium accumulation to the critical bubble at low damage rates to include spontaneous nucleation through stochastic vacancy fluctuation at high damage rates.

From the work presented in this section, several conclusions can be drawn. First, the barrier to transition from bubbles to voids was identified as the thermal emission of vacancies and can be overcome either through helium accumulation or through stochastic vacancy fluctuations. Second, the variation in the migration energy demonstrated that helium accumulation by the critical bubble is the only nucleation pathway to voids at higher temperature (520°C) while stochastic vacancy accumulation is active at intermediate temperatures (432-480°C). This was confirmed with an analysis of the void nucleation parameter across three orders of magnitude in helium concentration. Third, the void nucleation parameter showed that spontaneous void nucleation is likely at high damage rates and impossible at low damage rates. Helium trapping was shown to increase helium on dislocation loops and in the matrix with increasing damage rate, leaving less available for cavities. The higher matrix helium concentration makes spontaneous nucleation more likely. Thus, the mechanism of bubble to void transition shifts from being driven by the accumulation of helium to the critical bubble at low damage rates to being driven by stochastic vacancy fluctuation at high damage rates.

6.3 The Suitability of the Cavity Growth Rate Equation to Bubbles and Voids in Reactor

As the cavity growth rate equation has been shown to account for bubble nucleation and void nucleation with dual ion irradiation, the same analysis can be applied to reactor irradiation in

the BOR-60 reactor to determine if the same mechanisms hold. First the roots of the cavity growth rate equation will be compared to the experimental cavity size distributions to determine if the same mechanisms of bubble nucleation and void nucleation apply.

6.3.1 Extrapolation of the Cavity Growth Rate Equation to Reactor Irradiation

Similar to the analysis presented in Section 6.1, the experimentally determined bubble peak in the cavity size distributions will be compared with r_b^* from Eq. 6.3 using two helium partitioning schemes: assuming all helium in cavities (Eq. 6.8) and assuming helium is partitioned by sink strength (Eq. 6.9) to determine the helium atoms per cavity. This comparison is made in Figure 6.17.

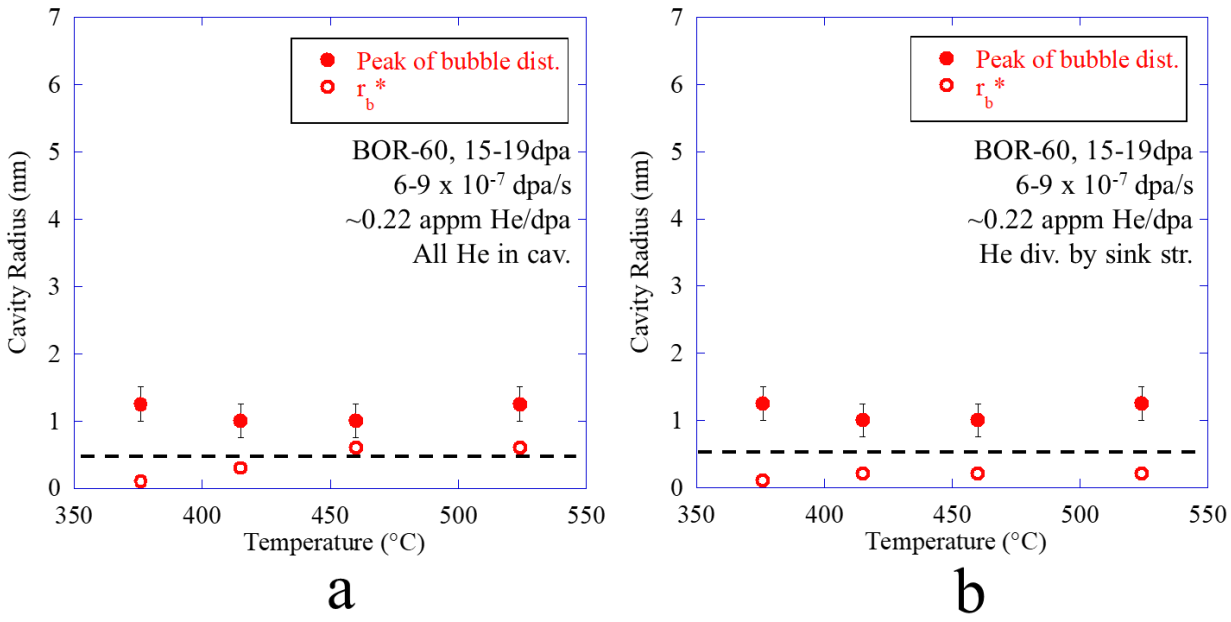

Figure 6.17. Comparison of the experimentally determined bubble peak in the cavity size distributions for the BOR-60 irradiations and the first root of the cavity growth rate equation for each series assuming (a) all helium is in cavities or (b) helium is divided in the microstructure by sink strength. The dashed line is the smallest size bin used for analysis.

In the BOR-60 irradiations, all the calculated stable bubble radii are below the measured values. In the two lower temperature experiments have the calculated stable bubble radius below a practical visibility threshold for TEM characterization. The higher temperature experiments have a calculated stable bubble radius with a reasonable 0.5 nm difference in radius from the peak of

the cavity size distributions. At the low damage rates of BOR-60 irradiations, the calculated bubble radii all drop to below TEM resolution when helium is partitioned by sink strength. To examine the fate of helium, the same helium trapping process described in Section 6.1 was used with Eq. 6.12 and Eq. 6.13 and solved as a function of time in Figure 6.18. The sink strengths from the characterized microstructure were included as static, time independent features with binding energies of 1.0 eV for dislocation lines, 2.3 eV for dislocation loops and 3.6 eV for bubbles. Like the dual ion irradiations, dislocation lines reach a steady concentration quickly. the dislocation loops saturate with helium and the bubbles overtake the dislocation loops by 0.2 dpa, about an order of magnitude earlier. At 17 dpa, there is about two orders of magnitude more helium in bubbles than dislocation loops and thus, the fate of helium can be assumed to have all helium in bubbles. The cavity growth rate equation is likely able to accommodate bubble nucleation in reactor relevant irradiation conditions.

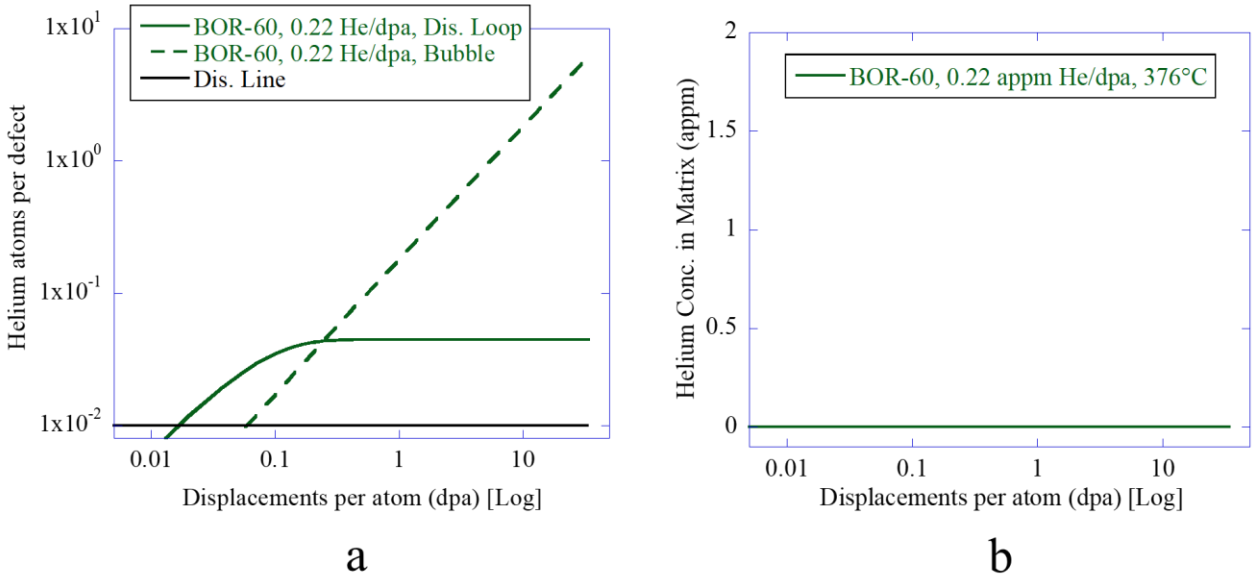

Figure 6.18. Solutions to a trapping-detrapping process consisting of dislocation loops, bubbles, and dislocation lines showing a) the number of helium atoms per defect, and b) concentration of helium in the matrix as a function of displacement per atom.

To assess void nucleation, a comparison of the calculated r^* and r_v^* values and the valleys of the experimental cavity size distributions for BOR-60 irradiation is shown in Figure 6.19 with

all helium in cavities. At all BOR-60 conditions, the calculated radii are significantly larger than the experimental valley in the size distribution. The thermal barrier to void nucleation is too wide to overcome at the low damage rates of reactor irradiation and results in unreasonably large r^* and r_v^*.

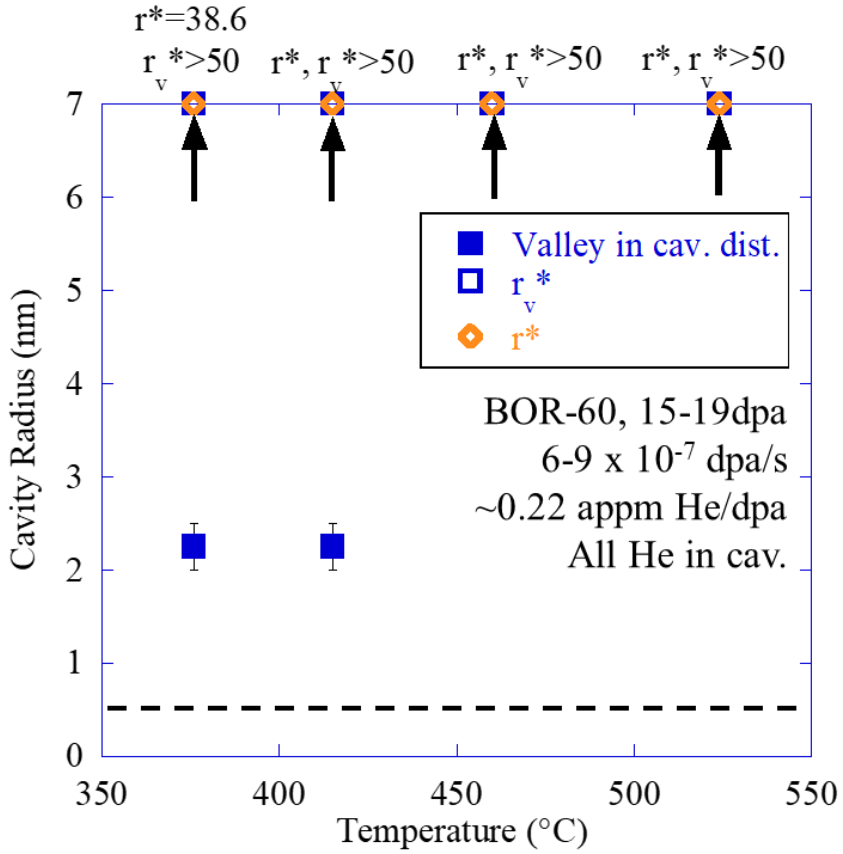

Figure 6.19. Comparison of the experimentally determined valley in the cavity size distributions for the BOR-60 irradiations and the calculated $r^*$and r_v^*, from the cavity growth rate equation using the helium partitioning scheme identified previously. The dashed line is the smallest size bin used for analysis.

To determine the important parameters for void nucleation, the sensitivity of the roots of the cavity growth rate equation can be assessed using Eq. 6.2, resulting in Table 6.2 for the significance related to the BOR-60 irradiations. The significance of the helium co-injection rate on r_b^* is one of the few factors with significance at BOR-60 relevant conditions. Like the dual ion

irradiation conditions, the second root of the cavity growth rate equation was most sensitive to the vacancy migration energy, surface energy and vacancy formation energy.

Table 6.8. Table containing significance related to the BOR-60 irradiations of several input parameters on the roots of the cavity growth rate equation. A value of 0* means the calculated root was greater than 50 nm in radius and was not evaluated. The helium rate is fixed at 0.22 appm He/dpa.

	376°C, 8 × 10^{-7} dpa/s		**415°C, 8 × 10^{-7} dpa/s**		**460°C, 7 × 10^{-7} dpa/s**		**524°C, 7 × 10^{-7} dpa/s**	
Input Parameter (below)	r_b*	r_v*	r_b*	r_v*	r_b*	r_v*	r_b*	r_v*
a	0	1.91	0	1.91	0	0*	0	0*
Bias	0	-0.94	0	-0.94	0	0*	0	0*
γ	0	1.00	-0.03	0.99	-0.05	0*	-0.07	0*
ω_i	0	0	0	0	0	0*	0	0*
ω_v	0	0.96	0	0.97	0	0*	0	0*
r_i	0	0	0	0	0	0*	0	0*
Grain size	0	-0.06	0	-0.15	0	0*	0	0*
E_m^i	0	0	0.0004	0	0	0*	0	0*
E_m^v	0	-10.8	0	-10.4	0	0*	0	0*
E_f^v	0	-27.4	0	-26.2	0	0*	0	0*
T	0	37.9	0	35.3	0.03	0*	0.05	0*
He/dpa	0.03	0	0.03	0.04	0.05	0*	0.07	0*
dpa/s	0	-0.97	0	-0.97	0	0*	0	0*

With the effect of helium on void nucleation included based on the previous discussion of bubbles, other parameters can be explored. Even with a large variation of the calculated stable radii from the vacancy migration energy of 0.63±0.06 eV as was done for the analysis of the dual ion irradiated T91, the thermal barrier to void nucleation results in unreasonably large r^* and r_v^* and virtually identical to the data presented in Figure 6.19. The remaining highly significant parameters identified are the surface energy and vacancy formation energy. The reported surface energy for bcc iron ranges from 1.75 J/m^2 (used in this work) to 2.62 J/m^2 [200–204]. A larger surface energy makes it harder for voids to stabilize and would not bring the calculated r^* or r_v^*

closer to the valley size distributions. During irradiation, solutes may segregate to the surface of a nucleating cavity, changing the surface energy locally [207–209] resulting in a different effective surface energy and corresponding change in the thermal emission of vacancies. From the characterization of BOR-60 irradiated T91, radiation induces the enrichment of nickel and silicon at grain boundaries [146]. Similar segregation to the surfaces of cavities is expected. Very little grain boundary segregation was observed with dual ion irradiation and therefore, by extension, there should be little change in surface energy at cavity interfaces. Bulk surface energies for the solute may be used as an approximation for a completely coated cavity surface. The surface energy for nickel ranges from 2.1 J/m^2 to 2.5 J/m^2 with an average of about 2.3 J/m^2 [210] and make stabilization of voids more difficult. The surface energy for amorphous silicon is approximately 1.05±0.14 J/m^2 [211]. Using this surface energy of 1.05 J/m^2, results in roots of r_b^*=0.16 nm, r^*=11.8 nm, and r_v^*=33.6 nm, still significantly larger than the valley in the cavity size distributions. In order to get a reduction of r^* to the experimental value of about 2 nm, a surface energy of 0.1 J/m^2 must be used, which is physically unreasonable. A reasonable variation in surface energy does not result in the agreement of the cavity growth rate equation and the experimental cavity size distributions for BOR-60 irradiated T91.

In addition to the surface energy, the remaining highly sensitive parameter is the vacancy formation energy. The vacancy formation energy was measured to be about 1.60±0.1 eV from positron annihilation spectroscopy [205,206] with 1.6 eV used in this work. A higher vacancy formation energy reduces the thermal emission and makes the bubble to void transition occur at smaller sizes. However, even with the large variation of the calculated stable radii from the vacancy formation energy, shown in Table 6.9, the thermal barrier to void nucleation is still too wide to overcome at the low damage rates of reactor irradiation. With only variations of single

independent variables, there is no method for the roots of the cavity growth rate equation, r^* or r_v^*, to reach the experimentally observed valley in the cavity size distribution with the current understanding of the physical processes.

Table 6.9. Table with the impact of the high sensitivity of the vacancy formation energy on calculated radii for BOR-60 irradiations.

				$E_f^v = 1.5\ eV$		$E_f^v = 1.6\ eV$		$E_f^v = 1.7\ eV$	
Type of Irradiation	Temperature °C	Valley in cav. size dist. (nm)	$S_{E_f^v}^{\left(\frac{dr}{dt}=0\right)}$	r^*	r_v^*	r^*	r_v^*	r^*	r_v^*
BOR-60	376	2.0±0.25	27.4	> 50 nm	> 50 nm	38.6	> 50 nm	9.4	11.2
BOR-60	415	2.25±0.25	26.2	> 50 nm	> 50 nm	> 50 nm	> 50 nm	14.7	17.8

From the discussion of the Damage Rate Series in Section 6.2, helium accumulation to the critical bubble appears to be the only mechanism for void nucleation at low damage rates while spontaneous nucleation from vacancy fluctuation is active at high damage rates. Then, from the critical bubble model of void nucleation bubbles produced in reactor should be able to gather enough helium to overcome the thermal barrier and nucleate voids. To estimate the amount of helium needed per cavity, the growth rate equation was solved using several values for the amount of helium per cavity: 3 helium atoms per cavity representative of having all helium produced during irradiation equally divided among the observed bubbles from Eq. 6.8, 1000 helium atoms per cavity which is near the mechanical equilibrium limit for helium in 1 nm radius bubbles, and enough helium atoms (7.2×10^5 helium atoms/cavity) to have only one root r^* in the cavity growth rate equation. The growth rates for cavities as a function of cavity radius are displayed in Figure 6.20.

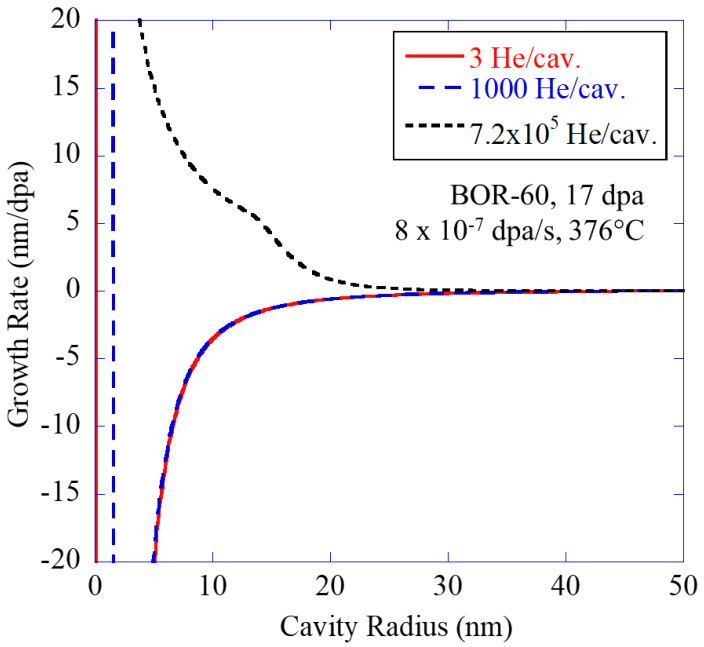

Figure 6.20. Solutions to the cavity growth rate equation using reactor irradiation conditions of 376°C, 8×10^{-7} dpa/s and the associated microstructure using three different helium concentrations per cavity.

With up to 1000 helium atoms per cavity, the second root r_v^* is greater than 50 nm and is physically unreasonable. Even with a large amount of helium to reach r^*, the root is about 38 nm. There is no physically reasonable amount of helium available from reactor irradiation to reach the critical bubble for void nucleation. Furthermore, the critical bubble radius of about 38 nm is nowhere near the experimental valley in the cavity size distribution. No reasonable variation in the vacancy migration energy, vacancy formation energy, surface energy, or amount of helium resulted in an agreement between the model and experiment. Therefore, homogenous nucleation through critical bubble model is not the mechanism of void nucleation in reactor irradiated T91.

The cavity growth rate equation and critical bubble model assume a homogeneous microstructure with a homogenized vacancy supersaturation. Cavities also nucleate on specific features in the microstructure, such as dislocations [212–214], precipitates [215–217], and grain boundaries [218] resulting in heterogenous nucleation not considered in the critical bubble model explicitly. Being an engineering alloy, T91 contains many microstructure features in the

normalized and tempered condition prior to irradiation such as a dislocation line network on the order of $10^{14} – 10^{15}$ m^{-2} in areal density. Recent work of Kohnert et al. [219] examined the spatial effect of the local strain field induced by dislocations on point defect absorption. For three-dimensional dislocation networks, the line direction and Burger's vector of each dislocation segment might arrange in a variety of orientations. When dislocations of opposite line direction interact, they can produce volumes where the local supersaturation of vacancies is higher than a homogenized case, which reduces the critical size necessary to nucleate voids. To estimate the number of these possible sites, the areal density can be converted to an estimated volume density by raising it to the three halves power, resulting in a volume density of about 10^{21}-10^{22} m^{-3}. Assuming the orientation of dislocation lines is randomized in the material, the density of sites is reduced by ½ to have pairs of dislocation lines, reduced by another ½ assuming the directions can be either towards or away from the nearest line, and reduced by another 1/3 for the three dimensional nature of the line network. From these assumptions, the density of local supersaturation sites is on the order of 10^{20}-10^{21} m^{-3}. This estimation is the same order of magnitude as the density of voids in the BOR-60 irradiated T91 (about 7×10^{20} m^{-3}). Local heterogenous nucleation of voids is likely responsible for producing the vacancy supersaturation needed for void nucleation.

6.3.2 The Agreement of Reactor and Dual Ion Irradiation across Damage Rates

Despite the differences in void nucleation mechanisms, as well as irradiation parameters (damage rate, temperature, helium injection rate), dual ion irradiation and BOR-60 irradiation were able to achieve similar cavity size distributions at 17 dpa and 35 dpa, shown in Figure 6.21 for convenience. The reason is the importance of heterogeneous void nucleation in the reactor case and that the choice of ion irradiation parameters resulted in the same helium trapping-detrapping

ratio as in reactor. There are three major irradiation parameters that change between these matching cases: damage rate, temperature, and helium injection rate. The relationship between damage rate and temperature for cavities is fairly well understood [73,220–222]. As the damage rate increases, the temperature must be increased to avoid an increase in point defect recombination. The shift from 376°C to 445°C from reactor to ion irradiation follows this idea when increasing the damage rate. However, an increase in the helium co-injection rate was also needed to match ion irradiation to reactor irradiation.

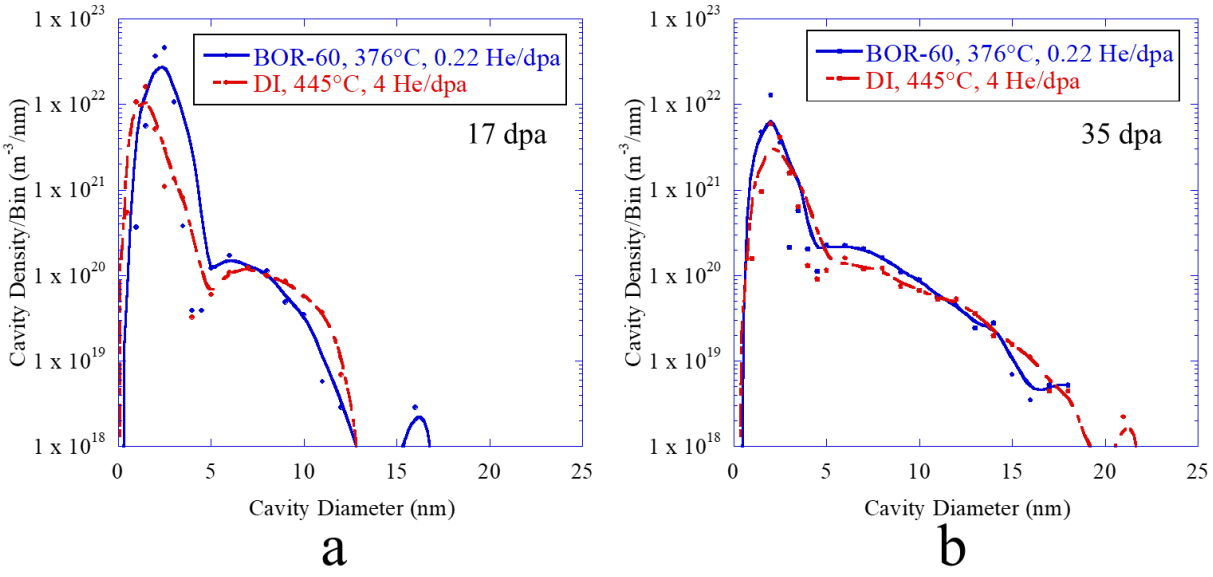

Figure 6.21. Comparison of the cavity size distributions for T91 irradiated in the BOR-60 reactor to 17.1 dpa with about 8×10^{-7} dpa/s at 376°C with 0.22 appm He/dpa and dual ion irradiated to 16.6 dpa at 445°C with 4 appm He/dpa at 7×10^{-4} at (a) 17 dpa and (b) 35 dpa.

To compare the role of helium on void nucleation between ion and reactor irradiation, the helium trapping-detrapping rate equations in Eq. 6.12 and Eq. 6.13 were solved for the two cases where the cavity and dislocation microstructure were found to be experimentally identical: dual ion irradiation to 16.6 dpa at 445°C with 4.34 appm He/dpa and BOR-60 irradiation to 17.1 dpa at 376°C with 0.22 appm He/dpa. Additionally, the ion irradiation with the same He/dpa as BOR-60 is included. The time dependent solutions are displayed in Figure 6.22, combining Figure 6.5 and

Figure 6.20. The sink strengths from the characterized microstructure were included as static, time independent features with binding energies of 1.0 eV for dislocation lines, 2.3 eV for dislocation loops and 3.6 eV for bubbles.

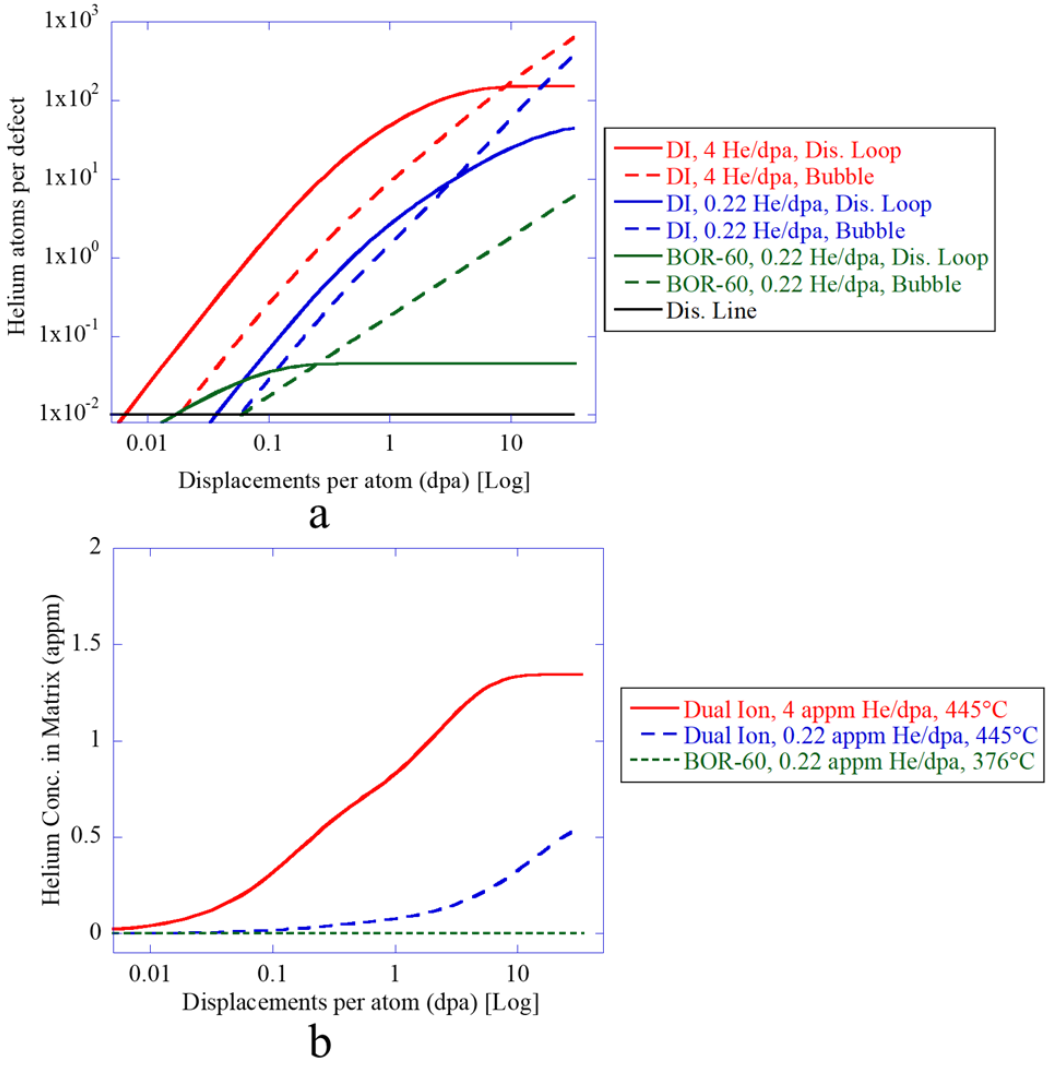

Figure 6.22. Solutions to a trapping-detrapping process consisting of dislocation loops, bubbles, and dislocation lines showing a) the concentration of helium in the matrix, and b) the number of helium atoms per defect as a function of displacement per atom.

The fate of helium calculated in Figure 6.22 shows the behavior for reactor and ion irradiation. In all cases shown in Figure 6.22, the dislocation lines saturate with helium quickly as these features have the lowest binding energy for helium. With ion irradiation, the dislocation

loops and bubbles quickly begin to accumulate helium. The amount of helium in dislocation loops reaches a steady state at about 3 dpa and helium continues to flow to bubbles beyond this point. However, in the reactor irradiation, the dislocation loops saturate with helium and the bubbles overtake the dislocation loops by 0.2 dpa, about an order of magnitude earlier. At 17 dpa, there is about two orders of magnitude more helium in bubbles in reactor than with dual ion irradiation. The increased helium injection rate per second with ion irradiation results in more helium trapped at dislocation loops relative to reactor irradiation. Both reactor and ion irradiation have the dominant trap for helium transition between microstructure features based on the binding energy of helium in the order of weakest to strongest traps.

To examine the differences in helium trapping between reactor and ion irradiation further, the ratio of helium arriving at the defect and helium thermal detrapping is calculated for a microstructural feature, i, using:

$$\left(\frac{He\ trapping}{He\ detrapping}\right)_i = \frac{\frac{k_i^2 D_{He} C_{He}}{N_i \Omega}}{n_g^i \nu_0 \exp\left(\frac{-E_b^i}{kT}\right)} \qquad \text{Eq. 6.21}$$

with the same parameters and calculations as Eq. 6.12 and Eq. 6.13. The helium trapping-detrapping ratio for dislocation loops and cavities can be displayed as a function of displacement damage (Figure 6.23 and Figure 6.24a) or time (Figure 6.24b) comparing BOR-60 irradiation and the Damage Rate Series of dual ion irradiations.

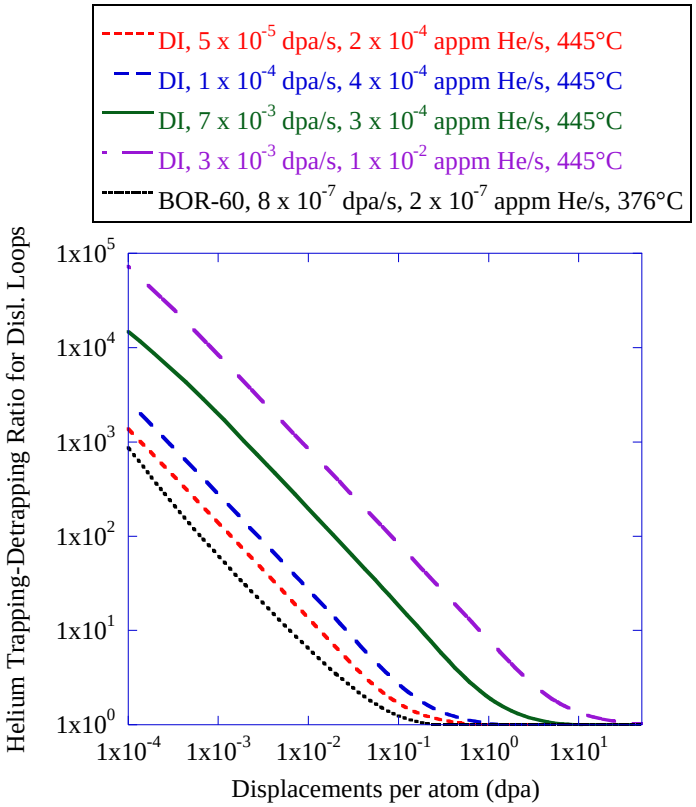

Figure 6.23. Solutions to the helium trapping-detrapping ratio as a function of displacement damage for BOR-60 irradiation and the Damage Rate Series of dual ion irradiations for dislocation loops.

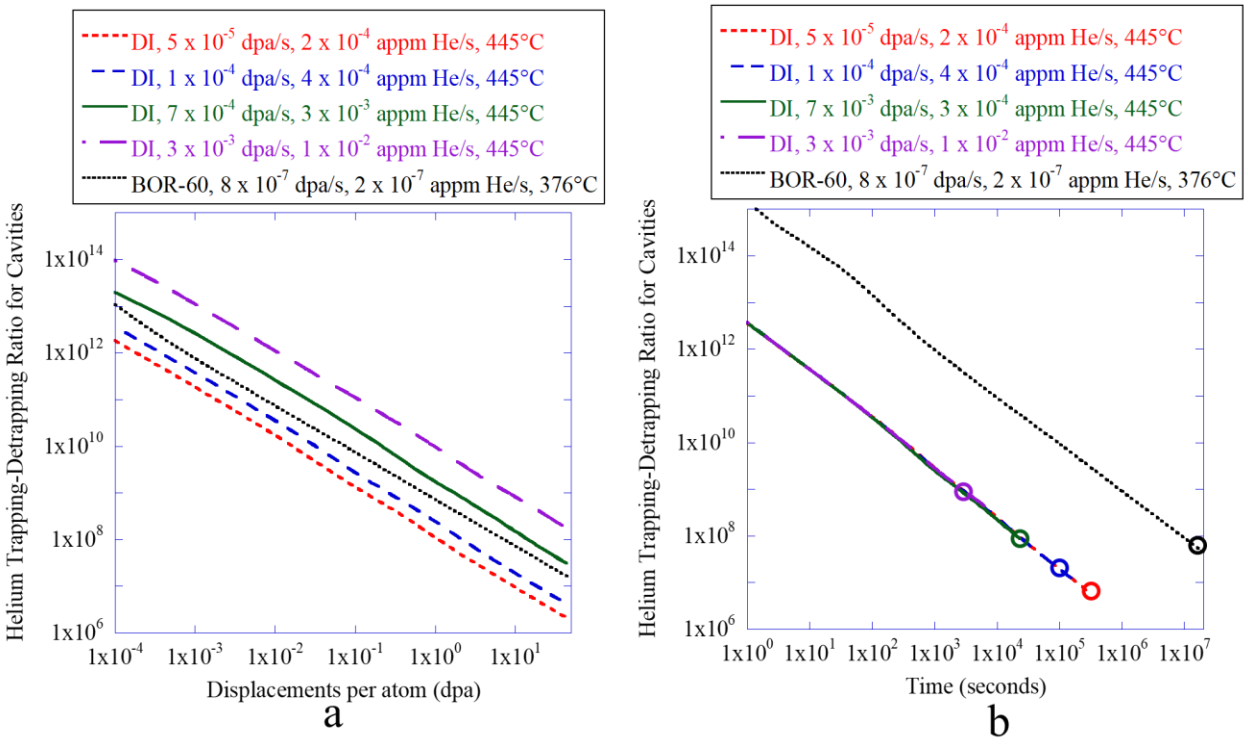

Figure 6.24. Solutions to the helium trapping-detrapping ratio for cavities as a function of (a) displacement damage and (b) time for BOR-60 irradiation and the Damage Rate Series of dual ion irradiations The open circles represent 17 dpa at each damage rate.

The helium trapping-detrapping ratios with time are independent from the damage rate (Figure 6.24b). The difference in trapping behavior is solely dependent on the time and temperature through the diffusion of helium and thermal detrapping rate. From Figure 6.23, the BOR-60 irradiation reaches steady state helium trap and release rates at dislocation loops at lower dpa compared to any of the dual ion irradiations. However, because of the lower temperature, the detrapping rate is lower meaning it takes more time to reach this steady state with reactor irradiation. The dual ion irradiations, thus, accumulate more helium at dislocation loops compared to reactor. The trapping ratio of helium at cavities is much higher for BOR-60 irradiation at all irradiation times (Figure 6.24b). However, the trapping ratio is the same at 17 dpa for the conditions where the cavity microstructures matched. The increased helium retention at cavities with time in BOR-60 and increased helium retention at dislocation loops in ion irradiation needs

to be offset with a higher helium injection rate during ion irradiation at a higher temperature to achieve the same ratio of helium trapping and releasing from cavities (Figure 6.25b).

From the discussion thus far, a conclusion can be drawn on why the cavity size distributions were matched with dual ion irradiation with an increase in temperature, helium injection rate, and damage rate relative to reactor irradiation. The bubble nucleation rate decreases with increasing damage rate through the increased point defect recombination [73,220–222] and decreased helium per cavity (Figure 6.13). The bubble nucleation rate decreases with temperature through an exponential reduction in helium trapping relative to detrapping (Eq. 6.21 and Figure 6.24) with a smaller increase through the increased vacancy absorption (Figure 6.7) and increases with helium injection rate (Figure 5.13) through the helium gas pressure (Eq. 6.4). The void nucleation rate through the promotion of bubbles in the critical bubble model decreases with increasing damage rate through the decreased helium per cavity (Figure 6.15), decreases with temperature through a reduction in helium trapping relative to detrapping (Eq. 6.21 and Figure 6.24) and increase in thermal emission of vacancies (Figure 6.7), and increases with helium injection rate from the combination of Figure 6.5 and Eq. 6.21. Thus, an increase in the helium injection rate was needed to compensate for the temperature and damage rate. The combination of helium trapping behavior and heterogeneous nucleation in reactor are likely responsible for the match in the cavity size distributions between reactor and dual ion irradiation despite the dual ion irradiation following homogenous void nucleation mechanisms at a higher temperature and damage rate.

Chapter 7: Conclusions

This chapter presents the significant conclusions drawn from the results presented in Chapter 5: and the discussion in Chapter 6: . The conclusions first focus on addressing the objective proposed in Chapter 3: : **To determine the mechanisms that control cavity nucleation in dual ion irradiated T91 steel over a range of temperature, helium injection rates, and damage rates**. Additionally, several other conclusions were drawn.

- The bubble nucleation rate decreases with increasing damage rate through the increased point defect recombination, decreases with temperature through a reduction in helium trapping relative to detrapping, and increases with helium injection rate.
- The void nucleation rate through the promotion of bubbles in the critical bubble model decreases with increasing damage rate through the increased point defect recombination, decreases with temperature through a reduction in helium trapping relative to detrapping and reduction in vacancy supersaturation, and increases with helium injection rate.
- The mechanism of bubble to void transition shifts from being driven by the accumulation of helium to the critical bubble at low damage rates to being driven by stochastic vacancy fluctuation at high damage rates.
- Both reactor and ion irradiation have the dominant trap for helium transition between microstructure features based on the binding energy of helium in the order of weakest to strongest traps.

- The homogeneous cavity growth rate equation, and by extension the critical bubble model, was unable to predict or replicate void nucleation in reactor irradiated T91.
- Local heterogenous nucleation of voids is likely responsible for producing the vacancy supersaturation needed for void nucleation in reactor irradiated T91.
- The combination of helium trapping behavior and heterogeneous nucleation in reactor are likely responsible for the match in the cavity size distributions between reactor and dual ion irradiation despite the dual ion irradiation following homogenous void nucleation mechanisms at a higher temperature and damage rate.

Chapter 8: Future Work

The results and findings of this dissertation provided insight into the roles of temperature, helium co-injection rate, and irradiation damage rate on cavity nucleation. However, there are many unanswered questions and areas which merit further study.

The effect of helium on the transition to growth dominant swelling. In this work, only one level of displacement damage was examined with single independent variable changes to determine cavity nucleation mechanisms. As the amount of radiation damage is increased, the microstructure will continue to evolve with the growth of voids, additional nucleation of bubbles, and possibly the formation of radiation induced precipitates. At high levels of damage, the sink strength of the cavities is expected to increase and become balanced with the remaining sinks in the microstructure. Tracking this sink strength evolution against the continued nucleation and growth of cavities will provide insight into how the bubbles nucleated at low damage levels influence the microstructure over the lifetime of a component.

The role of heterogeneous nucleation on cavity nucleation. In this work, much of the analysis considered a homogeneous critical bubble model as the primary nucleation mechanism at high damage rates. In reactor relevant damage rates, however, the roles of precipitate-matrix interfaces, dislocations, and solute impurities are likely to play a larger role in cavity nucleation. The heterogenous nucleation sites are expected to lower the barrier for bubbles to transition to unstably growing voids and will be relevant at lower vacancy supersaturation values, such as those for reactor irradiation. Additional studies on other possible nucleation sites for cavities and the spatial heterogeneity of the microstructure need to be performed.

The effects of hydrogen implantation on cavity nucleation. In this work, helium was considered as the primary gas atom responsible for the nucleation and stabilization of cavities. However, in reactor, hydrogen is produced through (n,p) reactions and can also serve to nucleate cavities through the formation of H_2 gas inside a vacancy cluster [223,224] or through chemical bonding between the alloying elements and hydrogen. Additional dual ion irradiations using iron ions and hydrogen co-implantation can isolate the role of hydrogen on cavity nucleation. Furthermore, hydrogen gas accumulation with helium gas accumulation appears to have a synergistic effect on cavity growth that is poorly understood [225–228]. Triple ion beam irradiations with iron ions, helium co-injection, and hydrogen co-injection simultaneously will assess the roles of these gases on cavity nucleation in an environment closer to reactor irradiation.

Appendices

Appendix A - Temperature Histograms

As the results, discussions, and conclusions partially depend on the irradiation temperature, the temperature histograms for each irradiation performed for this thesis are presented in this appendix.

Temperature Series

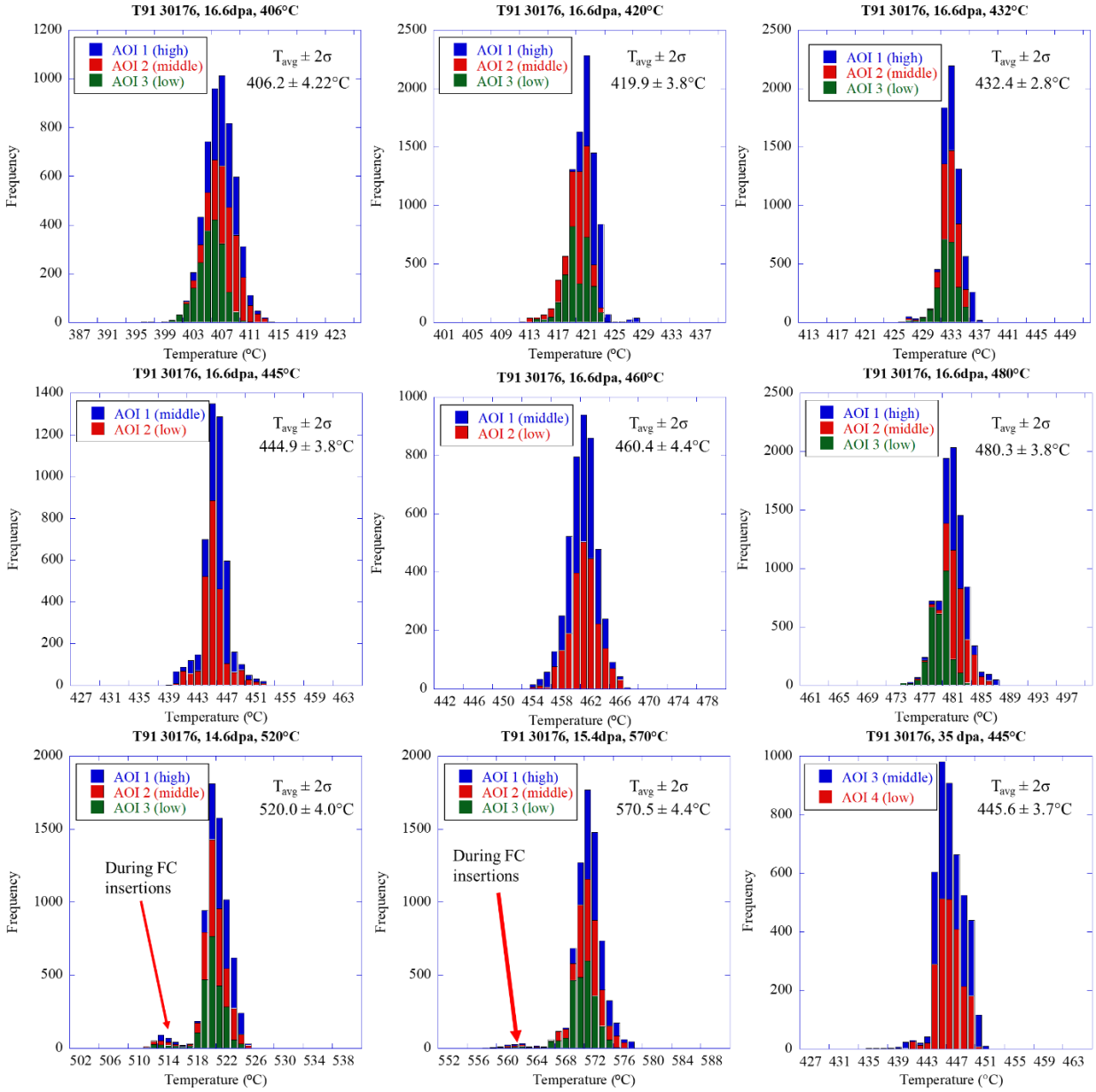

Figure A.1. Temperature histograms for temperature series of ion irradiations on T91 heat 30176 to 16.6 dpa with 5 MeV Fe^{2+} ions and energy degraded He^{2+} ions with 4 appm He/dpa and damage rates of 5-8 × 10^{-4} dpa/s.

Helium Rate Series

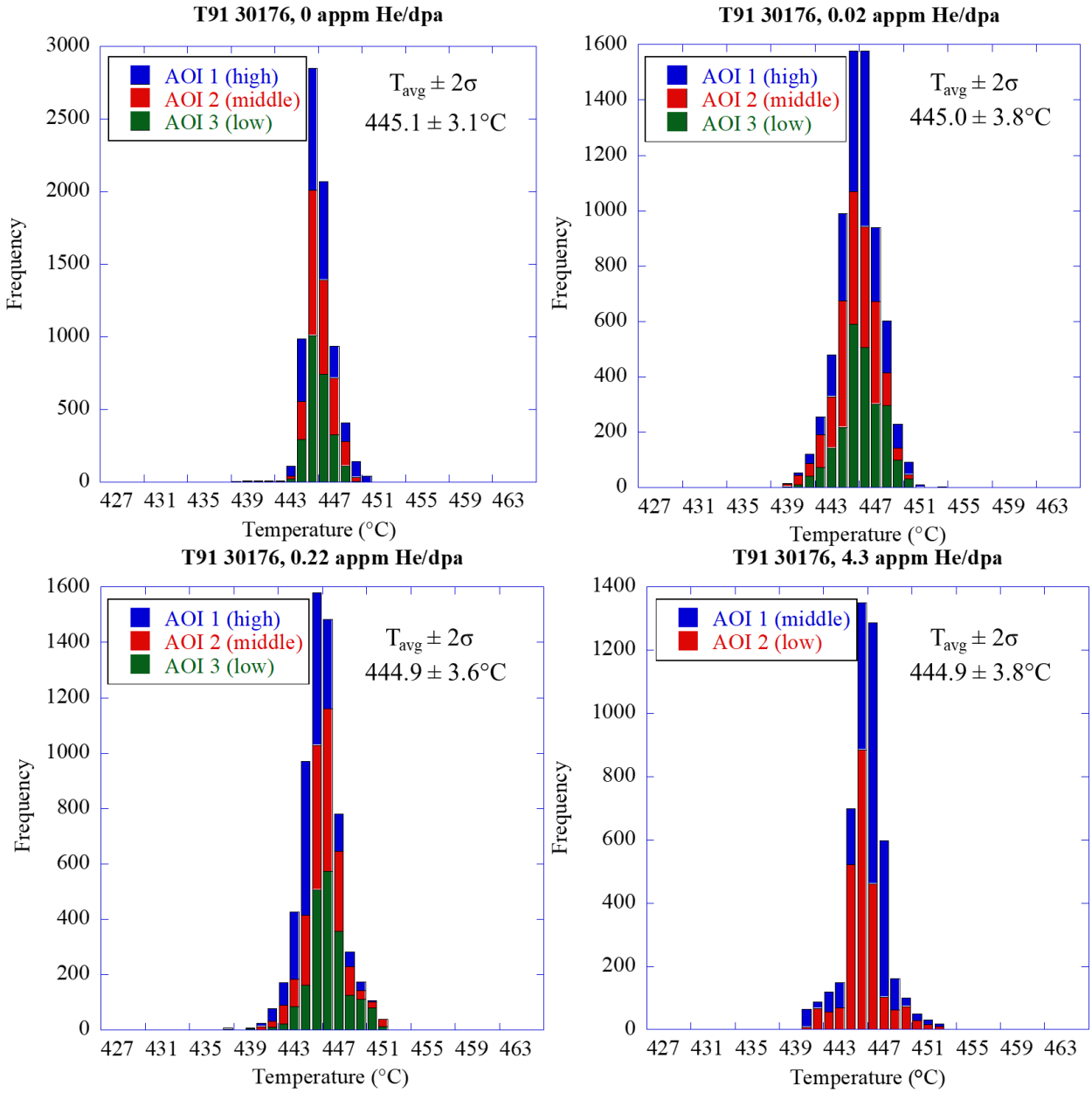

Figure A.2. Temperature histograms for helium rate series of ion irradiations on T91 heat 30176 to 16.6 dpa with 5 MeV Fe^{2+} ions and energy degraded He^{2+} ions at 445°C and damage rates of 7-8 × 10^{-4} dpa/s.

Damage Rate Series

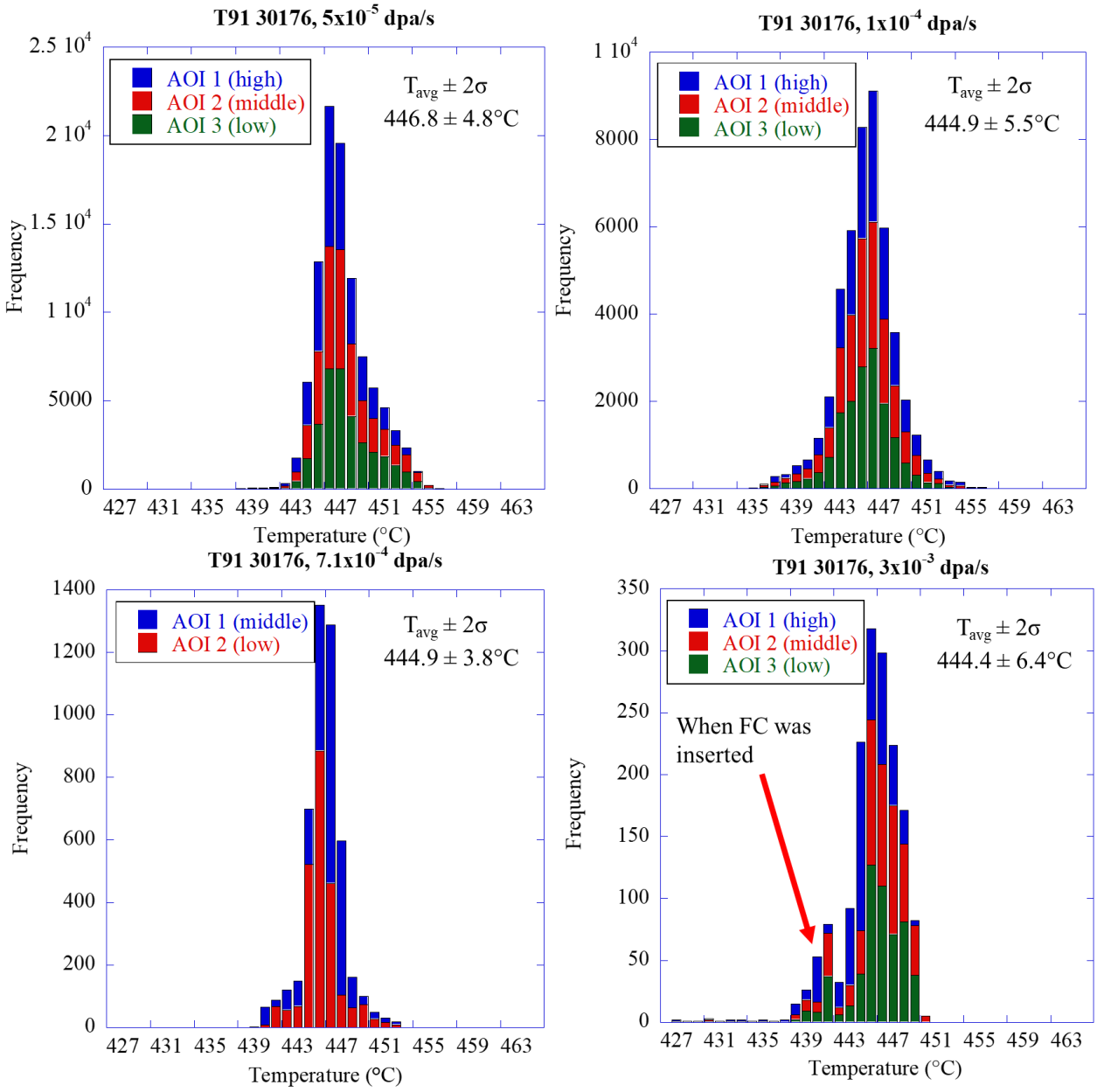

Figure A.3. Temperature histograms for damage rate series of ion irradiations on T91 heat 30176 to 16.6 dpa with 5 MeV Fe^{2+} ions and energy degraded He^{2+} ions at 445°C with 4 appm He/dpa.

Appendix B - Benchmarking Helium Injection Through a Thin Foil Energy Degrader

As the results, discussions, and conclusions depend on the helium injection rate, the methodology and benchmarking experiments to validate the physics of a rotating thin foil energy degrader are presented in this appendix. Portions of this appendix have been published as an article [148] and repeated here for reference.

A thin foil energy degrader can distribute light ions in a sample across the ion implantation range using a mono-energetic ion beam. A common method of controlling the light ion distribution in the target is to use multiple foils with different thicknesses on a rotating wheel [229]. The implantation profile will have localized peaks based on the thickness of the foils used in the wheel. A second method uses a single foil rotated in front of the beam [230]. The foil is rotatable to increase the electronic energy loss and scattering of the beam by changing the path length of the ion beam through the foil. By controlling the time spent at each angle during rotation, the depth of implantation can be manipulated to form any concentration profile of interest to the user. This work presents the description of a detailed computational methodology for a rotating thin foil energy degrader for use with monoenergetic MeV light ion beams. The effects of energy loss, scattering, and raster scanning are considered for calculation of the energy-degraded ion beam flux and fluence. Experiments to benchmark and validate the methodology are presented as a proof-of-concept. The holder consists of a stainless-steel frame that secures a thin foil using a crimp, shown in Figure B.4 containing a 2.6 μm thick Al foil. The holder was attached to a rotatable feedthrough and controlled with a programmable stepper motor capable of rotating in 0.01° increments. A

custom program written in LabVIEW^{TM} was developed to control the rotation of the foil from 0° to 60° degrees of rotation in both clockwise and counterclockwise directions.

Figure B.4. The thin foil energy degrader used at the Michigan Ion Beam Laboratory for control of the implantation range of a light ion beam during multi-ion irradiation through foil rotation. The holder is shown with a 2.6 μm aluminum foil loaded and held taut by a crimp inside the holder frame.

As the foil is rotated to increase electronic loss, the spatial flux profile also changes. To assess the ion flux as a function of both position and energy, a simple calculation method was developed using Stopping and Range of Ions in Matter (SRIM-2013) [149]. Ions enter a foil of known thickness with known ion energy, E_0, and at a foil angle of θ_0. An assumption is made that the ions are perfectly focused going into the foil as a standard input to SRIM. SRIM was then run to provide distributions in energy, position, and direction of the ions exiting the foil using the Transmit.txt output file option. One hundred thousand ions were used as an input to provide a large sample size for the resulting distributions.

To develop accurate spatial distributions of ions using SRIM, the thickness of the thin foil must be known. The foil thickness was measured using several methods: direct measurement with a micrometer, Rutherford Backscattering (RBS) of the foil placed on a carbon substrate, and by measuring the transmission of the ion beam current through the thin foil. To demonstrate these measurements, aluminum foils of 99.0%+ purity and varying thicknesses obtained from Goodfellow Inc. were used for all the experiments described in this work. RBS was used with a 988 keV proton beam with a detector at 160° to calculate the thickness of the aluminum foil using SimNRA [231] to match the front and back edges of the aluminum signal. The transmission through the foil was measured by taking the ratio of current in a suppressed Faraday cup before the foil and a suppressed Faraday cup after the foil in the multi-beam chamber for a deuterium ion beam in an energy range from 600 keV to 900 keV in 20 keV increments. The calculated transmission profile was estimated using SRIM to determine the ratio of ions expected at the Faraday cup. Thickness measurements using three different techniques were in good agreement; 2.4 ± 0.5 μm by micrometer, 2.6 ± 0.1 μm using transmission of the ion beam, and 2.58 ± 0.02 μm by RBS, Figure B.5.

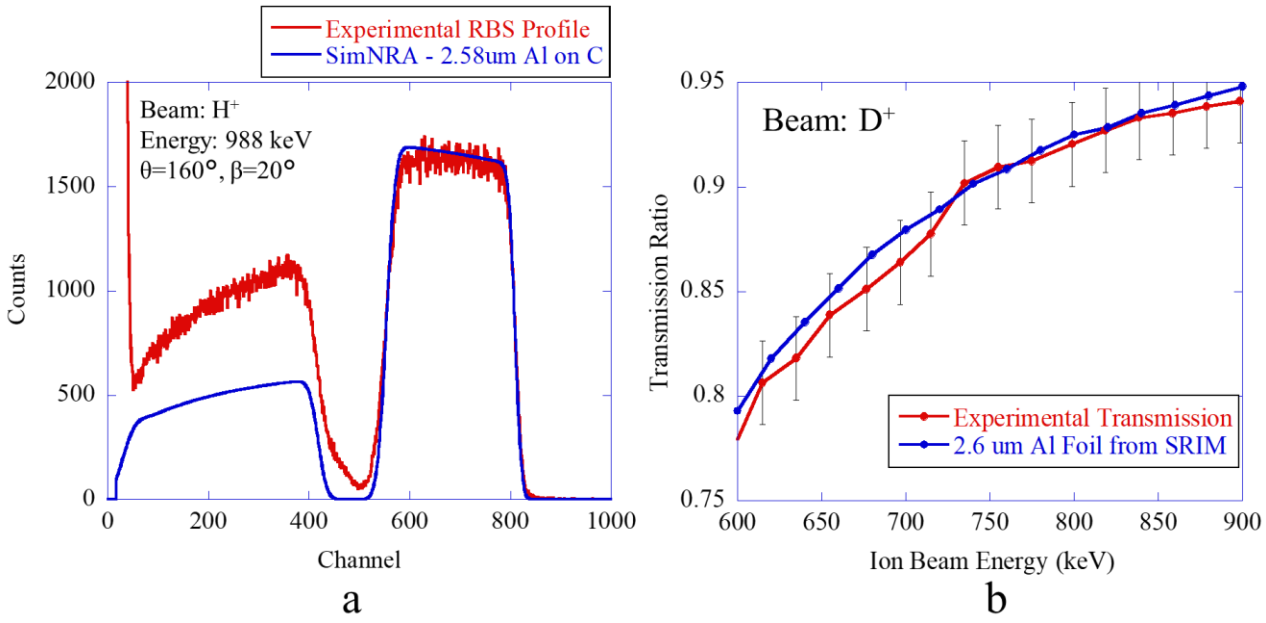

Figure B.5. Comparison between thin foil thicknesses measured with RBS (a) and transmission of an ion beam (b). As the foil thickness controls the amount of energy loss and scattering, the thickness measurement is done with multiple techniques to determine the thickness within ±0.1 µm.

Using the measured thickness of the aluminum foil, SRIM was used to calculate the energy, E, position vector in three dimensions, $\boldsymbol{r}$, and direction vector, $\boldsymbol{\varphi}$, in three dimensions for each ion exiting the foil and for each angle of foil rotation, $\boldsymbol{\theta}$, in one degree increments. Individual ions were then propagated from the foil to the sample surface following the direction vectors calculated with SRIM without any additional forces to alter the beam trajectory (Figure B.6). This resulted in a "plume" of ions forming a curved distribution. To ensure an even distribution of ions across the sample surface, the effects of raster scanning the beam were considered. The plume of ions was copied and added to itself with a small change (1 mm) in the raster scanned direction. This process was repeated until the entire raster scanned distance along the x and y directions of scanning were covered. The same variation in position would be used for a defocused ion beam passing through the foil and would be used for this simulation. The position and direction of each ion were then rotated to match the geometry between the ion beam's original direction and the irradiation stage. For the multi-beam setup used in this thesis, the light ion beams impinge on the sample surface at

60° to the normal of the stage surface. SRIM was used after this geometric adjustment to calculate the implantation distribution of the energy degraded ions for each angle of foil rotation. Although the foil can rotate to higher angles beyond 60°, the increased amount of scattering from the apparent thickness significantly reduces the ion beam current density at the irradiation stage and makes these angles impractical for multi-ion beam irradiations.

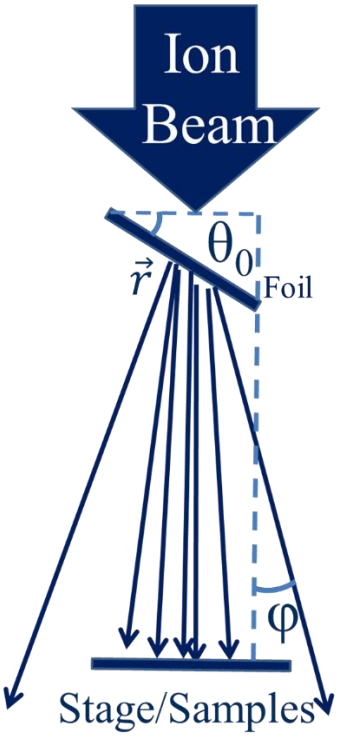

Figure B.6. A schematic of the foil degrader geometry considered for SRIM based calculations based on the foil rotation angle, $\boldsymbol{\theta}$, position of the ions after degradation, $\boldsymbol{r}$, and direction of ions from the original direction, $\boldsymbol{\varphi}$.

To determine the implantation depth profile of a rotating foil energy degrader and the dosimetry of scattered and energy degraded ions, a methodology was developed. A brief overview of this methodology/technique is described in [148]. Our methodology used to calculate the energy degradation and scattering of ions is shown as a flowchart in Figure B.7. The methodology can be broken down into the calculation of three physical phenomena. First, ions enter a foil of known thickness with known ion energy, E_0, and an incident angle of θ and exit the foil with a position

vector $\vec{r}$ and direction vector $\vec{\varphi}$. Second, the ions transverse through the vacuum following a straight line until the ions arrive at the Faraday cup (FC) or at the sample a certain distance away from the foil. Finally, ions implant into the sample based on its surface area.

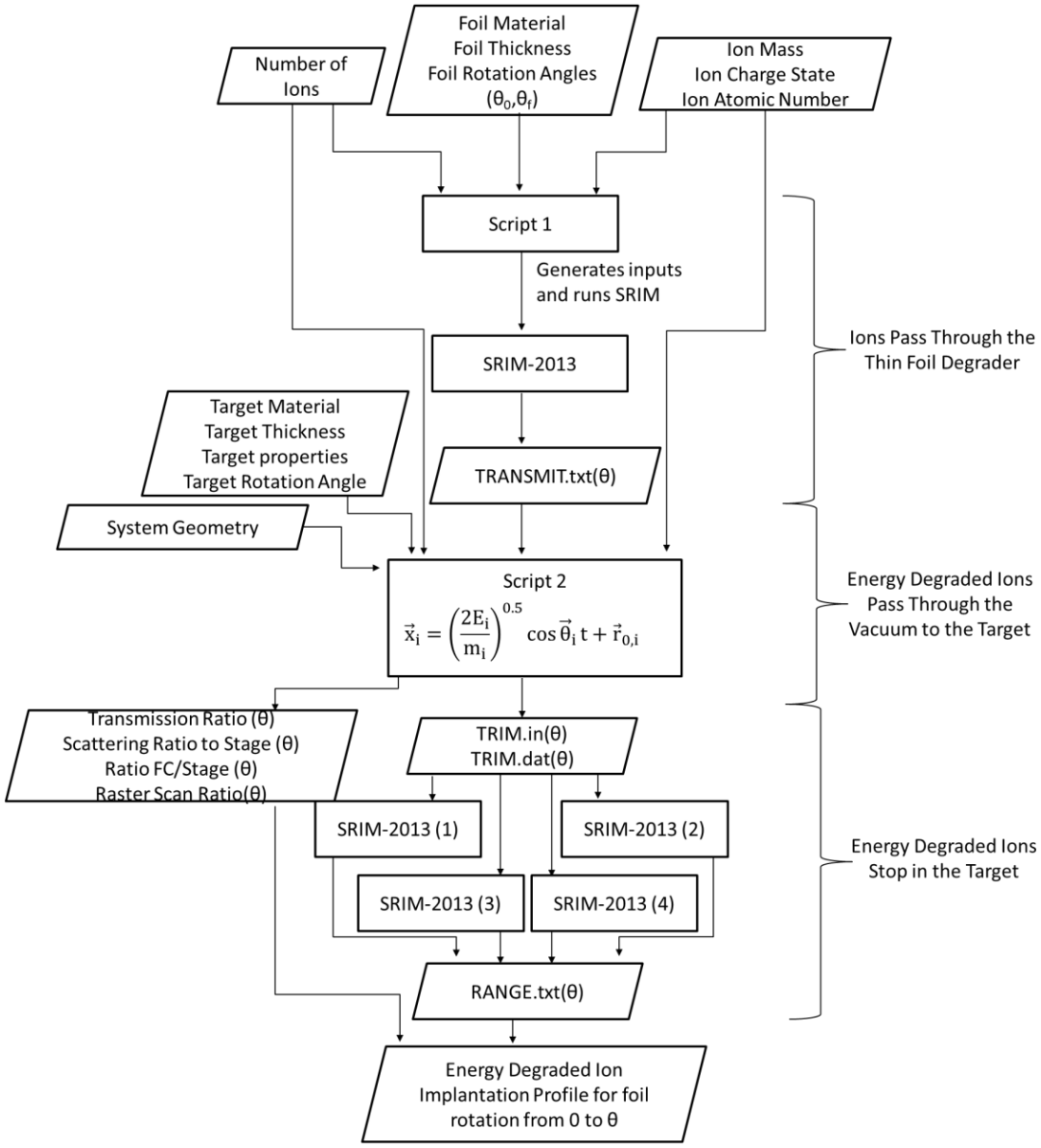

Figure B.7. A flowchart of the computational methodology used to calculate the energy degradation, scattering, and implantation of light ions with a thin foil energy degrader.

The first section of the methodology addresses what happens to the ions in the thin foil. The script takes as input the mass of the light ion in amu, the initial positive charge state of the

ion, the atomic number of the light ion, the total number of ions for the calculation, the foil material, the foil thickness, the initial angle of foil rotation θ_0 typically 0°, the final angle of foil rotation θ_f, and the rotation steps between θ_0 and θ_f. From these parameters, the script generated TRIM.in files for each angle of foil rotation and ran them in the Stopping and Range of Ions in Matter (SRIM-2013 [149]) program by calling the TRIM.exe executable. The resulting output is a TRANSMIT.txt file for each foil rotation angle, θ, containing the energy, position vector, and direction vector for each transmitted ion. In this calculation it is assumed that all the ions start at the origin before they interact with the foil. This assumption will be addressed in the next calculation section.

The second section of the methodology concerns how the direction and position of the ions leaving the foil travel through the vacuum to the FC and sample. This script takes as input the TRANSMIT.txt files, the ion mass, the atomic number of the ions, the target material composition, the target thickness, the target properties (such as the displacement energy, lattice binding energy, and surface energy), and the sample angle relative to the initial ion beam direction. Additionally, the geometry of the system such as the distances from the foil to the sample, the foil to the Faraday cup, and between the Faraday cup and the sample, the opening of the Faraday cup, and the target surface area are inputs to this section of the methodology. After reading in the TRANSMIT.txt file, the ions are translated across the vacuum using Eq. B.1 and a timestep of one picosecond until the distance between the Faraday cup is reached. The number of ions inside the circular opening of the Faraday cup is calculated and stored. Then, the ions are propagated again using Eq. B.1 until the ions reach sample. At this point, the energy, position, and direction of each ion hitting the desired surface area on the sample are tallied. The ion scattering becomes significant with increased foil rotation angle. The calculated ion distributions for a 2.1 MeV helium ion beam

passing through a nominally 3 foil is displayed in Figure B.8. The distance from the foil to the samples is 26 cm.

$$\vec{x}_i = \left(\frac{2E_i}{m_i}\right)^{0.5} \cos \vec{\varphi}_i \, t + \vec{r}_{0,i} \qquad \text{Eq. B.1}$$

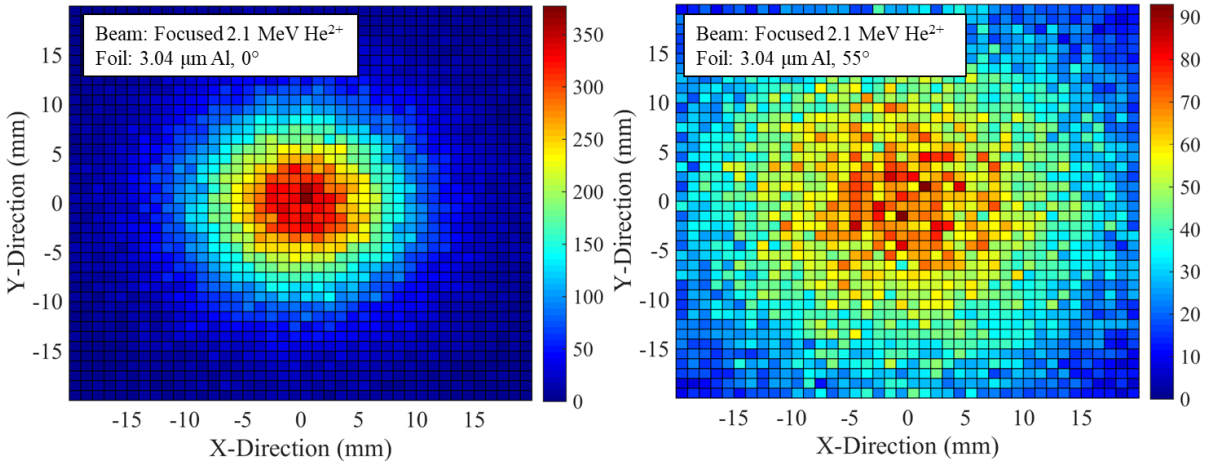

Figure B.8. Heat maps showing the distributions of energy degraded helium ions after travelling 26 cm in vacuum for the foil held at 0° and 55°.

From the ratio of the number of ions in the TRANSMIT.txt file and the initial input ions, a transmission ratio is obtained as a function of foil rotation angle, $R_{Tr}(\theta_i)$. The ratio of the ions hitting the sample to the initial number of ions in the initial SRIM calculation is also obtained as a function of rotation angle, $R_{St}(\theta_i)$. Finally, the number of ions at the Faraday cup and the number of ions hitting the desired surface area on the target stage are given in a ratio as a function of foil angle, $R_{FC-St}(\theta_i)$. The position and direction of each ion were then rotated to match the geometry between the ion beam's original direction and the irradiation stage. The energy, position, and direction of ions hitting the target are then compiled with the target material composition and properties to generate a TRIM.in for the target and TRIM.dat for the energy degraded ions as a function of foil rotation angle. To obtain smooth implantation profiles, the ions hitting the target surface are copied and compiled with itself if there are less than fifty thousand ions in the TRIM.dat

file. To assess the distribution of ions across the sample surface, the effects of raster scanning the beam were included in the calculation. To do that, the ion distribution was copied and added to itself with a small change (1 mm) in the raster scanned direction. This process was repeated until the entire raster scanned distance defined by slit apertures in the beamline along the x and y directions of scanning were covered. The raster scanned distribution was then normalized by the total number of ions in the distribution. The ratio of ions hitting the target surface with raster scanning to the ratio of ions hitting the target surface without raster scanning is quantified as a reduction in intensity of the ion beam as a function of foil rotation angle, $R_{Rs}(\theta_i)$. An example of the dependence of $R_{St}(\theta_i)$ and $R_{Rs}(\theta_i)$ on the foil rotation angle is included in Figure B.9.

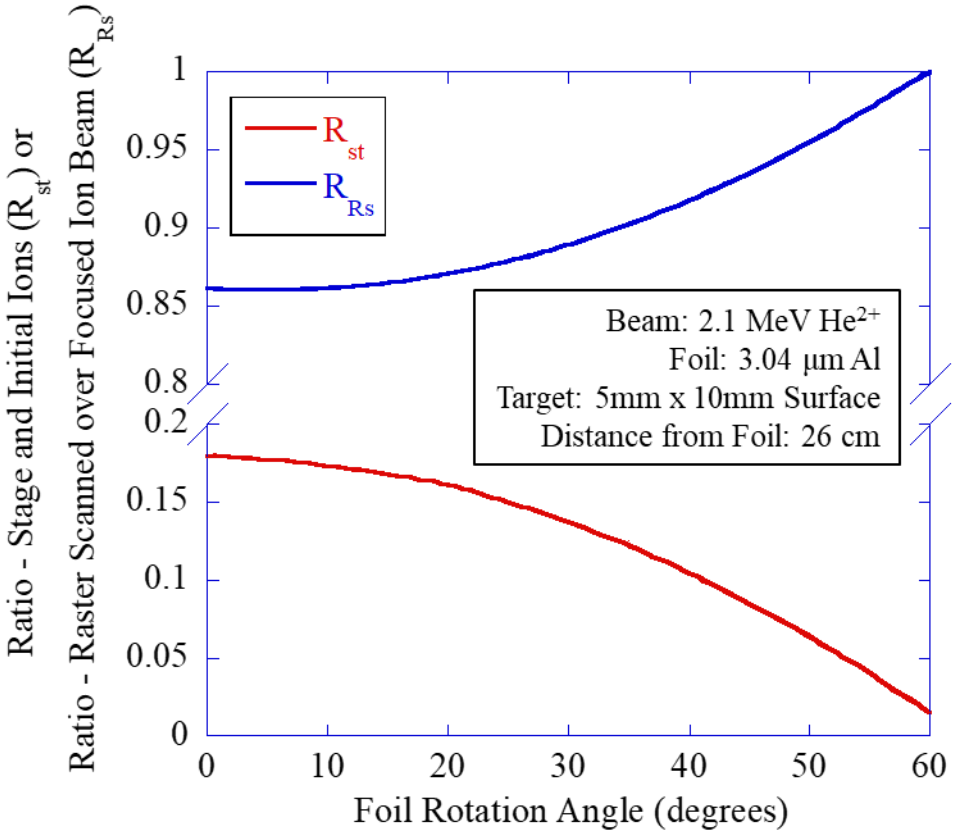

Figure B.9. An example of the dependence of the ratio of the ions hitting the target stage to the initial number of input ions, $R_{St}(\theta_i)$, and ratio of ions hitting the target surface with and without raster scanning $R_{Rs}(\theta_i)$.

The final section of the methodology address what happens as the ions come to rest in the target material. The TRIM.in and TRIM.dat generated by the previous section are divided among four copies of SRIM-2013 and run in a pseudo-parallel manner to reduce the computation time. The resulting output is the RANGE.txt implantation file as a function of foil rotation angle and distance from the surface, $I(x, \theta_i)$. The full implantation profile for a foil degraded beam is calculated using Eq. B.2 with the ion flux before the foil degrader and N as the density of atoms in the target material.

$$P(x) = \sum_{\theta_i=0^\circ}^{\theta_f} \frac{I(x,\theta_i)}{N} \frac{t_{\theta_i}}{\sum_{\theta_i=0^\circ}^{\theta_f} t_{\theta_i}} * R_{Tr}(\theta_i) * R_{St}(\theta_i) * R_{Rs}(\theta_i) * Ion\ Flux \qquad \text{Eq. B.2}$$

The remaining term in this equation is the time spent at each angle of rotation, t_{θ_i}. This is a user defined parameter and alters the relative contribution of an individual rotation angle to the final implantation profile. The time coefficient is the independent parameter to determine the overall shape of the implantation profile and controlled via a stepper motor external to the vacuum system and a rotatable feedthrough.

By measuring the position of the ions in the plane normal to the beam direction, the position and directional components of the calculations were assessed. To assess the position and direction experimentally, a 3 MeV He^{++} ion beam focused to a Full Width Half Maximum (FWHM) of 2 mm was passed through a 2.6 μm thick aluminum foil oriented perpendicular to the ion beam. An experimental setup consisting of a 1 mm diameter miniature suppressed Faraday cup faced the ion beam at 26 cm from the foil. The current was measured along x and y directions in 1 mm increments over a 25 mm travel distance in each direction to obtain the flux distribution. The experimental and computational beam intensity profiles are shown in Figure B.10. The overall shapes are in excellent agreement. The relative intensity to the center peak was calculated to provide a comparison point between the ion beam current measured experimentally, and the

number of ions used computationally in the SRIM based method described previously. The experimental profile was found to be wider than the computational profile, but this is expected. The experimental profile was derived from a 2 mm FWHM beam and the computational profile assumed a perfect line of ions. The difference in FWHM between the profiles was approximately 2 mm, likely resulting from this assumption.

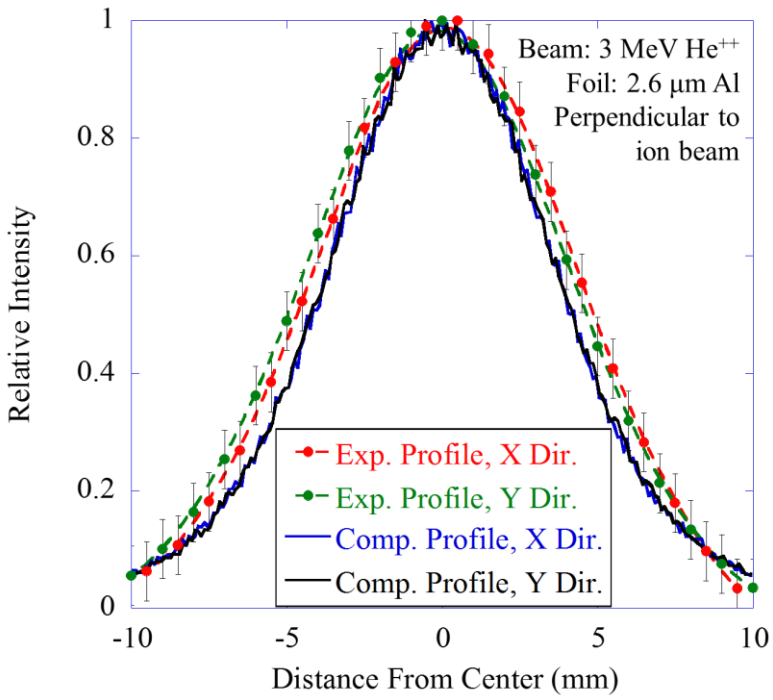

Figure B.10. Comparison between experimental and computational beam profiles for a foil held perpendicular to a light ion beam showing excellent agreement in the shape of the helium ion beam after passing through a thin aluminum foil.

Although the rotation of the foil is used primarily to control the energy loss of the ions, the relative amount of scattering in the foil must also be measured as a function of rotation angle to quantify effects of rotation on the beam current. Using a 3.0 MeV He^{++} ion beam in both focused (2 mm FWHM) and raster-scanned conditions, the intensity of the ion beam relative to the focused beam was measured and compared to the computed intensity expected using SRIM. As shown in Figure B.11 for both beam conditions, the peak intensities were in good agreement with foil rotation. From the measurement of the shape of the profile (Figure B.10) and the relative intensity

loss during rotation (Figure B.11), the results from SRIM were found to adequately assess the direction, position and intensity of a thin foil degraded light ion beam. Because of the reduction in beam intensity with increasing rotation angle, achieving a uniform implantation profile requires the foil to be held for a longer time at the higher rotation angles. Between 0° and 30°, the loss in beam intensity from scattering is not significant and each angle can be rotated through quickly. For degrader angles greater than 30°, the time required to the same implanted ion concentration at each angle increases, for example for a hold time of 1 s at 30°, the hold times at 45°, 53°, 56°, and 60° are 30 s, 140 s, 150 s, and 500 s. respectively. However, Faraday cup measurements and profiling could not include an assessment of the energy of the degraded light ions.

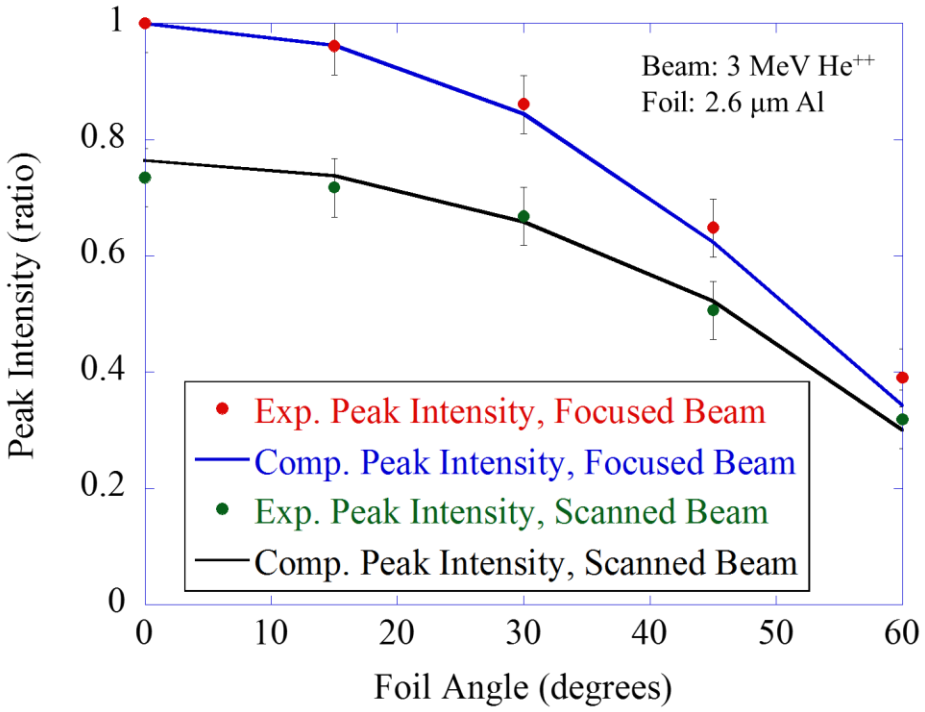

Figure B.11. Comparison between experimental and computational beam profiles for a foil held perpendicular to a helium ion beam showing when the foil is rotated, the computed intensity matches well with the experimental intensity for both focused and raster scanned beam conditions.

Accurate dosimetry is critical to quantifying the number of implanted ions from degraded helium ion beams. For an energy degraded helium ion beam, the amount of scattering from the foil

degrader makes a Faraday cup measurement insufficient to quantify the dose at the target area without accounting for the distance between the Faraday cup and the target area. To determine the ion flux at the irradiation stage, the scattering and intensity measurements from the calculation method described previously are used to determine the ratio of the number of ions measured at the Faraday cup to the number of ions impacting a specified area on the irradiation stage. The current in the Faraday cup is recorded during irradiation and modified using this ratio to determine the ion beam flux on the irradiated area.

To confirm the dosimetry calculation methodology for the energy degraded helium ions, a series of two helium implantations into high purity silicon at room temperature were performed. In the first helium implantation experiment, mono-energetic helium ions were injected into a high purity single crystal silicon substrate from Virginia Semiconductor with energies of 380 keV and then 140 keV to fluences of 2.0×10^{17} ions/cm^2 using the 400 kV NEC Ion Implanter at the Michigan Ion Beam Laboratory (MIBL). The higher energy ion implantation was performed first to minimize the impact of the radiation damage induced by helium ions on the implantation profile shape. The helium ion beam was raster scanned over a 25 mm by 25 mm square area with four Faraday cups with 1 cm^2 area each occupying a corner of the square. The current density is recorded on the Faraday cups and used with a charge integrator to determine the fluence of the helium ion beam.

For the second helium implantation experiment, the silicon was implanted using a raster scanned 2.1 MeV He^{2+} ions from the 1.7 MV General Ionex Tandetron accelerator at MIBL. The implantations were performed with three conditions: without a thin foil to 1.0×10^{17} ions/cm^2, passing through a 3.04 μm Al foil with the foil held perpendicular to the beam (0°) to a fluence of 1.3×10^{17} ions/cm^2 and with the foil rotated to 55° to a fluence of 0.9×10^{17} ions/cm^2. The He^{2+}

charge state was chosen as the thin foil may strip an additional electron off a He^+ ion beam and result in a distribution of charge states between He^+ and He^{2+} at the Faraday cup [232], making ion flux measurements complex. A 3 μm thick aluminum foil 99.0%+ purity was purchased from Goodfellow Inc. for this experiment The thickness of the foil was measured using Rutherford Backscattering Spectrometry (RBS) to have a thickness of 3.04 μm The Al foil was positioned 26 cm in front of the silicon target with the Faraday cup positioned between the foil and the silicon sample approximately 16 cm from the foil. The Faraday cup had a radius of 1.27 cm. The silicon specimen was positioned to have the helium ions hit the sample surface at an incident angle of 60°. The slit aperture was set to have an area of 5 mm horizontally and 10 mm vertically, resulting in a area of 10 mm × 10 mm on the silicon specimen surface. A diagram of the experimental setup for this implantation is in Figure B.12. For the mono-energetic helium implantations, the SRIM-2013 program was used to calculate the implantation profiles using the helium ion implantation distribution in Range.txt output file multiplied by the ion fluence and divided by the atomic density of silicon, 5×10^{22} at/cm^3. A similar methodology was followed for the energy-degraded helium ions to obtain a calculated helium implantation based on periodic Faraday cup insertions and the calculated Faraday cup to stage ratio, $R_{FC-St}(\theta_i)$, for foil rotation angles of 0° and 55°.

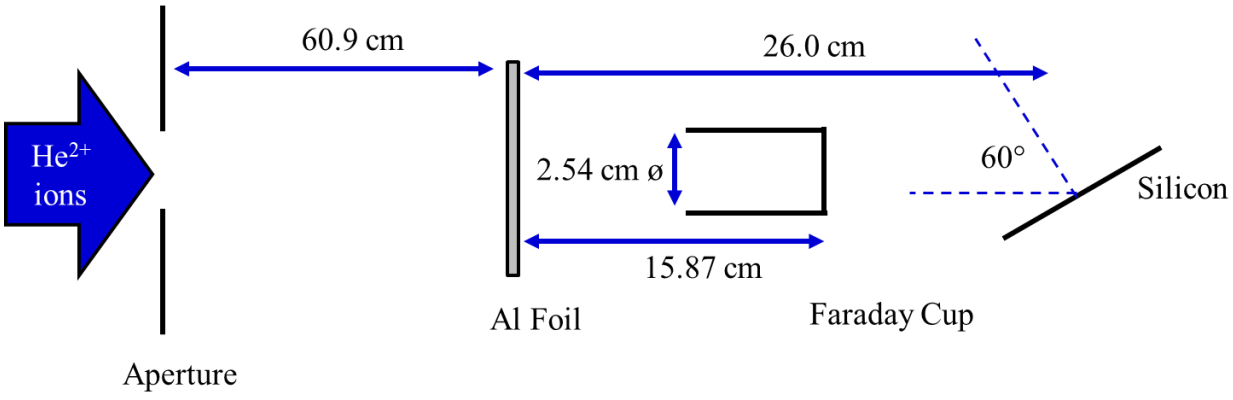

Figure B.12. A schematic of the system for helium implantations with 2.1 MeV He^{2+} ions and a thin Al foil energy degrader. The figure is not drawn to scale.

Following each implantation, elastic backscattering spectrometry (EBS) measurements were performed to measure the helium depth distribution and the integrated fluence. The cross section of elastic backscattered protons by Helium-4 were measured by Miller [233] and Godinho [234] in difference energy ranges and are available through the IBANDL database [235] for a scattering angle of 165°. The cross sections from the database were combined to obtain the $^4He(p,p_0)^4He$ cross section in the energy range from 596 keV to 5384 keV as shown in Figure B.13.

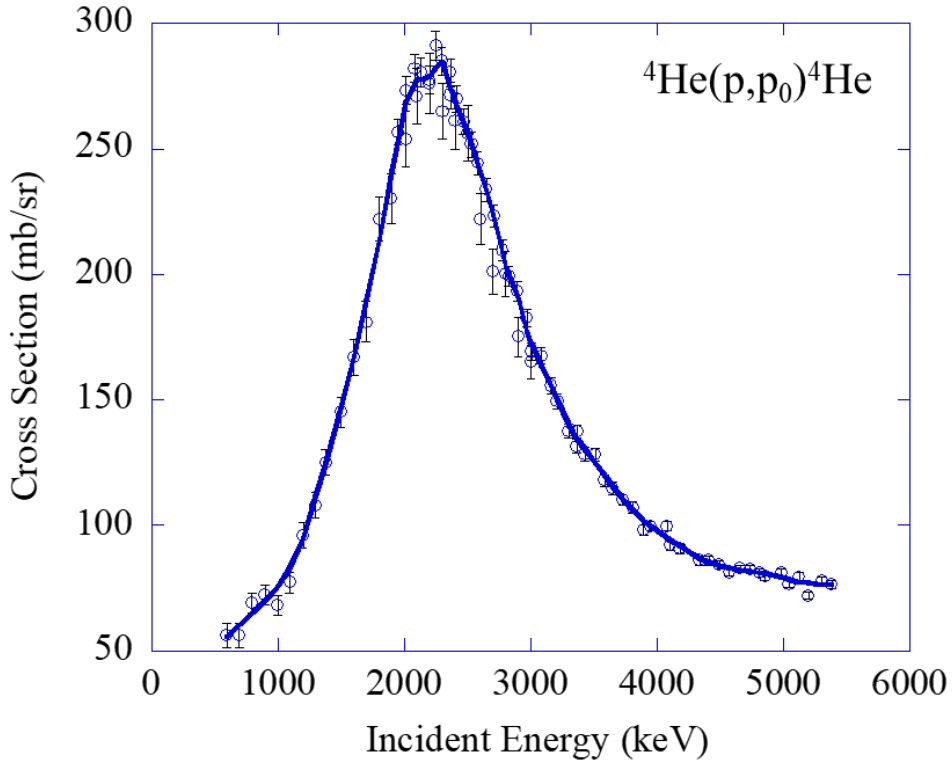

Figure B.13. Elastic backscattering cross sections used for helium concentration analysis from [233–235].

Elastic backscattering measurements were performed in the IBA geometry with Ortec BU-012-050-100 detector and a scattering angle (θ) of 165°, sample tilt angle (α) of either -35° or -55°, and an exit angle (β) of 50° or 70° using 2.38 MeV H^+ ions as the incident particles on helium implanted and non-helium implanted areas of the silicon sample. The sample tilt angles were

chosen to maximize the depth resolution of the helium implantation profiles with the higher tilt angle used to measure shallower implantations. The resulting measurements were analyzed using the SimNRA program [231]. First, the front edge of the silicon RBS signal and the Si(p,p_0)Si reaction using the cross sections from [236] in the helium implanted silicon was fit to determine the particles/sr for the spectra. The spectra for the non-helium implanted silicon was scaled to the same intensity as the silicon front edge in the spectra from the helium implanted silicon. The two spectra were subtracted to isolate the signal from the helium backscatter reaction. The resulting helium only spectra was then fit using SimNRA and the combined Miller and Godinho cross sections to produce the helium concentration profile with depth.

To confirm the helium implantation range with a thin foil energy degrader, a TEM transparent lamella was produced from the helium implanted silicon using a standard FIB liftout method as transmission electron microscopy inherently has a higher spatial resolution than EBS. A low energy ion beam was used (5 keV and 2 keV) when the foil was still relatively thick (around 150 nm) to thin the foil to a final thickness around 100 nm, which effectively eliminated TEM-visible FIB damages induced at high beam energy. Scanning transmission electron microscopy bright field (STEM-BF) images were collected at a magnification of 80kx using a JEOL 2100F at the Michigan Center for Materials Characterization (MC^2) to examine black dot defects generated by the helium implantation.

As the number of visible defects was significantly large for hand counting techniques, the black dot defects were identified and analyzed with Trainable Weka Segmentation [237], a machine learning plugin in Fiji [159] based on the approach taken in [238]. The segmentation model was trained on multiple STEM-BF images of black dot defects in Si. A small fraction of false positives and false negatives occurred in the black dot defect identification, but they do not

significantly impact the depth analysis. Each group of pixels positively identified as a black dot defect was gathered in 100 nm depth bins to estimate the depths of the helium implantation profiles.

The results for each EBS measurement with contributions from RBS, the $Si(p,p_0)Si$ reaction and the $^4He(p,p_0)^4He$ reaction are included in Figure B.14. As seen in this figure, the helium signal appeared at low channel numbers in an area of the silicon signal where no other reactions were captured. An example of the resulting signal is displayed in Figure B.15 showing the helium signal peaks in isolation. The comparison of the measured profiles from fitting this isolated spectra using SimNRA and the implantation profiles calculated from SRIM are included in Figure B.16. The locations of each peak measured with EBS were found to be accurate with the calculation from SRIM. The peaks were integrated with depth to calculate the measured fluence of helium ions for each peak. The results are included in Table B.1 with comparison to the fluence values calculated from the Faraday cups during implantation. The integrated fluence of helium in each peak agreed with the fluence expected from Faraday cups measurements during the helium implantation. Therefore, EBS measurements can be used to accurately measure the amount of helium implanted and confirm the energy distribution of implanted ions through a comparison of the location of the implanted helium with SRIM.

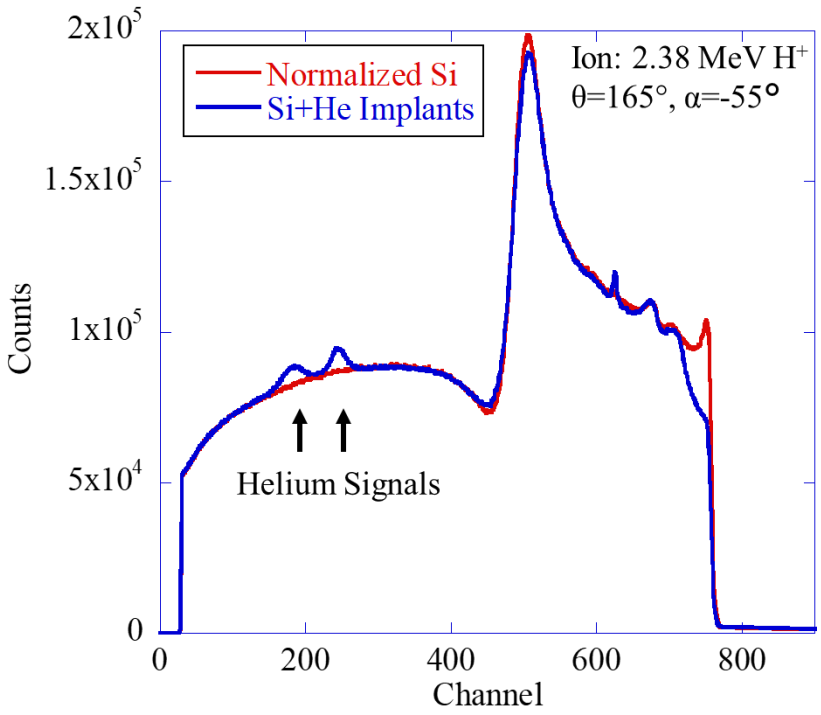

Figure B.14. EBS spectra of the helium implanted silicon sample.

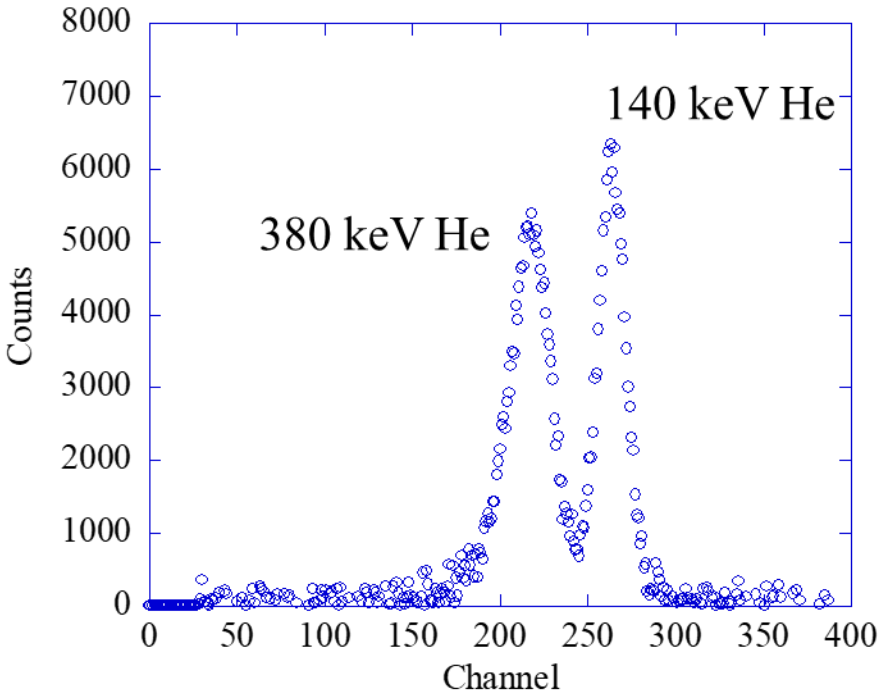

Figure B.15. Spectra of $He^4(p,p_0)He^4$ events of 140 keV and 380 keV He^+ ions implanted into silicon.

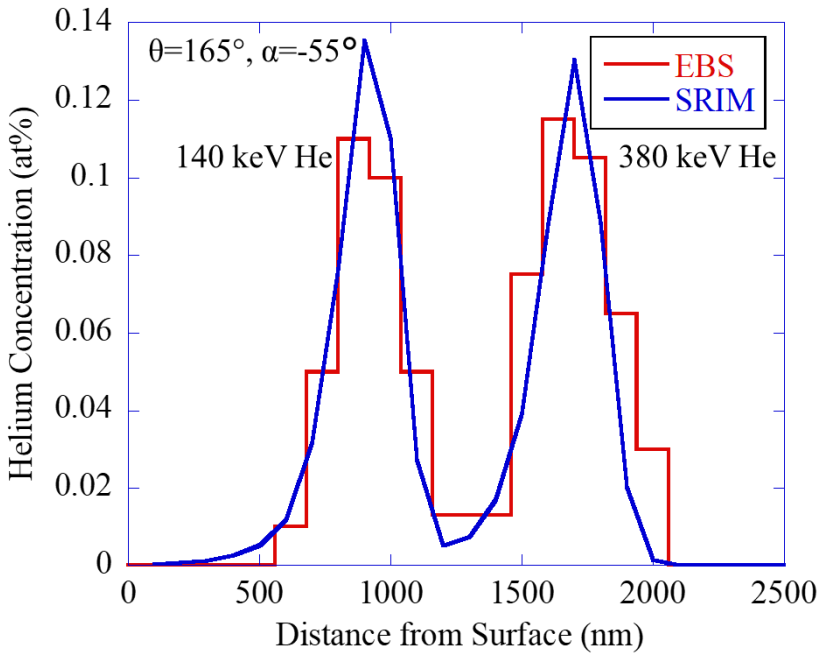

Figure B.16. Comparison of the calculated helium implantation profile from SRIM (blue) and measured by EBS (red) for 140 keV and 380 keV He^+ ions in silicon.

Table B.1. Comparison of the helium implantation fluences from the FC measurements during ion implantation and from the EBS measurements to confirm the accuracy of EBS measurements.

Helium Energy (keV)	Measured Fluence from FCs (ions/cm^2)	Measured Fluence from EBS (ions/cm^2)
140	2.0×10^{17}	$2.1\pm0.2 \times 10^{17}$
380	2.0×10^{17}	$2.3\pm0.2 \times 10^{17}$

EBS spectra were collected after each implantation for 2.1 MeV He^{2+} implanted silicon without the foil degrader and with the foil degrader at 0° and 55°. The implantation profiles are shown in Figure B.17. The helium implantation profile from the 55° foil implantation is shallower (or closer to the surface) and wider than the other profiles. Part of the difference in height is from the lower fluence injected for this implantation. However, at higher foil rotation angles, the energy straggling and scattering are increased compared to lower angles. This energy straggling widens the implantation peak and is likely responsible for the wider implantation profile observed with the 55° foil implantation.

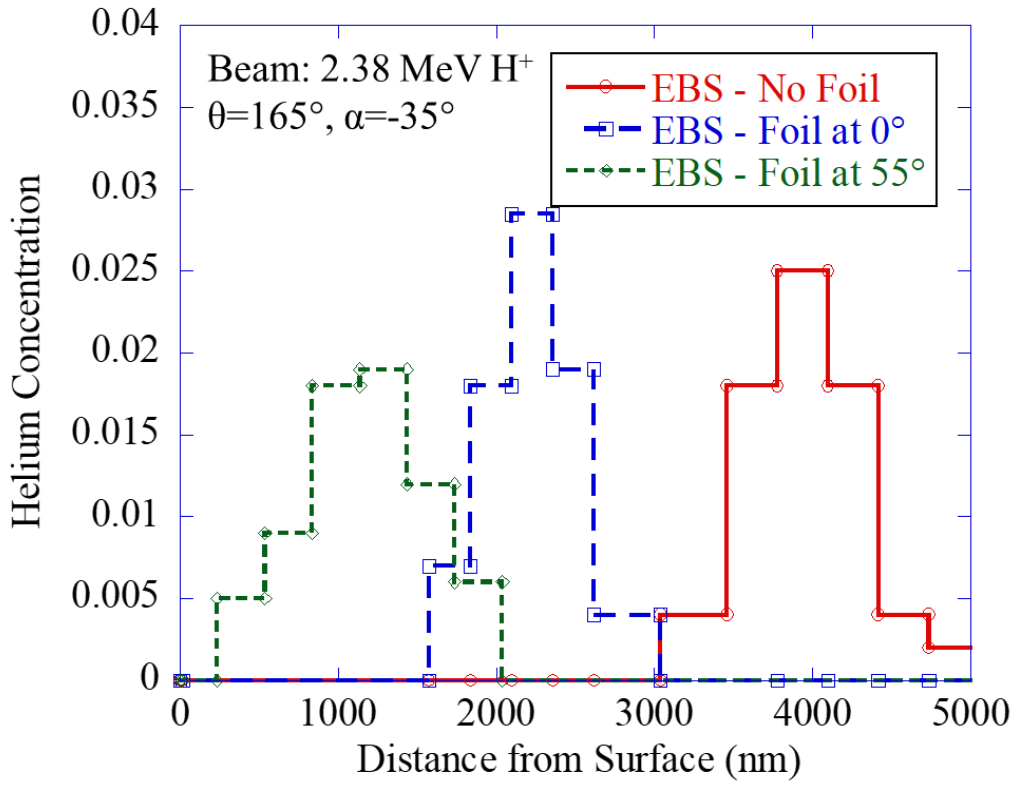

Figure B.17. Helium concentration profiles determined by EBS for 2.1 MeV He^{2+} implanted into silicon without a foil degrader and with the foil degrader held at 0° and 55°.

Similarly, three distinct bands of a high density of black dot defects were observed in the STEM-BF images, shown in Figure B.18. The microstructure of the single crystal silicon exhibited very few visible defects outside the helium implantation area and thus, the examined defects can be attributed to the helium ion implantations. The number of defects identified through the Trainable Weka Segmentation as a function of distance from the surface is presented in Figure B.19. The height differences in the peaks are likely from the contrast differences in the individual images used for the Weka segmentation analysis. The overall shape and height of each defect band were consistent with the EBS measurements of the individual helium implantation peaks. The two foil degraded implantations overlapped in their defect production profiles and were unable to be separated using STEM-BF.

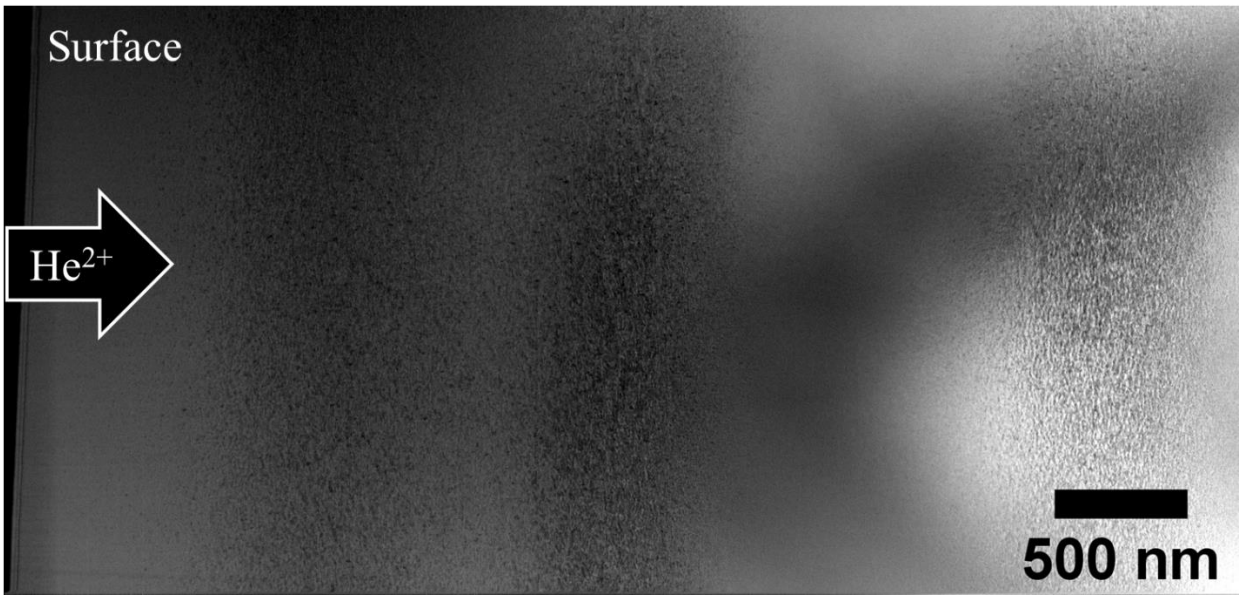

Figure B.18. STEM-BF image of 2.1 MeV He^{2+} implanted into silicon without a foil degrader and with the foil degrader held at 0° and 55° showing the three implanted regions.

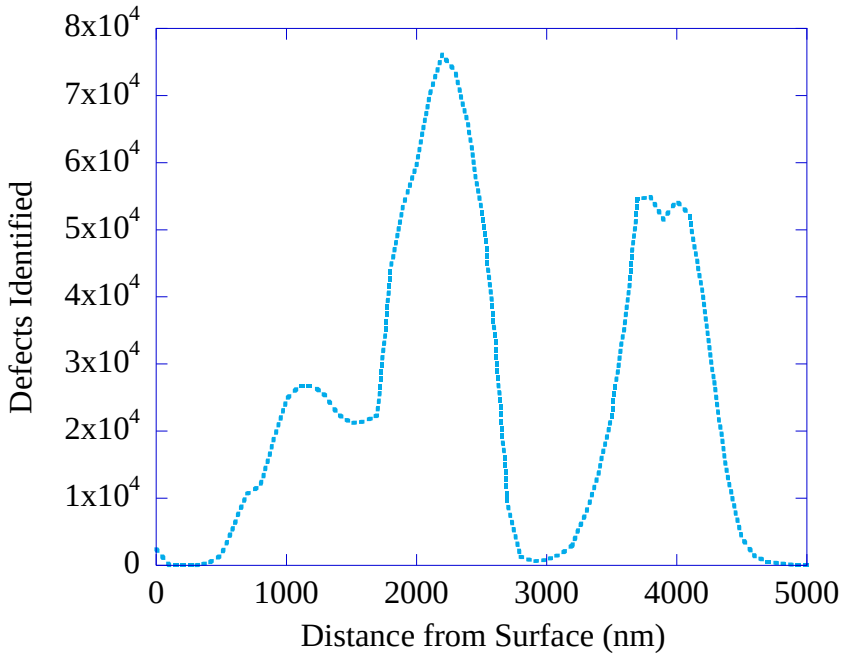

Figure B.19. Defects identified with Weka segmentation analysis as a function of distance from the surface based on the STEM-BF images in Figure B.18.

The comparison of the implantation profiles from SRIM-2013 using the methodology described previously, the EBS measurements, and the Weka segmentation analysis of black dot defects are presented in Figure B.20. The height of the defect profile from Weka segmentation was

arbitrarily scaled to be compared with the SRIM simulations and EBS measurements as the absolute number of defects identified is not important to the comparison. Overall, there is excellent agreement between all the measurements. The locations of the peaks measured with EBS and TEM are consistent with the predicted ion ranges from SRIM, even after a thin Al foil energy degrader. The integration of the EBS measurements of each peak to obtain the fluence is presented in Table B.2. The fluence amounts measured agreed with the fluences calculated from periodic Faraday cup insertions. Thus, the methodology used to calculate the helium implantation profile using SRIM through a thin foil energy degrader was found to be accurate.

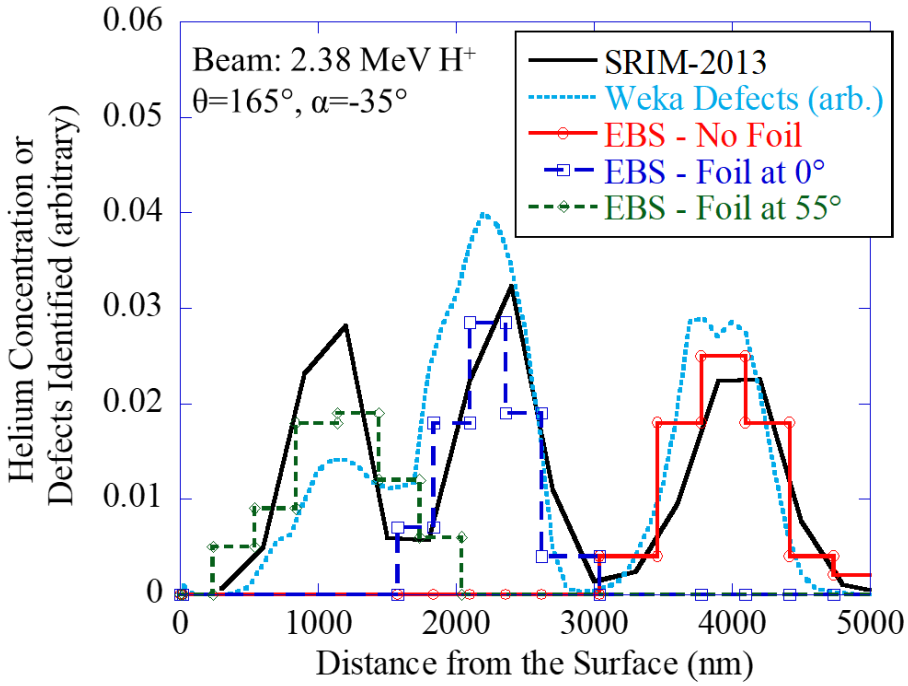

Figure B.20. Comparison of the helium implantation profiles calculated with SRIM, measured with EBS, and analyzed with Weka segmentation based on STEM-BF images.

Table B.2. Comparison of helium implantation fluences from the FC measurements during ion implantation with a thin foil energy degrader and from the EBS measurements to confirm the methodology of calculating the implantation profile of energy degraded helium ions.

Foil Rotation	Measured Fluence from FCs (ions/cm^2)	Measured Fluence from EBS (ions/cm^2)
No foil	1.0×10^{17}	$1.0\pm0.1 \times 10^{17}$
0°	1.3×10^{17}	$1.2\pm0.2 \times 10^{17}$
55°	0.9×10^{17}	$0.85\pm0.2 \times 10^{17}$

References

[1] G.S. Was, T. Allen, Radiation-induced segregation in multicomponent alloys: Effect of particle type, Mater. Charact. 32 (1994) 239–255. doi:10.1016/1044-5803(94)90101-5.

[2] G.S. Was, J.T. Busby, T. Allen, E.A. Kenik, A. Jenssen, S.M. Bruemmer, J. Gan, A.D. Edwards, P.M. Scott, P.L. Andresen, Emulation of neutron irradiation effects with protons : validation of principle, J. Nucl. Mater. 300 (2002) 198–216.

[3] G.S. Was, Z. Jiao, E. Getto, K. Sun, A.M. Monterrosa, S.A. Maloy, O. Anderoglu, B.H. Sencer, M. Hackett, Emulation of reactor irradiation damage using ion beams, Scr. Mater. 88 (2014) 33–36. doi:10.1016/j.scriptamat.2014.06.003.

[4] G.S. Was, Fundamentals of Radiation Materials Science, Springer New York, New York, NY, 2017. doi:10.1007/978-1-4939-3438-6.

[5] G.S. Was, Challenges to the use of ion irradiation for emulating reactor irradiation, J. Mater. Res. 30 (2015) 1158–1182. doi:10.1557/jmr.2015.73.

[6] E. Getto, Z. Jiao, A.M. Monterrosa, K. Sun, G. Was, Effect of pre-implanted helium on void swelling evolution in self-ion irradiated HT9, J. Nucl. Mater. 462 (2015) 458–469. doi:10.1016/j.jnucmat.2015.01.045.

[7] S.J. Zinkle, L.L. Snead, Opportunities and limitations for ion beams in radiation effects studies: Bridging critical gaps between charged particle and neutron irradiations, Scr. Mater. 143 (2018) 154–160. doi:10.1016/j.scriptamat.2017.06.041.

[8] G.S. Was, S. Taller, Z. Jiao, A.M. Monterrosa, D. Woodley, D. Jennings, T. Kubley, F. Naab, O. Toader, E. Uberseder, Resolution of the carbon contamination problem in ion

irradiation experiments, Nucl. Instruments Methods Phys. Res. Sect. B Beam Interact. with Mater. Atoms. 412 (2017). doi:10.1016/j.nimb.2017.08.039.

[9] P.J. Maziasz, R.L. Klueh, J.M. Vitek, Helium Effects on Void Formation in 9Cr-1MoVNb and 12Cr-1MoVW Irradiated in HFIR, J. Nucl. Mater. 141–143 (1986) 929–9337. doi:10.2172/5124729.

[10] D.S. Gelles, A. Kohyama, Microstructural Examination of HT-9 in the FFTF/MOTA to 110 dpa, in: Fusion React. Mater. Semiannu. Prog. Rep. Period End. March 31, 1989, Department of Energy DOE/ER-031316, Oak Ridge, TN, 1989: p. 193.

[11] C.Y. Hsu, D.S. Gelles, T.A. Lechtenberg, Microstructural Examination of 12% Cr Martensitic Stainless Steel After Irradiation at Elevated Temperatures in FFTF, in: F.A. Garner, N.H. Packan, A.S. Kumar (Eds.), Radiation-Induced Chang. Microstruct. ASTM STP 955, American Society for Testing and Materials, Philadelphia, PA, 1987: p. 545.

[12] K. Asano, Y. Kohno, A. Kohyama, G. Ayrault, Microstructural Evolution of HT9 Under Dual-Beam Charged Particle Irradiation, J. Nucl. Mater. 157 (1988) 912–915.

[13] A. Kohyama, G. Ayrault, N. Igata, Microstructural evolution in dual-ion irradiated 316ss under various helium injection schedules, J. Nucl. Mater. 122 (1984) 224–229. doi:10.1016/0022-3115(84)90600-7.

[14] F. Wan, Q. Zhan, Y. Long, S. Yang, G. Zhang, Y. Du, Z. Jiao, S. Ohnuki, The behavior of vacancy-type dislocation loops under electron irradiation in iron, J. Nucl. Mater. 455 (2014) 253–257. doi:10.1016/j.jnucmat.2014.05.048.

[15] K. Farrell, P.J. Maziasz, E.H. Lee, L.K. Mansur, Modification of radiation damage microstructure by helium, Radiat. Eff. 78 (1983) 277–295. doi:10.1080/00337578308207378.

[16] H. Seto, N. Hashimoto, H. Kinoshita, S. Ohnuki, Effects of multi-beam irradiation on defect formation in Fe – Cr alloys, J. Nucl. Mater. 417 (2011) 1018–1021. doi:10.1016/j.jnucmat.2011.01.053.

[17] E.A. Kenik, The influence of helium on microstructural evolution in an ion-irradiated low-swelling stainless steel, J. Nucl. Mater. 85–86 (1979) 659–663. doi:10.1016/0022-3115(79)90335-0.

[18] A.F. Rowcliffe, E.H. Lee, High temperature radiation damage phenomena in complex alloys, J. Nucl. Mater. 108–109 (1982) 306–318. doi:10.1016/0022-3115(82)90500-1.

[19] A. Hishinuma, N.H. Packan, E.H. Lee, L.K. Mansur, Effects of pulsed and/or dual ion irradiation on microstructural evolution in a Ti and Si modified austenitic alloy, J. Nucl. Mater. 122 (1984) 260–265. doi:10.1016/0022-3115(84)90607-X.

[20] E.H. Lee, N.H. Packan, L.K. Mansur, Effects of pulsed dual-ion irradiation on phase transformations and microstructure in Ti-modified austenitic alloy, J. Nucl. Mater. 117 (1983) 123–133. doi:10.1016/0022-3115(83)90018-1.

[21] W.J. Choyke, J.N. Mcgruer, J.R. Townsend, J.A. Spitznagel, N.J. Doyle, F.J. Venskytis, Helium effects in ion-bombarded 304 stainless steel, J. Nucl. Mater. 85–86 (1979) 647–651. doi:10.1016/0022-3115(79)90333-7.

[22] E. Getto, K. Sun, A.M. Monterrosa, Z. Jiao, M.J. Hackett, G.S. Was, Void swelling and microstructure evolution at very high damage level in self-ion irradiated ferritic-martensitic steels, J. Nucl. Mater. 480 (2016) 159–176. doi:10.1016/j.jnucmat.2016.08.015.

[23] A.M. Monterrosa, Z. Jiao, G.S. Was, The influence of helium on cavity evolution in ion-irradiated T91, J. Nucl. Mater. 509 (2018) 707–721. doi:10.1016/j.jnucmat.2018.06.033.

[24] N.H. Packan, K. Farrell, Simulation of first wall damage: Effects of the method of gas implantation, J. Nucl. Mater. 85–86 (1979) 677–681. doi:10.1016/0022-3115(79)90338-6.

[25] L.K. Mansur, W.A. Coghlan, Mechanisms of helium interaction with radiation effects in metals and alloys: A review, J. Nucl. Mater. 119 (1983) 1–25. doi:10.1016/0022-3115(83)90047-8.

[26] R.L. Klueh, D.R. Harries, High-Chromium Ferritic and Martensitic Steels for Nuclear Applications, American Society for Testing and Materials, Bridgeport, NJ, 2001.

[27] F.B. Pickering, No Title, Int. Met. Rev. 211 (1976) 227.

[28] J. Orr, F.R. Beckitt, G.D. Fawkes, Ferritic Steels for Fast Reactor Steam Generators, Volume 1, British Nuclear Energy Society, London, 1978.

[29] F.B. Pickering, Microstructural Developments and Stability in High Chromium Ferritic Power Plant Steels, The Institute of Materials, London, 1997.

[30] W. Tofaute, No Title, Arch. Fur Eisenhuttenwes. 8 (1935) 499.

[31] V.G. Rivlin, G. V. Raynor, No Title, Int. Met. Rev. 1 (1980) 21.

[32] D. Peckner, I.M. Bernstein, Handbook of Stainless Steels, McGraw-Hill, New York, NY, 1977.

[33] F.B. Pickering, No Title, in: Stainl. Steels ’84, The Institute of Metals, London, 1985: p. 2.

[34] K. Anderko, K. David, W. Ohly, M. Schirra, C. Wassilew, No Title, in: J.W. Davis, D.J. Michel (Eds.), Top. Conf. Ferritic Steels Use Nucl. Energy Technol., The Metallurgical Society of AIME, Warrendale, PA, 1984: p. 299.

[35] B.A. Chin, R.C. Walkaways, No Title, in: J.W. Davis, D.J. Michel (Eds.), Top. Conf. Ferritic Steels Use Nucl. Energy Technol., The Metallurgical Society of AIME, Warrendale, PA, 1984: p. 347.

[36] K. Anderko, L. Schäfer, E. Materna-Morris, Effect of the δ-ferrite phase on the impact properties of martensitic chromium steels, J. Nucl. Mater. 179–181 (1991) 492–495. doi:10.1016/0022-3115(91)90132-Q.

[37] K.J. Irvine, D.J. Crowe, F.B. Pickering, No Title, J. Iron Steel Inst. 195 (1960) 386.

[38] D.S. Gelles, Effects of Irradiation on Low Activation Ferritic Alloys: A Review, Reduc. Act. Mater. Fusion React. ASTM STP 1047. (1990) 113. doi:10.1520/stp24953s.

[39] J.Z. Briggs, T.D. Parker, The Super 12% Cr Steels. J. Z. Briggs und T. D. Parker. 1965 , 1270 Avenue of the Americas, New York, N.Y. 10020. 220 S., zahlr. Tabellen, Climax Molybdenum Company, New York, 1965. doi:10.1002/maco.19660170738.

[40] S.R. Keown, F.B. Pickering, No Title, in: Creep Strength Steel High Temp. Alloy., The Metals Society, London, 1974: p. 134.

[41] V. Foldyna, Z. Kubon, No Title, in: A. Strang (Ed.), Perform. Bolting Mater. High Temp. Plant Appl., The Institute of Materials, London, 1995: p. 175.

[42] V. Foldyna, Z. Kubon, No Title, in: A. Strang, D.J. Gooch (Eds.), Microstruct. Dev. Stab. High Chromium Ferritic Power Plant Steels, The Institute of Materials, London, 1997: p. 73.

[43] K.J. Irvine, No Title, J. Iron Steel Inst. 200 (1962) 820.

[44] H. Schneider, No Title, Foundry Trades J. 108 (1960) 562.

[45] W.B. Delong, No Title, Met. Prog. 77 (1960) 98.

[46] M. Schirra, No Title, Stahl Und Eisen. 112 (1992) 117.

[47] J.M. Vitek, R.L. Klueh, Precipitation Reactions during the Heat Treatment of Ferritic Steels, Metall. Trans. A. 14 (1983) 1047–1055. doi:10.1007/BF02659853.

[48] T. Lauritzen, W.L. Bell, S. Vaidyanathan, No Title, in: J.W. Davis, D.J. Michel (Eds.),

Top. Conf. Ferritic Steels Use Nucl. Energy Technol., The Metallurgical Society of AIME, Warrendale, PA, 1984: p. 623.

[49] A. Iseda, Y. Sawaragi, S. Kato, F. Masuyama, No Title, in: Proc. 5th Int. Conf. Creep Mater., ASM International, Materials Park, OH, 1992: p. 389.

[50] P. Patriarca, S.D. Harkness, J.M. Duke, L.R. Cooper, No Title, Nucl. Technol. 28 (1976) 516.

[51] F.B. Pickering, Physical Metallurgy and the Design of Steels, Applied Science Publishers, London, 1983.

[52] A. Alamo, J.C. Brachet, A. Castaing, C. Lepoittevin, F. Barcelo, Physical metallurgy and mechanical behaviour of FeCrWTaV low activation martensitic steels: Effects of chemical composition, J. Nucl. Mater. 258–263 (1998) 1228–1235. doi:10.1016/S0022-3115(98)00190-1.

[53] H. Finkler, M. Schirra, No Title, Steel Res. 67 (1996) 328.

[54] J.C. Brachet, No Title, in: I. Tamura (Ed.), Heat Treat. Mater. Heat Surf. ’92, Japan Society for Heat Treatment, Tokyo, 1992: p. 89.

[55] J.-C. Brachet, L. Gavard, C. Boussidan, C. Lepoittevin, S. Denis, C. Servant, Modelling of phase transformations occurring in low activation martensitic steels, J. Nucl. Mater. 258–263 (1998) 1307–1311. doi:10.1016/S0022-3115(98)00197-4.

[56] L. Pilloni, F. Attura, A. Calza-Bini, G. De Santis, G. Filacchioni, A. Carosi, S. Amato, Physical metallurgy of BATMAN II Ti-bearing martensitic steels, J. Nucl. Mater. 258–263 (1998) 1329–1335. doi:10.1016/S0022-3115(98)00199-8.

[57] J. Orr, D. Burton, No Title, in: D. Coutsouradis, J.H. Davidson, J. Ewald, P. Greenfield, T. Khan, M. Malik, D.B. Meadowcroft, V. Regis, R.B. Scarlin, F. Schubert, D. V. Thornton

(Eds.), Mater. Adv. Power Eng. 1994, Part 1, Kluwer Academic Publishers, Dordrecht, The Netherlands, 1994.

[58] E.A. Little, D.R. Harries, F.B. Pickering, S.R. Keown, Effects of heat treatment on structure and properties of 12%Cr steels, Met. Technol. 4 (1977) 205–217.

[59] J. Nutting, No Title, in: J.W. Davis, D.J. Michel (Eds.), Top. Conf. Ferritic Steels Use Nucl. Energy Technol., The Metallurgical Society of AIME, Warrendale, PA, 1984: p. 3.

[60] F.B. Pickering, No Title, in: Proc. 4th Int. Conf. Electron Microsc., Springer Verlag, Berlin, 1958: p. 665.

[61] B.S. Greenwell, S.M. Beech, No Title, in: A. Strang (Ed.), Rupture Ductility Creep Resist. Steels, The Institute of Metals, London, 1991: p. 103.

[62] S. Cierjacks, K. Ehrlich, E. Materna-Morris, L. Schafer, M. Schirra, C. Wassilew, No Title, in: F. Abe, A. Hishinuma, A. Kohyama, M. Suzuki (Eds.), Proc. IEA Work. Ferritic-Martensitic Steels, Vol. II, Japan Atomic Energy Research Institute, Tokai Research Establishment, Tokai, Japan, 1993: p. 125.

[63] T. Gladman, Physical Metallurgy of Microalloyed Steels, The Institute of Materials, London, 1997.

[64] H. Berns, F. Krafft, No Title, in: A. Strang (Ed.), Rupture Ductility Creep Resist. Steels, The Institute of Materials, London, 1991: p. 116.

[65] R. Schäublin, P. Spätig, M. Victoria, Microstructure assessment of the low activation ferritic/ martensitic steel F82H, J. Nucl. Mater. 258–263 (1998) 1178–1182. doi:10.1016/S0022-3115(98)00182-2.

[66] G.S. Was, Fundamentals of Radiation Material Science, 1st Editio, Springer, 2007.

[67] M. Nastasi, J.W. Mayer, J.K. Hirvonen, Ion-Solid Interactions: Fundamentals and

Applications, Cambridge University Press, 1996.

[68] F.A. Garner, M.B. Toloczko, B.H. Sencer, Comparison of swelling and irradiation creep behavior of fcc-austenitic and bcc-ferritic / martensitic alloys at high neutron exposure, J. Nucl. Mater. 276 (2000) 123–142.

[69] J.P. Wharry, G.S. Was, The mechanism of radiation-induced segregation in ferritic-martensitic alloys, Acta Mater. 65 (2014) 42–55. doi:10.1016/j.actamat.2013.09.049.

[70] C. Cawthorne, E.J. Fulton, Voids in Irradiated Stainless Steel, Nature. 216 (1967) 575–576.

[71] K.C. Russell, Nucleation of Voids in Irradiated Metals, Acta Metall. 19 (1971) 753–758.

[72] K.C. Russell, Thermodynamics of gas-containing voids in metals, Acta Metall. 20 (1972) 899–907.

[73] L.K. Mansur, Theory of transitions in dose dependence of radiation effects in structural alloys, J. Nucl. Mater. 206 (1993) 306–323. doi:10.1016/0022-3115(93)90130-Q.

[74] K. Krishan, Ordering of Voids and Gas Bubbles in Radiation Environments., Radiat. Eff. 66 (1982) 121–155. doi:10.1080/00337578208222474.

[75] K.L. Wong, H.-J. Lee, J.-H. Shim, B. Sadigh, B.D. Wirth, Multiscale modeling of point defect interactions in Fe–Cr alloys, J. Nucl. Mater. 386–388 (2009) 227–230. doi:10.1016/j.jnucmat.2008.12.092.

[76] A.A. Kohnert, M.A. Cusentino, B.D. Wirth, Molecular statics calculations of the biases and point defect capture volumes of small cavities, J. Nucl. Mater. 499 (2018) 480–489. doi:10.1016/j.jnucmat.2017.12.005.

[77] W.G. Wolfer, Advances in Void Swelling and Helium Bubble Physics, J. Nucl. Mater. 122 & 123 (1984) 367–378.

[78] a. V. Karasiov, L.R. Greenwood, Neutron flux spectra and radiation damage parameters for the Russian BOR-60 and SM-2 reactors, (n.d.).

[79] J.M. Vitek, R.L. Klueh, Microstructure of 9Cr-1MoVNb Steel Irradiated to 36 dpa at Elevated Temperatures in HFIR, J. Nucl. Mater. 122–123 (1984) 254–259.

[80] E.A. Little, Microstructural evolution in irradiated ferritic-martensitic steels: transitions to high dose behaviour, J. Nucl. Mater. 206 (1993) 324–334.

[81] E. Wakai, N. Hashimoto, Y. Miwa, J.P. Robertson, R.L. Klueh, K. Shiba, S. Jistukawa, Effect of helium production on swelling of F82H irradiated in HFIR, J. Nucl. Mater. 283–287 (2000) 799–805.

[82] E. Wakai, Y. Miwa, N. Hashimoto, J.P. Robertson, R.L. Klueh, K. Shiba, K. Abiko, S. Furuno, S. Jitsukawa, Microstructural study of irradiated isotopically tailored F82H steel, J. Nucl. Mater. 307–311 (2002) 203–211. doi:10.1016/S0022-3115(02)01261-8.

[83] J.J. Kai, R.L. Klueh, Microstructural analysis of neutron-irradiated martensitic steels, J. Nucl. Mater. 230 (1996) 116–123. doi:10.1016/0022-3115(96)00165-1.

[84] A. Kimura, M. Narui, H. Kayano, Effects of alloying elements on the post-irradiation microstructure of 9%Cr-2%W low activation martensitic steels, J. Nucl. Mater. 191–194 (1992) 879–884. doi:10.1016/0022-3115(92)90599-G.

[85] B.H. Sencer, J.R. Kennedy, J.I. Cole, S.A. Maloy, F.A. Garner, Microstructural stability of an HT-9 fuel assembly duct irradiated in FFTF, J. Nucl. Mater. 414 (2011) 237–242. doi:10.1016/j.jnucmat.2011.03.050.

[86] J. Van Den Bosch, O. Anderoglu, R. Dickerson, M. Hartl, P. Dickerson, J.A. Aguiar, P. Hosemann, M.B. Toloczko, S.A. Maloy, SANS and TEM of ferritic-martensitic steel T91 irradiated in FFTF up to 184 dpa at 413°C, J. Nucl. Mater. 440 (2013) 91–97.

doi:10.1016/j.jnucmat.2013.04.025.

[87] D.S. Gelles, Microstructural examination of commercial ferritic alloys at 200 dpa, J. Nucl. Mater. 237 (1996) 293–298.

[88] R. Sindelar, J.J. Kai, D. Plumton, R. Dodd, G. Kulcinski, Microstructural Modification of 21/4 Cr-1Mo Steel by Irradiation with 14 MeV Nickel Ions, Nucl. Instruments Methods Phys. Res. 16 (1986) 260–269.

[89] J.G. Gigax, T. Chen, H. Kim, J. Wang, L.M. Price, E. Aydogan, S.A. Maloy, D.K. Schreiber, M.B. Toloczko, F.A. Garner, L. Shao, Radiation response of alloy T91 at damage levels up to 1000 peak dpa, J. Nucl. Mater. 482 (2016) 257–265. doi:10.1016/j.jnucmat.2016.10.003.

[90] L. Shao, C.C. Wei, J. Gigax, a. Aitkaliyeva, D. Chen, B.H. Sencer, F. a. Garner, Effect of defect imbalance on void swelling distributions produced in pure iron irradiated with 3.5 MeV self-ions, J. Nucl. Mater. 453 (2014) 176–181. doi:10.1016/j.jnucmat.2014.06.002.

[91] G.S. Was, Fundamentals of Radiation Materials Science: Metals and Alloys, Springer, 2007.

[92] A. Hishinuma, L.K. Mansur, Critical radius for bias-driven swelling - a further analysis and its application to bimodal cavity size distributions, J. Nucl. Mater. 118 (1983) 91–99. doi:10.1016/0022-3115(83)90184-8.

[93] A.. Dvoriashin, S.. Porollo, Y.. Konobeev, F.A. Garner, Influence of high dose neutron irradiation on microstructure of EP-450 ferritic–martensitic steel irradiated in three Russian fast reactors, J. Nucl. Mater. 329–333 (2004) 319–323. doi:10.1016/j.jnucmat.2004.04.309.

[94] G. Ayrault, Cavity Formation During Single- and Dual-Ion Irradiation in a 9Cr-1Mo

Ferritic Alloy, J. Nucl. Mater. 114 (1983) 34–40.

[95] R. Hide, K. Kusanagi, M. Taguchi, Microstructural Change in Ferritic Steels Under Heavy Ion Irradiation, Eff. Radiat. Mater. 14th Int. Symp. ASTM STP 1046. (1989) 61–72.

[96] G.S. Was, Fundamentals of Radiation Materials Science, Springer Berlin Heidelberg, Berlin, Heidelberg, 2007. doi:10.1007/978-3-540-49472-0.

[97] J.J. Kai, G.L. Kulcinski, 14 MeV nickel-ion irradiated HT-9 ferritic steel with and without helium pre-implantation, J. Nucl. Mater. 175 (1990) 227–236.

[98] P.A. Schmidt, P.R. Malmberg, J.A. Sprague, J.E. Westmoreland, Swelling Behavior of Commercial Ferritic Alloys, EM-12 and HT-9, as Assessed by Heavy Ion Bombardment, in: Irradiat. Eff. Microstruct. Prop. Met., American Society for Testing and Materials, Philadelphia, PA, 1976: p. 227.

[99] E. Wakai, T. Sawai, K. Furuya, A. Naito, T. Aruga, K. Kikuchi, S. Yamashita, S. Ohnuki, S. Yamamoto, H. Naramoto, S. Jistukawa, Effect of triple ion beams in ferritic / martensitic steel on swelling behavior, J. Nucl. Mater. 307–311 (2002) 278–282.

[100] M.B. Toloczko, F. a. Garner, V.N. Voyevodin, V. V. Bryk, O. V. Borodin, V. V. Mel'Nychenko, a. S. Kalchenko, Ion-induced swelling of ODS ferritic alloy MA957 tubing to 500 dpa, J. Nucl. Mater. 453 (2014) 323–333. doi:10.1016/j.jnucmat.2014.06.011.

[101] N. Hashimoto, R.L. Klueh, Microstructural evolution of nickel-doped 9Cr steels irradiated in HFIR, J. Nucl. Mater. 305 (2002) 153–158. doi:10.1016/S0022-3115(02)01026-7.

[102] Y. Katoh, R.E. Stoller, Y. Kohno, A. Kohyama, Modeling the Effects of Damage Rate and He/dpa Ratio on Microstructural Evolution, J. Nucl. Mater. 194 (1992) 1144–1149.

[103] Y. Katoh, R.E. Stoller, Y. Kohno, A. Kohyama, Numerical Estimation of Synergistic

Effects of Displacement Damage and Helium Generation on Microstructural Evolution, Mater. Trans. JIM. 33 (1992) 795–801.

[104] W. V. Green, M. Victoria, T. Leffers, B.N. Singh, eds., No Title, in: Work. Eff. Recoil Energy Spectr. Nucl. Transmutations Evol. Microstruct., Lugano, 1988.

[105] C. Abromeit, Aspects of simulation of neutron damage by ion irradiation, J. Nucl. Mater. 216 (1994) 78–96. doi:10.1016/0022-3115(94)90008-6.

[106] R.E. Stoller, The influence of helium on microstructural evolution: Implications for DT fusion reactors, J. Nucl. Mater. 174 (1990) 289–310. doi:10.1016/0022-3115(90)90242-F.

[107] K. Farrell, Experimental effects of helium on cavity formation during irradiation—a review, Radiat. Eff. 53 (1980) 175–194. doi:10.1080/00337578008207114.

[108] J.A. Spitznagel, W.J. Choyke, J. Lauer, B.O. Hall, J.N. McGruer, J.R. Townsend, R.B. Irwin, Evolution of cavity size distributions in dual-ion irradiated austenitic stainless steel and Fe-Cr-Ni ternary alloys, J. Nucl. Mater. 117 (1983) 198–207. doi:10.1016/0022-3115(83)90024-7.

[109] J.A. Spitznagel, W.J. Choyke, N.J. Doyle, R.B. Irwin, J.R. Townsend, J.N. McGruer, Critical cavity sizes in dual-ion bombarded 304 SS part I: Experiment, J. Nucl. Mater. 108–109 (1982) 537–543. doi:10.1016/0022-3115(82)90525-6.

[110] T. Muroga, H. Watanabe, N. Yoshida, H. Kurishita, M.L. Hamilton, Microstructure and Tensile Properties of Neutron-Irradiated Cu and Cu-Sni Containing Isotopically Controlled Boron, J. Nucl. Mater. . 225 (1995) 137–145.

[111] T. Muroga, H. Watanabe, N. Yoshida, Effects of solid transmutants and helium in copper studied by mixed-spectrum neutron irradiation, J. Nucl. Mater. 258–263 (1998) 955–960. doi:10.1016/S0022-3115(98)00123-8.

[112] T. Muroga, N. Yoshida, The influence of isotopically controlled boron addition on void swelling of nickel irradiated in FFTF, J. Nucl. Mater. 191–194 (1992) 1254–1258. doi:10.1016/0022-3115(92)90675-B.

[113] J.L. Brimhall, E.P. Simonen, Effect of helium on void formation in nickel, J. Nucl. Mater. 68 (1977) 235–243. doi:10.1016/0022-3115(77)90242-2.

[114] Q. Xu, T. Yoshiie, K. Sato, Effects of hydrogen and helium produced by transmutation reactions on void formation in copper isotopic alloys irradiated with neutrons, J. Nucl. Mater. 386–388 (2009) 363–366. doi:10.1016/j.jnucmat.2008.12.127.

[115] S.J. Zinkle, K. Farrell, H. Kanazawa, Microstructure and cavity swelling in reactor-irradiated dilute copper-boron alloy, J. Nucl. Mater. 179–181 (1991) 994–997. doi:10.1016/0022-3115(91)90258-9.

[116] S.J. Zinkle, K. Farrell, Void swelling and defect cluster formation in reactor-irradiated copper, J. Nucl. Mater. 168 (1989) 262–267. doi:10.1016/0022-3115(89)90591-6.

[117] B.N. Singh, M. Eldrup, A. Moslang, Effects of hot implantation of helium in copper on bubble formation within grains and on grain-boundaries, in: A.S. Kumar, D.S. Gelles, R.K. Nanstad, E.A. Little (Eds.), Eff. Radiat. Mater. 16th Int. Symp. ASTM STP 1175, American Society for Testing and Materials Special Technical Publication, W Conshohocken, 1994: pp. 1061–1073.

[118] B.N. Singh, A. Horsewell, Effects of fission neutron and 600 MeV proton irradiations on microstructural evolution in OFHC-copper, J. Nucl. Mater. 212–215 (1994) 410–415. doi:10.1016/0022-3115(94)90095-7.

[119] S.J. Zinkle, Dual Ion Irradiation of Copper, in: Fusion React. Mater. Semiannu. Prog. Rep. Period End. Sept. 30, 1987, DOE/ER-0313/3, 1986: pp. 86–89.

[120] Y.E. Kupriiyanova, V. V. Bryk, O. V. Borodin, A.S. Kalchenko, V.N. Voyevodin, G.D. Tolstolutskaya, F.A. Garner, Use of double and triple-ion irradiation to study the influence of high levels of helium and hydrogen on void swelling of 8-12% Cr ferritic-martensitic steels, J. Nucl. Mater. 468 (2016) 264–273. doi:10.1016/j.jnucmat.2015.07.012.

[121] H. Ogiwara, H. Sakasegawa, H. Tanigawa, M. Ando, Y. Katoh, a Kohyama, Void swelling in reduced activation ferritic/martensitic steels under ion-beam irradiation to high fluences, J. Nucl. Mater. 307–311 (2002) 299–303. doi:10.1016/S0022-3115(02)01078-4.

[122] E. Wakai, K. Kikuchi, S. Yamamoto, T. Aruga, M. Ando, H. Tanigawa, T. Taguchi, T. Sawai, K. Oka, S. Ohnuki, Swelling behavior of F82H steel irradiated by triple/dual ion beams, J. Nucl. Mater. 318 (2003) 267–273. doi:10.1016/S0022-3115(03)00122-3.

[123] S. Hiwatashi, Y. Kohno, K. Asakura, a. Kohyama, Microstructural developments in Fe-Cr-W low activation ferritic steels under dual beam charged particle irradiation, J. Nucl. Mater. 179–181 (1991) 709–713. doi:10.1016/0022-3115(91)90187-C.

[124] T. Yamamoto, Y. Wu, G. Robert Odette, K. Yabuuchi, S. Kondo, A. Kimura, A dual ion irradiation study of helium–dpa interactions on cavity evolution in tempered martensitic steels and nanostructured ferritic alloys, J. Nucl. Mater. 449 (2014) 190–199. doi:10.1016/j.jnucmat.2014.01.040.

[125] A. Bhattacharya, E. Meslin, J. Henry, A. Barbu, S. Poissonnet, B. Décamps, Effect of chromium on void swelling in ion irradiated high purity Fe–Cr alloys, Acta Mater. 108 (2016) 241–251. doi:10.1016/j.actamat.2016.02.027.

[126] D. Brimbal, E. Meslin, J. Henry, B. Décamps, A. Barbu, He and Cr effects on radiation damage formation in ion-irradiated pure iron and Fe-5.40 wt.% Cr: A transmission electron microscopy study, Acta Mater. 61 (2013) 4757–4764.

doi:10.1016/j.actamat.2013.04.070.

[127] K.C. Russell, The Theory of Void Nucleation in Metals, Acta Metall. 26 (1978) 1615–1630.

[128] C. a. Walsh, J. Yuan, L.M. Brown, A procedure for measuring the helium density and pressure in nanometre-sized bubbles in irradiated materials using electron-energy-loss spectroscopy, Philos. Mag. A. 80 (2009) 1507–1543. doi:10.1080/01418610008212134.

[129] S. Fréchard, M. Walls, M. Kociak, J.P. Chevalier, J. Henry, D. Gorse, Study by EELS of helium bubbles in a martensitic steel, J. Nucl. Mater. 393 (2009) 102–107. doi:10.1016/j.jnucmat.2009.05.011.

[130] Y. Wu, G.R. Odette, T. Yamamoto, J. Ciston, P. Hosemann, AN ELECTRON ENERGY LOSS SPECTROSCOPY STUDY OF HELIUM BUBBLES IN NANOSTRUCTURED FERRITIC ALLOYS, 2013.

[131] J. Rife, S. Donnelly, A. Lucas, J. Gilles, J. Ritsko, Optical Absorption and Electron-Energy-Loss Spectra of Helium Microbubbles in Aluminum, Phys. Rev. Lett. 46 (1981) 1220–1223. doi:10.1103/PhysRevLett.46.1220.

[132] D. Taverna, M. Kociak, O. Stéphan, a. Fabre, E. Finot, B. Décamps, C. Colliex, Probing Physical Properties of Confined Fluids within Individual Nanobubbles, Phys. Rev. Lett. 100 (2008) 035301. doi:10.1103/PhysRevLett.100.035301.

[133] L.K. Mansur, E.H. Lee, P.J. Maziasz, A.P. Rowcliffe, Control of helium effects in irradiated materials based on theory and experiment, J. Nucl. Mater. 141–143 (1986) 633–646. doi:10.1016/0022-3115(86)90066-8.

[134] R.E. Stoller, G.R. Odette, A comparison of the relative importance of helium and vacancy accumulation in void nucleation, Radiation-Induced Chang. {…}. (1987) 358–370.

[135] R.E. Stoller, Y.N. Osetsky, An atomistic assessment of helium behavior in iron, J. Nucl. Mater. 455 (2014) 258–262. doi:10.1016/j.jnucmat.2014.06.020.

[136] H. Van Swygenhoven, L.M. Stals, The Greenwood-Foreman-Rimmer loop punching mechanism as applied to helium bubble growth in nickel implanted with 5 keV He + ions at 273 K, Radiat. Eff. 78 (1983) 157–163. doi:10.1080/00337578308207368.

[137] G.W. Greenwood, A.J.E. Foreman, D.E. Rimmer, The role of vacancies and dislocations in the nucleation and growth of gas bubbles in irradiated fissile material, J. Nucl. Mater. 1 (1959) 305–324.

[138] W. Wilson, C. Bisson, M. Baskes, Self-trapping of helium in metals, Phys. Rev. B. 24 (1981) 5616–5624. doi:10.1103/PhysRevB.24.5616.

[139] C.S. Deo, M. a. Okuniewski, S.G. Srivilliputhur, S. a. Maloy, M.I. Baskes, M.R. James, J.F. Stubbins, Helium bubble nucleation in bcc iron studied by kinetic Monte Carlo simulations, J. Nucl. Mater. 361 (2007) 141–148. doi:10.1016/j.jnucmat.2006.12.018.

[140] C.S. Deo, M. a. Okuniewski, S.G. Srivilliputhur, S. a. Maloy, M.I. Baskes, M.R. James, J.F. Stubbins, The effects of helium on irradiation damage in single crystal iron, J. Nucl. Mater. 367–370 (2007) 451–456. doi:10.1016/j.jnucmat.2007.03.117.

[141] R.E. Stoller, G.R. Odette, Analytical solutions for helium bubble and critical radius parameters using a hard sphere equation of state, J. Nucl. Mater. 131 (1985) 118–125. doi:10.1016/0022-3115(85)90450-7.

[142] Y. Dai, G.R.R. Odette, T. Yamamoto, The Effects of Helium in Irradiated Structural Alloys, Elsevier, 2012. doi:10.1016/B978-0-08-056033-5.00006-9.

[143] Y. Dai, X.J. Jia, K. Farrell, Mechanical properties of modified 9Cr-1Mo (T91) irradiated at ≤300 °C in SINQ Target-3, J. Nucl. Mater. 318 (2003) 192–199. doi:10.1016/S0022-

3115(03)00100-4.

[144] E1019, Standard Test Methods for Determination of Carbon, Sulfur, Nitrogen, and Oxygen in Steel, Iron, Nickel, and Cobalt Alloys by Various Combustion and Inert Gas Fusion Techniques, ASTM Stand. i (2018) 1–22. doi:10.1520/E1019-18.2.

[145] ASTM Standard E1097, Standard Guide for Determination of Various Elements by Direct Current Plasma Atomic Emission Spectrometry, i (2012) 1–8. doi:10.1520/E1097-12.

[146] Z. Jiao, S. Taller, K. Field, G. Yeli, M.P. Moody, G.S. Was, Microstructure evolution of T91 irradiated in the BOR60 fast reactor, J. Nucl. Mater. 504 (2018). doi:10.1016/j.jnucmat.2018.03.024.

[147] A. Monterrosa, The Role of Pre-Implanted Helium and Carbon on Cavity Evolution in Ion-Irradiated T91, (2018). https://deepblue.lib.umich.edu/handle/2027.42/143960.

[148] S. Taller, D. Woodley, E. Getto, A.M. Monterrosa, Z. Jiao, O. Toader, F. Naab, T. Kubley, S. Dwaraknath, G.S. Was, Multiple ion beam irradiation for the study of radiation damage in materials, Nucl. Instruments Methods Phys. Res. Sect. B Beam Interact. with Mater. Atoms. 412 (2017) 1–10. doi:10.1016/j.nimb.2017.08.035.

[149] J.F. Ziegler, M.D. Ziegler, J.P. Biersack, SRIM - The stopping and range of ions in matter (2010), Nucl. Instruments Methods Phys. Res. Sect. B Beam Interact. with Mater. Atoms. 268 (2010) 1818–1823. doi:10.1016/j.nimb.2010.02.091.

[150] Standard Practice for Investigating the Effects of Neutron Radiation Damage Using Charged-Particle Irradiation, West Conshohocken, PA, 2016. doi:10.1520/E0521-16.

[151] M.J. Hackett, C. Xu, BOR-60 Temperature and Damage Calculations for M98 to M102A Micro-runs, (n.d.).

[152] L.R. Greenwood, R.K. Smither, SPECTER: Neutron Damage Calculations for Materials

Irradiations, Argonne, IL, 1985.

[153] J.-C.C. Sublet, J.W. Eastwood, J.G. Morgan, M. Fleming, M.R. Gilbert, The FISPACT-II User Manual, Abingdon, Oxfordshire, 2015.

[154] M.B. Chadwick, M. Herman, P. Obložinský, M.E. Dunn, Y. Danon, A.C. Kahler, D.L. Smith, B. Pritychenko, G. Arbanas, R. Arcilla, R. Brewer, D.A. Brown, R. Capote, A.D. Carlson, Y.S. Cho, H. Derrien, K. Guber, G.M. Hale, S. Hoblit, S. Holloway, T.D. Johnson, T. Kawano, B.C. Kiedrowski, H. Kim, S. Kunieda, N.M. Larson, L. Leal, J.P. Lestone, R.C. Little, E.A. McCutchan, R.E. MacFarlane, M. MacInnes, C.M. Mattoon, R.D. McKnight, S.F. Mughabghab, G.P.A. Nobre, G. Palmiotti, A. Palumbo, M.T. Pigni, V.G. Pronyaev, R.O. Sayer, A.A. Sonzogni, N.C. Summers, P. Talou, I.J. Thompson, A. Trkov, R.L. Vogt, S.C. van der Marck, A. Wallner, M.C. White, D. Wiarda, P.G. Young, ENDF/B-VII.1 nuclear data for science and technology: Cross sections, covariances, fission product yields and decay data, Nucl. Data Sheets. 112 (2011) 2887–2996. doi:10.1016/j.nds.2011.11.002.

[155] C.M. Parish, N.A.P. Kiran Kumar, L.L. Snead, P.D. Edmondson, K.G. Field, C. Silva, A. Marie Williams, K. Linton, K.J. Leonard, LAMDA: Irradiated-Materials Microscopy at Oak Ridge National Laboratory, Microsc. Microanal. 21 (2015) 1003–1004. doi:10.1017/S1431927615005814.

[156] K. Sun, Resolution Limits for JEOL 2100F and JEOL 2010F at the Michigan Center for Materials Characterization, (n.d.).

[157] B. Yao, D.J. Edwards, R.J. Kurtz, G.R. Odette, T. Yamamoto, Multislice simulation of transmission electron microscopy imaging of helium bubbles in Fe, J. Electron Microsc. (Tokyo). 61 (2012) 393–400. doi:10.1093/jmicro/dfs065.

[158] T. Malis, S.C. Cheng, R.F. Egerton, EELS log-ratio technique for specimen-thickness measurement in the TEM, J. Electron Microsc. Tech. 8 (1988) 193–200. doi:10.1002/jemt.1060080206.

[159] J. Schindelin, I. Arganda-Carreras, E. Frise, V. Kaynig, M. Longair, T. Pietzsch, S. Preibisch, C. Rueden, S. Saalfeld, B. Schmid, J.Y. Tinevez, D.J. White, V. Hartenstein, K. Eliceiri, P. Tomancak, A. Cardona, Fiji: An open-source platform for biological-image analysis, Nat. Methods. 9 (2012) 676–682. doi:10.1038/nmeth.2019.

[160] E.M. Getto, The Co-Evolution of Microstructure Features in Self-Ion Irradiated HT9 at Very High Damage Levels, University of Michigan, 2016. doi:2027.42/135912.

[161] B. Yao, D.J. Edwards, R.J. Kurtz, TEM characterization of dislocation loops in irradiated bcc Fe-based steels, J. Nucl. Mater. 434 (2013) 402–410. doi:10.1016/j.jnucmat.2012.12.002.

[162] I.R. Brearley, D.A. MacInnes, An improved equation of state for inert gases at high pressures, J. Nucl. Mater. 95 (1980) 239–252. doi:10.1016/0022-3115(80)90365-7.

[163] Z. Chang, D. Terentyev, N. Sandberg, K. Samuelsson, P. Olsson, Anomalous bias factors of dislocations in bcc iron, J. Nucl. Mater. 461 (2015) 221–229. doi:10.1016/j.jnucmat.2015.03.025.

[164] T. Jourdan, Influence of dislocation and dislocation loop biases on microstructures simulated by rate equation cluster dynamics, J. Nucl. Mater. 467 (2015) 286–301. doi:10.1016/j.jnucmat.2015.09.046.

[165] W.G. Wolfer, The dislocation bias, J. Comput. Mater. Des. 14 (2007) 403–417. doi:10.1007/s10820-007-9051-3.

[166] F.S. Ham, Stress-Assisted Precipitation on Dislocations, J. Appl. Phys. 30 (1959) 915–

926. doi:10.1063/1.1735262.

[167] S.I. Golubov, B.N. Singh, H. Trinkaus, On recoil-energy-dependent defect accumulation in pure copper Part II. Theoretical treatment, Philos. Mag. A Phys. Condens. Matter, Struct. Defects Mech. Prop. 81 (2001) 2533–2552. doi:10.1080/01418610108217162.

[168] B.H. Sencer, J.R. Kennedy, J.. . Cole, S.A. Maloy, F.A. Garner, Microstructural analysis of an HT9 fuel assembly duct irradiated in FFTF to 155 dpa at 443°C, J. Nucl. Mater. 393 (2009) 235–241. doi:10.1016/j.jnucmat.2009.06.010.

[169] G.R. Odette, On mechanisms controlling swelling in ferritic and martensitic alloys, J. Nucl. Mater. 155–157 (1988) 921–927. doi:10.1016/0022-3115(88)90442-4.

[170] G.P. Walters, The electron irradiation of pure Fe-Cr-Ni alloys in the temperature range 400 to 700° C, J. Nucl. Mater. 136 (1985) 263–279. doi:10.1016/0022-3115(85)90014-5.

[171] J.L. Brimhall, L.A. Charlot, E.P. Simonen, Effect of pulsed irradiation on void swelling in nickel, J. Nucl. Mater. 104 (1981) 1147–1150. doi:10.1016/0022-3115(82)90755-3.

[172] M.J. Caturla, C.J. Ortiz, Effect of self-interstitial cluster migration on helium diffusion in iron, J. Nucl. Mater. 362 (2007) 141–145. doi:10.1016/j.jnucmat.2007.01.017.

[173] A. van Veen, A.. Fedorov, A.. Ryazanov, Influence of thermal treatment on helium trapping at fine-size precipitates in V–4Cr–4Ti, J. Nucl. Mater. 258–263 (1998) 1400–1403. doi:10.1016/S0022-3115(98)00292-X.

[174] H.L. Heinisch, F. Gao, R.J. Kurtz, E. a. Le, Interaction of helium atoms with edge dislocations in α-Fe, J. Nucl. Mater. 351 (2006) 141–148. doi:10.1016/j.jnucmat.2006.02.027.

[175] J. Hetherly, E. Martinez, M. Nastasi, a. Caro, Helium bubble growth at BCC twist grain boundaries, J. Nucl. Mater. 419 (2011) 201–207. doi:10.1016/j.jnucmat.2011.08.009.

[176] H.Q. Deng, W.Y. Hu, F. Gao, H.L. Heinisch, S.Y. Hu, Y.L. Li, R.J. Kurtz, Diffusion of small He clusters in bulk and grain boundaries in a -Fe, 442 (2013) 667–673. doi:10.1016/j.jnucmat.2013.02.063.

[177] F. Gao, H.L. Heinisch, R.J. Kurtz, Diffusion of He interstitial and di-He cluster at grain boundaries in α-Fe, J. Nucl. Mater. 367-370 A (2007) 446–450. doi:10.1016/j.jnucmat.2007.03.021.

[178] M.A. Tschopp, F. Gao, K.N. Solanki, He–V cluster nucleation and growth in α-Fe grain boundaries, Acta Mater. 124 (2017) 544–555. doi:10.1016/j.actamat.2016.11.027.

[179] F. Gao, H.L. Heinisch, R.J. Kurtz, Diffusion of He interstitials in grain boundaries in a-Fe, J. Nucl. Mater. 351 (2006) 133–140. .%5Cpdf terenty%5CGao_He_diffusion_at_GB.pdf.

[180] Y. Wu, G.R. Odette, T. Yamamoto, J. Ciston, P. Hosemann, An electron eneregy loss spectroscopy study of helium bubbles in nanostructured ferritic alloys, Fusion React. Mater. Progr. 54 (2013) 173–179.

[181] R. Sugano, K. Morishita, Effects of dislocation on thermal helium desorption from iron and ferritic steel, 311 (2002) 941–945.

[182] X.Z. Cao, Q. Xu, K. Sato, T. Yoshiie, Effects of dislocations on thermal helium desorption from nickel and iron, J. Nucl. Mater. 417 (2011) 1034–1037. doi:10.1016/j.jnucmat.2010.12.212.

[183] X. Hu, K.G. Field, S. Taller, Y. Katoh, B.D. Wirth, Impact of neutron irradiation on thermal helium desorption from iron, J. Nucl. Mater. 489 (2017) 109–117. doi:10.1016/j.jnucmat.2017.03.034.

[184] T. Zhu, S. Jin, Y. Gong, E. Lu, L. Song, Q. Xu, L. Guo, X. Cao, B. Wang, The influence of dislocation and hydrogen on thermal helium desorption behavior in Fe9Cr alloys, J.

Nucl. Mater. 495 (2017) 244–248. doi:10.1016/j.jnucmat.2017.08.027.

[185] C.C. Fu, F. Willaime, Ab initio study of helium in α-Fe: Dissolution, migration, and clustering with vacancies, Phys. Rev. B - Condens. Matter Mater. Phys. 72 (2005) 1–6. doi:10.1103/PhysRevB.72.064117.

[186] H.L. Heinisch, F. Gao, R.J. Kurtz, Atomistic modeling of helium interacting with screw dislocations in α-Fe, J. Nucl. Mater. 367–370 (2007) 311–315. doi:10.1016/j.jnucmat.2007.03.035.

[187] R.J. Kurtz, H.L. Heinisch, F. Gao, Modeling of He–defect interactions in ferritic alloys for fusion, J. Nucl. Mater. 382 (2008) 134–142. doi:10.1016/j.jnucmat.2008.08.020.

[188] E. Torres, C. Judge, H. Rajakumar, A. Korinek, J. Pencer, G. Bickel, Atomistic simulations and experimental measurements of helium nano-bubbles in nickel, J. Nucl. Mater. 495 (2017) 475–483. doi:10.1016/j.jnucmat.2017.08.044.

[189] G. Amarendra, B. Viswanathan, A. Bharathi, K.P. Gopinathan, Nucleation and growth of helium bubbles in nickel studied by positron-annihilation spectroscopy, Phys. Rev. B. 45 (1992) 10231–10241. doi:10.1103/PhysRevB.45.10231.

[190] C.D. Judge, V. Bhakhri, Z. Jiao, R.J. Klassen, G. Was, G.A. Botton, M. Griffiths, The effects of proton irradiation on the microstructural and mechanical property evolution of inconel X-750 with high concentrations of helium, J. Nucl. Mater. 492 (2017) 213–226. doi:10.1016/j.jnucmat.2017.04.045.

[191] R.E. Stoller, G.R. Odette, B.D. Wirth, Primary damage formation in bcc iron, J. Nucl. Mater. 251 (1997) 49–60. doi:10.1016/S0022-3115(97)00256-0.

[192] D. Stewart, Y. Osetskiy, R. Stoller, Atomistic studies of formation and diffusion of helium clusters and bubbles in BCC iron, J. Nucl. Mater. 417 (2011) 1110–1114.

doi:10.1016/j.jnucmat.2010.12.217.

[193] L. Yang, X.T. Zu, Z.G. Wang, F. Gao, X.Y. Wang, H.L. Heinisch, R.J. Kurtz, Interaction of helium–vacancy clusters with edge dislocations in α-Fe, Nucl. Instruments Methods Phys. Res. Sect. B Beam Interact. with Mater. Atoms. 265 (2007) 541–546. doi:10.1016/j.nimb.2007.10.007.

[194] ASTM A213, Standard Specification for Seamless Ferritic and Austenitic Alloy-Steel Boiler, Superheater, and Heat-Exchanger Tubes, (2011) 1–14. doi:10.1520/A0213.

[195] S.J. Zinkle, Radiation-induced effects on microstructure, Elsevier, 2012. doi:10.1016/B978-0-08-056033-5.00003-3.

[196] K.L. Wong, H.J. Lee, J.H. Shim, B. Sadigh, B.D. Wirth, Multiscale modeling of point defect interactions in Fe-Cr alloys, J. Nucl. Mater. 386–388 (2009) 227–230. .%5Cpdf terenty%5CWong09_JNM_PDef_in_FeCr.pdf.

[197] S. Choudhury, L. Barnard, J.D. Tucker, T.R. Allen, B.D. Wirth, M. Asta, D. Morgan, Ab-initio based modeling of diffusion in dilute bcc Fe-Ni and Fe-Cr alloys and implications for radiation induced segregation, J. Nucl. Mater. 411 (2011) 1–14. doi:10.1016/j.jnucmat.2010.12.231.

[198] P. Olsson, Ab initio study of interstitial migration in Fe-Cr alloys, J. Nucl. Mater. 386–388 (2009) 86–89. doi:10.1016/j.jnucmat.2008.12.065.

[199] C.C. Fu, F. Willaime, P. Ordejón, Stability and mobility of mono- and Di-interstitials in α-Fe, Phys. Rev. Lett. 92 (2004) 1–4. doi:10.1103/PhysRevLett.92.175503.

[200] S. Schönecker, X. Li, B. Johansson, S.K. Kwon, L. Vitos, Thermal surface free energy and stress of iron, Sci. Rep. 5 (2015) 1–7. doi:10.1038/srep14860.

[201] A.T. Price, H.A. Holl, A.P. Greenough, The surface energy and self diffusion coefficient

of solid iron above 1350°C, Acta Metall. 12 (1964) 49–58. doi:10.1016/0001-6160(64)90053-7.

[202] B.C. Allen, The surface tension of liquid transition metals at their melting points, Trans. AIME. 227 (1963) 1175.

[203] W.R. Tyson, W.A. Miller, Surface free energies of solid metals: Estimation from liquid surface tension measurements, Surf. Sci. 62 (1977) 267–276. doi:10.1016/0039-6028(77)90442-3.

[204] F.R. de Boer, R. Boom, W.C.M. Mattens, A.R. Miedema, A.K. Niessen, Cohension in metals: Transition Metal Alloys, North-Holland, Amsterdam, 1988.

[205] H.E. Schaefer, K. Maier, M. Weller, D. Herlach, A. Seeger, J. Diehl, Vacancy formation in iron investigated by positron annihilation in thermal equilibrium, Scr. Metall. 11 (1977) 803–809. doi:10.1016/0036-9748(77)90079-5.

[206] H. Matter, J. Winter, W. Triftshäuser, Phase transformations and vacancy formation energies of transition metals by positron annihilation, Appl. Phys. 20 (1979) 135–140. doi:10.1007/BF00885934.

[207] W.G. Wolfer, L.K. Mansur, The capture efficiency of coated voids, J. Nucl. Mater. 91 (1980) 265–276. doi:10.1016/0022-3115(80)90226-3.

[208] L. Mansur, W. Wolfer, Influence of a surface coating on void formation, J. Nucl. Mater. 70 (1978) 825–829. http://www.sciencedirect.com/science/article/pii/0022311578903537.

[209] F.A. Garner, W.G. Wolfer, The effect of solute additions on void nucleation, J. Nucl. Mater. 102 (1981) 143–150. doi:10.1016/0022-3115(81)90554-7.

[210] W. Luo, W. Hu, K. Su, F. Liu, The calculation of surface free energy based on embedded atom method for solid nickel, Appl. Surf. Sci. 265 (2013) 375–378.

doi:10.1016/j.apsusc.2012.11.015.

[211] S. Hara, S. Izumi, T. Kumagai, S. Sakai, Surface energy, stress and structure of well-relaxed amorphous silicon: A combination approach of ab initio and classical molecular dynamics, Surf. Sci. 585 (2005) 17–24. doi:10.1016/j.susc.2005.03.061.

[212] E. Martínez, D. Schwen, A. Caro, Helium segregation to screw and edge dislocations in α-iron and their yield strength, Acta Mater. 84 (2015) 208–214. doi:10.1016/j.actamat.2014.10.066.

[213] B.N. Singh, a. J.E. Foreman, Helium diffusion and bubble nucleation in the dislocation core during irradiation, J. Nucl. Mater. 191–194 (1992) 1265–1268. doi:10.1016/0022-3115(92)90677-D.

[214] A. Bhattacharya, E. Meslin, J. Henry, F. Leprêtre, B. Décamps, A. Barbu, Combined effect of injected interstitials and He implantation, and cavities inside dislocation loops in high purity Fe-Cr alloys, J. Nucl. Mater. 519 (2019) 30–44. doi:10.1016/j.jnucmat.2019.03.043.

[215] D. Sun, P. Zhang, J. Ding, J. Zhao, Helium behavior in different oxides inside ODS steels: A comparative ab initio study, J. Nucl. Mater. 507 (2018) 101–111. doi:10.1016/j.jnucmat.2018.04.048.

[216] H.J. Jung, D.J. Edwards, R.J. Kurtz, T. Yamamoto, Y. Wu, G.R. Odette, Structural and chemical evolution in neutron irradiated and helium-injected ferritic ODS PM2000 alloy, J. Nucl. Mater. 484 (2017) 68–80. doi:10.1016/j.jnucmat.2016.11.022.

[217] J. Chen, P. Jung, W. Hoffelner, H. Ullmaier, Dislocation loops and bubbles in oxide dispersion strengthened ferritic steel after helium implantation under stress, Acta Mater. 56 (2008) 250–258. doi:10.1016/j.actamat.2007.09.016.

[218] a. J.E. Foreman, B.N. Singh, Helium flux to grain boundaries during irradiation, J. Nucl. Mater. 149 (1987) 266–268. doi:10.1016/0022-3115(87)90486-7.

[219] A.A. Kohnert, L. Capolungo, A novel approach to quantifying the kinetics of point defect absorption at dislocations, J. Mech. Phys. Solids. 122 (2019) 98–115. doi:10.1016/j.jmps.2018.08.023.

[220] A.D. Brailsford, R. Bullough, The rate theory of swelling due to void growth in irradiated metals, J. Nucl. Mater. 44 (1972) 121–135. doi:10.1016/0022-3115(72)90091-8.

[221] L.K. Mansur, Correlation of neutron and heavy-ion damage. II. The predicted temperature shift if swelling with changes in radiation dose rate, J. Nucl. Mater. 78 (1978) 156–160. doi:10.1016/0022-3115(78)90514-7.

[222] L.K. Mansur, Correlation of neutron and heavy-ion damage, J. Nucl. Mater. 78 (1978) 156–160. doi:10.1016/0022-3115(78)90514-7.

[223] Y.X. Wei, N. Gao, D. Wang, C. Chen, L.P. Guo, Effect of hydrogen atom concentration on hydrogen migration and bubble evolution in bcc iron, Nucl. Instruments Methods Phys. Res. Sect. B Beam Interact. with Mater. Atoms. 461 (2019) 83–87. doi:10.1016/j.nimb.2019.09.025.

[224] E. Hayward, C. Deo, Energetics of small hydrogen-vacancy clusters in bcc iron., J. Phys. Condens. Matter. 23 (2011) 425402. doi:10.1088/0953-8984/23/42/425402.

[225] T. Tanaka, K. Oka, S. Ohnuki, S. Yamashita, T. Suda, S. Watanabe, E. Wakai, Synergistic effect of helium and hydrogen for defect evolution under multi-ion irradiation of Fe–Cr ferritic alloys, J. Nucl. Mater. 329–333 (2004) 294–298. doi:10.1016/j.jnucmat.2004.04.051.

[226] S.T. Picraux, J. Bøttiger, N. Rud, Enhanced hydrogen trapping due to He ion damage, J.

Nucl. Mater. 63 (1976) 110–114. doi:10.1016/0022-3115(76)90311-1.

[227] N. Sekimura, T. Iwai, Y. Arai, S. Yonamine, A. Naito, Y. Miwa, S. Hamada, Synergistic effects of hydrogen and helium on microstructural evolution in vanadium alloys by triple ion beam irradiation, J. Nucl. Mater. 283–287 (2000) 224–228. doi:10.1016/S0022-3115(00)00341-X.

[228] J. Marian, T. Hoang, M. Fluss, L.L. Hsiung, A review of helium–hydrogen synergistic effects in radiation damage observed in fusion energy steels and an interaction model to guide future understanding, J. Nucl. Mater. 462 (2015) 409–421. doi:10.1016/j.jnucmat.2014.12.046.

[229] A. Kohyama, Y. Katoh, M. Ando, K. Jimbo, A new Multiple Beams–Material Interaction Research Facility for radiation damage studies in fusion materials, Fusion Eng. Des. 51–52 (2000) 789–795. doi:10.1016/S0920-3796(00)00181-2.

[230] S. Hamada, Y. Miwa, D. Yamaki, Y. Katano, T. Nakazawa, K. Noda, Development of a triple beam irradiation facility, J. Nucl. Mater. 258–263 (1998) 383–387. doi:10.1016/S0022-3115(98)00232-3.

[231] M. Mayer, SIMNRA, a simulation program for the analysis of NRA, RBS and ERDA, AIP Conf. Proc. 475 (1999) 541–544. doi:10.1063/1.59188.

[232] R.O. Sayer, Semi-empirical formulas for heavy-ion stripping data, Rev. Phys. Appliquée. 12 (1977) 1543–1546. doi:10.1051/rphysap:0197700120100154300.

[233] P.D. Miller, G.C. Phillips, Scattering of Protons from Helium and Level Parameters in Li5, Phys. Rev. 112 (1958) 2043–2047.

[234] V. Godinho, F.J. Ferrer, B. Fernández, J. Caballero-Hernández, J. Gómez-Camacho, A. Fernández, Characterization and validation of a-Si magnetron-sputtered thin films as solid

he targets with high stability for nuclear reactions, ACS Omega. 1 (2016) 1229–1238. doi:10.1021/acsomega.6b00270.

[235] Ion Beam Analysis Nuclear Data Library, (2019). http://www-nds.iaea.org/ibandl/.

[236] R. Amirikas, D.N. Jamieson, S.P. Dooley, Measurement of (p, p) elastic cross sections for C, O and Si in the energy range 1.0-3.5 MeV, Nucl. Inst. Methods Phys. Res. B. 77 (1993) 110–116. doi:10.1016/0168-583X(93)95531-9.

[237] I. Arganda-Carreras, V. Kaynig, C. Rueden, K.W. Eliceiri, J. Schindelin, A. Cardona, H.S. Seung, Trainable Weka Segmentation: A machine learning tool for microscopy pixel classification, Bioinformatics. 33 (2017) 2424–2426. doi:10.1093/bioinformatics/btx180.

[238] R.D. Hanbury, G.S. Was, Oxide growth and dissolution on 316L stainless steel during irradiation in high temperature water, Corros. Sci. 157 (2019) 305–311. doi:10.1016/j.corsci.2019.06.006.